A portable multi-modal micro-imaging system for automated scanning and image stitching applications

By

ADAM NAQVI

School of Engineering and Advanced Technology
MASSEY UNIVERSITY

A thesis submitted to Massey University in accordance with the requirements of the degree of MASTER OF ENGINEERING in the School of Engineering and Advanced Technology.

JUNE 2019

Abstract

Microscopic imaging is an important element in many fields like biology, medicine, diagnostics, engineering, and materials research. Muti-modal microscopes are ideal for imaging samples that reveal unseen structures that could not otherwise be seen with normal bright-field microscopes. Point-of-care micro-imaging devices are ones that can deliver the features of a microscope in areas where access to a laboratory or medical facilities are scarce.

This thesis presents the development of a portable micro-imaging system that uses multi-modal illumination to image samples in bright-field, fluorescence, ambient and laser diffraction modes. A systematic design method has been used to develop the system from the conceptual phase to a working prototype. The system incorporates variable magnification through an inverted turret system and a GUI application for live image view, automatic scanning, auto-focusing and image processing.

The utility of the system is demonstrated through imaging stained biological samples for a local industry application. The acquired images are measured against sharpness and noise. It is observed that the sharpness and noise of the images produced vary with the type of sample: samples with higher contrast generally produce sharper images with less noise. It has also been found that diffused ambient illumination produces the most consistent sharpness and noise scores between magnifications. Performance of algorithms used is discussed and improvements are suggested for building a more compact and stable platform including a method to calibrate measurements for particle size estimation.

Dedication and acknowledgements

Thanks to all those who had supported me throughout this research project. I would like to express my great appreciation to Dr Khalid Arif for his advice, mentorship, providing resources when I needed them and for giving his time so generously to this project. Thanks to my family for their continued support, especially my mother for her positivity, encouragement and patience. Thanks to the staff in the electronics lab and workshop who allowed me to use the facilities to manufacture parts. I would also like to extend my gratitude to the Institute of Environmental Science and Research (ESR) who kindly provided real biological samples to test and characterize the system.

AUTHOR'S DECLARATION

I declare that the work in this thesis was carried out in accordance with the requirements of the University's Regulations and Code of Practice for Research Degree Programmes and that it has not been submitted for any other academic award. Except where indicated by specific reference in the text, the work is the candidate's own work. Work done in collaboration with, or with the assistance of, others, is indicated as such. Any views expressed in the thesis are those of the author.

SIGNED: ..... DATE: .....

TABLE OF CONTENTS

List of Tables

Table **Page**

List of Figures

Figure **Page**

List of Acronyms

CR Customer Requirement. 34

EC Engineering Characteristics. 35

ESR Environmental Science and Research. 131

FLP Fuzzy Linear Programming. 38

ICE Image Composite Editor. 19

LP Linear Programming. 39

MOLP Multi-Objective Linear Programming. 39

PDS Product Design and Selection. viii, 33

QFD Quality Function and Deployment. 33

TEM Transmission Electron Microscopy. 20

List of Definitions

Dichroic mirror A mirror that acts as a high-pass filter for light waves. 81

Diffraction grating A plate created with specific width bands that allow laser light to be diffracted into different modes. 13

Fluorescent sample A sample that emits (or fluoresces) a certain wavelength of light when excited by a certain wavelength of light. 79

Ghost images Usually unfocused duplicate images appearing on a captured image. 86

Infinity corrected objective lens An objective lens that causes light rays to become parallel rather than converge. 78

Neutral optical density filter A filter that reduces the intensity of incoming light rays. 78

Oil immersion objectives An objective lens that requires oil to be used. 13

Pedograph The analysis of a footprint or a device used to obtain footprints for analysis. 21

Phase contrast microscopy A type of microscopy that converts phase shifts in light passing through phase objects into contrast. 14

Phase objects Objects that produce a phase shift when light rays pass through them. xxiii

Photon Elementary particle of light. 10

Point-of-care In the medical context, relating to medical testing, or the usage of a medical device, at the time and location of required care i.e. 'bedside'. 1

Reflectance Ability of an object or surface to reflect light. viii, 79

CHAPTER 1

INTRODUCTION

Microscopy is a field that has benefited both industrial and research sectors. It has been used extensively in medical research such as observing micro-organisms to find causes and cures for diseases [32, 33]. Microscopes have important features, such as variable magnification and automated scanning, and are increasingly required at point-of-care sites where access to medical or laboratory facilities are not readily available [34, 35]. Point-of-care portable micro-imaging field devices address this issue and have seen an increasing level of research in the past with scope for further development. Multi-modal microscope systems are ones that employ the use of different modes of illumination to see the same sample under different lighting conditions - often revealing details not previously seen in more standard forms of illumination. There is a gap for the design of a portable micro-imaging device that uses different forms of illumination and that incorporates variable magnification and automated scanning.

1.1 Motivation

Standard desk-top microscope systems are bulky [36–38] and are unable to be used in point-of-care applications or similar [39, 40]. This research aims to create a portable multi-modal micro-imaging system that incorporates variable magnification and automated scanning features to address this problem. By doing so, the design will effectively demonstrate that it can be done and also be used as a basis to develop further micro-imaging systems for potential uses in point-of-care applications.

Variable magnification is required because it is a standard feature in most microscopes and is usually required to see a sample in more detail.

The use of automated scanning is useful because, at times, an operator is trying to find a particular object within a sample, such as sperm cells in a crime scene sample, and locating it

manually can be a tedious task. As such, using an automated scanning feature will avoid the operator having to do this.

The aim of this project is to research and design a portable multi-modal micro-imaging system that incorporates variable magnification and automated scanning.

1.2 Objectives

To achieve the aims of this research, the following objectives have been identified:

- Development of a research platform that incorporates:

  Bright-field, fluorescence and laser diffraction illumination

  Variable magnification

  Automated scanning

- Verification of both optical and mechanical simulation models

1.3 Thesis Outline

- Chapter 1 is the introduction chapter which relates the background and motivation behind the research
- Chapter 2 contains the literature review of microscopy history, elements of microscopy, image processing, previous designs, design methodologies
- Chapter 3 details the design development of the research platform
- Chapter 4 verifies the mechanical and optical simulations models.
- Chapter 5 shows the development of the software aspect of the platform
- Chapter 6 shows the results of the platform including the quality of the images and performance of the software algorithms. This section also details the industry application of the system where samples from the Institute of Environmental Science and Research (ESR) were sampled. The specific objective was to characterize the images produced by the current system with the ESR samples
- Chapter 7 discusses the results from Chapter 6
- Chapter 8 concludes the work and talks about future work

CHAPTER 2

LITERATURE REVIEW

Microscope development is not a new field in the last century. A great number of designs and layouts have emerged for clinical, industrial and lab environments. In this chapter an overview of the recent developments is presented with focus on miniaturized, compact, all-in-one, point-of-care systems.

2.1 History of Microscopy (721BC - 1830AD)

Microscopy is the field of study where a sample is magnified, usually with a lens or series of lenses placed inside a tubular structure, to see the samples' magnified physical appearance. The first recorded objects that resembled lenses date back to 721-705BC [41]. These appeared to be polished plano-convex pieces of rock crystal but were later found upon examination to be objects of jewelry [41]. The first practical use of lenses came around 1280 in Florence, Italy, where they were used as eyeglasses to aid vision [41].

Around the year 1595 it was found, most likely by Dutch spectacle makers Zacharias Janssen or his father Hans Janssen, that if two or more lenses were put together, rather than one, they would magnify the object even greater: this principle would be used to make the telescope and compound microscope. The telescope being credited to Hans Lippershey, a spectacle maker who happened to also live in the same town, and the microscope credited to either Zacharias or Hans Janssen.

Against popular opinion, Galileo did not invent the telescope: he rather constructed his own one in 1609 after coming to know of one made in the Netherlands [42]. Cornelius Drebbel was a Dutch instrument maker who was known to have made microscopes [42]. Although Drebbel most likely did not invent the microscope, Galileo is known to have made a microscope after he saw one of Drebbel's ones that had been taken to Italy [42]. Galileo's microscope consisted of a

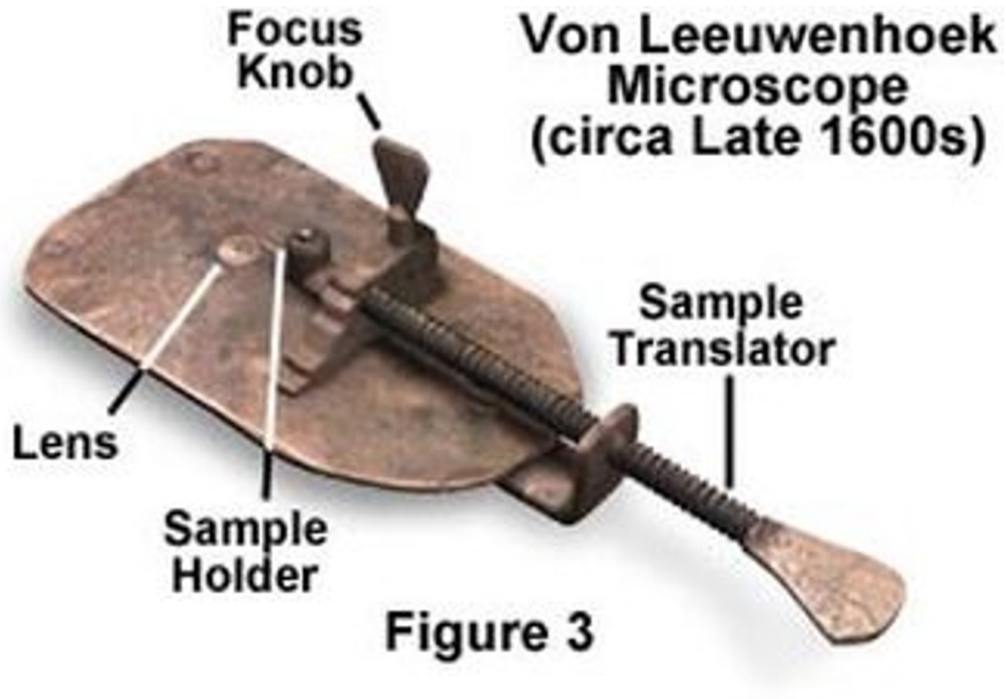

Figure 2.1: One of Leeuwenhoek's microscopes, found in [2]

tubular design of two pieces: one fitting into the other with a sliding action allowing the focus to be adjusted [42].

One of the earliest recorded works of microscopic observations were done in 1625 and 1630 of a bee and weevil by Federico Cesi and Francesco Stelluti [42]. Most likely these observations were made by the microscope device sent by Galileo as it was known that he had sent a microscope to Cesi in Rome [42].

Anthony Leeuwenhoek, from Holland, often known as the father of microscopy, manufactured his own lens with more curvature than previous lenses, allowing him to magnify by up to 300 times with resolution of up to 1.4 microns. He was the first to discover and document scientific experiments with microorganisms including bacteria, sperm cells and blood cells. Figure 2.1 shows one of his many microscopes.

Robert Hooke created the first real book on microscopic observations called 'Micrographia' [3]. In his book, he explained the construction of a single lens microscope as well as his compound microscope (see Fig. 2.2). More importantly, the book detailed natural and artificial objects from things like the point of a sewing needle to the eyes of insects. He also coined the term "cell" in one of his earlier works after looking at the tiny compartments of thin slices of cork.

Light refracts when it enters a medium of different density, for example when light goes from air to glass. Lenses work on this principal, where the light diffracts as it hits the spherical edge of the lens and usually converges to a point. In a perfect lens, light would focus at a single point, however, in reality, light rays focus at different points causing distortions in the image: this is

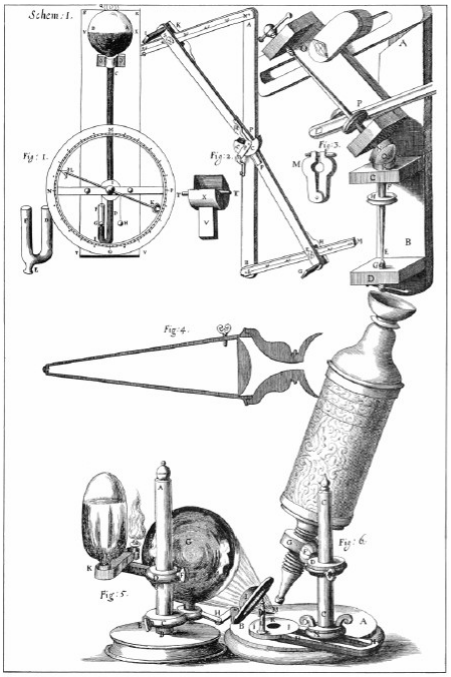

Figure 2.2: Hooke's Compound Microscope seen in 'Micrographia' [3]

known as spherical aberration.

From first principles, we know that white light is made up of different colours. In the same refraction process mentioned above, different wavelengths of light diffract at different angles. For a lens, this means that the focal point of different wavelengths of light will be at different points causing fringes around the magnified image [42]: this is known as chromatic aberration.

It was most likely due to spherical and chromatic aberration that Hooke used single lens microscopes [42] although despite these shortcomings, he still preferred to use the compound microscope [41].

Chromatic aberration was overcome in the 1730s by Chester Hall after he noticed that 'flint glass' dispersed colours more than 'crown glass'. George Bass, the lens maker who was asked to make it, noticed what was going on and made the first achromatic telescope - although he did not share his findings for 20 years. Another telescope maker, John Dolland, met with Bass and from hearing about flint and crowned glass, did his own experiments and patented the achromatic lens [41]. The achromatic lenses worked well for telescopes, but it would not be until the beginning the 19th century that they would be available for microscopes [41] due to their difficulty to manufacture.

Attempts to overcome spherical aberration were also made. One method was to simply use a lens with smaller curvature - but this limits the use to low magnification lenses. Another method was to introduce an aperture to allow light only from around the centre - but this reduces the resolution. Using multiple lenses only perpetuates the error with each lens: for both chromatic

and spherical aberration. In 1830, Joseph Lister came up with the idea that if you place several lenses of lower magnification at certain distances then spherical aberration will only be present in the first lens but not the others. It was not until later that his findings and prototypes were eventually used [41].

2.2 Hardware Development

2.2.1 Portability

Most modern microscopes are still desk-top systems that are restricted to the laboratory or clinical environments [19]. For areas such as point-of-care, where they are increasingly required, this presents a problem because they are unable to be moved easily and draw their power from electrical outlets. It is for this reason that for point-of-care environments, microscopes should be designed to be portable. Here we investigate two areas that contribute to microscopes portability: folded optics and batteries. We present research on optical systems that have incorporated them and the benefits that they have provided.

2.2.1.1 Folded Optics

Folded optics is where the path of light is altered, usually through mirrors or beam-splitters, to normally reduce the overall size of the imaging system. Reducing the size of the imaging system makes it more compact and increases portability.

Periscopes are one of the most common examples of folded optics often used in submarines. Their basic working principle is to use two mirrors positioned 45° to the incident light ray. The light ray comes in and is redirected from one end to the other end (see Figure 2.3) . For the case of a submarine, if folded optics had not been used, the vessel may have had to surface to a higher level using an elongated telescope to see above water.

Binoculars use folded optics to transfer the path of light from the objectives to the eye piece. In the case of the porro-prism binoculars design (see Figure 2.4), the light comes through the objective lens and is redirected by the porro-prisms towards the eye piece. Without these prisms the length of the binoculars would be longer and less compact.

The cassegrain telescope was invented in 1672 by a priest named Laurent Cassegrain [43]. The telescope works by using folded optics through concave mirrors that redirect light onto a convex mirror which then focuses the light to the image plane (see Figure 2.5). Although the design was invented in the year 1672, its adoption came much later in comparison to other telescope designs: after 1900, but is now the standard in the design of research telescopes and radio antennas such as in the Goldstone Observatory [44].

Researchers at the University of California, San Diego created a lens that used folded optics like a cassegrain telescope [7]. The lens was made from a calcium fluoride substrate that was diamond machined to have aspheric mirrors profiles that directed and focused light back and

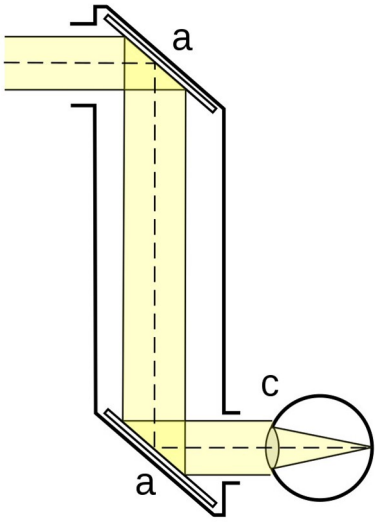

Figure 2.3: Periscope, found in [4]

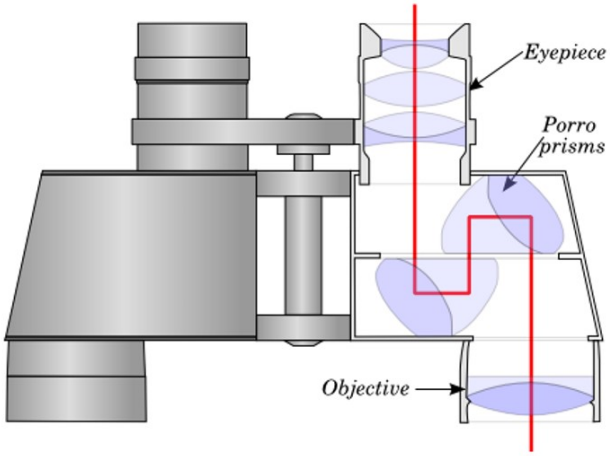

Figure 2.4: Typical porro-prism bincoulars, found in [5]

forth from an opposite planar mirror to a CCD sensor (see Figure 2.6). By using this system, they could effectively get an aperture diameter of 27mm, a numerical aperture of 0.7, a field-of-view of 0.12rad and a 38mm effective focal length within the space 68mm diameter x 5mm thick. The lens was demonstrated with a prototype camera module. By using folded optics, the weight of the system was reduced.

2.2.1.2 Batteries

Most standard desktop microscopes are constrained to using power from an electrical power outlet. Batteries facilitate power to a system so remove the need to connect to an electrical power outlet. Developments in longer lasting battery technology allowed for microscopes to draw power from them rather than power outlets, thereby facilitating portability. The research presented

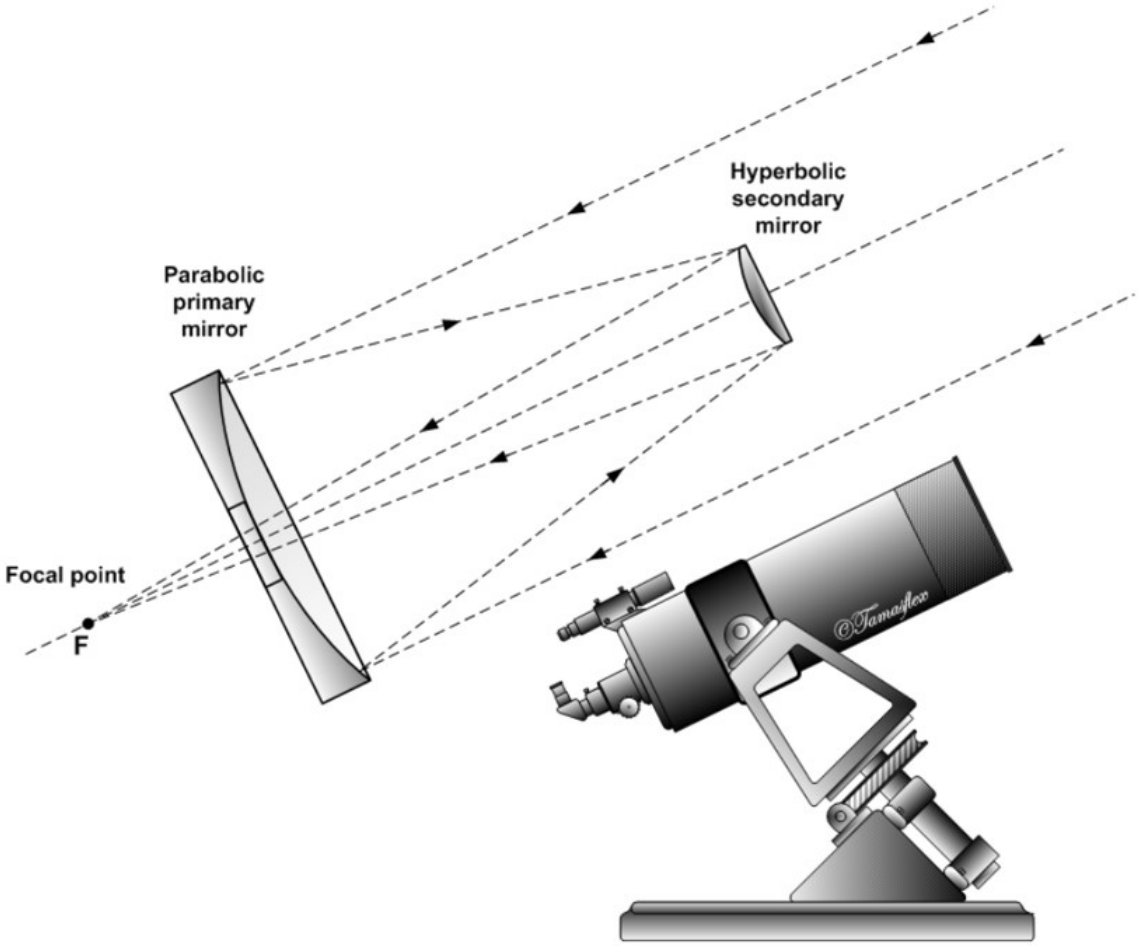

Figure 2.5: Working principle of Cassegrain Telescope , found in [6]

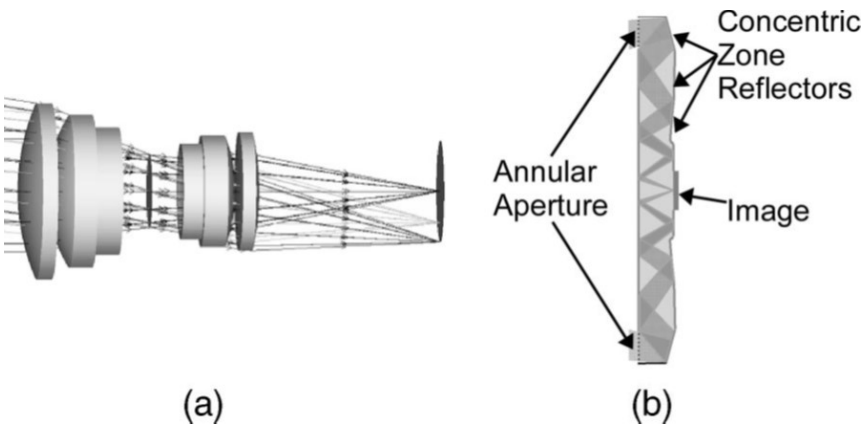

Figure 2.6: (a) Traditional refractive optics and (b) Annular folded optics concept where a series of aspheric mirror profiles direct and focus light (image is found as Fig.1 in [7] and has been reprinted with permission from [7] © The Optical Society)

here outlines three different rechargeable battery technologies in use today and examples of batteries used in portable microscopic systems.

2.2.1.2.1 Nickel Metal Hydride (NiMH)

A nickel-metal hydride battery uses a nickel oxide-hydroxide positive electrode and a hydrogen absorbing alloy as a negative electrode. They are often used in high-drain devices such as digital cameras mainly because of their low internal resistance. Typically they will have a 1.2V of nominal cell voltage, energy density of 240 Wh/L and charge retention, based on a 20°C, of 3-6 months [45].

2.2.1.2.2 Nickel Cadmium (NiCd)

Nickel-cadmium batteries use a nickel based positive electrode and cadmium as the negative electrode. Manufactured since 1909, mainly for heavy-duty industrial uses and eventually being used for portable devices after development of a sealed Ni-Cd battery [45]. They usually have a low specific energy but good performance at high discharge rates and have a 1.2V of nominal cell voltage, energy density of 100 Wh/L and charge retention, based on a 20°C, of 3-6 months [45]. They have been superseded by Nickel Metal Hydride batteries due to cadmium being a toxic element.

2.2.1.2.3 Lithium Ion (Li-Ion)

Lithium ion batteries usually have a lithium-doped cobalt oxide cathode and a graphite anode, although anodes have also taken on lithium titanate and tin-cobalt alloys with further research being done on using silicon ones as well. They typically have a 4.1V of nominal cell voltage, energy density of 400 Wh/L and charge retention, based on a 20°C, of 9-12 months [45]. Lithium ion batteries have applications in electric cars, smart phones, digital cameras and power tools. They have advantages of being both light weight and having a high energy density.

2.2.1.2.4 Applications of Battery in Microscopy

In 1997, researchers at San José University reported on the design of a battery powered atomic force microscope using piezoresistive cantilever [46]. The 6V Ni-Cd battery came from a camcorder and was sufficient in driving the scanning tube and detection electronics. The system used 1.8W of power and could scan continuously for about seven hours on a single battery charge.

Erickson et al demonstrated the use of a 12V MN21 cell battery to power a micro-fluidic device [47]. In their work, they characterize the power usage of their battery with a power cycling experiment using an equivalent resistor circuit. The results show that the battery could withstand as many as 40 successive flushing-dispensing cycles. Tsai et al [48] developed a battery powered system for single-HeLa-cell trapping and analyses.

2.2.2 Illumination Methods

Illumination is a necessary aspect of any microscope. Without illumination, the sample would not be able to be viewed. Different forms of illumination allow different kinds of details to be seen. Here we present five different kinds of illumination methods: bright-field, fluorescence, laser, dark field and ambient illumination and state their benefits and disadvantages.

2.2.2.1 Bright-field

Bright-field illumination method is where the sample is illuminated with white light and is the most standard form of illumination method. Since the beginning of microscopes, this was the main form of illumination method up until fluorescence microscopes started getting developed from the beginning of the 20th century [49]. Figure 2.7 shows a typical bright-field illumination setup for a desk-top microscope. The illuminator first emits white light towards the sample which goes through the objective. The sample then radiates this light through the objective lens, where the latter takes the radiated light and brings it to a focus on the sensor plane by using a tube lens.

2.2.2.2 Fluorescence

Fluorescence illumination is where a sample fluoresces at a specific wavelength of light to reveal details that may not have been possible to see with other forms of illumination such as bright-field.

In terms of the physics, a photon is first absorbed by a fluorescent molecule at a specific wavelength which causes the electrons in the molecule to go from their initial ground state to a higher excited state. From here, the electrons quickly collapse back to their initial ground state and, in doing so, release energy as fluorescent photons. These fluorescent photons vibrate at a lower frequency and have a longer wavelength than the photons that were first absorbed by the molecule because some of the energy is lost in the process of electrons collapsing to their initial ground state [50].

The method of fluorescence imaging works by first staining the sample with a fluorescent dye or using a sample that naturally fluoresces such as chlorophyll [51]. The light first passes through a fluorescence excitation filter and hits the sample which then fluoresces back light. This light then passes through an emission filter which only allows a certain wavelength of light to pass through (see Figure 2.8 of a typical fluorescent setup). This light is then projected onto a sensor plane such as that on camera. The resulting image shows only the fluorescent part of the sample. Figure 2.9 shows an image from the Nikon B-2A long-pass emission filter cube whose wavelength characteristics can be seen in Figure 2.10.

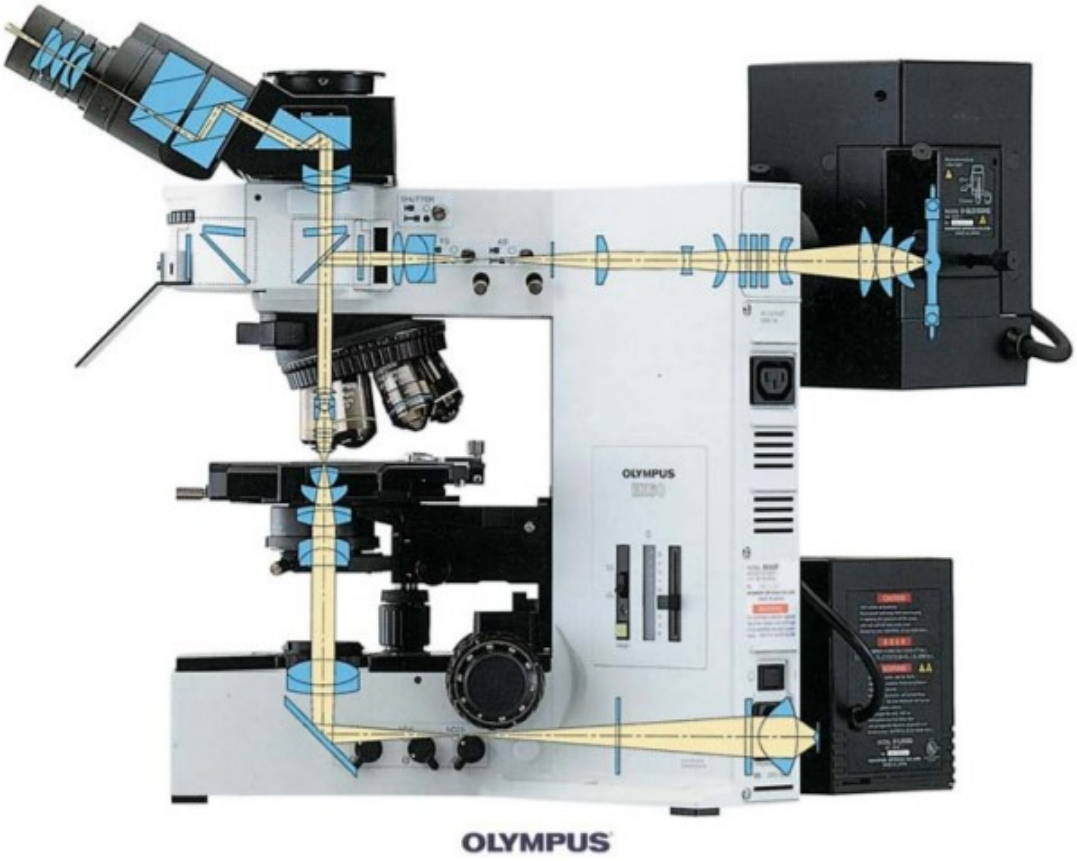

Figure 2.7: Common setup of standard microscopes (found as Color Plate 4-1 in [8])

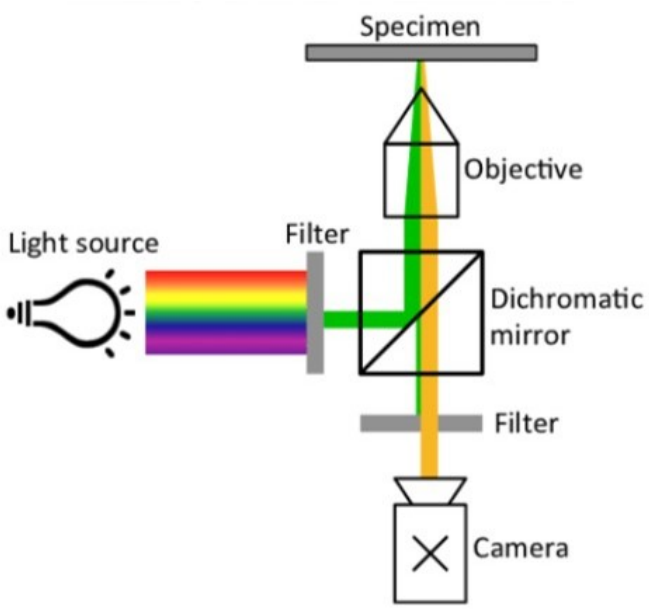

Figure 2.8: Basic setup of epi-fluorescent microscope (found as Fig. 6.2 in [9])

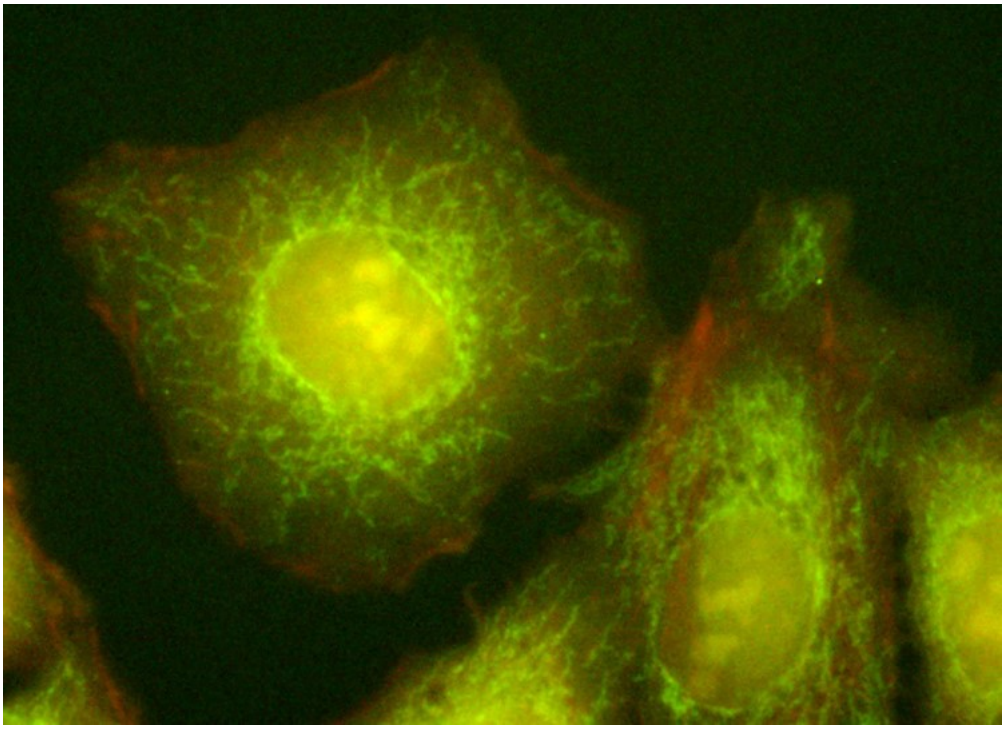

Figure 2.9: HeLa Cell Mitchondria observed with the Nikon B-2A Long-pass filter cube (found in [10])

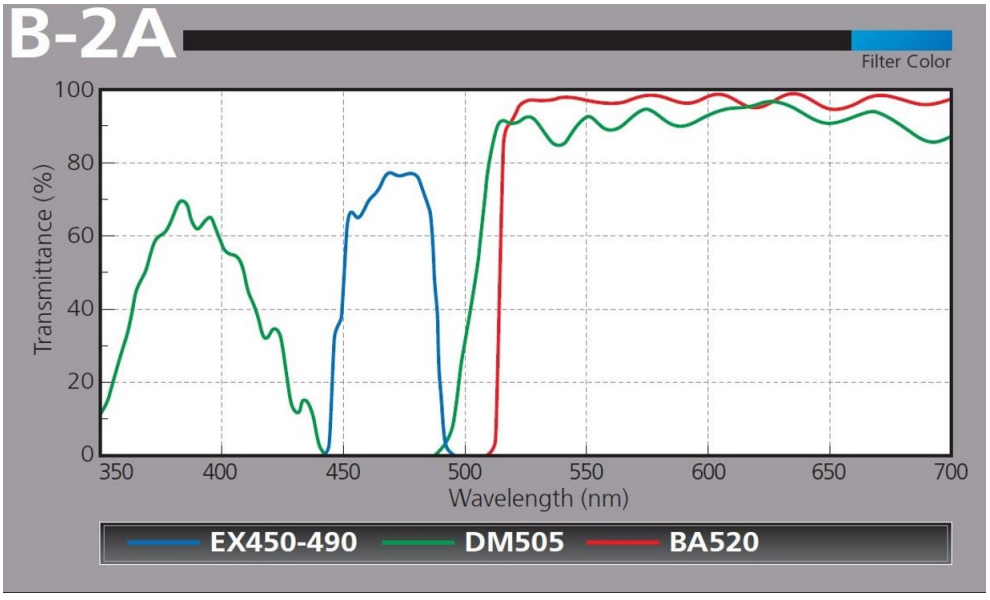

Figure 2.10: Wavelength characteristics of the B-2A filter cube set (found on page 4 of [11])

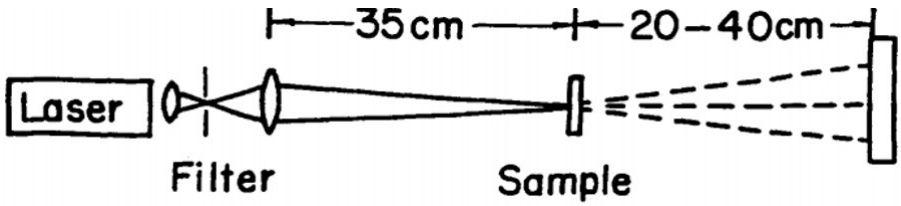

Figure 2.11: Laser diffraction setup (found as Fig. 1 from [12])

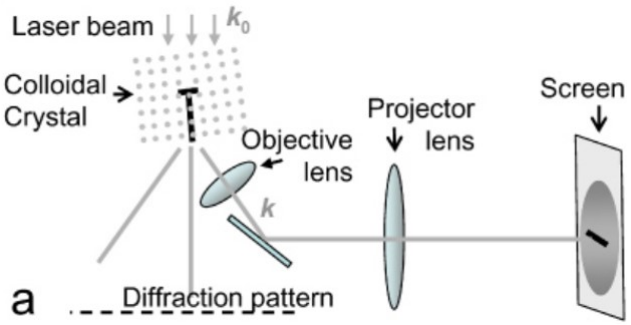

Figure 2.12: Schalls laser diffraction microscopy setup (found as Fig. 6(a) from [13])

2.2.2.3 Laser Diffraction

Laser diffraction is where a laser is directed at a diffraction grating and diffracted modes appear. These modes can come as n levels of diffraction depending on the distances in the grating.

We know light diffracts around an object and this diffraction is much more visible as the object gets smaller and smaller. Namely, with Youngs famous double slit experiment, light was determined to travel in waves and exhibited diffraction. Laser diffraction can be setup, similar to Young's experiment, such as in Figure 2.11 where a Gaussian intensity profile is achieved through a pinhole filter. Setups that combine microscopy such as the one by Schall [13] (see Figure 2.12) which used a colloidal crystal to achieve the diffraction grating have also been made. Specifically, Schall used the system to study defect propagation in a colloidal crystal [13].

2.2.2.4 Dark Field

In a normal illumination setup, all diffracted light rays travel through the objective after reflecting off the sample. In dark-field illumination, light rays that are diffracted at generally oblique angles illuminate the sample and the non-diffracting light rays simply do not pass onto the sample. Dark-field illumination is usually facilitated through the use of an illumination source coupled with an annular ring, as can be seen in Figure 2.13. As light only travels on the outside, it causes the background of the sample to be dark and the sample itself to be much more apparent (see Figure 2.14).

Where high magnification is required in conjunction with oil immersion objectives, one could use a special type of condenser lens such as a paraboloid or cardioid condenser lens. For the case

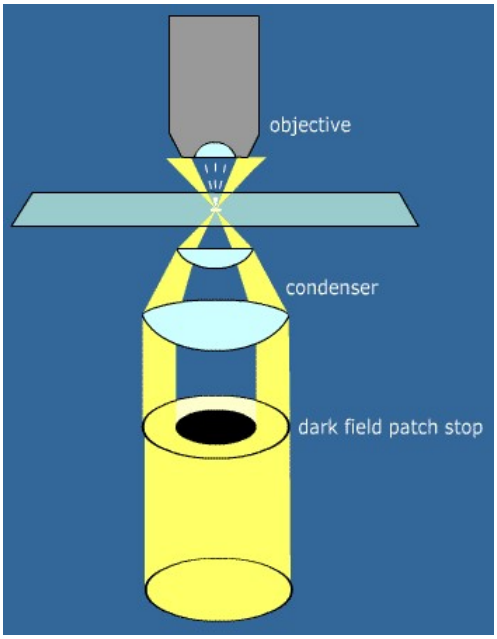

Figure 2.13: Basic setup of dark-field microscopy (found in [14])

of the paraboloid lens, light comes through an annulus, similar to that used in phase contrast microscopy, as a planar wavefront and reflects of the paraboloidal surface on the periphery of the lens. A cardioid condenser lens is similar but uses a spherical convex mirror to reflect the hollow cylinder of light onto the cardioid surface at the peripheral [50]. As both the cardioid and paraboloidal condenser lenses use reflective optics, rather than refractive optics, there is no chromatic aberration [50].

2.2.2.5 Ambient

Ambient illumination comes from a source of light that is readily available such as sunlight or the lighting inside a room. This light is usually not supposed to be for microscope illumination but the microscope can still use it or be designed to incorporate it. Lee and Yang [52] developed a smart-phone based chip-scale microscope using ambient illumination that came from sources such as the sun or a lamp. They used the principle of the shadow imaging method whereby a sample is placed directly on an image sensor and the photodioides of each pixel is used to create an image of the sample.

2.2.3 Variable Magnification

The ability to change magnification in microscopy is a standard feature in most desk-top microscopes manufactured today [8]. It is required because the user may wish to see smaller features in more detail [17]. Giacomelli et al. [53] made an NLM system that incorporated the use of variable magnification to speed up disease detection by first looking at a biological sample at

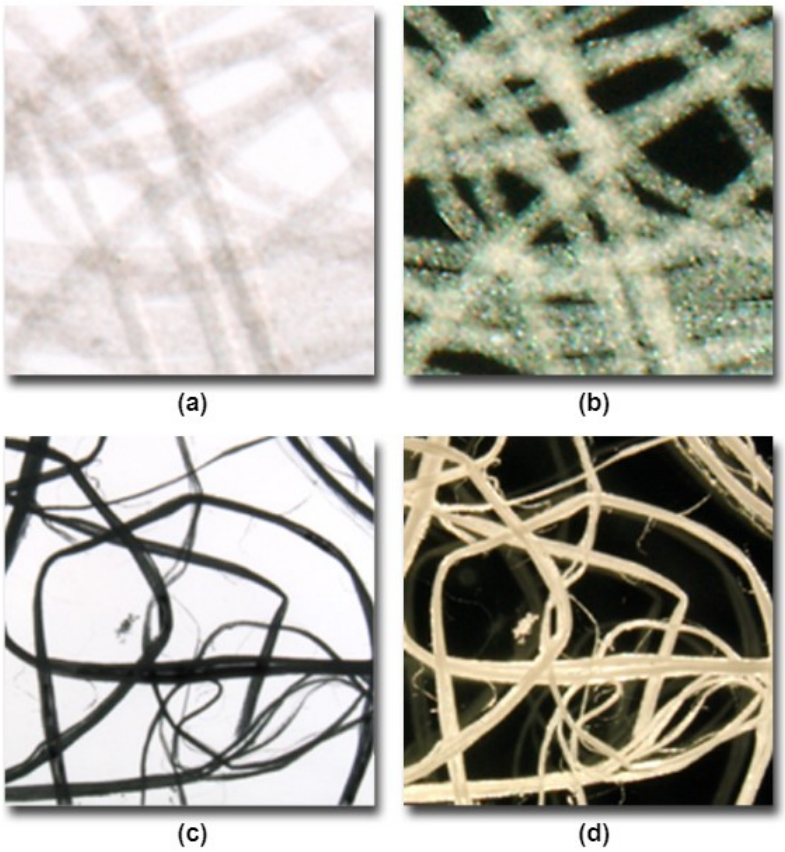

Figure 2.14: Images comparing bright-field images, (a) and (b), and dark-field images, (c) and (d), of nylon fibres (found in [15])

lower magnification and, where a suspicious area was found, went forward and looked at that area at a higher magnification. The research presented here shows how most microscopes currently achieve variable magnification and also on the few that change magnification differently to standard microscopes.

The turret system is standard to cycle through different objective lenses. This allows them to change their magnification as required. The turret works by rotating an outside ring manually which rotates a system of gears that rotate the turret up to the next objective lens. The rotation can also be made automatic with the use of a stepper motor. An example of a turret system can be seen in Figure 2.7.

Groot and Biegen [35] used a standard turret that was controlled through software in their work on designing a new interference objective for 3-D interference microscopy .

An example of an alternative design to the turret was one made by John McArthur. He created a microscope in the 1930s where he used a slide that housed the objective lenses. When the magnification needed to be changed, the slide could be moved to position a different objective lens in place (see Fig. 2.15).

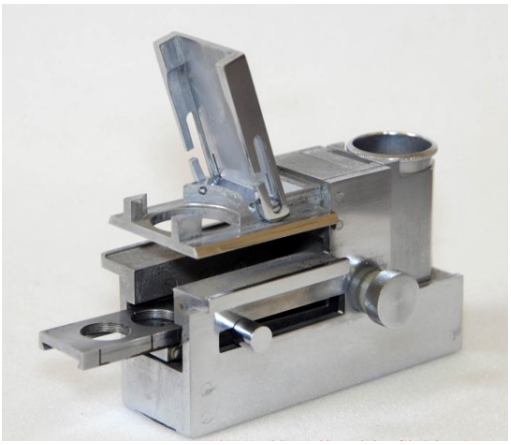

Figure 2.15: A McArthur Microscope c.1945 (found in [16])

A design that changed objectives with a pivot motion was made by Stewart [17] for GE Healthcare Bio-Sciences Corporation. Shown in Figure 2.16, the design could house two to three objective lenses and included two links: one to switch between objective lenses and the other to control the alignment of the lens position.

2.2.4 Stage Design

Stage design is an important aspect of microscope design. This is because the stage holds the sample and usually controls the x,y and z directions of the sample and subsequently the stage itself.

Siefert and Folling, on behalf of Leica Microsystems, patented a new microscope stage design [18]. Their design brought the turn dials for the x and y axis next to each other and achieved finer movement with the use of reduction gears (see Figure 2.17).

Schaefer et al [19] made an automatic scanning stage using cd-drive stepper motors and modified cd-drive bases. The system was able to successfully undertake field-of-view translations and take images of a sample. Their system can be seen in Figure 2.18.

Ma et al [54] reported on the design of an automated microscope stage. They used two stepper motors and put them onto an existing optical microscope. For controlling the stage, they used three DSP controllers , one was responsible for the control unit, LCD and position of microscope stage, and the other two controlled the two stepper motors.

OpenStage was a low-cost motorized platform designed by researchers at the Cold Spring Harbor Laboratory [55]. Their design utilized high-quality stepper motors in place of linear actuators and used commonly available hobby components for the electronics controls, like an arduino. They state that they were able to achieve positioning repeatability of 1μm in the x-y direction and 0.1μm in the z direction. They could control the motion of the stage with a hand-held control pad as well as through PC serial port.

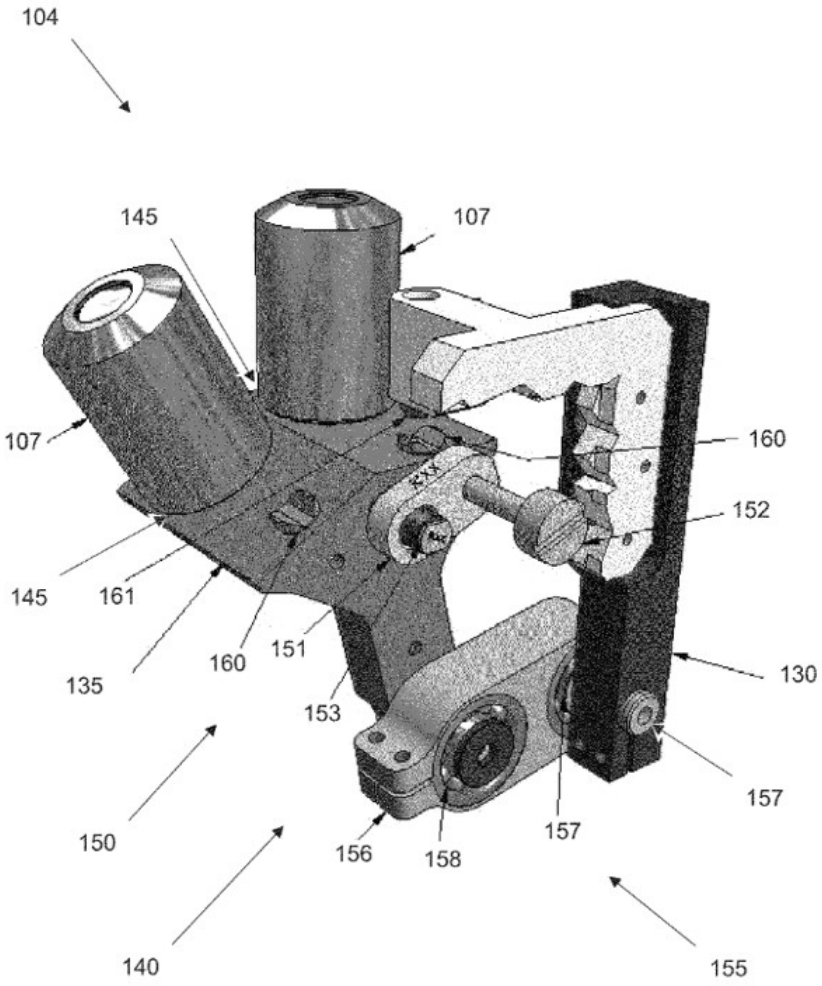

Figure 2.16: Objective lens changer design by GE Healthcare Bio-Sciences Corporation (found as Fig. 4 in [17])

2.3 Software Development

Software development was researched in three areas: software stitching, image processing and auto-focusing.

2.3.1 Software stitching

2.3.1.1 Increasing field of view through software stitching

Normal microscopes have a fixed field of view only being able to change the image as the stage moves. Although this allows a viewer to see different parts of the sample, it does not give one full picture of the sample at the same resolution. Allowing one to have a larger field of view gives an image at a magnification without compromising resolution which can be useful for areas such as particle recognition. Here we present research on one technique, image stitching, that is used

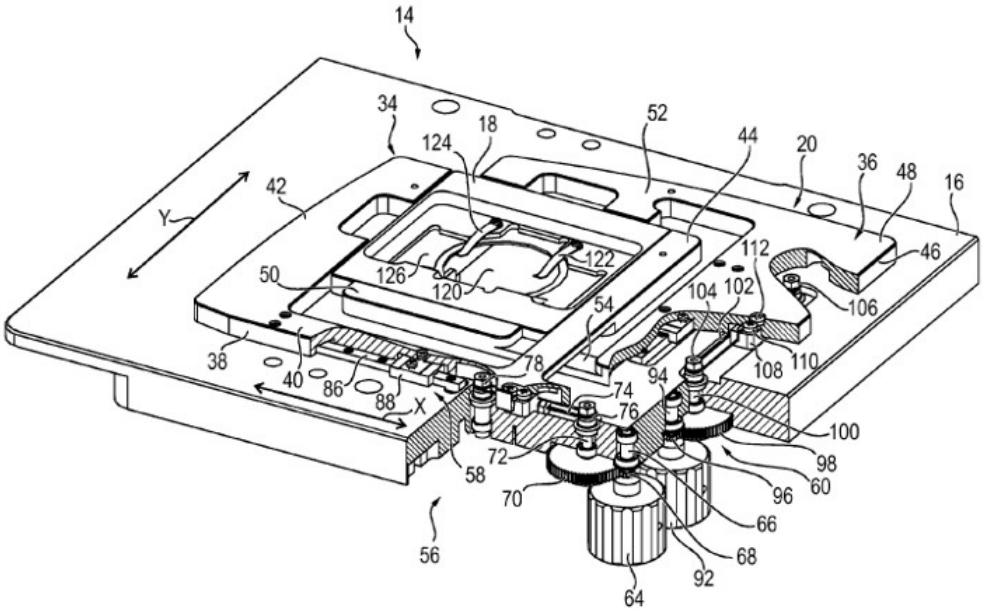

Figure 2.17: Microscope stage design by Leica Microsystems (found as Figure. 4 in [18])

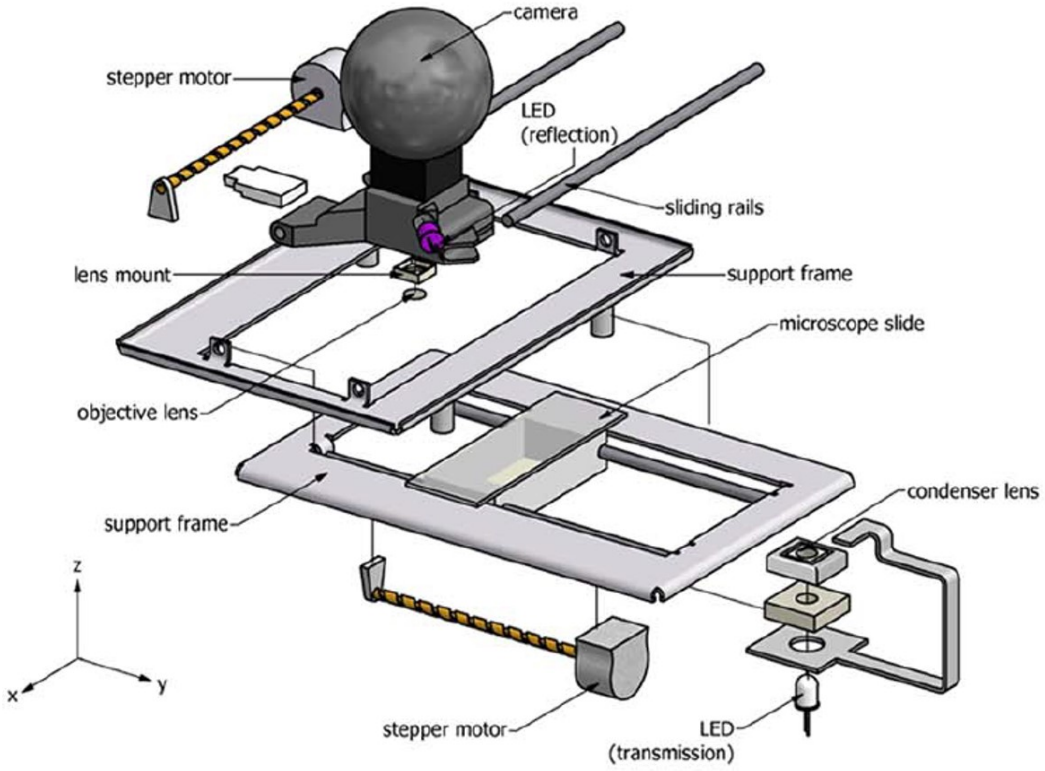

Figure 2.18: Automatic scanning stage by Schaefer et al (found as Figure. 2(a) in [19] and has been reprinted with permission from [19] © The Optical Society)

Figure 2.19: Example of a stitched image (found as Figure 6(a) in [20])

to increase the field of view of a microscope. Image stitching is the process by which several partial images of one object or scene are 'stitched' together to form one whole image that has a larger field of view (see Figure 2.19). A larger field of view allows you to see more detail in one image than you would with a smaller field of view. A higher detailed image can be used for post-processing applications such as cell counting, particle counting or sickle cell detection.

Thevenaz and Unser [56] developed a semi-automated software solution to the stitching problem. Their approach relied on an accurate pairwise registration of images and on computation reduction. Their ImageJ plugin, MosaicJ, requires the user to arrange the images roughly and their plugin does the rest. They showed their results through a biological sample of a mouse pup, cerebellum and a blood smear.

Brown and Lowe [20] worked on the problem of 2-D image stitching by finding matches using invariant local features. From their results, they state that their process is invariant to the order, scale, illumination and orientation of the images. The application for this would be most useful in creating a large 2-D panoramic image, taken from one point of view, that had no sequential order. Based on their research, they developed a C++ implementation called AutoStitch that is now available as a mobile application as well.

Ma et al [57] presented research on the use of AutoStitch on microscopic samples. They used samples from both a bright-field microscope and a scanning electron microscope. In their results, they state that the application could be used for microscopic samples.

2.3.1.2 Image Stitching Tools

2.3.1.2.1 Microsoft Image Composite Editor

Microsoft Image Composite Editor (ICE) was made by the Microsoft Research group in 2008 [58]. Since its beginning, it has had multiple updates and is now on version 2.0.3 [58]. The software is free and, although it is not open source, it does have a support forum that the developers participate in [59]. ICE does stitching in two parts: image alignment and image

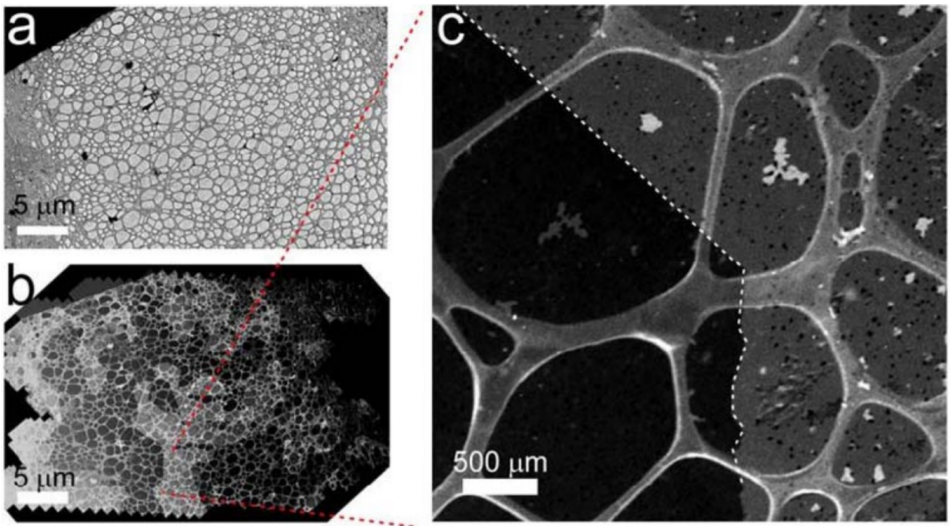

Figure 2.20: BF and DF TEM images of MoS2 films. (a) BF TEM image of the MoS2 film. (b) DF TEM image of the same region showing a large MoS2 grain across the whole film. The DF image shown in (b) was obtained by stitching 507 different DF images, acquired with a spacing of 3 μm under the same microscope conditions. (c) An individual DF image acquired from the square area shown in (b) (found as FigS10 in [21])

composition. Image alignment is done based on using the image features found in the work of Winder et al. [60]. In their work, they produced efficient local descriptors which have a 13.2% error at 13 bytes storage per descriptor, compared with 26.1% error at 128 bytes for SIFT [60]. Image composition is done with the work of Agarwala et al.[61] who developed a framework for combining a group of images into a single composite image using graph-cut optimisation to choose good seams from the images; and gradient-domain fusion, a technique based on Poisson equations, to further reduce artifacts in the final composite image. ICE has been used in several applications in research including the medical and materials science field, for example Gulati et al.[62] used it to stitch 156 macroscopic images of explantation of hearts from patients with and without fibrosis; and Najmaei et al.[21] used it to stitch 507 microscopic dark-field TEM images of MoS_2 (see Figure 2.20). Faridul et al.[63] used ICE in their work on a method for pre-processing images before stitching. Gross et al. [59] presented a statistical examination of image stitching software packages for use with unmanned aerial vehicles. They assessed ICE, Pix4D and Photoscan Pro for the application of digital aerial photography for small unmanned aerial systems. They found ICE produced the fewest visual errors and was the most cost effective solution for photogrammetric applications.

2.3.1.2.2 OpenCV

OpenCV (Open Source Computer Vision) is an open-source image and video processing library that was developed by the Intel Research lab in Russia [64] and released in 1999 [65]. It has a large community of users and contributors having had over 2.5 million downloads and more than

40000 people in the user group [65]. Although it is written in C/C++, it now has wrappers for C# (Emgu CV) and Python for its use in development in other platforms, among other languages. In the context of stitching, OpenCV uses a similar pipeline as the one reported by Brown and Lowe in [20] and can be seen in Figure 2.21. Similar to ICE, the stitcher class also has two stages: image registration and composition. In the case of [20], the automatic panorama stitching is done as follows:

1. Extract SIFT features from all n images
2. Find k nearest-neighbours for each feature using a k-d tree
3. For each image:
   3.1. Select m candidate matching images that have the most feature matches to this image
   3.2. Find geometrically consistent feature matches using RANSAC to solve for the homography between pairs of images
   3.3. Verify image matches using a probabilistic model
4. Find connected components of image matches
5. For each connected component:
   5.1. Perform bundle adjustment to solve for the rotation θ_1, θ_2, θ_3 and focal length f of all cameras
   5.2. Render panorama using multi-band blending

OpenCV stitching has been used in many areas of research. Keatsamarn et al. [66] used OpenCV stitching for the development of an alternative method for generating a pedograph. Vaishnav et al. [67], implemented previous mosaicking techniques with the OpenCV stitching pipeline to montage corneal nerves; and Reina et al. used it for stitching, tracking and colour identification for their work on a virtualized arena for swarm robotics research with Kilobot robots.

2.3.1.2.3 ImageJ

ImageJ is a java based image processing program. It is open-source but has built in libraries of .JAR files that can be used individually in java applications. Fiji is a distribution of ImageJ that uses modern software engineering practices and focuses on biological image analysis [68]. Fiji has several image processing plugins including a stitching plugin. The stitching plugin allows a stitch to be done as 'Pairwise Stitching' or 'Grid/Collection Stitching'. Grid Collection stitching is used for stitching a large collection of images. The stitching algorithm is based on the work of Preibisch et al. [23] who developed a method to stitch large collections of 3D confocal images. The method is based on the Fourier Shift Theorem and determines all possible translations between pairs of

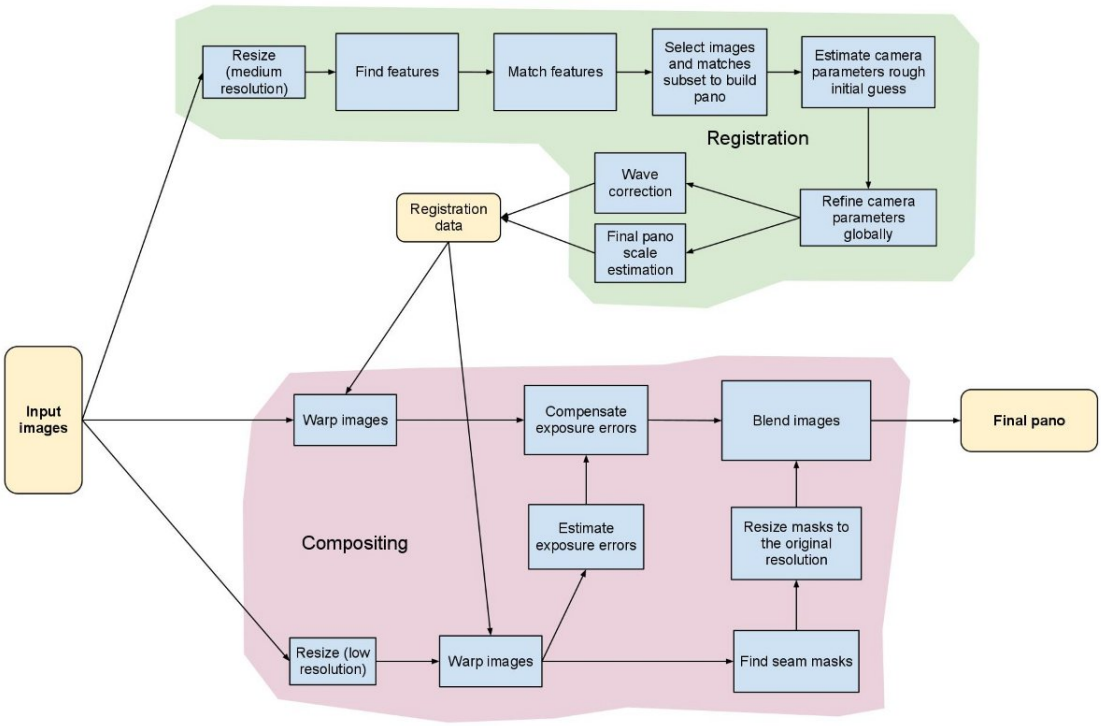

Figure 2.21: OpenCV stitching pipeline (found in [22])

3D images, ultimately finding the best suited arrangement of the group of images. The algorithm also has a brightness compensation, works on both 2D and 3D images and for small image sets does not require pre-existing knowledge of the image sequence. Figure 2.22 shows an example of a 3-D stitched image produced by ImageJ of a Drosophila larva. Kumar [69] used the stitching plugin in his work on designing and implementing a closed-loop imaging pipeline to update the imaging protocol in real-time during time-lapse microscopy of a growing cell population. Millis and Tyska [70] used 'Grid/Collection Stitching' as part of a protocol they designed for stitching large datasets obtained for assessment of tissue-level protein distribution. Monkemoller et al. [71] used the Fiji stitching plugin to stitch 3D-SIM images of several multi-colour labeled LSEC's. According to the researchers, this was important because 3D-SIM is limited in its field-of-view by the objective lens so taking image samples at 40μm intervals allowed them to have enough overlap to produce a larger stitched image that provided a single overview image.

2.3.2 Microscopic Image Processing

Image processing can be an important feature for analysis of captured microscopic images. The research presented here shows three different image processing techniques used and their benefits as well as two image processing tools.

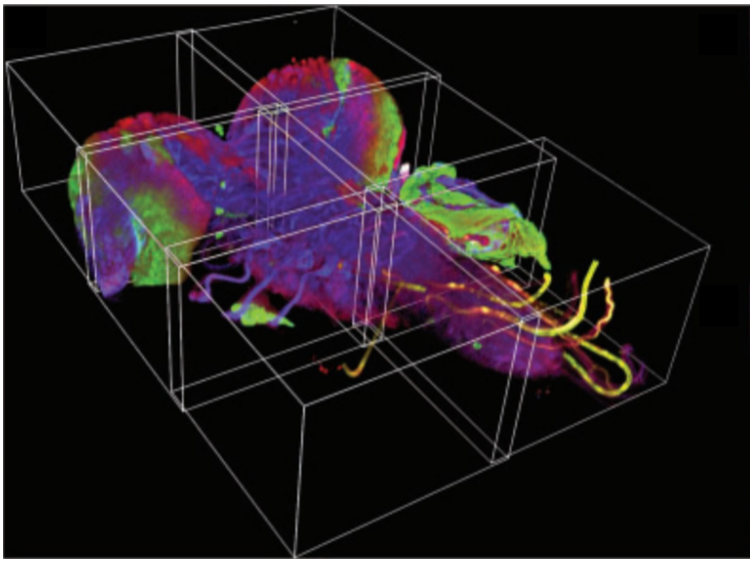

Figure 2.22: The 3D visualization of stitched 2×3 mosaic of the central nervous system of a Drosophila larva (found as Figure 1(A) in [23])

Figure 2.23: Example of particle counting used for detecting the number of fish in a video sequence (found as Figure 9 in [24])

2.3.2.1 Particle Counting

Particle counting, also called blob counting, is the process by which particles are counted to be used for research and diagnosis. An example can be seen in Figure 2.23 where the number of fish are counted in a video sequence to help research in fish population estimation.

A complete blood count is one example of a diagnostic tool that utilizes cell counting. The process counts the number of each type of cell, such as red or white, which can be further used to determine if the patient has a disease. Several works have been done on the research of particle counting for the application of counting cells. Lempitsky and Zisserman [72] presented a supervised learning-framework for counting objects, notably mentioning cells from microscopic images. In their experiments, they used the microscopic fluorescent images from [73] as a test data set. Breslauer et al [74] developed a light microscope system that was mountable to a mobile phone for telemedicne applications. They demonstrated their system by imaging P. falciparum-

infected and sickle red blood cells in bright-field illumination . They also used LED excitation for fluorescence illumination to image M. tuberculosis-infected sputum samples. They went further with the tuberculosis samples by doing bacillus counting albeit on a computer for simplicity.

2.3.2.2 Area and perimeter estimation

Perimeter and area estimation of particles can be an important part of analyzing particles. For example, Goldberg et al [75] developed "in situ dual fluorescence detection techniques for measuring apoptosis and proliferation simultaneously in single dishes of cells". In their work they measured the perimeter, area, longest diameter and average diameter of 100 TUNEL positive nuclei showing signs of condensation. These measurements were then used to create a statistical formula to differentiate between apoptotic and normal RPM nuclei.

A review article of recent advances was published in 2012 of morphological cell image analysis by Chen et al [76]. The article mentioned how perimeter and area of cells, among other extracted features, can be used to then calculate features such as displacement, protrusiveness and ellipticity which can then be further used for example to see the dynamic changes of human cancerous glioma cells.

2.3.2.3 Image Processing Tools

2.3.2.3.1 Aforge.NET

Aforge is an image processing and artificial intelligence library which was originally developed by Andrew Kirillov for the .NET framework and released in December 21 2006 [77] with its current revision on version 2.2.5. Being based on a .NET framework, Aforge is ideal for .NET applications such as windows forms visual studio applications done in C#. Aforge also has many libraries for image processing analysis such as particle/blob counting, colour enhancement and feature detectors [78]. The framework has found several uses in research such as Sholeh's work on white blood cell segmentation for fresh blood smear images where the segmentation method they used was developed using the Aforge framework [79]. Sharma et al. [80] used Aforge for generating the RGB and gray histograms in their work on exploring deep learning methods for computer-aided classification in HE stained histopathological whole slide images of gastric carcinom. The Aforge shape detection method was used in Khans [81] work on developing an industrial image processing application for baked goods.

2.3.2.3.2 OpenCV

This section describes OpenCV in the context of an image processing library for the purpose of achieving objectives such as blob/cell counting or shape detection. A general introduction to OpenCV can be seen in Section 2.3.1.2. OpenCV has been used extensively in image analysis such as blob detection and blob counting. Gupta [82] used OpenCV's blob detection in his C++ application which analyzes the identification of a specific cellular body using image processing.

Li et al.[83] used OpenCV for moving vehicle detection, tracking and counting using on a C++ interface. Their results state that they achieved an accuracy rate of 97.1% for their virtual detector method and 98.4% for their blob tracking method, and that they could detect, track and count most vehicles successfully. Kong et al. [84] described a method for counting people in crowds from a single camera and implemented their estimation system with OpenCV and DirectShow. Their method took into account feature normalization as well as variant camera orientation. They concluded that their system works well for the majority of their testing data but would still require work on more complex situations such as overlap among pedestrians.

2.3.3 Auto-focusing

There have been many auto-focusing methods developed for different applications. Pertuz et al. [85] summarized many methods for measuring focus of an image including several auto-focus methods. Here we detail three auto-focus methods from their work.

2.3.3.1 Tenengrad variance method

This method uses "variance of the image gradient as a focus measure" [85] and was originally used for auto-focusing in work of Pacheco et al [86]. Pacheco et al specifically used the auto-focus method for diatom auto-focusing in bright-field microscopy. The formula for the method is as follows:

$$\phi_{x,y} = \sum_{(i,j) \in \Omega(x,y)} (G(i,j) - \overline{G})^2$$

Where $\overline{G}$ is the mean value within $\Omega(x,y)$ of the gradient magnitude, which is computed as: G = $\sqrt{G_x^2 + G_y^2}$.

2.3.3.2 Gray-level local variance

This method uses the local variance of gray-levels to measure the focus of an image [85]. The idea being that a well focused image would have high variation in grey levels so therefore they can give a focus measure, where the focus measure based on the local variance is given by the global variance.

2.3.3.3 Histogram Range

The histogram range method computes the histogram, H, within every $\Omega(x,y)$. The formula for it is as follows:

$$\phi = max(k|H > 0) - min(k|H > 0)$$

It has been used as a focus measure for auto-focusing in the works of Firestone et al. [87], Santos et al. [88] and Sun et al. [89]. Firestone et al. and Sun et al. both deal with applications of automated microscopy which is similar to the research direction pursued in this thesis.

2.4 Microscope designs comparable to our research direction

2.4.1 University of British Columbia

The first is a development by students from University of British Colombia [19] who used readily available optical components from a disk drive. Their system incorporated bright-field and fluorescence illumination and magnified the image with the lens from the optical pickup. The bright-field illumination was achieved through a white LED and fluorescence was done with a UV LED. Scanning and auto-focusing were done through a software application while stitching was done with Adobe CS3. The auto-focusing algorithm measured the sharpness of the image at five equidistant positions, found the point of highest sharpness and then moved to that point. The process repeats until the minimum z-axis movement is reached. Their system has a volume of 1728cm^2 and a weight of <1kg. In their discussion of their results, they stated that their microscope has similar results to a conventional laboratory microscope.

2.4.2 University of California Berkeley, Smart Phone Microscope

In 2009, a team at the University of California Berkeley, published a paper on the design of a mobile phone based clinical microscope [74]. Their system was setup with a phone camera as the sensor at one end then followed by an eyepiece, emission filter, objective lens, sample slide, condenser lens, excitation filter, collector lens and LED. The size of the system was the thickness of the phone coupled with the tube frame that had a distance of approximately 300mm. To image in fluorescent mode, they would keep the filters as they are and would simply remove them for bright-field illumination. As stated in their paper, their system was able to capture useful high-resolution images of blood and sputum.

2.4.3 Miller et al

Miller et al. [90] developed a battery-operated portable microscope that uses bright-field and fluorescence illumination. Similar to the work of Breslauer et al. [74], their prototype uses LED for illumination and has variable magnification through a turret system similar to a standard microscope. Specifically, they used a white LED torch for bright-field imaging and a separate blue LED torch for fluorescence imaging. They changed the illumination modes by changing the torches. They were able to achieve a size of 75mm x 130mm x 180mm.

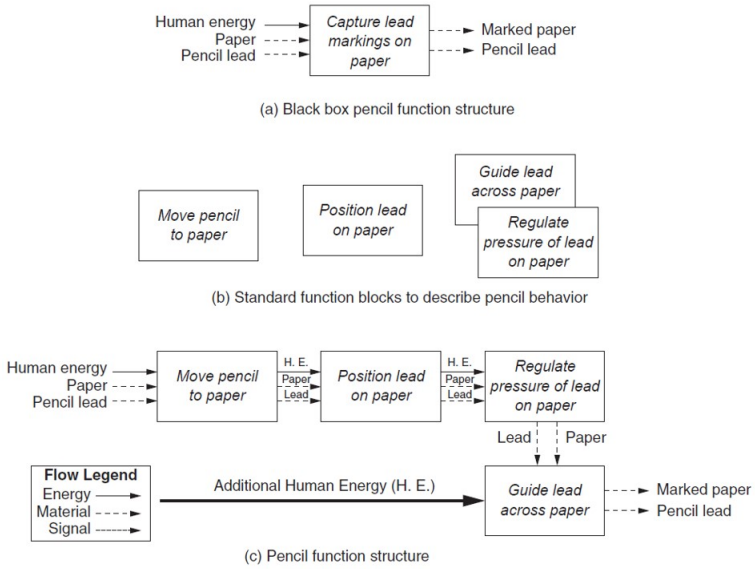

Figure 2.24: Example of systematic design being used to construct functional blocks for a mechanical pencil (found as Figure 6.7 in [25])

2.5 Design and Creative Methodology

Design methodology is the specific process by which something is designed. There have been many methodologies developed through the last two centuries notably after world war two. This had to do with engineers and scientists wanting to standardise the design process. Here we will talk about five different types of design methodologies that can be used throughout design from brainstorming to creation of concepts and all the way to final design. These have been mainly referenced from the book Engineerng Design by Dieter [25].

2.5.1 Systematic Design

Systematic design is a structured design methodology developed in Germany in the 1920s. Two German engineers, Wolfgang Beitz and Gerhard Pahl, formalized the technique in their book, 'Engineering Design: A Systematic Approach' [91]. In the methodology, all technical systems are represented as transducers, where the environmental variables such as material flow, energy flow and signals interact with these systems. If we taken an example from [25], a mechanical pencil is modelled as a transducer (see Figure 2.24). At first we can make a basic black box functional block where the inputs are human energy, paper and pencil lead; function is to capture lead markings on paper; and outputs are marked paper and pencil lead: the pencil lead has not run out. This can then be further elaborated to accommodate more functional blocks such as 'Position lead on paper' and 'Guide lead across paper'. Finally a connected functional block can be made to show the full function structure.

Systematic design has been continuously used throughout its beginning and still finds

relevance in the development of products and research today. Bakker et al. [92] used Systematic Design in successfully designing an autonomous weeding platform. In their work they stated that the use of the Systematic Design method provided structure to the design process, gave a good overview of the complete design and, because of its structured approach, forced the designer to look at alternative solutions which "decreases the probability of heuristic bias and increases the quality of the outcome".

Ore et al. [93] developed an HIRC (Human Industrial Robot Collaboration) design method, based on Systematic Design method, for the starting stages of the production development processes.

Tomiyama et al. [94] discusses design methodologies for use in educational and industrial applications. They detail that Systematic Design has been continually updated and revised for new developments in engineering fields: it now covers major topics in mechanical design. They go on to say that the method would be suitable for graduate engineers or academics.

2.5.2 Synectics

Synectics was developed in the 1940's by the Cambridge Research Group. The groups aim was to "uncover the psychological mechanisms basic to creative activity". Synectics is undertaken in three phases. In the first phase, the problem is looked at from all angles so as to understand it. The second phase uses four types of analogies to find creative solutions. These analogies are as follows: direct analogy, fantasy analogy, personal analogy and symbolic analogy.

Direct analogy is where one seeks to find a close physical analogy to the design problem. An example from [25] shows how describing the motion of electrons around a nucleus can be thought like the motion of natural satellites like the moon around Earth. Another example is biomimetics: the idea of drawing inspiration from biological systems. The Shinkansen bullet train drew inspiration from the kingfisher bird which had a beak that allowed it to dive from air to water with minimal losses [95] [96]. They used this beak design on the nose of the train which saw the elimination of the sonic boom that people would experience for up to 400 metres when the train would enter a tunnel. In the same project, the engineers studied the quietness of owls and found that owls achieved this through their serrated feathers. Serrated feathers produce small vortexes breaking up the large vortexes that normally produce noise [95], therefore allowing the owl to fly quieter than other birds. They used this principal to design serrations on the pantograph, the part of the train that receives electricity from overhead wires, and were successful in reducing noise on the train [95].

Fantasy analogy is one which takes all the constraints of the problem away and allows one to imagine a completely ideal solution. For instance, the navy have a problem where they need to get custom parts made. An ideal solution would be to have a machine that simply makes it instantly from telling it what you need. Another example, taken from [25], relates the problem of having to find your car in the parking lot. An ideal solution would be that the car could appear

instantly before you or if it drove by itself. The Tesla Model 3 has a 'Summon' feature that allows the car to come to you, albeit a maximum distance of approximately 12 metres. Although this may seem trivial, the idea may have come from a Synectic exercise or similar.

Personal Analogy is where one puts themselves in the position of the product or process design problem. In [25], an example was given of imagining oneself as a vacuum cleaner. Dirt could be sucked up like drinking from a straw; dirt could also be picked up from our hands by combing it through the carpet.

Symbolic Analogy is where the the elements of the design problem are replaced with symbols and then those same symbols are transformed in some way to create solutions to the problem. In mathematics, the Fourier Transform is used to transform a function in the time domain into the frequency domain and is used extensively in many branches of engineering. Specifically in software engineering, the JPEG compression format uses the fourier transform to reduce the size of RAW images while still retaining the required image information.

2.5.3 TRIZ

TRIZ is an acronym for 'Teoriya Resheniya Izobreatatelskikh Zadatch' meaning 'Theory of Inventive Problem Solving'. It is a design methodology that is focused on creating new inventive solutions to problems. The process was created after World War II by a Russian inventor named Genrich Altshuller. Altshuller worked in the Soviet Navy and was seeking to increase the creative skill of the design engineers. He looked at Synectics but sought a better methodology, so he and his colleagues worked on their own methodology, reading around 1.5 million author certificates: the equivalent of patents in the United States. From here they formed the basis of TRIZ as a codified way to create solutions, based on their study of novel inventions. TRIZ has four different ways to generate creative solutions:

1. Increase the ideality of a product or system
2. Identify the product's place in its evolution to ideality and force the next step
3. Identify key physical or technological contradictions in the product and revise the design to overcome them using inventive principles
4. Model a product or system using substance-field (Su-Field) analysis and apply candidate modifications

TRIZ lists 40 inventive principles that can be used to create solutions (see Figure 2.25).

2.5.4 Axiomatic Design

Axiomatic design was formally developed in 1990 by Dr. Nam P. Suh, a mechanical engineering professor at MIT, in his book 'Principles of Design' [97]. Suh's intention was to create fundamental

TABLE 6.9
The 40 Inventive Principles of TRIZ

Names of TRIZ Inventive Principles	
1. Segmentation	21. Rushing through
2. Extraction	22. Convert harm into benefit
3. Local quality	23. Feedback
4. Asymmetry	24. Mediator
5. Combining	25. Self-service
6. Universality	26. Copying
7. Nesting	27. An inexpensive short-lived object instead of an expensive durable one
8. Counterweight	28. Replacement of a mechanical system
9. Prior counteraction	29. Use of a pneumatic or hydraulic construction
10. Prior action	30. Flexible film or thin membranes
11. Cushion in advance	31. Use of porous material
12. Equipotentiality	32. Change the color
13. Inversion	33. Homogeneity
14. Spheroidality- Curvature	34. Rejecting and regenerating parts
15. Dynamicity	35. Transformation of physical and chemical states of an object
16. Partial or overdone action	36. Phase transition
17. Moving to a new dimension	37. Thermal expansion
18. Mechanical vibration	38. Use strong oxidizers
19. Periodic action	39. Inert environment
20. Continuity of useful action	40. Composite materials

Figure 2.25: The 40 inventive principles that can be utilised in TRIZ (found as Table 6.8 in [25])

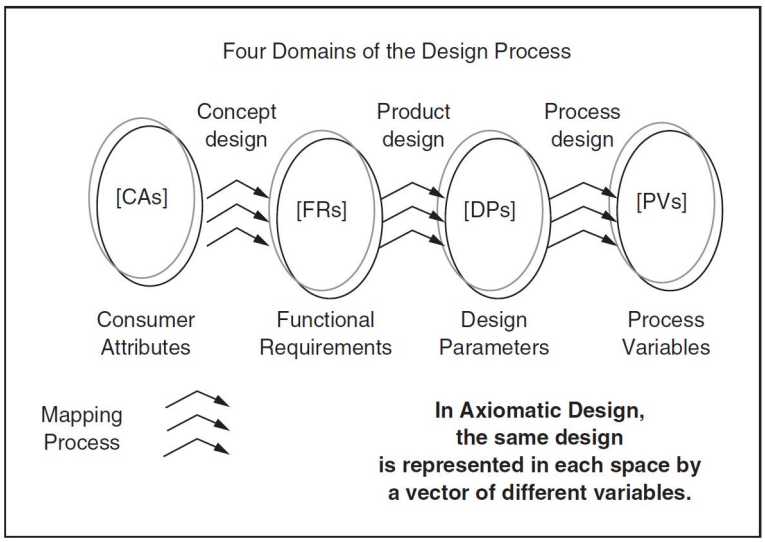

Figure 2.26: The design process from an Axiomatic Design perspective (found as Figure 6.11 in [25])

laws or principles for engineering design that could be then used for the foundation of a theory of design [25]. Axiomatic design follows the process shown in Figure 2.26.

Functional requirements (FR) are those that can be associated with verbs relating to the design. For example, in the design of a lathe, the main functional requirement could be 'Remove metal' which could then have sub-functional requirements such as 'Supply power', 'work piece rotation' or 'Support for work-piece and tool-holder'. Figure 2.27 shows an example of a hierarchy of functional requirements for a lathe.

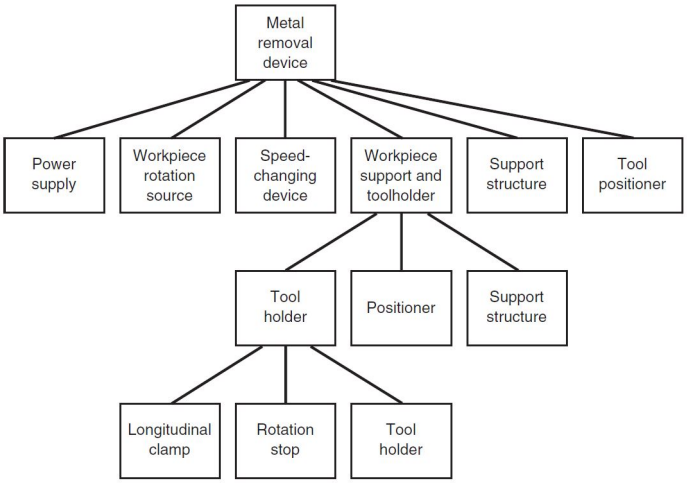

Figure 2.27: Hierarchical display of functional requirements for a metal cutting lathe (found as Figure 6.12 in [25])

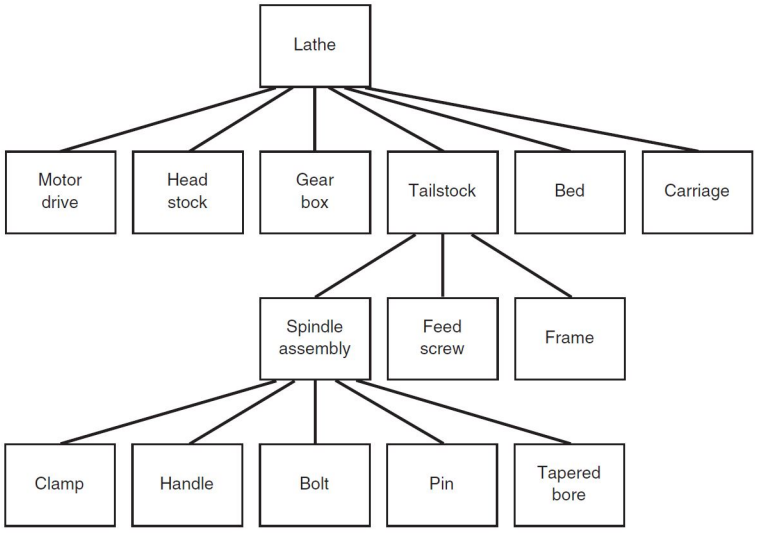

Figure 2.28: Hierarchical display of design parameters for a metal cutting lathe (found as Figure 6.13 in [25])

Design parameters (DP) are those that are associated with nouns relating to design. For example, for the functional requirement 'remove metal' a design parameter could be 'Lathe'. Similarly, for the sub-functional requirements 'Supply power', 'work piece rotation' and 'Support for work-piece and tool-holder', design parameters could be 'Motor drive', 'Head stock' and 'Tail stock' respectfully. Figure 2.28 shows an example of a hierarchy of functional requirements for a lathe.

Process variables (PV) are the variables of the processes that result in the physical design from the set of design parameters. In the context of a real world product, this means the manufacturing processes.

Axiomatic design uses a matrix to evaluate the impact on a specific function requirement by a design parameter. The matrix takes the following formula:

$$\{FR\} = [A]\{DP\} \tag{2.1}$$
$$[A] = \frac{\{FR\}}{\{DP\}}$$

$$[A] = \begin{bmatrix} A_{11} & A_{12} & A_{13} & A_{...} & A_{1n} \\ A_{21} & A_{22} & A_{23} & A_{...} & A_{2n} \\ A_{31} & A_{32} & A_{33} & A_{...} & A_{3n} \\ A_{41} & A_{...} & A_{...} & A_{...} & A_{2n} \\ ... & ... & ... & ... & A_{(m-1)n} \\ A_{m1} & A_{m2} & ... & A_{(m(n-1)} & A_{mn} \end{bmatrix} \tag{2.2}$$

$$A_{ij} = \frac{\partial FR_i}{\partial DP_j} \tag{2.3}$$

Where {FR} is an m x 1 matrix of functional requirements, {DP} is an n x 1 matrix of design parameters and 'A' is an m x n matrix. [A] represents the impact, or change in, a specific functional requirement with respect to a given design parameter.

There are two 'axioms' in the design: independence axiom and information axiom. The independence axiom can be stated as creating a design where each design parameter only influences one functional parameter - such a design is said to be uncoupled. The matrix for an uncoupled design can be seen in Equation 2.4.

$$[A] = \begin{bmatrix} A_{11} & 0 & 0 & 0 & 0 \\ 0 & A_{22} & 0 & 0 & 0 \\ 0 & 0 & A_{33} & 0 & 0 \\ 0 & 0 & 0 & A_{44} & 0 \\ 0 & 0 & 0 & 0 & A_{55} \end{bmatrix} \tag{2.4}$$

Achieving an uncoupled design can be difficult and often most designs are decoupled or coupled, as seen in equations 2.5 and 2.6 respectively or a combination of the two.

$$[A] = \begin{bmatrix} A_{11} & A_{12} & A_{13} & A_{14} & A_{15} \\ 0 & A_{22} & A_{23} & A_{24} & A_{25} \\ 0 & 0 & A_{33} & A_{34} & A_{35} \\ 0 & 0 & 0 & A_{44} & A_{45} \\ 0 & 0 & 0 & 0 & A_{55} \end{bmatrix} \tag{2.5}$$

$$[A] = \begin{bmatrix} A_{11} & A_{12} & A_{13} & A_{14} & A_{15} \\ A_{21} & A_{22} & A_{23} & A_{24} & A_{25} \\ A_{31} & A_{32} & A_{33} & A_{34} & A_{35} \\ A_{41} & A_{42} & A_{43} & A_{44} & A_{45} \\ A_{51} & A_{52} & A_{53} & A_{54} & A_{55} \end{bmatrix} \tag{2.6}$$

The information axiom can be thought of, after having completed the independence axiom, as a principle to select the design that uses the least amount of information content [98].

Axiomatic design has been used in applications in research since its beginning. Xi et al [99] presented the design and analysis of a re-configurable parallel robot using the Design for Reconfigurability (DfR) method detailed in the work of Chen et al [100]. The DfR method is closely based on the axiomatic design method.

Lo and Hellander [98] used axiomatic design for two case studies: one involving the design of a workstation for microscope usage and the other on the design of a drivers compartment.

2.5.5 Product Design and Selection (PDS)

Product design and selection (PDS) was developed by Liu [1] in 2011 and integrates fuzzy quality function deployment (QFD) with a prototype product selection model.

The method has two main phases:

- Establishment of fuzzy QFD
- Evaluation and selection of prototype products

It uses customer questionnaires to derive decisions related to design and production. The method is also suited for a 'team' of individuals, usually from different fields of study, who work collaboratively throughout the PDS process.

2.5.5.1 PDS Method

This section describes the steps of the PDS method.

1. Establishment of fuzzy QFD
    1.1. Compute the relative importance of customer requirements
        1.1.1. Form a team where each member should have experience and expertise in product design and development. Members of the team can be from different departments, for example finance, sales or engineering.
        1.1.2. Conduct an initial customer survey or market research to identify all possible customer requirements

1.1.3. Based on the customer requirements taken from research, design a customer questionnaire to acquire the relative importance of each Customer Requirement (CR)

1.1.4. The relative importance of each customer requirement is calculated using a pairwise comparison: where the customer assesses relative importance ratings between pairs of customer requirements in terms of linguistic variables. Linguistic variables are represented in this study as triangular fuzzy numbers (TFN). An example of TFN can be as follows:

$$\widetilde{A} = (a_1, a_2, a_3)$$

Where $a_1 \leq a_2 \leq a_3$.

1.1.5. Generate a fuzzy pairwise comparison matrix for each customer where:

$$[\widetilde{PC}_{ij}(k)]_{mxm}$$

is the importance rating of CR_i compared to CR_j from customer k. Note that

$$\widetilde{PC}_{ij}(k) = \frac{1}{\widetilde{PC}_{ji}(k)}$$

1.1.6. Use the DSW algorithm proposed by Dong et al.[101] to derive the fuzzy sets which are represented by α-cuts.

1.1.7. Relative importance of a customer requirement, CR_i for a particular customer matrix k can be then computed with:

$$RICR_i^{\alpha} = \sum_{j=1}^{m} PC_{ij}^{\alpha}(k) \left(\sum_{i=1}^{m} \sum_{j=1}^{m} PC_{ij}^{\alpha}(k) \right)^{-1} \quad i, j = 1, 2, ..., m, \;\; k = 1, 2, ..., q$$

1.1.8. Then find the aggregated relative importance of CR_i with

$$RICR_i^{\alpha} = \frac{\sum_{k=1}^{q} RICR_i^{\alpha}(k)}{q}, \; i, j = 1, 2, ..., m, \;\; k = 1, 2, ..., q$$

1.2. Compute final importance of customer requirements

1.2.1. Do a competitive analysis

A. Assess performance ratings of company's product against competitors product for each customer requirement using linguistic variables (see Table 2.1). The performance rating allows determination of the intended market position of each customer requirement.

B. Improvement ratio of each customer requirement is determined by:

$$IR_i^{\alpha} = \frac{IMP_i^{\alpha}}{CP_i^{\alpha}}, \; i = 1, 2, ..., m,$$

Where IR_i^{α} is the improvement ratio of CR_i, IMP_i^{α} is the intended market position of CR_i and CP_i^{α} is the current performance of CR_i

Linguistic variable	Fuzzy Number
Absolutely unimportant (AU)	(1/9, 1/7, 1/5)
Strongly unimportant (SU)	(1/7, 1/5, 1/3)
Weakly unimportant (WU)	(1/5, 1/3, 1)
Equally important (EI)	(1, 1, 1)
Weakly important (WI)	(1, 3, 5)
Strongly important (SI)	(3, 5, 7)
Absolutely important (AI)	(5, 7, 9)

Table 2.1: Linguistic variables used in the customer questionnaire (found as Table 2 in [1])

C. By analyzing the current performance and the intended market position of each CR, the team can determine which CRs will be the sales points

1.2.2. The final (adjusted) importance of CRs is then computed by combining the relative importance of CRs, the improvement ratio, and the sales point using formula:

$$FICR_i^\alpha = RICR_i^\alpha \cdot IR_i^\alpha \cdot SP_i^\alpha, i = 1,2,...,m,$$

Where $FICR_i^\alpha$ is the final importance of CR_i and SP_i^α is the level of sales point for CR_i

1.3. Compute the final importance of Engineering Characteristics (EC)

1.3.1. Translate customer requirements into list of EC's in technical perspectives

1.3.2. Use graphical symbols to express the level of relationships between CR's and EC's

1.3.3. Establish relationship matrix

1.3.4. Absolute importance of ECs is then computed by integrating both the final importance of CRs and the relationships matrix:

$$AIEC_j^\alpha = \sum_{i=1}^{m} (FICR_i^\alpha \cdot R_{ij}^\alpha),\ i = 1,2,...,m,\ j = 1,2,...,n,$$

Where $AIEC_j^\alpha$ is the absolute importance of EC_j and R_{ij}^α is the level of relationship between CR_i and EC_j.

1.3.5. Compute final importance of engineering characteristics using Khoo and Ho's [102] formula:

$$FIEC_j^\alpha = AIEC_j^\alpha + \frac{1}{n-1} \sum_{i=1, i\neq j}^{n} (AIEC_j^\alpha \cdot C_{ij}^\alpha),\ i,j = 1,2,...,n$$

Where $FIEC_j^\alpha$ is the final importance of EC_j and C_{ij}^α is the level of correlation between EC_i and EC_j, $i \neq j$. This now gives you the final importance of CR's and EC's.

1.3.6. Determine ranking orders of CR's and EC's using Chen and Lu's [103] fuzzy ranking method. Assume $\tilde{A}_i$ and $\tilde{A}_j$ are two fuzzy numbers i and j respectively. The left and right dominance are calculated as follows:

$$D_{ij}^{L} = \frac{1}{n+1} \sum_{k=0,n} (l_{ik} - l_{jk})$$

$$D_{ij}^{R} = \frac{1}{n+1} \sum_{k=0,n} (r_{ik} - r_{jk})$$

where

$$l_{ik} = \inf_{x \in R} \{x | \mu_{\tilde{A}_i}(x) \geq \alpha_k\},\ l_{jk} = \inf_{x \in R} \{x | \mu_{\tilde{A}_j}(x) \geq \alpha_k\}$$

$$r_{ik} = \sup_{x \in R} \{x | \mu_{\tilde{A}_i}(x) \geq \alpha_k\},\ r_{jk} = \sup_{x \in R} \{x | \mu_{\tilde{A}_j}(x) \geq \alpha_k\}$$

Note that α_k represents the kth α-cut, α_k = k/n, k$\in \{0, 1, 2, ..., n\}$.

1.3.7. Total dominance of $\tilde{A}_i$ over $\tilde{A}_j$ is integrated as:

$$D_{ij}(\beta) = \beta \cdot D_{ij}^{R} + (1 - \beta) \cdot D_{ij}^{L}$$

Where β is an optimistic index. Note comparison between $\tilde{A}_i$ and $\tilde{A}_j$ is made using the following relations:

i If $D_{ij}(\beta) > 0$, then $A_i > \tilde{A}_j$

ii If $D_{ij}(\beta) = 0$, then $A_i = \tilde{A}_j$

iii If $D_{ij}(\beta) < 0$, then $A_i < \tilde{A}_j$

The ranking result helps to identify important CR's and EC's for subsequent product design and development.

2. Evaluation and selection of prototype products

The goal of this stage is to select the best prototype product based on EC's and company's production demands

2.1. Construct a fuzzy decision matrix

2.1.1. Obtain weights of EC's and company's production demands

2.1.1.1. For EC's, the final importance can be treated as the weight of the evaluation criteria whereas for company's production demands the final importance of EC's should be normalized:

$$NWEC_j^{\alpha} = \frac{FIEC_j^{\alpha}}{FIEC^{max}}, j = 1, 2, ..., n,$$

Where $NWEC_j^{\alpha}$ is the normalized weights of EC_j and $FIEC^{max}$ is the right end of the largest $FIEC_j^{\alpha}$ when α = 0, for j=1,2,...,n. After normalization, the values of final importance of ECs will be within the interval [0, 1].

2.1.1.2. Use the ratio estimation method, which is used in SMART, to determine the weights of company's production demands.

2.1.1.3. Select appropriate linguistic variables, from Table 2.1, to express relative importance of production demands compared to least important EC (or the smallest of $NWEC_{aj}$).
Final weights of all evaluation criteria are calculated as follows:

$$FWC_j^{\alpha} = \begin{cases} NWEC_j^{\alpha},\ j = 1,2,...,n, \\ RIPD_j^{\alpha} \cdot NWEC_{min}^{\alpha},\ j = n+1, n+2, ..., n+s, \end{cases}$$

Where FWC_j^{α} is the final weight of criterion j, $NWEC_{min}^{\alpha}$ is the smallest of $NWEC_j^{\alpha}$ and $RIPD_j^{\alpha}$ is the relative importance of production demand j compared to $NWEC_{min}^{\alpha}$.

2.1.1.4. Assess performance ratings of prototype products with regard to each evaluation criterion. Use linguistic variables from Table 2.1 to assess performance ratings, where a fuzzy decision matrix is made like the following:

$$\begin{array}{c} \\ A_1 \\ A_1 \\ \vdots \\ A_r \end{array} \begin{array}{c} \begin{array}{cccc} C_1 & C_2 & \cdots & C_{n+s} \end{array} \\ \begin{bmatrix} \widetilde{X}_{11} & \widetilde{X}_{12} & \cdots & \widetilde{X}_{1(n+s)} \\ \widetilde{X}_{21} & \widetilde{X}_{22} & \cdots & \widetilde{X}_{2(n+s)} \\ \vdots & \vdots & \ddots & \vdots \\ \widetilde{X}_{r1} & \widetilde{X}_{r2} & \cdots & \widetilde{X}_{r(n+s)} \end{bmatrix} \end{array}$$

Where A_i is the prototype product (alternative) i, C_j is the evaluation criterion j and $\widetilde{X}_{ij}$ is the assessed performance rating of prototype product i with respect to criterion j.

2.1.2. Determine the ranking order of all prototype products with respect to each evaluation criterion using Chen and Lus [103] fuzzy ranking method. Take the assumption that the ranking results of prototype products for evaluation criteria $C_1, C_2 ... C_n$ are : $A_j > A_r > ... > A_i$; $Ar > Aj > ... > A_i$; ...; $A_r > A_i > ... > A_j$ respectively. Construct a ranking matrix as follows:

$$\begin{array}{c} \\ 1st \\ 2nd \\ \vdots \\ rth \end{array} \begin{array}{c} \begin{array}{cccc} C_1 & C_2 & \cdots & C_{n+s} \end{array} \\ \begin{bmatrix} A_j & A_r & \cdots & A_r \\ A_r & A_j & \cdots & A_i \\ \vdots & \vdots & \ddots & \vdots \\ A_i & A_i & \cdots & A_j \end{bmatrix} \end{array}$$

2.1.3. If performance ratings of two (or more) prototype products, with regards to one evaluation criterion, are the same then they are assigned to the same ranks.

Which is then transformed into a weight-ranking matrix, represented by α-cuts, as follows:

$$\begin{array}{c} \\ 1st \\ 2nd \\ \vdots \\ rth \end{array} \begin{array}{c} \begin{array}{cccc} C_1 & C_2 & \cdots & C_{n+s} \end{array} \\ \begin{bmatrix} FWC_1^\alpha \cdot X_{j1}^\alpha & FWC_2^\alpha \cdot X_{r2}^\alpha & \cdots & FWC_{n+s}^\alpha \cdot X_{r(n+s)}^\alpha \\ FWC_1^\alpha \cdot X_{r1}^\alpha & FWC_2^\alpha \cdot X_{j2}^\alpha & \cdots & FWC_{n+s}^\alpha \cdot X_{i(n+s)}^\alpha \\ \vdots & \vdots & \ddots & \vdots \\ FWC_1^\alpha \cdot X_{i1}^\alpha & FWC_2^\alpha \cdot X_{i2}^\alpha & \cdots & FWC_{n+s}^\alpha \cdot X_{j(n+s)}^\alpha \end{bmatrix} \end{array} =$$

$$\begin{array}{c} \\ 1st \\ 2nd \\ \vdots \\ rth \end{array} \begin{array}{c} \begin{array}{cccc} C_1 & C_2 & \cdots & C_{n+s} \end{array} \\ \begin{bmatrix} WP_{j1}^\alpha & WP_{r2}^\alpha & \cdots & WP_{r(n+s)}^\alpha \\ WP_{r1}^\alpha & WP_{j2}^\alpha & \cdots & WP_{i(n+s)}^\alpha \\ \vdots & \vdots & \ddots & \vdots \\ WP_{i1}^\alpha & WP_{i2}^\alpha & \cdots & WP_{j(n+s)}^\alpha \end{bmatrix} \end{array}$$

2.1.4. Calculate the aggregated weight of each product prototype A_r in different ranks by summing the corresponding elements in the weight-ranking matrix:

$$WP_{r2}^\alpha + ... + WP_{r(n+s)}^\alpha$$

2.1.5. Create an aggregated weight matrix as follows:

$$\begin{array}{c} \\ A_1 \\ A_2 \\ \vdots \\ A_r \end{array} \begin{array}{c} \begin{array}{cccc} 1st & 2nd & \cdots & rth \end{array} \\ \begin{bmatrix} AW_{11}^\alpha & AW_{12}^\alpha & \cdots & AW_{1r}^\alpha \\ AW_{21}^\alpha & AW_{22}^\alpha & \cdots & AW_{2r}^\alpha \\ \vdots & \vdots & \ddots & \vdots \\ AW_{r1}^\alpha & AW_{r2}^\alpha & \cdots & AW_{rr}^\alpha \end{bmatrix} \end{array}$$

2.2. Formulate a fuzzy linear programming (FLP) problem

2.2.1. The aggregated weight matrix can then be formulated as a fuzzy linear assignment problem as follows:

$$Max \sum_{i=1}^{r} \sum_{j=1}^{r} AW_{ij}^\alpha t_{ij}$$

$$S.T. \sum_{i=1}^{r} t_{ij} = 1,\ j = 1,2,...,r,$$

$$\sum_{i=1}^{r} t_{ij} = 1,\ i = 1,2,...,r,$$

$$\forall t_{ij} = 0 or 1$$

Where t_{ij} is the value of prototype product i in rank j. If t_{ij} = 1, prototype product i is actually ranked jth; otherwise, prototype product i is not ranked jth.

2.2.2. Solve FLP problem using Rommelfangers [104] method to obtain the final ranks of all prototype products

2.2.2.1. FLP problem is first converted to a multi-objective linear programming problem (MOLP). The converted result of the above FLP problem then becomes:

$$\text{Max} \sum_{i=1}^{r}\sum_{j=1}^{r} \underline{AW}_{ij}^{\alpha} t_{ij}$$

$$\text{Max} \sum_{i=1}^{r}\sum_{j=1}^{r} \overline{AW}_{ij}^{\alpha} t_{ij}$$

$$\text{S.T.} \sum_{i=1}^{r} t_{ij} = 1,\ j = 1,2,...,r,$$

$$\sum_{j=1}^{r} t_{ij} = 1,\ i = 1,2,...,r,$$

$$\forall t_{ij} = 0 or 1$$

Where $\underline{AW}_{ij}^{\alpha}$ and $\overline{AW}_{ij}^{\alpha}$ are the left and right ends of the interval AW_{ij}^{α} respectively.

2.2.2.2. Use weighting method to convert MOLP problem into a crisp linear programming (LP) problem as follows:

$$\text{Max } \lambda \sum_{i=1}^{r}\sum_{j=1}^{r} \underline{AW}_{ij}^{\alpha} t_{ij} + (1-\lambda) \sum_{i=1}^{r}\sum_{j=1}^{r} \overline{AW}_{ij}^{\alpha} t_{ij}$$

$$\text{S.T.} \sum_{i=1}^{r} t_{ij} = 1,\ j = 1,\ 2,...,r,$$

$$\sum_{j=1}^{r} t_{ij} = 1,\ i = 1,\ 2,...,r,$$

$$\forall t_{ij} = 0\ or\ 1$$

Where λ is the weight of the first objective function in the above MOLP problem, $0 \leq \lambda \leq 1$.

The value of k is defined as 0.5 because both objective functions are equally important. Note that the converted LP problem is a 0–1 integer programming problem and that software, such as LINGO, can be applied to solve the crisp LP problem. The end solution shows the final ranking of each prototype product and helps to select the best prototype product [1].

2.6 Discussion

This discussion section details the findings from the literature review of hardware developments, software developments and design methodologies and provides a structure for the statement of research direction.

2.6.1 Hardware Development

This section describes four areas of hardware development: portability, illumination methods, variable magnification and stage design.

2.6.1.1 Portability

Portability was shown to have been achieved in two ways: folded optics and batteries. From the examples provided in Section 2.2.1.1, folded optics can help in reducing the size of the overall optical system. A reduction in size means a system that could be lighter and easier to move around which helps in achieving the portable objective of this design. Therefore, where possible, folded optics should be used in the design.

Batteries were also found to help make the system portable because they take out the need to plug into a power outlet. From the three different battery technologies presented, lithium ion batteries had the highest energy density and charge retention in comparison to nickel metal hydride and nickel cadmium batteries. Lithium ion batteries had also been used in more closely relevant applications to our intended design direction of portable electronics such as cameras, smart phones and powertools. For these reasons discussed, lithium ion would be a suitable choice in the battery technology used to achieve portability in the design.

2.6.1.2 Illumination Methods

Illumination methods were researched to see how they worked, how they were setup and what advantages they offered to an optical system. Both bright-field and fluorescence illumination methods had relatively simple setups and common optical components such as a light source and objective lens. Bright-field works well with transparent samples and fluorescence is useful for fluorescent samples. Laser diffraction also has a simple setup: requiring only the diffraction grating as an extra optical component and can use the same light path as bright-field illumination. The diffraction patterns produced by laser diffraction have generally been used to determine size estimation. Dark-field illumination has a similar setup to bright-field however it requires the use of an annular ring. The annular ring can be a particular issue because it may require well defined alignment to achieve a proper dark-field illuminated image on the camera sensor. From this research, bright-field, fluorescence, laser diffraction seem to be readily achievable and dark-field may not be so readily achievable. Incorporating them is important to achieve our stated objectives of making a multi-modal illuminated system.

2.6.1.3 Variable Magnification

Variable magnification is a standard and useful feature in microscopes. It allows magnification to be changed to view an area at a higher magnification. The examples presented all achieved variable magnification by changing standard objective lenses. Using standard lenses like [74],

instead of trying to use existing in-built lenses, such as the case of [19] could allow for an easier design because it is a standard off-the-shelf part. Therefore, using standard objective lenses would be beneficial in the design.

2.6.1.4 Stage Design

Stage design is important because it defines the movement of the field of view. From the two physical examples shown, both brought advantages to their design. Schaefer et al. [19] demonstrated the use of modified CD drive components including the successful movement of the stage by the CD drive stepper motor. Leicas system achieved finer movement of the stage with the use of reduction gears. Other examples also used stepper motors to control the stage, where the OpenStage [55] design used higher quality stepper motors to naturally achieve more accuracy. Elements from the examples can be taken into the design depending on how the design develops but should be considered to achieve the automated scanning objective set out in this paper.

2.6.2 Software Development

2.6.2.1 Increasing field of view through software stitching

Software development was researched in two areas: increasing field of view through software stitching and using image processing to analyze image data. The idea of stitching images together is beneficial because it allows a larger field of view allowing you to see more detail from one stitched image compared to a single image from the set. From the examples presented, all were relevant to our research because they worked on stitching images from microscopic samples. Therefore, where possible, stitching should be implemented in the design of the system.

2.6.2.2 Image Stitching Tools

On investigating different image stitching tools, Microsoft Image Composite Editor (ICE), OpenCV and ImageJ had all been used in medical applications, among other applications such as material science, and all were free to use for research. For the work of Gross et al. [59], ICE was found to produce the fewest visual errors and was generally used in applications were raw images were required to be stitched with a standalone appliation. It is worth noting that the paper from Gross [59] compared ICE with Pix4D and Photoscan Pro in the context of aerial photography. ICE is not open-source, unlike OpenCV or ImageJ, and comes as a standalone platform. OpenCV has wrappers for C (EmguCV) and Python whereas ImageJ is solely meant for java applications. Compared to OpenCV, ImageJ and ICE have more stitching parameters such as being able to pre-define the sequence of images to make the stitching process faster. From how different researchers have applied the three stitching systems mentioned, there is general consensus that it depends on your application. If you have raw output images and need a tested application for microscopic samples, ICE or ImageJ could be used; if there is a need to make a custom C++, C# or

Python application then OpenCV could be used; if it's a custom application required in java then ImageJ might be suitable. It is worth mentioning that the images produced from our research may not have similar quality to the images from the examples shown in Section 2.3.1.2 such that a preliminary test may be required in the software development phase before proceeding with a particular stitching library or application.

2.6.2.3 Microscopic Image Processing

Microscopic image processing was researched in three areas: particle counting, perimeter estimation and area estimation. Particle counting was found to be a useful tool because, from the examples detailed, it could be used to count cells which would work favourably for our application. Area and perimeter estimation are also useful because they can be used in applications to study microscopic samples of biological specimens such as cells or, in the case of Goldberg et al. [75], for showing signs of condensation in positive nuclei. Basic calculations such as perimeter and area estimation can then be further used for calculating displacement, protrusiveness and ellipticity for the case of cells. Image processing tools such as Aforge and OpenCV both have readily available methods for calculating particle counting, perimeter and size estimation so it would make sense to implement it were possible in the design.

2.6.2.4 Microscopic Image Processing Tools

There were two image processing tools researched: Aforge.NET and OpenCV. Both libraries were open-source and, from the examples discussed, both tools had the capacity for particle counting and shape detection. Both had relevant medical applications in counting and detecting cells. If an application was developed in C# then both libraries could be suitable with EmguCV requiring a slightly longer setup than Aforge which only requires a simple DLL reference to the relevant library. OpenCV has the advantage of having a larger library and flexibility to develop on more platforms. It is worth mentioning that where researchers have used both libraries in one application [80][105], they used EmguCV for data processing and Aforge for image processing. The choice of hardware may also determine which development environment is used and subsequently which image processing library is used.

2.6.2.5 Auto-focusing

Auto-focusing was researched and three auto-focus algorithms were discussed: tenengrad variance method, gray-level local variance and histogram range. As per the work of Pertuz et al. [85], the tenengrad variance method achieved a higher relative focus quality in comparison to the other two for both Logitech's sequences and Sony's sequences. It also had applications in microscopy which made it more suitable than the other two.

2.6.3 Microscope designs comparable to our research direction

Three microscope designs were discussed in this section. The design from the University of British Columbia [19] used readily available components from disk drives to construct their stage design which is favourable because of the low cost of this approach. The University of California Berkeley [74] used a mobile phone for their design, and was setup similar to a standard optical setup but with the phone camera replacing the eyepiece. The use of the phone is useful because it allows all the computation to be done on the system rather than on a separate computer. Both the designs incorporated fluorescence illumination through the use of a UV LED and emission/excitation filters respectively. Miller et al.[90] and University of California Berkeley [74] had the two portable designs. Miller et al. achieved portability by using a battery in their design. They also used a turret with standard objective lenses. The lighting was done similar to [74] where a LED was used to illuminate the sample. Stitching and auto-focusing were only done in the design presented by [19] who used Adobe CS6 to stitch the images and the inbuilt lens to auto-focus respectively. From the research presented, the elements that could be considered in our design are: LED for illumination, in-built auto-focusing, using standard objective lenses and using a standard turret system design.

2.6.4 Design and Creative Methodology

In this section, five design methodologies were studied that had beginnings in the 1920's through to 2017. Systematic design, TRIZ, Synectics and Axiomatic design all had examples of being used today indicating that they were still relevant design methods. PDS was the most recent method but no researcher had specifically implemented it in their design. Systematic design offered a complete design method from brainstorming, conceptual design, detailed design and finally an end solution. TRIZ and Synectics were idea generation methods rather than complete design processes, although they produced innovative solutions in both research and industry applications when applied. Further comparing TRIZ and Synectics, TRIZ offered a more robust method for idea generation with its 40 inventive principles whereas Synectics was a more general method that relied on the designers' experience - a view paralled by Yilmaz and Seifert [106]. Fantoni et al. [107] commented that Synectics was a powerful tool but a "very low structured technique". They went on to argue that "too much abstraction" can lead to a multitude of concepts which is not realistically practical because it becomes increasingly difficult to select one. They however also stated that Synectics is still a good tool for overcoming fixation and a block in creativity. Axiomatic Design and PDS were the only two methods that readily utilized a mathematical approach to concept selection. PDS was a more thorough method, however, it was based on QFD and thus required research data, such as questionnaires, to be taken from clients who had a stake in the design. In the case of our design, this would mean getting this research data from a sizeable population of current users of microscopes to achieve significant results using the PDS method. Such a task may produce an insightful look into what requirements are in

industry at present, but as PDS is done by a "team" of individuals from several departments, a sole researcher may not be sufficient in achieving a proper and timely result. PDS also does not have any set methods to develop a concept such as Systematic Design does: it can only identify engineering requirements for a particular product and then select a prototype product based on those engineering requirements and companies production demands. Systematic design seems to be a suitable choice for the design method to use in our research because of its completeness of the entire design cycle and its continued relevance in research.

2.7 Statement of research direction

In this chapter hardware and software development have been researched. Three specific designs were studied in further detail to indicate the research direction we wish to progress in. With advancements in consumer market devices, a variety of low cost optical components are readily available which have facilitated many system designs for portable usage. We wish to undertake research in the development of a portable micro-imaging system that uses multi-modal illumination of bright-field, fluorescence and laser diffraction, and that has variable magnification and automated scanning.

CHAPTER 3

OPTO-MECHANICAL DEVELOPMENT

3.1 Systematic Design of Mechanical System

Following from Section 2.5.1, we have chosen to proceed with the systematic design approach developed by Beitz and Pahl [91]. They have divided the design process into four stages: planning and task clarification, conceptual design, embodiment design, detail design. As our system is research oriented, we will omit the detailed design phase that involves producing detailed drawings for manufacture. We will use this process in the development of the micro-imaging system.

3.1.1 Planning and Task Clarification

In this section we outline the overall requirements of the system. The system needs to have/be able to:

- Bright-field illumination
- Fluorescence illumination
- Laser diffraction
- Variable magnification
- Motor controlled x-axis and y-axis
- Motor controlled z-axis
- Scan an area of a sample slide

- Stitch scanned images
- Compact
- Portable

3.1.2 Conceptual Design

Broadly speaking, as [91] put it, "conceptual design specifies the principle solution". Following closely from the requirements list established in the previous section, the following three questions should now be asked:

1. Has the task been clarified sufficiently to allow the development of a solution in the form of a design?
2. Is a conceptual elaboration really needed, or do known solutions permit direct progress to the embodiment and detail design phases?
3. If the conceptual stage is indispensable, how and to what extent should it be developed systematically?

The answers to these questions are as follows:

1. Yes. We know the basic requirements of the system.
2. Conceptual elaboration is necessary because the known solutions investigated in the literature review of multi-modal optical systems do not have laser diffraction, bright-field and fluorescence in one system
3. It should be developed to the extent that the items from the requirement list are met.

From the second question, we can see that the conceptual design phase will have to proceed and, as such, the stage is defined through a series of steps (see Figure 3.1).

3.1.2.1 Abstracting to Identify the Essential Problems

In this stage of the conceptual design process, the requirement list is now abstracted in order to fully get the real purpose of the design. The process of abstraction, as stated in [91], is done with the following steps:

1. Eliminate personal preferences
2. Omit requirements that have no direct bearing on the function and the essential constraints
3. Transform quantitative into qualitative data and reduce them to essential statements

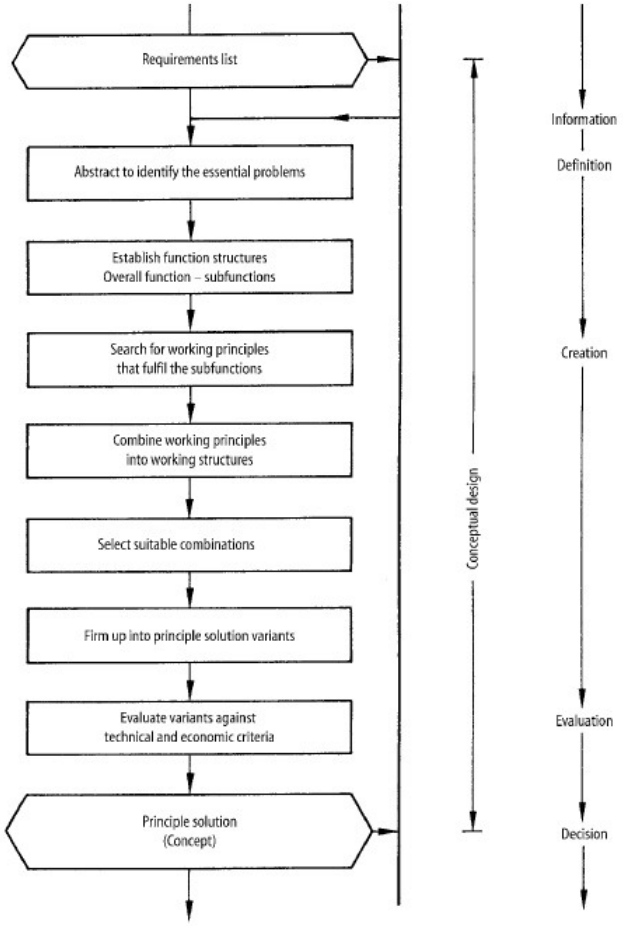

Figure 3.1: Process of Conceptual Design in Systemic Design Approach

4. As far as it is purposeful, generalise the results of the previous step
5. Formulate the problem in solution-neutral terms

Applying these steps to the requirement list from Section 3.1.1, the following abstract list was generated:

1. Use many modes of illumination
2. View details of sample that cannot be seen with normal sight
3. Produce a sharp image
4. Increase field of view
5. Easy to carry
6. Does not occupy significant space

3.1.2.2 Establishing Function Structures

The purpose of this section is to take the requirement list from Section 3.1.1 and visualize the solution-neutral relationship between inputs and outputs. This is done by making a block diagram comprised of function structures, and sub-function structures if required, while keeping the abstraction developed in the previous section in perspective. Function structures are block diagrams that illustrate the flow of materials, signals and energy with respect to a particular function. Our function structure can be seen in Figure 3.2. The overall function is to display a magnified image from the light source.

From this function structure we can see the areas that need to be developed, for example the change in magnification uses a turret system. Although the turret system is not specified in the requirement list, following from the literature review, it was found to be a standard item in most microscopes so taking it as a material input for the 'Choose Magnification' function seemed appropriate. This turret would need to be developed in the concept stage. The same can be said about the z-axis motors and x and y axis motors for the 'Adjust focus' and 'scan' functions respectively.

3.1.2.3 Find Working Principles for function structures

At this stage, the function structures established in the previous section now have to have working principles: real physical ways to make them function. As per [91], the method they use is Zwicky's morphological matrix [108] which sets up possible solutions in columns and the functions as rows. The morphological matrix for our system can be seen in Figure 3.3.

3.1.2.4 Developing working structures

Working structures are those that combine the working principles together to form one system. This idea is described in [91] as "system synthesis". In this stage, while developing a working structure, it is also important to select appropriate working principles.

From the morphological matrix, a set working structure was determined with the following working principles:

- Ramp to lift stage
- Turret system 2 as that is closest to what standard microscopes use. This will imply an upright design.
- Use an objective lens because it is a standard item and easily utilized
- Use a scan function that uses a snake algorithm because it can save time

As this is an original design, the focus must be centered around the overall function [91]: to display a magnified image. In saying so, we will omit the variable magnification and scan functions

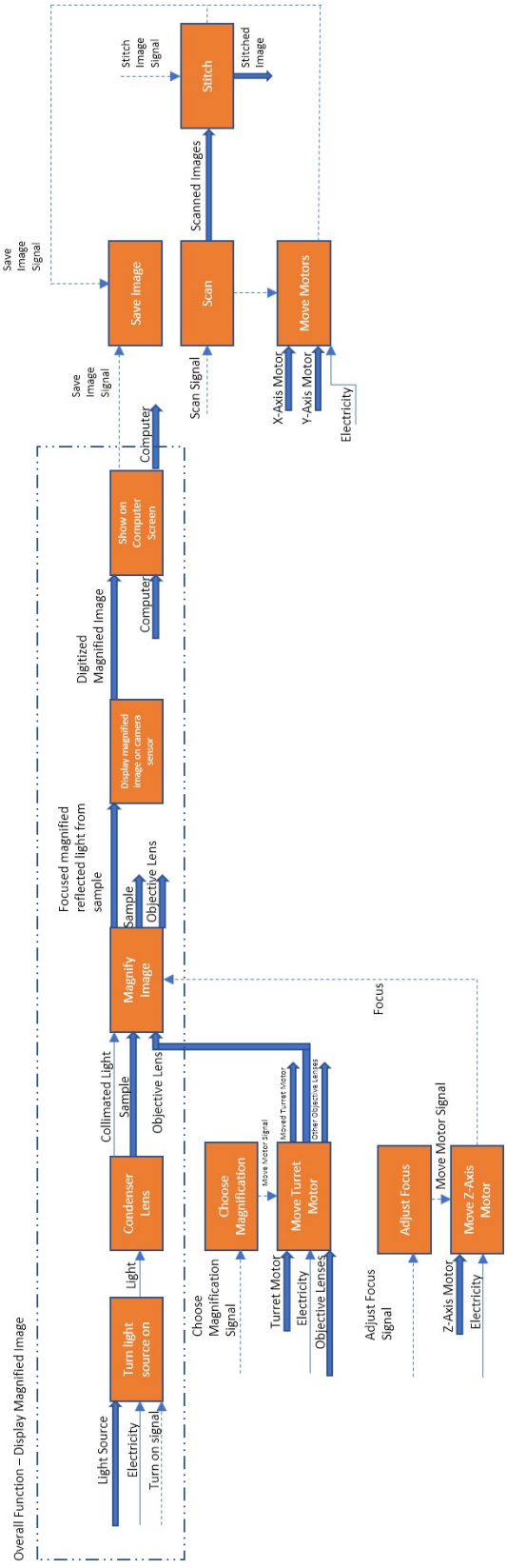

Figure 3.2: Overall function structure based on requirement list

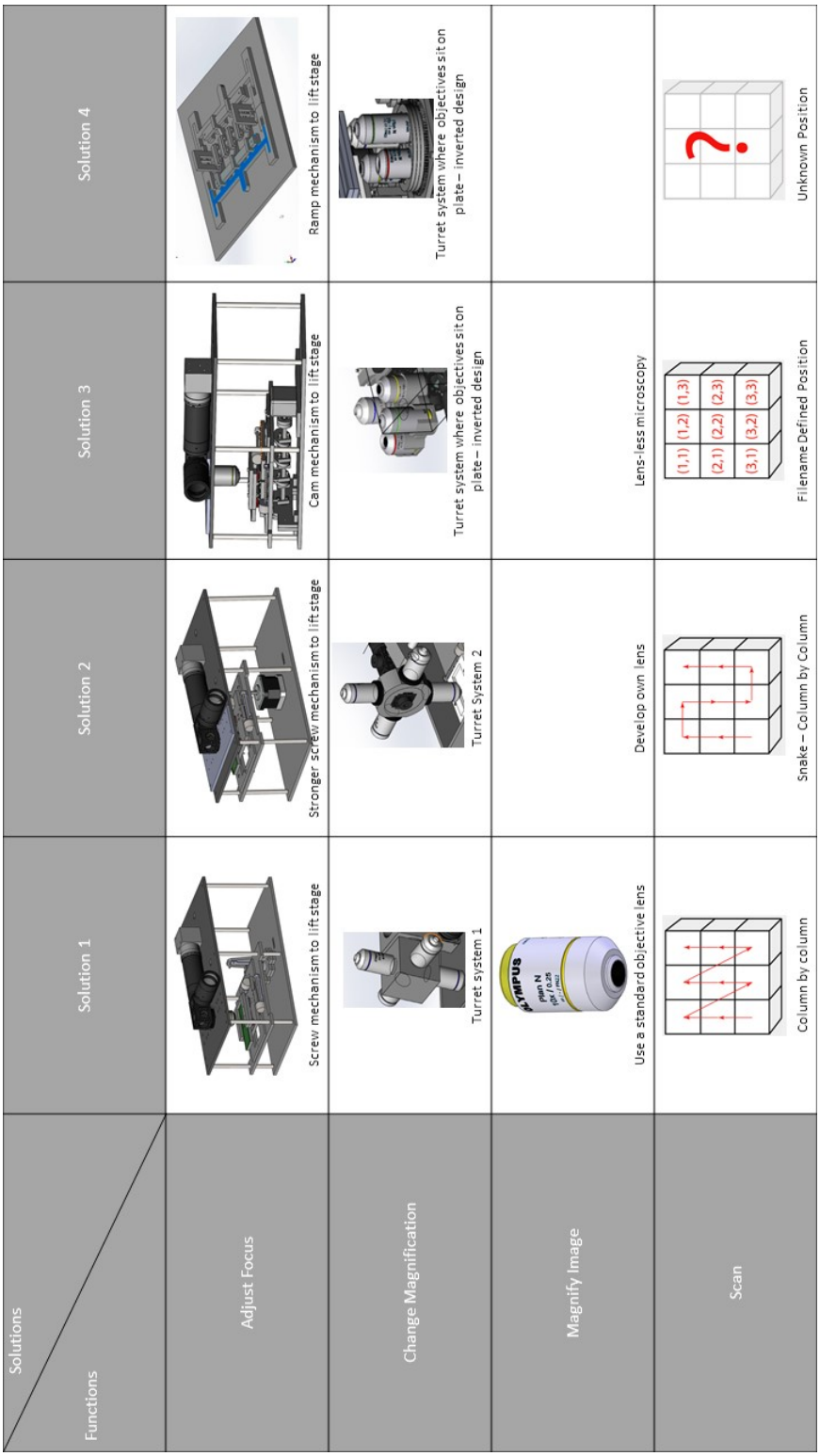

Figure 3.3: Morphological matrix of functions

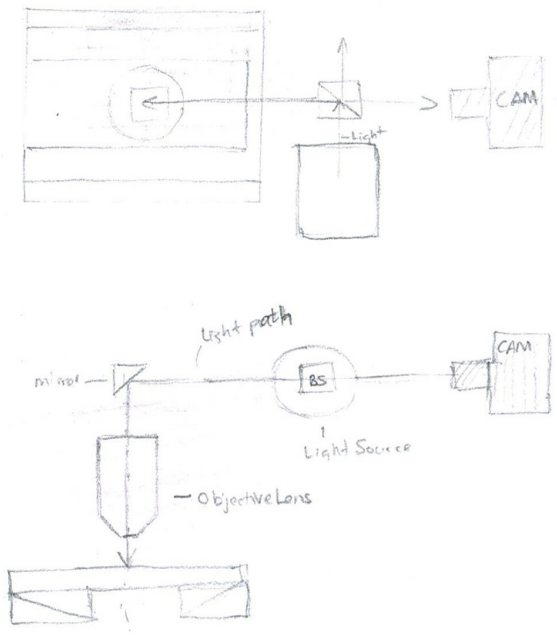

Figure 3.4: Initial sketch from working structure

temporarily and produce a working prototype based on using a single objective lens with an upright design. The working structure resulted in an initial concept sketch seen in Figure 3.4. We had to use a mirror and beam-splitter to allow for the light path to reflect off the sample as well as go to the camera.

3.1.2.5 Firming up into principle solution variants

In this stage, sketches, models and prototypes to test the principle solution can be made. Following closely from the previous section, here the system was made into an initial prototype.

3.1.2.5.1 Z-Axis

The first aspect of it was to make a functional system, but that required the stage to have an adjustable focus so we could get a sharp image. As such, we had to first get a functional z-axis first. Based on the working structure, we will develop a z-axis platform based on the ramp method. The first few sketches can be seen in Figure 3.5.

In these initial sketches, the full working principle behind the ramp lifting mechanism were being explored. A CAD design taking the idea of converting linear motion into rotational was also developed (see Figure 3.6) for the potential purpose of pushing the ramps.

This was then further developed to have the ramps come in from either side to lift the slide mechanism (see Figure 3.7).

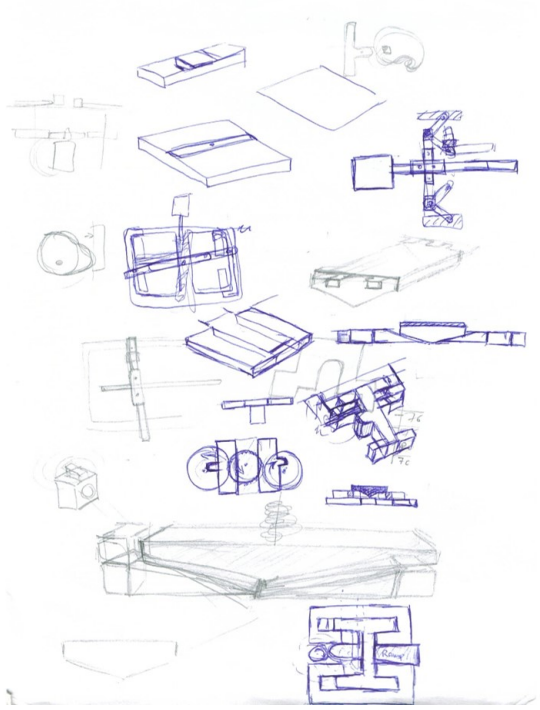

Figure 3.5: Initial sketches of z-axis mechanism

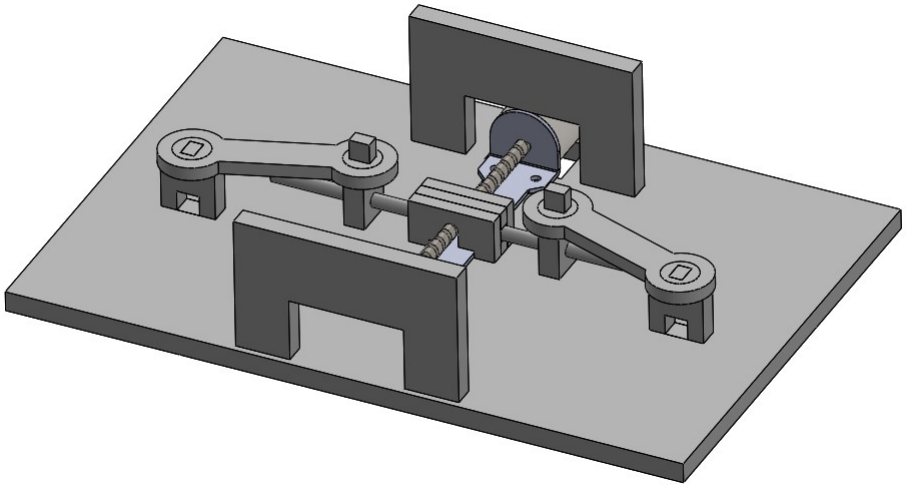

Figure 3.6: Initial z-axis mechanism converting linear motion into rotational

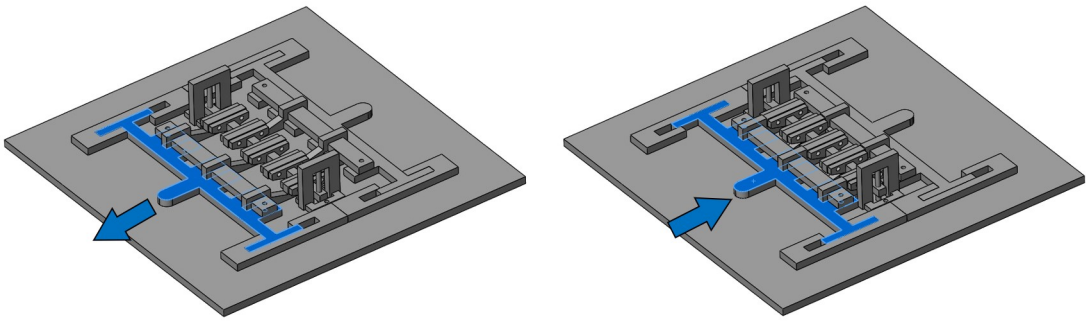

Figure 3.7: Z-axis mechanism with ramps. Note the selected surface in blue indicating the moving part

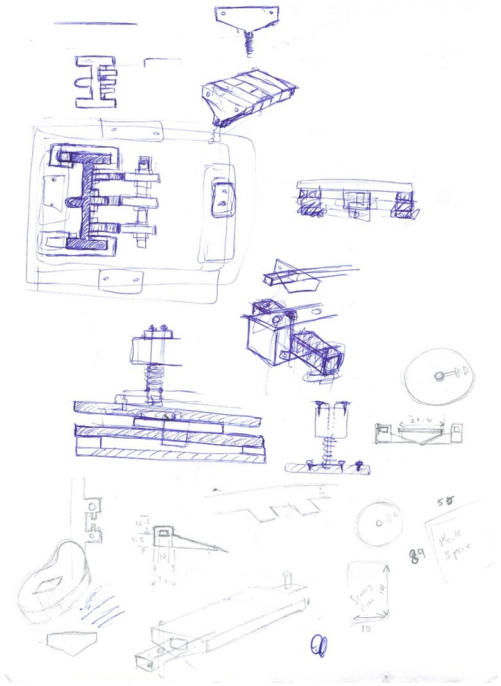

Figure 3.8: Sketches to develop working principles of z-axis mechanism

Sketches were made to find a way to make the mechanism have proper working principles (see Figures 3.8 and 3.9).

The mechanism was finally designed to have a cam mechanism and gears. It worked as follows: the motor would rotate and move a spur gear that would move a larger gear which would move two other spur gears. These two spur gears were connected to cams that would rotate a follower which had ramps attached to it (see Figure 3.10).

The prototype for this design was made out of acrylic because acrylic can be cut relatively quickly on the laser cutter. The prototype can be seen in Figure 3.11. The prototype did not perform well: the acrylic components were getting stuck in the sliding mechanism and the motor did not work.

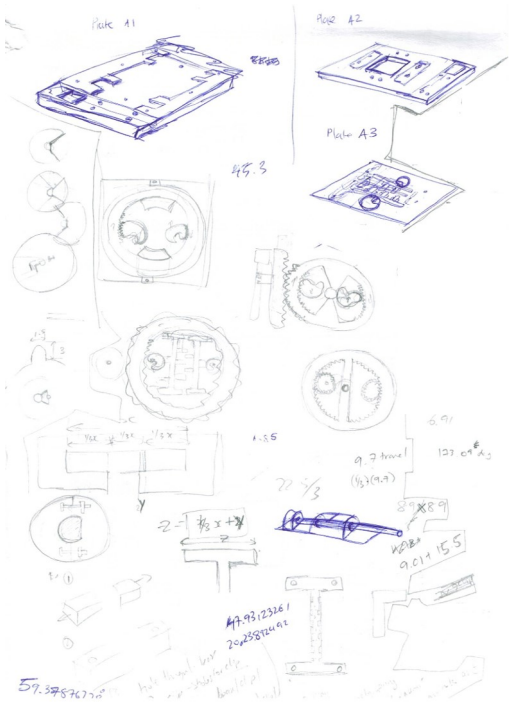

Figure 3.9: Sketches to develop working principles of z-axis mechanism

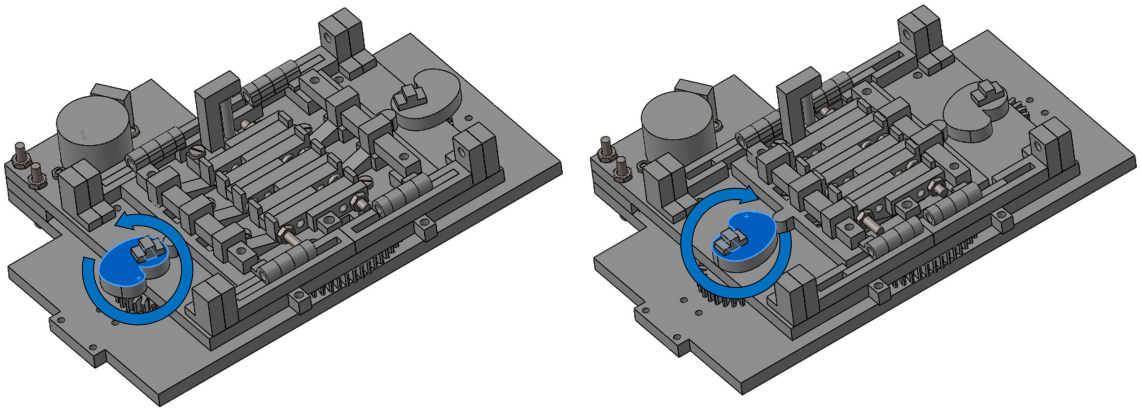

Figure 3.10: CAD Design of z-axis mechanism. Note the selected surface in blue indicating the moving part

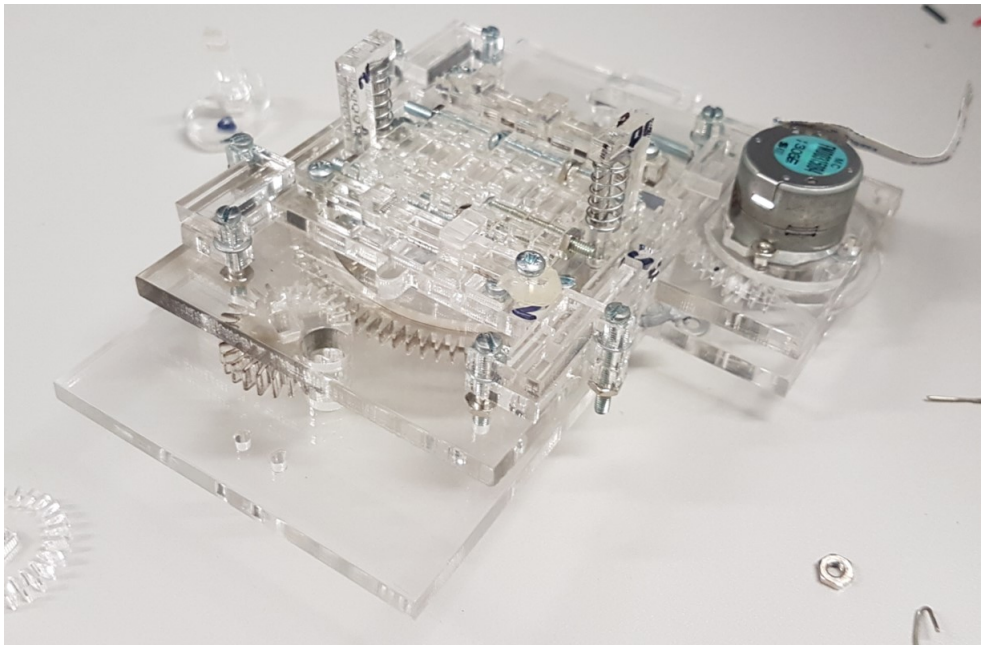

Figure 3.11: Z-axis prototype

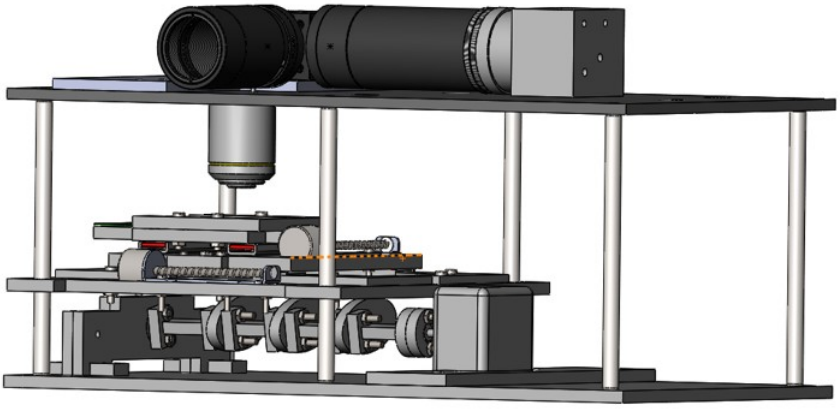

Figure 3.12: CAD Design of z-axis cam mechanism prototype

At this point, the z-axis mechanism had to be redesigned. On trying to make prototypes of both cam and screw mechanisms, (see Figures 3.12 and 3.13) these proved unsuccessful as well. It was here that we decided to use a standard z-axis mechanism from Edmund Optics (see Figure 3.14). While this had manual focus, it allowed us to proceed with the development of the rest of the system.

3.1.2.5.2 X-Y Axis

This section deals with the initial prototype of the x-y axis to reach a basic functional level. The

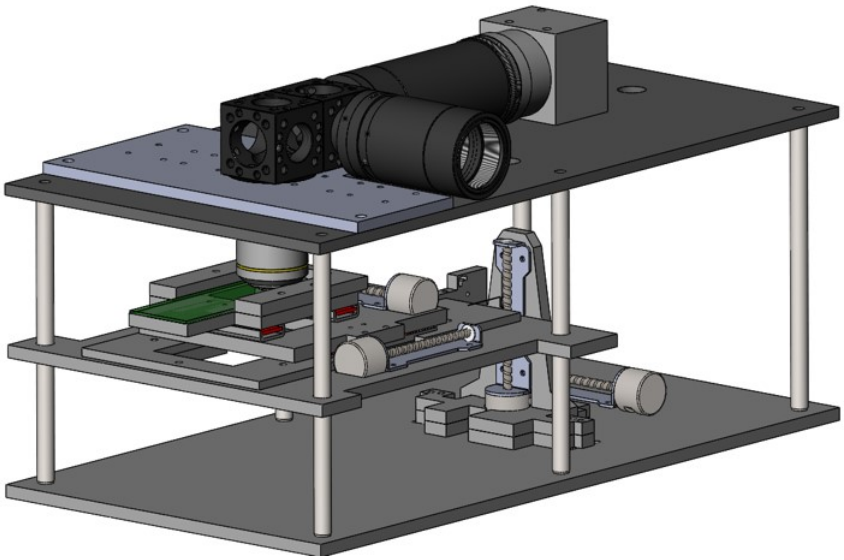

Figure 3.13: CAD Design of z-axis screw mechanism prototype

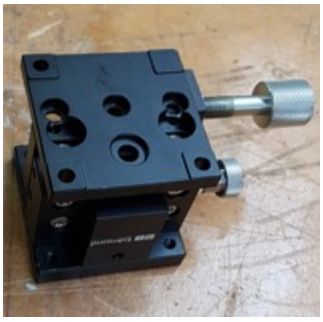

Figure 3.14: Edmund Optics Z-Axis Stage

stage had to move with very little friction so we used THK slides that had a friction coefficient of 0.003. The sample slide had a centered seat so it would be much more stabilized and acrylic was used for the base plates because it could be utilized into a prototype quicker when compared to other materials. Lead-screw stepper motors from DVD drives were also put in using a wire coiled around the thread of the lead-screw and attached by a screw onto the base plate. These motors were chosen because of their small size while still delivering the power required to move the bases. The calculations for justifying the use of these motors can be seen in Section 4.5.1. The prototype x-y axis stage can be seen in Figure 3.15.

3.1.2.5.3 Principle Concept

As per the initial sketch, seen in Figure 3.4, the full system CAD design was made (see Figure 3.16) and then the prototype was made from that (see Figure 3.17).

The prototype completed the overall function required: display a magnified image. It now needed to complete the rest of the functions that have been outlined in the previous sections.

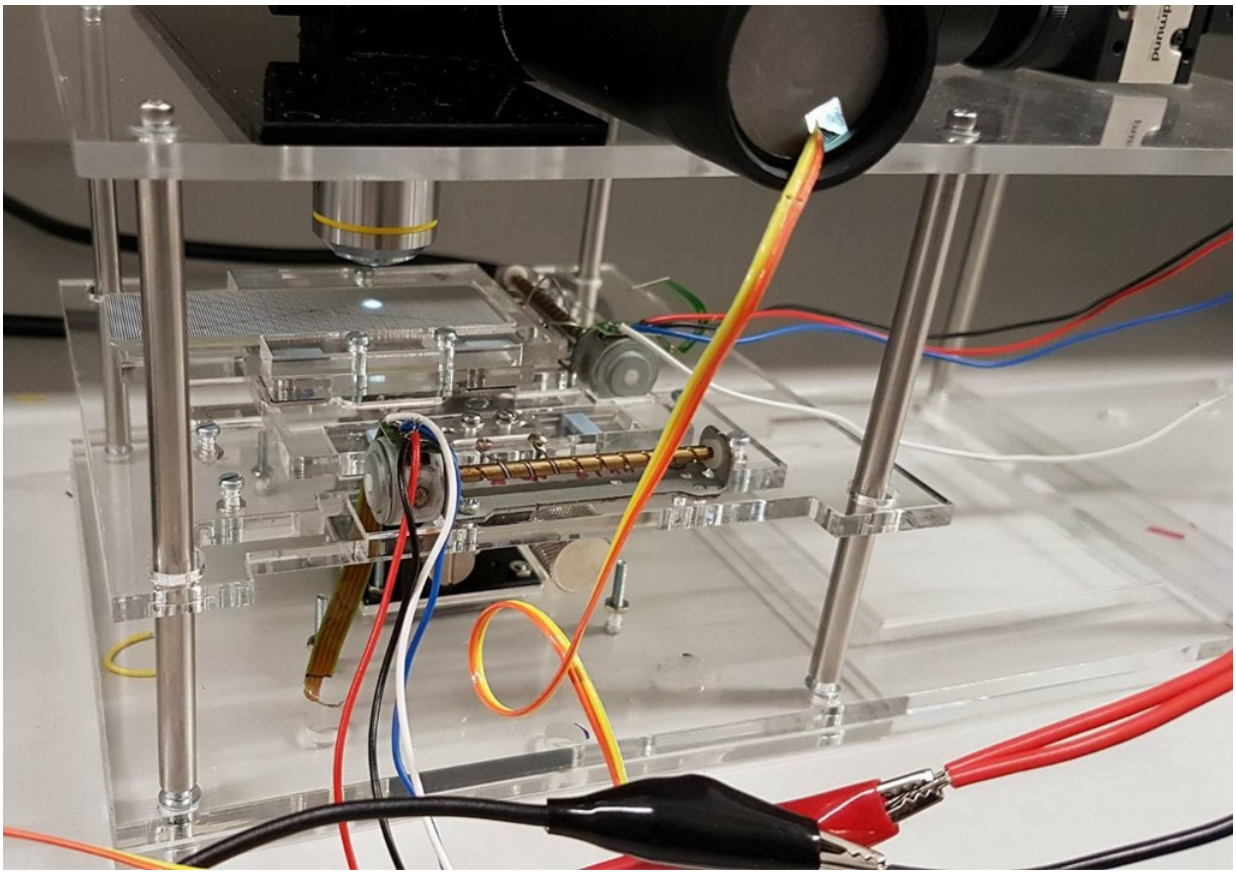

Figure 3.15: Initial x-y stage made with sample slide seat positioned in centre

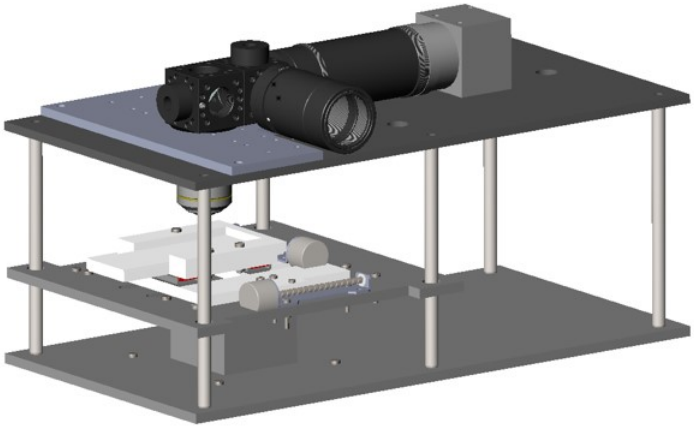

Figure 3.16: CAD design of principle concept

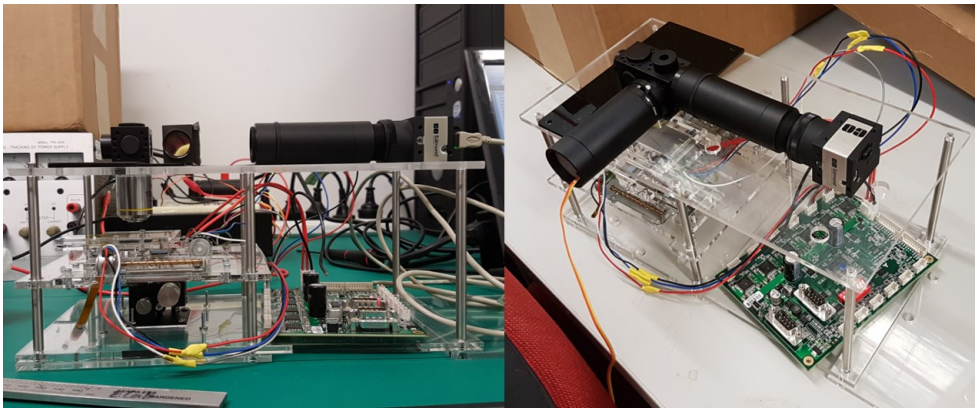

Figure 3.17: Prototype of principle concept

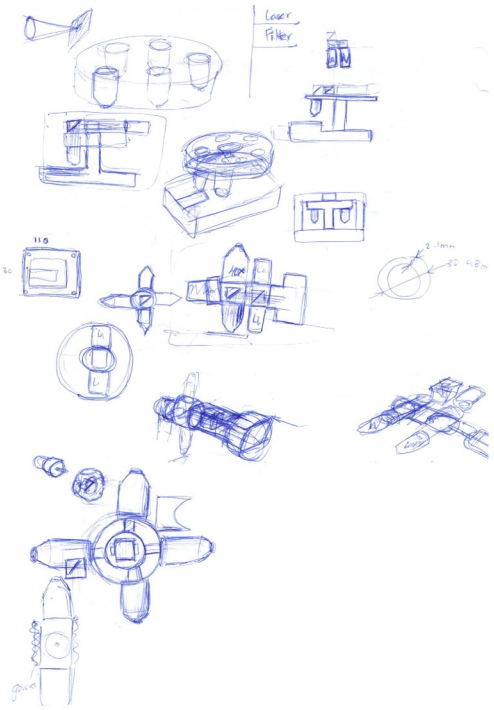

Figure 3.18: Initial sketches of variable magnification system

Here we continually made concepts alongside prototypes of the different functions. As such, in what follows of the concept phase, we will present the developments with individual focus on the z-axis stage, x-y stage, base, variable illumination and variable magnification. We start with the function of variable magnification. Initial sketches were building on the idea of a turret system (see Figures 3.18 and 3.19).

From these sketches CAD designs were made that were gradually developed. Figure 3.20 shows the initial stage 1 CAD design trying to incorporate variable magnification and multi-modal illumination into one system. Figure 3.21 shows a modification of this system where it uses

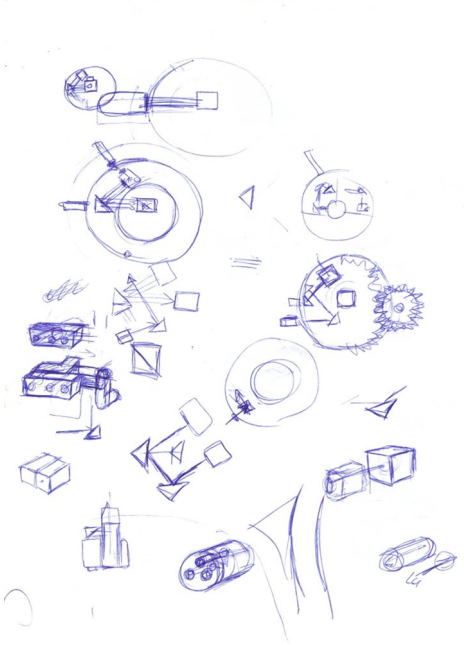

Figure 3.19: Initial sketches of variable magnification system

standard ThorLabs optical components and also a rotating circular turret for the multi-modal illumination similar to the objective turret.

By stage 3, see Figure 3.22, the circular turret for variable magnification was removed in order to keep the system more compact. Instead, the illumination modes were moved to keep parallel to the front face and linearly placed.

In stage 4, see Figure 3.23, the objectives sat on a turret - effectively turning the design into an inverted microscope. The inverted design was found to be advantageous because it allowed us to incorporate ambient illumination, such as from lighting in a room, to illuminate the sample. The inverted design is also advantageous because it provides easier access of putting slides onto the system as well as being closer to the center of mass of the system which makes it less prone to vibration [50]. The different modes of illumination: bright-field, fluorescence and laser, were accessed with a rotating mirror. The method of the rotating mirror being that, when a particular method of illumination is selected, the mirror, attached to possibly a servo motor, would rotate to that illumination source and redirect the light towards the sample which helps in reducing the size of the system.

Building from the design in stage 4, a z-axis was designed to similar to the mechanism from the Edmund Optics Z-Axis stage (see Figure 3.14). Namely, a lever would push the against a fixed mount that would lift the rest of the stage up.

Using an existing automatic z-axis that was available, the system was created to incorporate it (see Figure 3.26). We also designed a new stage for the microscope slide that would be manufactured out of 1mm steel plates (see Figure 3.25). Now the design met all the physical

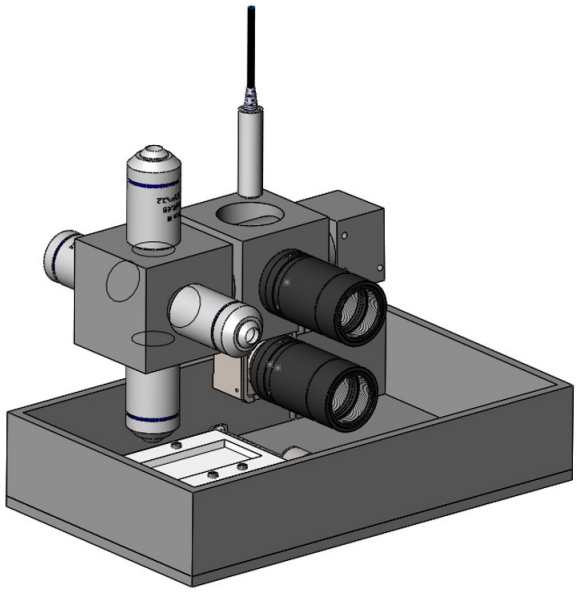

Figure 3.20: CAD design of system that incorporates variable magnification and multi-modal illumination (Stage 1)

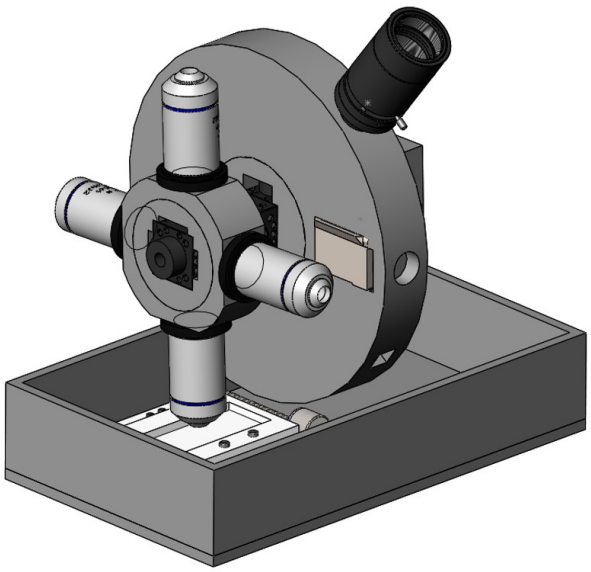

Figure 3.21: CAD design of system that incorporates variable magnification and multi-modal illumination (Stage 2)

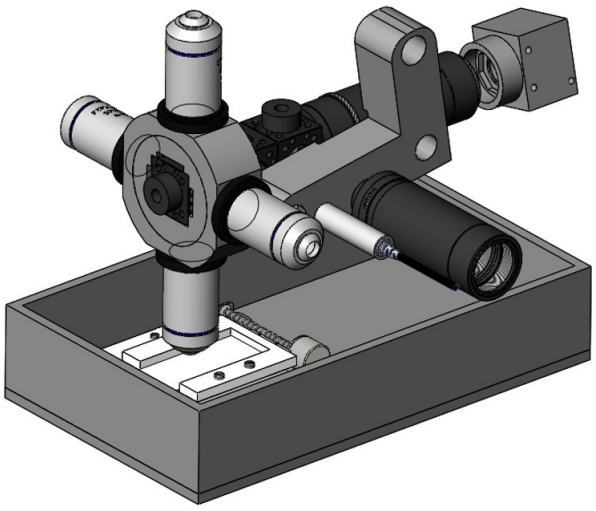

Figure 3.22: CAD design of system that incorporates variable magnification and multi-modal illumination (Stage 3)

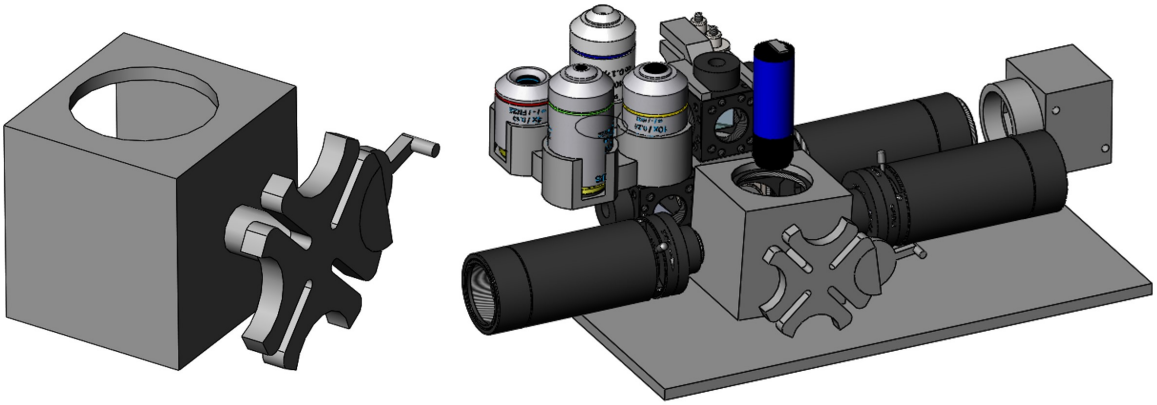

Figure 3.23: CAD design of system that incorporates variable magnification and multi-modal illumination (Stage 4)

requirements and a physical prototype would be next.

The prototype of stage 6 was made, as can be seen in Figure 3.27. Although, as stated before, it incorporated all the requirements, we found it was too large in size and would still need to be redesigned to be compact.

With the system to change the illumination and achieve variable magnification in place, the objective was now to make the design more compact. The design in Figure 3.28 placed the rotating mirror on the outside of the of the system. The stage had a major modification so that the slide holder was on the side rather than in the centre. By putting it on the side, the inverted design meant that the objectives did not have to be placed in alignment with the centre of the stage anymore (see Figure 3.29), as had been the case with the principle concept (see Figure 3.15). The z-axis mechanism was also changed by being replaced with a larger one in order to accommodate

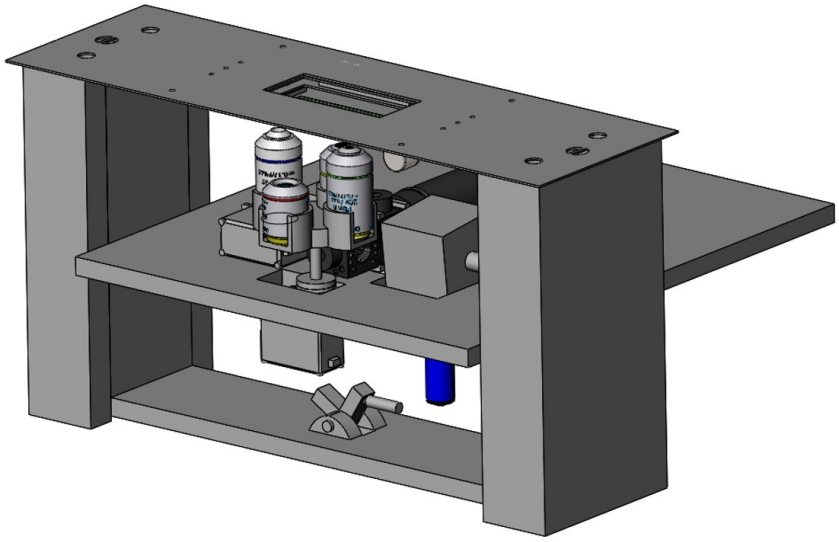

Figure 3.24: CAD design of system that incorporates variable magnification and multi-modal illumination (Stage 5)

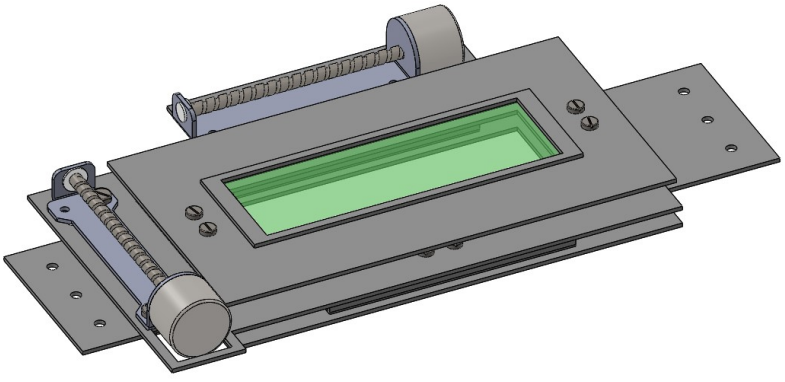

Figure 3.25: CAD design of microscope slide stage based on being manufactured out of 1mm steel plates

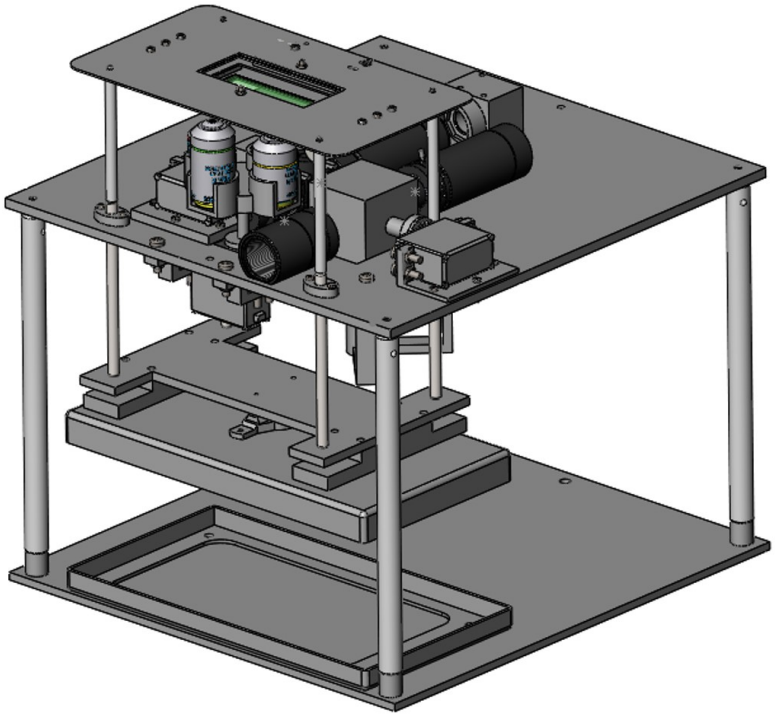

Figure 3.26: CAD design of system that incorporates variable magnification and multi-modal illumination (Stage 6)

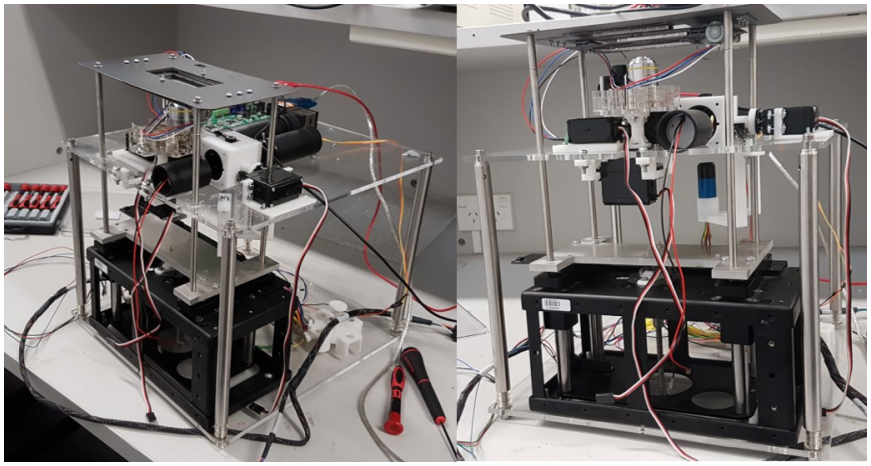

Figure 3.27: Prototype of Stage 6 design

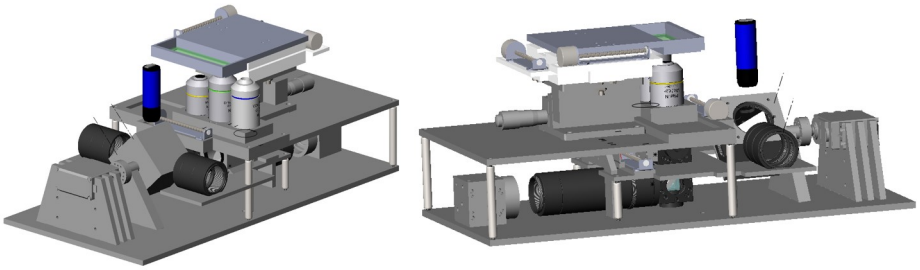

Figure 3.28: CAD design of more compact design (Stage 1)

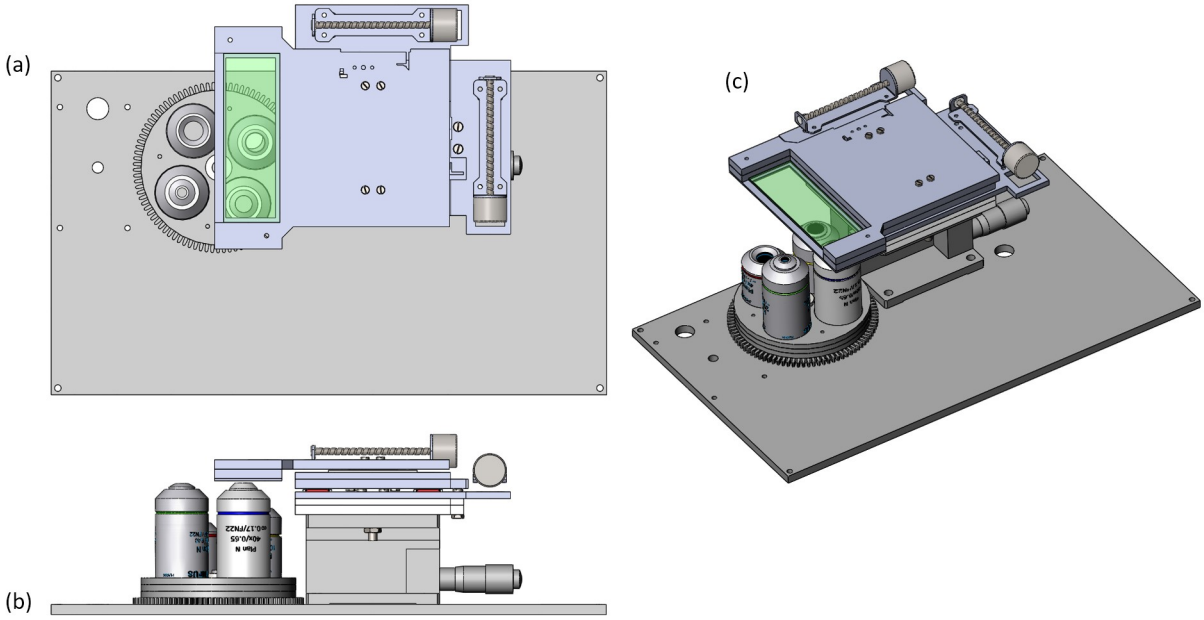

Figure 3.29: CAD design of stage with sample holder on the side. (a) Shows the top plane (b) shows the front plane and (c) shows the isometric view of the design

the width of the slide. The objectives were put on a linear slide just below and the rest of the optical components were placed below them.

To make it more compact, the rotating mirror was shifted inside by using another mirror to redirect the light towards the beam-splitter (see Figure 3.30). The objective lenses now sit on a turret and get rotated from a motor. Gears were also added to automatically rotate the focusing knob of the z-axis mechanism.

In stage 3, seen in Figure 3.31, posts were added for the stage so that it is one complete unit including adding an additional level below to house the micro-controllers.

In stage 4, seen in Figure 3.32, we switched the motor rotating the objective turret for a stronger one as the current one was not suitable. The gears controlling the z-axis motor were jamming as they turned so they had to be redesigned.

Figure 3.33 shows the final design. The only change here is that the gears had been redesigned

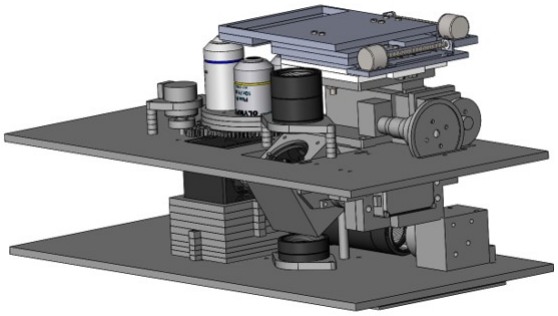

Figure 3.30: CAD design of more compact design (Stage 2)

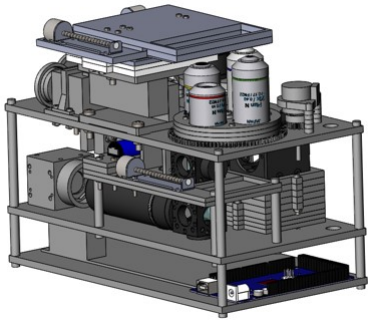

Figure 3.31: CAD design of more compact design (Stage 3)

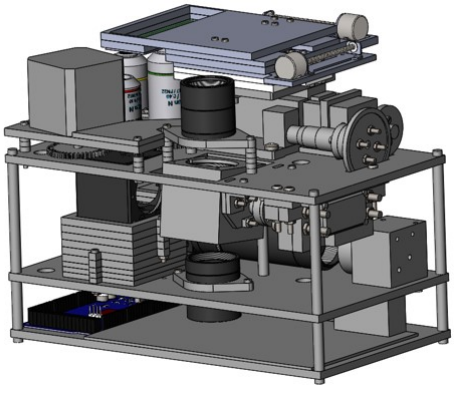

Figure 3.32: CAD design of more compact design (Stage 4)

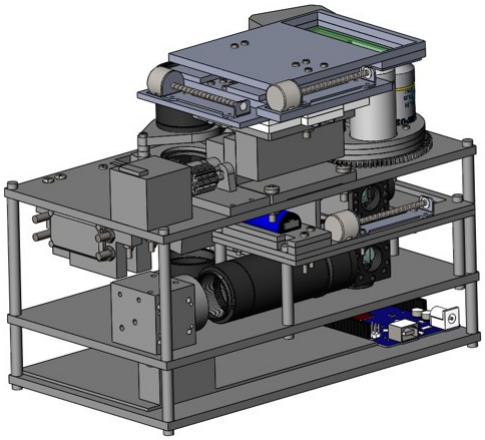

Figure 3.33: CAD design of more compact design (Stage 5)

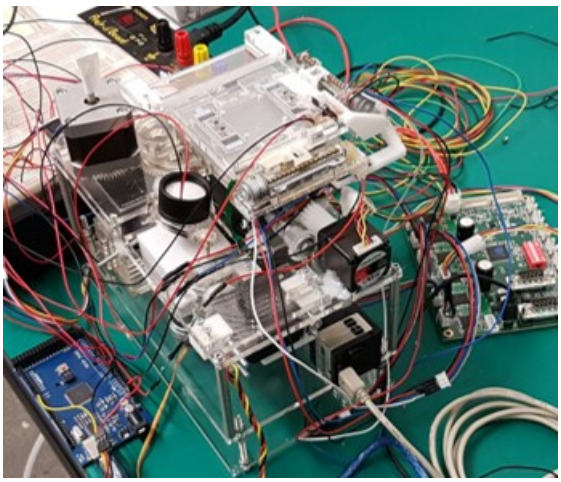

Figure 3.34: Prototype of stage 5 design

by using a long 3-D printed spur gear that was attached to the motor and rotated an acrylic gear fixed to the focusing knob of the z-axis stage. The prototype of this design can be seen in Figure 3.34. This concept is now our principle concept that we will take into the embodiment design stage.

3.1.3 Embodiment Design

As per [91], the embodiment design phase involves taking the principle concept and developing it further with respect to the different functions, producing final design drawings for manufacture. Embodiment design can follow a standard set of steps (see Figure 3.35), however, as [91] argues, particular problems may warrant a different direction to following it directly. The book [91] details the embodiment into 14 steps. We will put our focus into the 'operational' aspects of the system and will only consider steps 10, 11 and 12 which are:

- Evaluate layouts technically/economically.
- Fix preliminary overall layout
- Complete/optimise design by fixing weak areas found in evaluation phase

The succeeding sections show three iterations of the design to get a functional system that produces an appropriate result for bright-field, fluorescence and laser diffraction while evaluating the layout under the steps listed above.

3.1.3.1 Design 1

Seen in Figure 3.34, the first complete design that fulfilled all requirements utilized a rotating mirror concept to cycle through the different light sources. The servomotor, which had a connected 3-D printed housing that housed a mirror, rotated to one of three illuminated light sources. The illuminated light travelled to the rotated mirror and was then directed to a second mirror. At this stage a beam-splitter, for bright-field and laser illumination, or a fluorescent filter cube, for fluorescence illumination, was positioned to take in the incoming light from the second mirror. As the light passed, through the beam-splitter or the fluorescence filter, the light went through to the infinity corrected objective and illuminated the sample. The sample then reflected this light which then came back through the objective and into the beam-splitter (or fluorescence filter) and was redirected by a small 45 degree angled mirror by 90 degrees below. The light now passed through a tube lens and focused onto the CMOS sensor of the camera. We found that this concept produced sufficient results for bright-field but did not produce satisfactory results for fluorescence (see Figure 3.36) or laser diffraction. For this reason, we theorized that the problem was with the alignment of the lights. As the lights were statically positioned, this may have been a reason for misalignment which meant that the illuminating light was not able to come to its proper position.

3.1.3.2 Design 2

In this design a movable lighting design was made that allowed the lights to move around within a space of $\pm$ 10mm in the x or y directions. For the LED's, the design had a printed housing that secured the LED's with friction between the 3D printed part and the lens tube the LEDs were enclosed in. When testing the design, the lights were able to move as required but, on testing the fluorescence, moving the lights' position did not improve the quality of the images. From this, we could gather that the problem of low quality images did not in fact come from misalignment of the LED but from lack of flux. This could have been because of the two mirrors that redirected the light towards the beam-splitter, where the losses were significant when it came to the fluorescence cube. With this in mind, the next iterative design needed to have the fluorescence LED close to the beam-splitter.

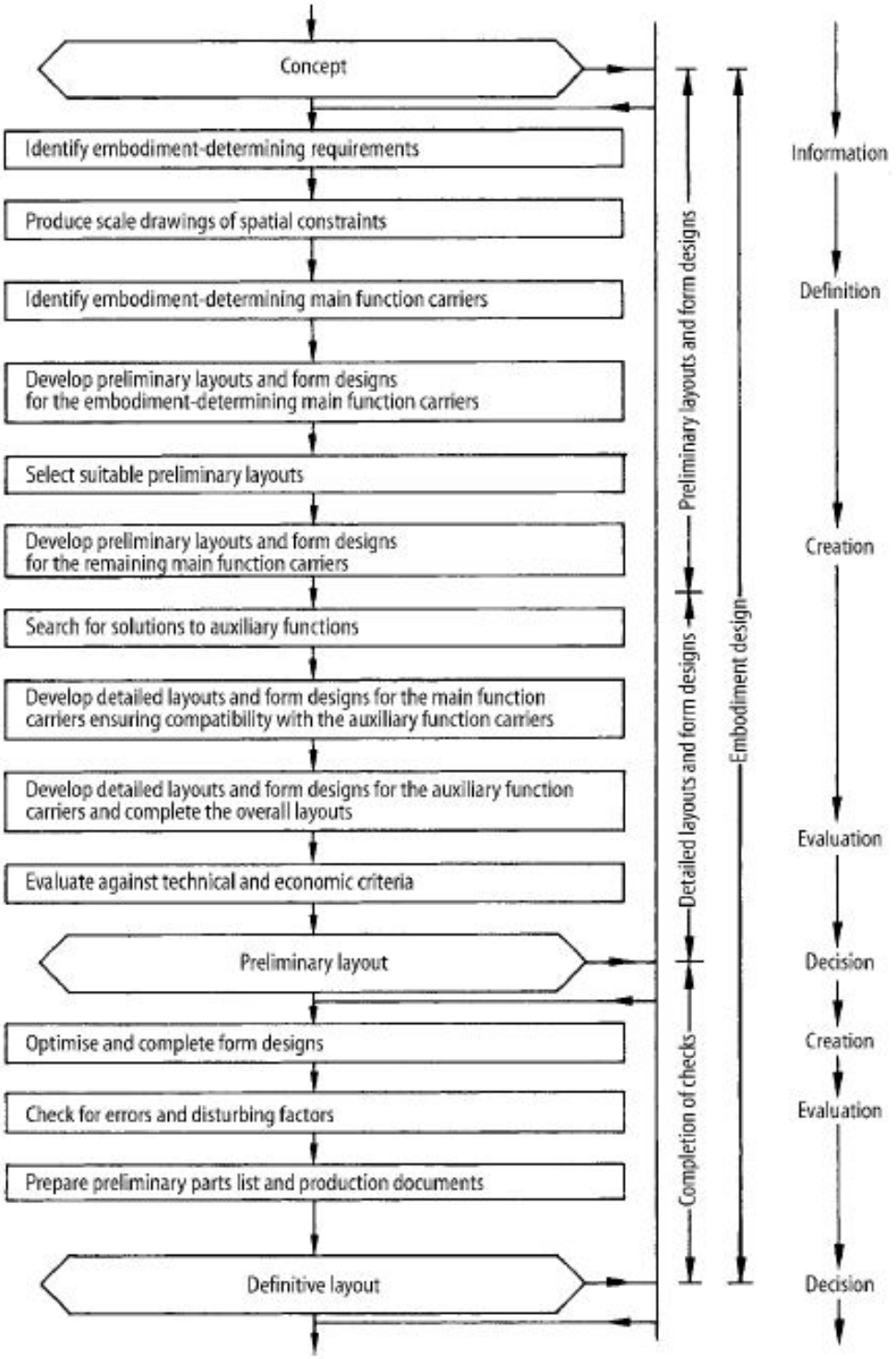

Figure 3.35: Embodiment design steps

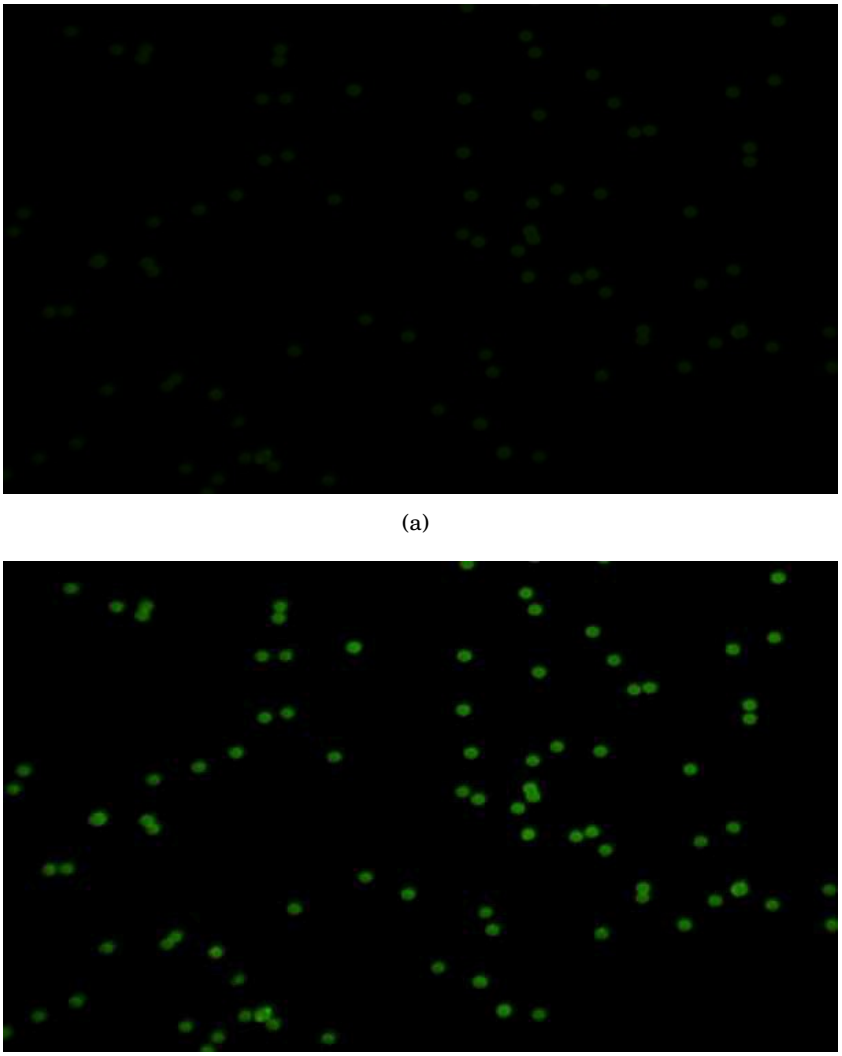

(a)

(b)

Figure 3.36: (a) Original fluorescent image result from Design 1 prototype of Dragon Green fluorescent microspheres (b) is the same image but with its brightness enhanced through Adobe Photoshop

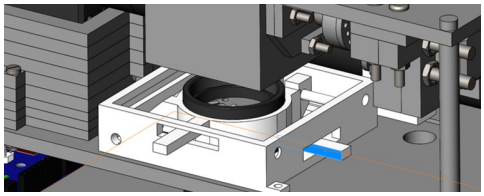

(a)

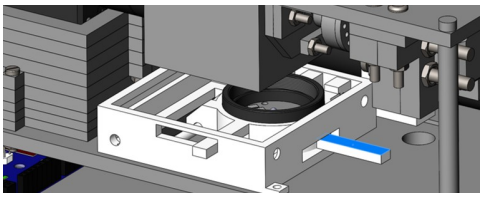

(b)

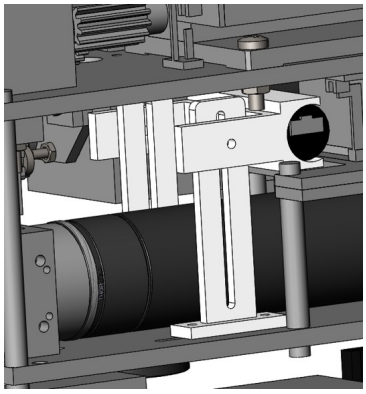

(c)

Figure 3.37: (a) Shows the adjustable sliding mechanism for moving the lighting to remove any misalignment (position 1) (b) is the same mechanism as (a) but at position 2 (c) is the adjustable mechanism for the laser diode

3.1.3.3 Final Design

In this third design, the mirrors were removed and the light sources were placed on a slide similar to the slide for the beam-splitter and fluorescence cube were on. Just like the beam-splitter slide, the light source slide moved linearly and was controlled with a small stepper motor that had a lead screw attached to it. In the case of the fluorescence, the sample was illuminated well and proper details could be seen (see Figure 3.38). Bright-field illumination produced much more concentrated illuminated areas so had to be diffused with 80gsm paper. Laser diffraction was achieved with the use of a camera with a larger sensing area and with an objective lens that had a larger numerical aperture of 0.65. There was also a Thorlabs infrared filter used in the tube lens area leading up to the camera sensor.

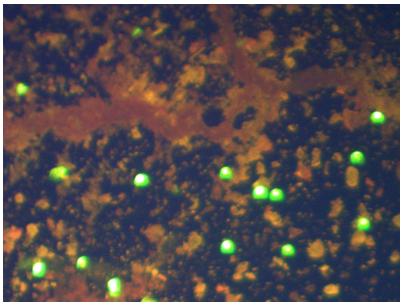

Figure 3.38: Fluorescence image from final design at 10x magnification

3.2 Principle of operation

This section details the principle of operation of the system designed as per the final design discussed in Section 3.1.3.3.

3.2.1 Bright-field Mode

Figure 3.39 shows the different paths of light in bright-field mode. The mode works as follows:

- A stepper motor first moves the bright-field light source into position
- The beam-splitter is then positioned to take in the incoming light (red arrow)
- Light splits into two components through the beam splitter (green arrow and orange arrow)
- Light goes through to the infinity corrected objective (green arrow), illuminates the sample and the sample reflects this light back (purple arrow)
- Light now goes through the beam-splitter again splitting into two (yellow arrow and blue arrow)
- The light that goes below the beam-splitter (blue arrow) reflects off a small mirror at 45°, hits the tube lens (pictured as a red circle) where it is focused onto the CMOS sensor of the camera.

3.2.2 Fluorescence Mode

Figure 3.40 shows the different paths of light in fluorescence mode. The mode works as follows:

- A stepper motor first moves the blue light source into position
- The fluorescence cube is then positioned to take in the incoming blue light (red arrow)

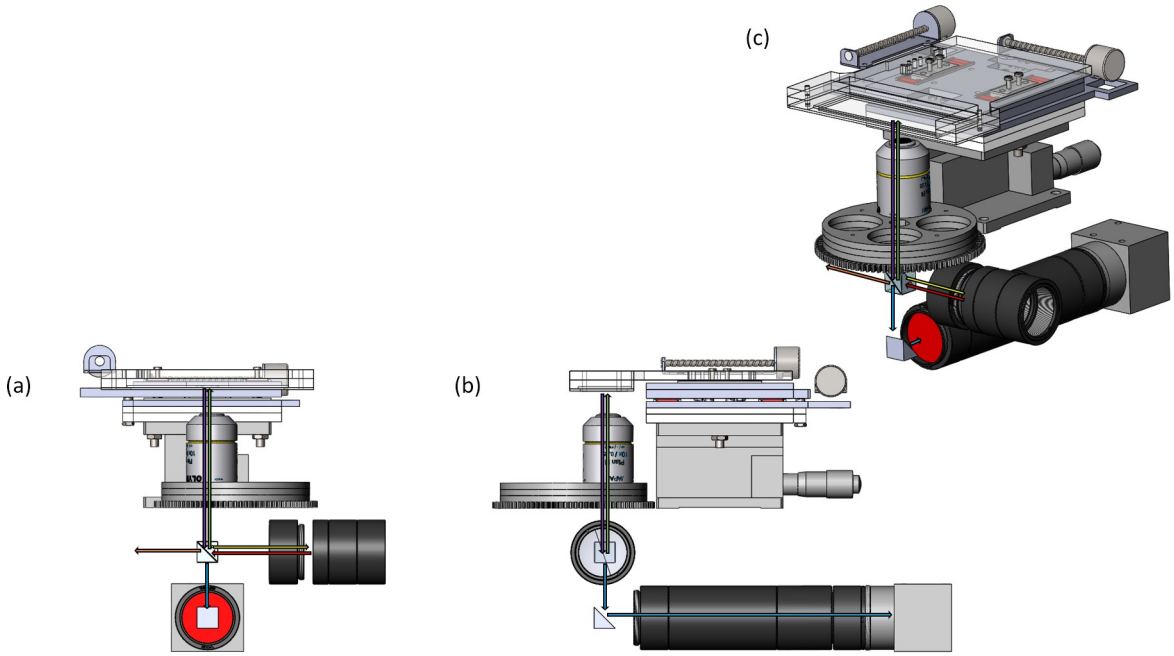

Figure 3.39: Bright-field mode principle of operation. (a) Shows the front plane, (b) the right plane and (c) the isometric view

- Blue light first hits a dichroic mirror which reflects all of it by 45° to an excitation filter (green arrow) where it is now excited light
- Excited light goes through to the infinity corrected objective lens (green arrow), illuminates the sample whereby the sample emits (or fluoresces) back light at a different wavelength (purple arrow)
- Emitted light now goes back to the filter cube where it is able to now pass through the dichroic mirror as well as the emission filter (blue arrow)
- Emitted light (blue arrow) now reflects off a small mirror at 45°, hits the tube lens (pictured as a red circle) where it is focused onto the CMOS sensor of the camera.

3.2.3 Laser Diffraction Mode

Figure 3.41 shows the different paths of light in laser diffraction mode. Our design shows the diffracted modes by taking the diffraction grating as a sample. The laser diffraction mode works as follows:

- A stepper motor first moves the laser into position
- The beam-splitter is then positioned to take in the incoming laser beam (red arrow)

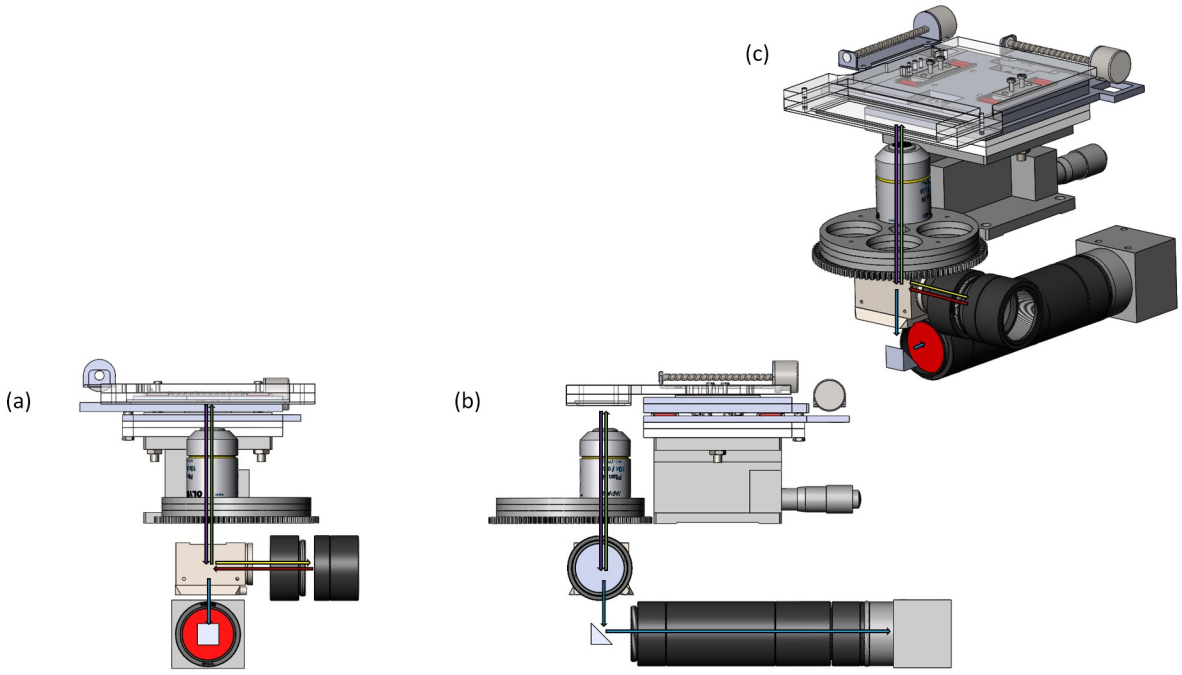

Figure 3.40: Fluorescence mode principle of operation. (a) Shows the front plane, (b) the right plane and (c) the isometric view

- Laser beam splits into two components through the beam-splitter (green arrow and orange arrow)
- Laser beam goes through to the infinity corrected objective (green arrow), hits the diffraction grating, whereby the diffracted modes are reflected back (purple arrow)
- Diffracted modes then travel through the beam-splitter again splitting into two (yellow arrow and blue arrow)
- Diffracted modes that goes below the beam-splitter (blue arrow) reflect off a small mirror at 45°, hit the tube lens (pictured as a red circle) where they are focused onto the CMOS sensor of the camera.

3.3 Discussion

This discussion section focuses on reviewing the Systematic design process in the context of the development of the prototype. Through the use of the Systematic design method, we were able to successfully go from the initial requirements through to a final working prototype that met those requirements. Throughout the concept and embodiment design phases, the development to the next stage of design was done qualitatively: a design was progressed based on whether it

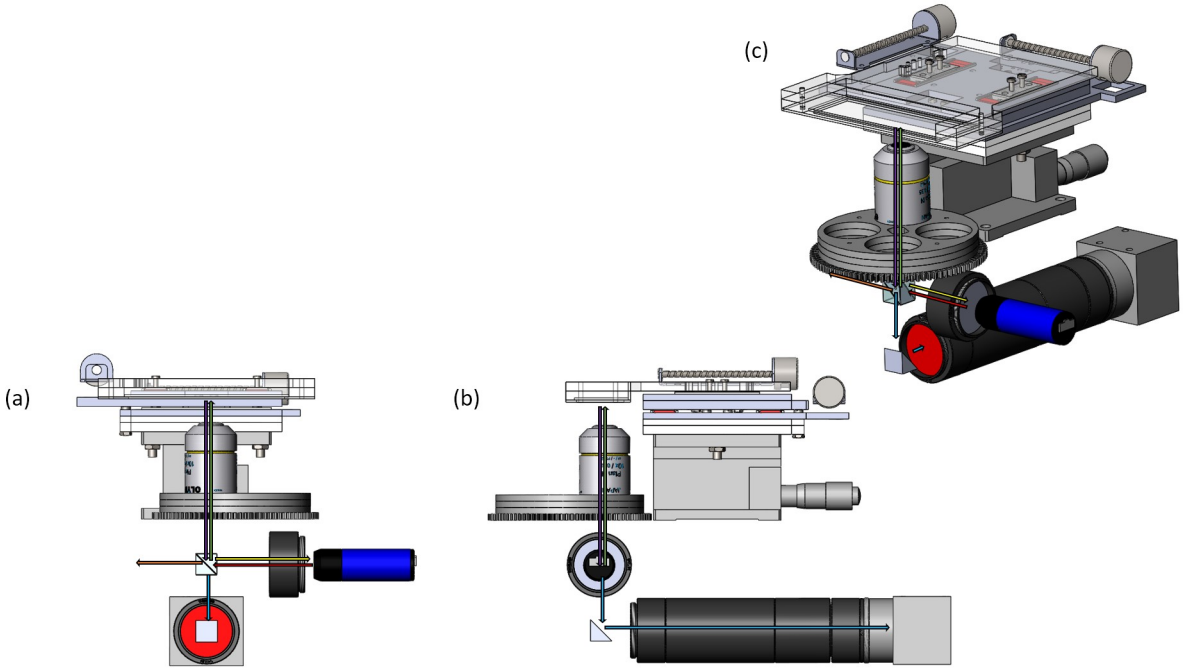

Figure 3.41: Laser diffracted principle of operation. (a) Shows the front plane, (b) the right plane and (c) the isometric view

was fulfilling the functional requirements set out in the ‘Planning and Task Clarification’ stage and where it had met the requirements, was further improved. For example, in Section 3.1.3.1, it was found that the design was able to produce a fluorescent image, technically fulfilling the requirements, however the image produced was not satisfactory. The design was then further improved until the final design had a good fluorescent image. The final design was assessed quantitatively as to whether it would function correctly in Chapter 5.

During Section 3.1.2.3, there was no way to generate solutions and relied completely on the designers experience and research. As such, it is probable that the solutions, such as the inverted design, could have been reached by incorporating idea generation methods such as TRIZ. This would parallel the work of Mayda and Börklü [109] who developed a new design model by integrating the Systematic Design method in conjunction with TRIZ. In their work, they used TRIZ as a "problem solver", "solution finder" and "solution improver" in the ‘determination of problems’ step, ‘searching for solutions to sub-functions’ step and ‘design evaluation’ step respectively. They went on to demonstrate their design methods’ application in a case study involving the design of a simple hole punch system. They found that TRIZ helped in "reducing design time by accelerating the process of solution finding" and "fostering designers towards innovation by focusing on conflicts and radical improvements". They quantified their results by measuring the design time using the Systematic Design model alone versus the Systematic Design model with TRIZ and found that incorporating TRIZ improved the design time by nearly three

times. The results from [109] show a successful result in integrating TRIZ with the Systematic Design method in comparison to using the Systematic Design method alone. It also shows that with any one theory or method of design, it cannot cover all of design: rather each one provides its own perspective that may improve design understanding and practice [110].

CHAPTER 4

OPTICAL AND MECHANICAL SIMULATION MODEL VERIFICATION

This chapter verifies the accuracy of the optical and mechanical simulation models of the final design, seen in Section 3.1.3.3, that were done in TracePro and SolidWorks respectively.

4.1 Optical Measurement Setup

The irradiance and optical power of the system were measured using the Thorlabs PM160 optical power meter. The setup can be seen in Figure 4.1.

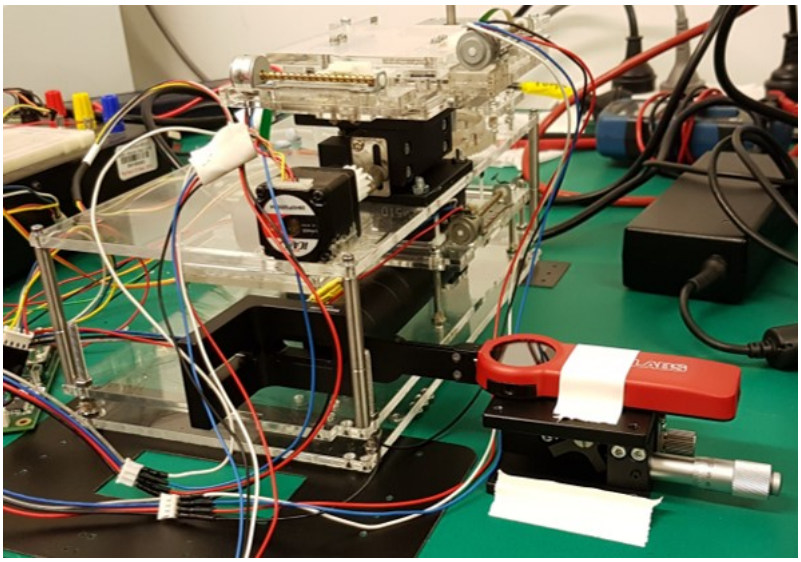

Figure 4.1: Optical Measurement Setup

The use of the PM160 is justified in Section 4.1.1. The camera was taken out and the PM160

sensor was put in its place. As the PM160 was rotatable, in respect to the shaft housing the sensor (see Figure 4.1), the main base was able to lie flat on an adjustable z-axis base that brought it up to the required height.

Figure 4.2: PM160 Si Sensor Power Meter (found in [26])

4.1.1 PM160 Si Sensor Power Meter

The PM160 is a silicon power sensor that is able to detect wavelengths from 400nm to 1100nm and is able to measure optical power from 10nW to 2mW [111]. Through the use of a neutral optical density filter, the optical power range can be extended to go from 2mW to 200mW. The added ability of the extended optical range is useful for our system because bright-field illumination usually has a higher irradiance whereas fluorescence can have it much lower because it filters only a specific wavelength of light. Hence, using the PM160 will allow us to measure irradiance of both forms of illumination with one device. It is useful to note that the wavelength of the light source should be known before measuring the intensity: the PM160 cannot be used to determine the intensity of a range of wavelengths from a particular light source. For example, if we set the PM160 to measure the intensity of 635nm wavelength and shine a 4mW 635nm laser on it, the output power will read close to 4mW. Setting the PM160 to measure 480nm, with the same 635nm laser, will cause the sensor to read a higher output power - which is not correct. Therefore, the wavelength of the light source has to be known beforehand.

4.1.2 Objective Lens

The objective lens we used for measurements in our physical system was a 10x infinity corrected objective lens with a numerical aperture of 0.25. We were not able to model this type of lens because we could not come across an accurate optical model of this objective to use in the simulation. We instead constructed a model from the book [112] of a 10x objective lens with a numerical aperture of 0.22 but at a standard 180mm distance from object to image: it was not infinity corrected. Because of the lower numerical aperture of 0.22, the simulated results should show less light as compared to our measured results.

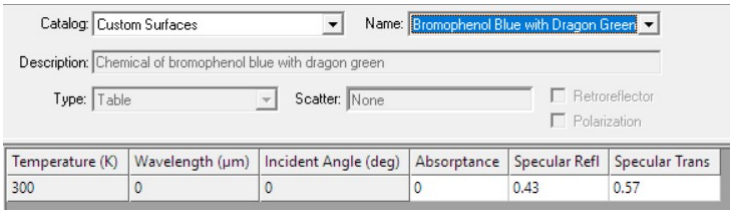

Figure 4.3: Custom tranmission and reflectance characteristics of Bromophenol Blue with Dragon Green Fluorescent Polystyrene Microshperes

4.1.3 Reflectance/Transmission of Sample

One of the main samples that we used to characterise the micro-imaging system built was Bangs Laboratories Dragon Green fluorescent sample polystyrene microspheres mixed with bromophenol blue. As the reflectance and transmission data of this sample in MatWeb was unavailable, this had to be measured to allow for accurate optical simulations. The transmission of the sample was measured with respect to the light coming in. If we take the light coming in as being 100%, then the transmitted and reflected light would both add to 100%. The reflectance and transmission of the sample of bromophenol blue with dragon green polystyrene particles was measured as 57% transmission and calculated as 43% reflectance. This measurement was determined using the laser illumination mode by measuring the amount of laser light coming onto the sample initially as 700mW and then measuring the amount transmitted as 400mW. By reasoning, this means that the amount reflected should be 300mW. This would mean that 400mW/700mW = 57% is transmitted and 300mW/700mW = 43% is reflected. Using this data, the sample plate was setup to have a custom property of having 57% transmission and 43% reflectance as seen in Figure 4.3.

4.2 Optical Simulation

The optical simulations for bright-field, fluorescence and laser diffraction were undertaken using TracePro for the purpose of verifying that the irradiance measurements on the sensor of the camera, in the simulation, matched the measured result from our measurements. Justification for the use of TracePro is discussed in more detail in Section 4.2.1.

4.2.1 TracePro

TracePro is an optical design software developed by Lambda Research Corporation and used in research and industry. The software was used to design optical systems for high-end applications such as the FIRST telescope [113], mars rover cameras and Long-Range Reconnaissance Imager (LORRI). We preferred the use of TracePro over other software because we had a copy of the software.

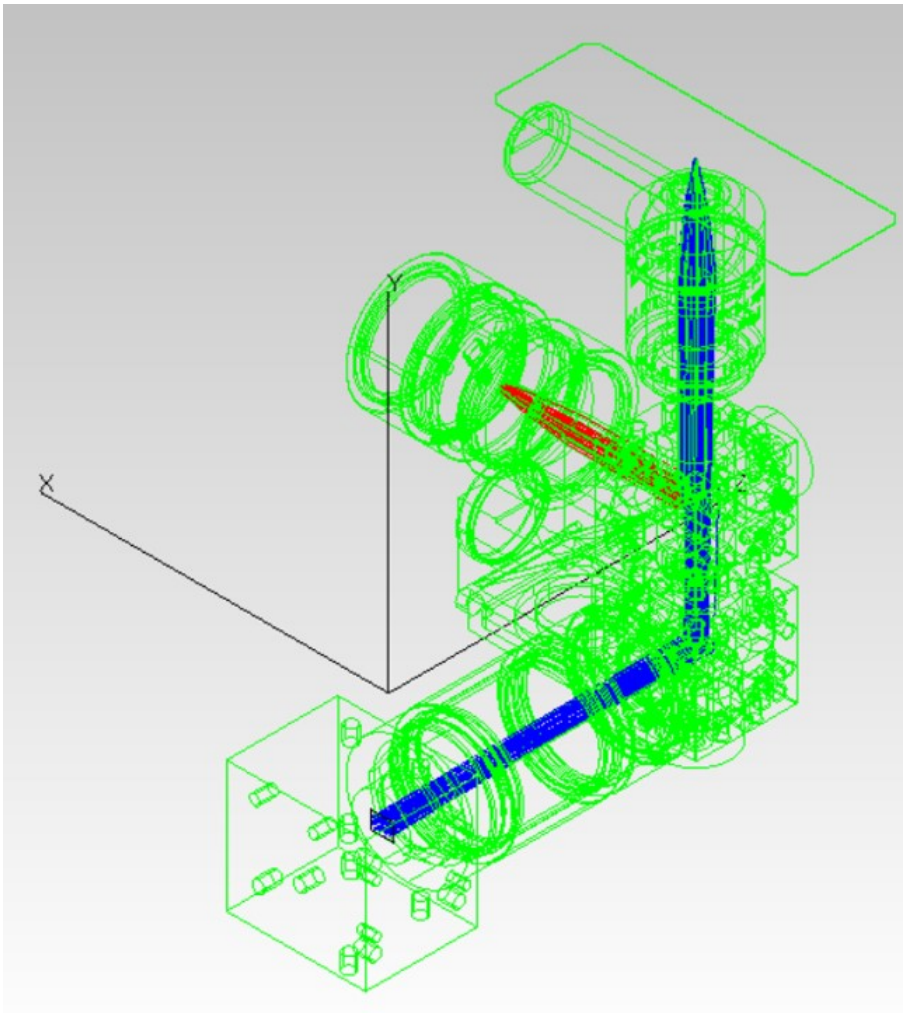

Figure 4.4: Bright-field simulation setup in TracePro

4.2.2 Bright-field

The light source for the bright-field simulation was setup with the LED data chosen as being from Osram Oslon SSL80 GW CS8PM1.CM. This model was chosen because it matched the step file in SolidWorks, the LED solid body showed that the LED model used was of Oslon SSL80 - thus we selected the same model categoery from the Osram data files available. The rest of the physical model set-up was imported as a step file as per normal. From Figure 4.4, we can see the setup and simulated rays and in Figure 4.5 we can see that the maximum irradiance was simulated to come as 13.23 W/m^2. Table 4.1 shows the measured irradiance is 13.92 W/m^2. These values are within approximately 5% of the measured value which indicates that the simulation holds up well for the bright-field simulation.

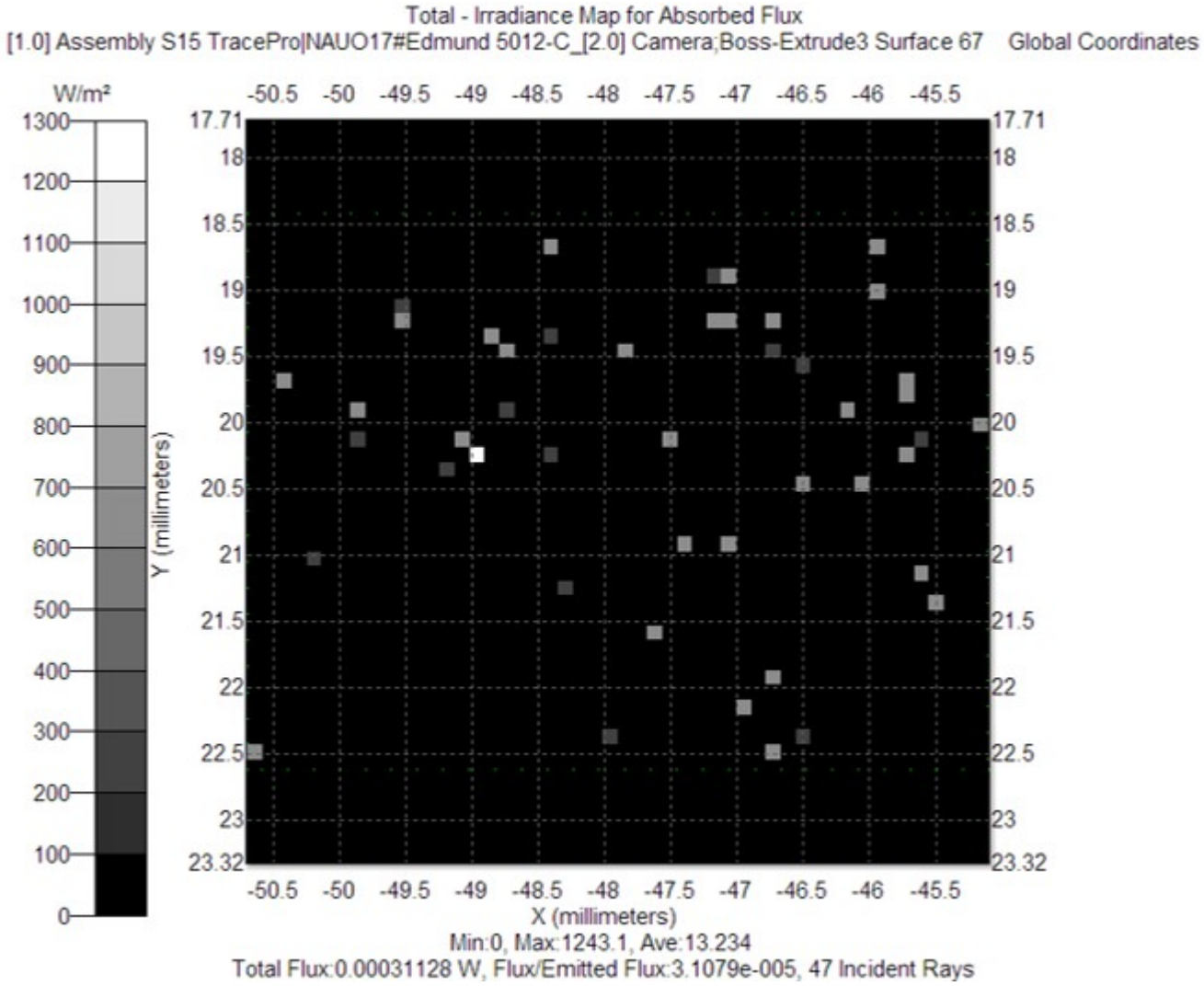

Figure 4.5: Bright-field simulation irradiance plot in TracePro

4.2.3 Fluorescence

4.2.3.1 Fluorescence Filter Cube

The fluorescence filter cube has three components: excitation filter, emission filter and dichroic mirror as explained in more detail in Section 4.3.6. In reference to this section, none of the properties of these three components were available as default surface properties in TracePro. Therefore we had to create a custom surface property for each component. The details of these can be seen in Appendix A.

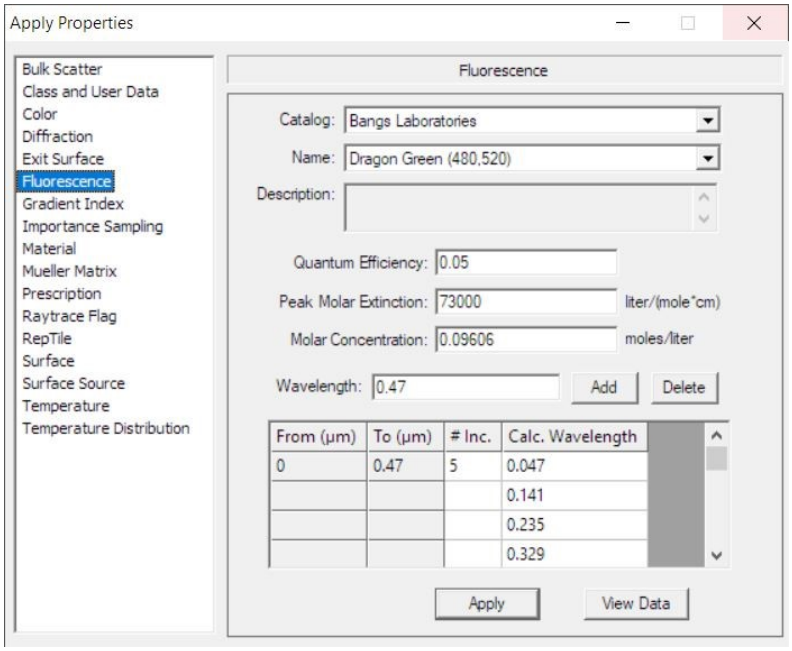

Figure 4.6: Example of the Fluorescent Property Editor feature in TracePro

4.2.3.2 Set-up

The light source for the fluorescence simulation was setup with the LED data chosen as being from Osram Oslon SSL80 GB CS8PM1.13. This model was chosen because when you opened the step file in SolidWorks, the LED solid body showed that the LED model used was of Oslon SSL80 - thus we selected the same model category from the Osram data files available. The rest of the physical model set-up was imported as a step file. The fluorescent material that we imaged to categorize fluorescence was specifically 'Bangs Laboratories FS07f Dragon Green' . Details of the preparation of the physical sample can be seen in Section 6.2. To model this material in TracePro, we applied the fluorescent property to the sample slide through TracePro's dedicated 'Fluorescent Property' editor (see Figure 4.6). Bangs Laboratories Dragon Green property was unavailable so it had to be custom made in TracePro. Appendix B has the details of the custom property made with the information that the FS07F material is excited by 480nm light and emits at a wavelength of 520nm. The emitted fluorescent rays were split coming from the sample slide to be 16 files. The fluorescence setup and simulated rays are shown in Figure 4.7. From the simulation, the irradiance plot (see Figure 4.8) shows us that the average irradiance is simulated to come out as approximately 0.0247W/m^2 and the measured result as seen in Table 4.1 is 0.0256W/m^2. The average simulated result is within 3.52% of the measured result indicating that it is a good simulation.

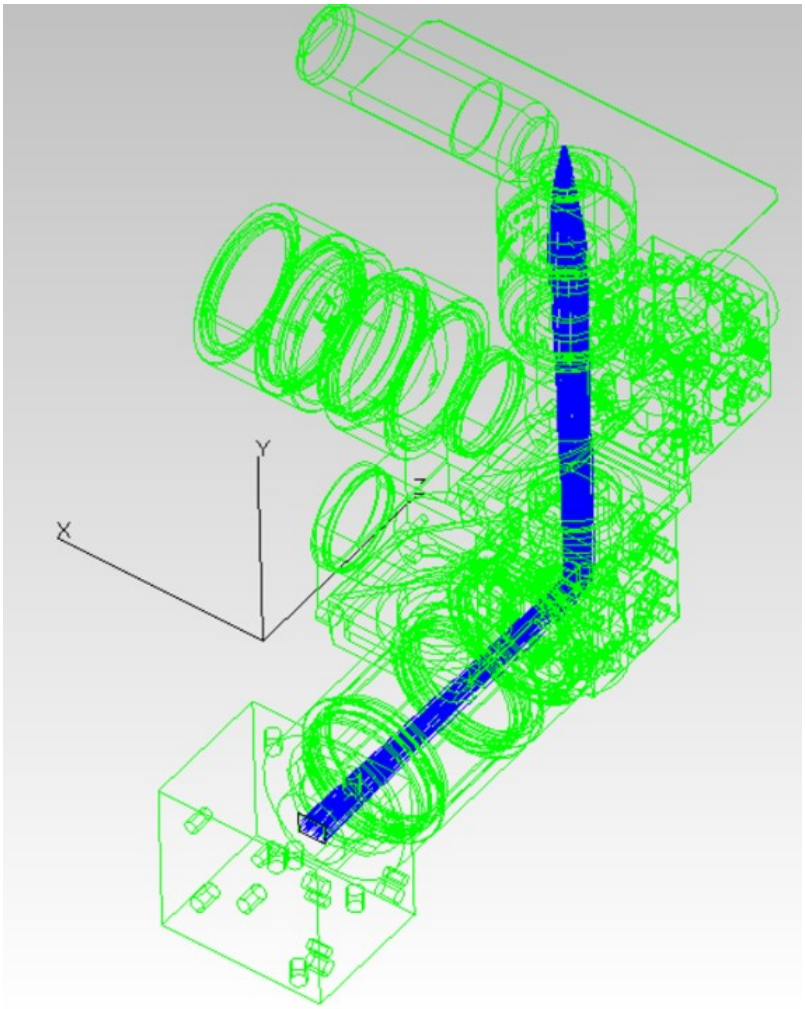

Figure 4.7: Fluorescence simulation setup in TracePro

Table 4.1: Measured Optical Characteristics from PM160 Sensor

Illumination Mode	**Wavelength Measured(nm)**	**Current(A)**	**Irradiance (W/m^2)**	**Optical Power(W)**
Bright-field	580	$1.51x10^{-6}$	13.92	$5.46x10^{-6}$
Fluorescence	520	$2.12x10^{-9}$	$2.56x10^{-2}$	$1x10^{-8}$
Laser	640	$2.3x10^{-6}$	16.86	$6.62x10^{-6}$

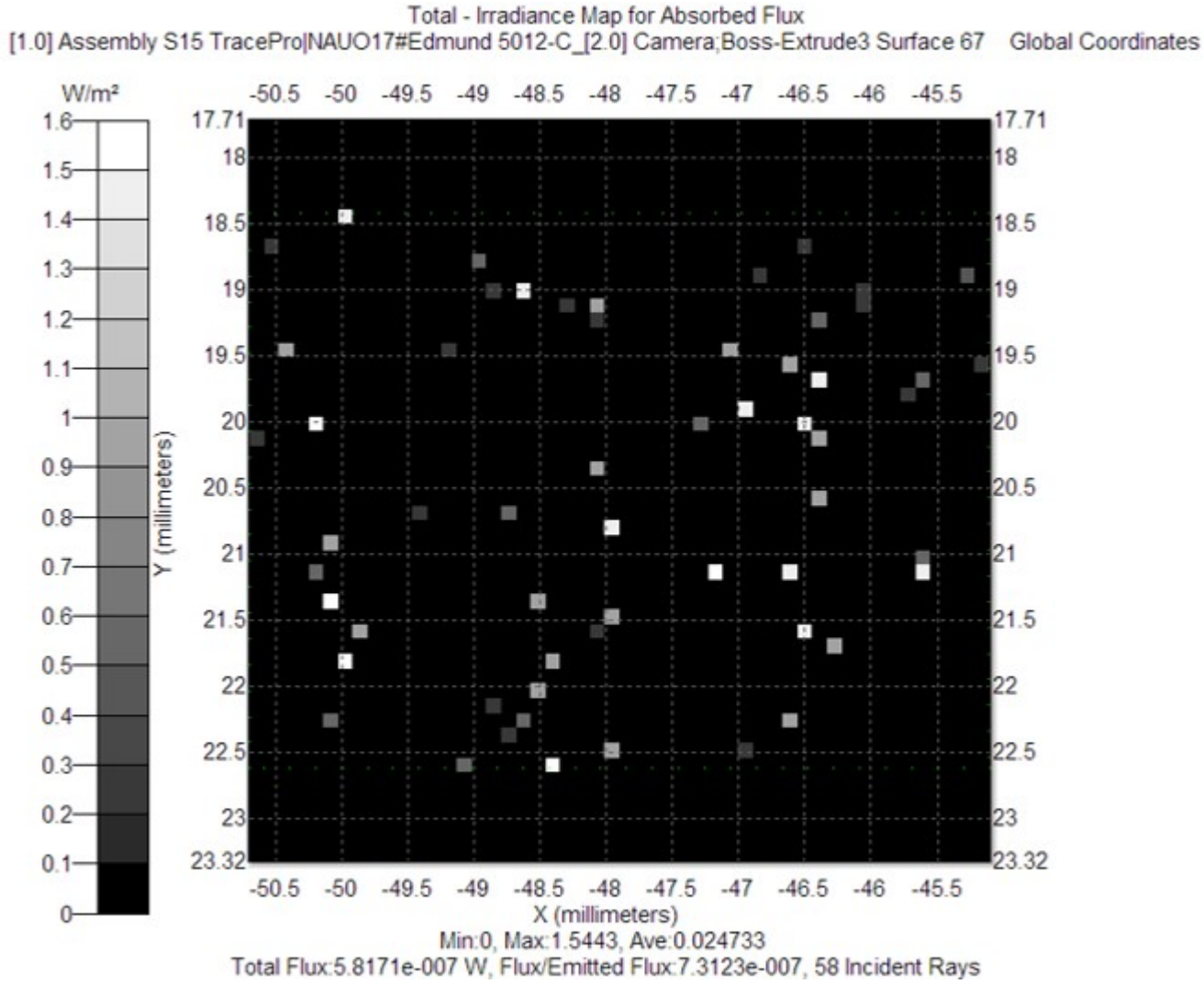

Figure 4.8: Fluorescent Irradiance Plot

4.2.4 Laser

The light ray data for the laser diffraction simulation was setup with an overall power of 4mW - matching the specifications of the laser (see Figure 4.9 of the simulation setup). The shape was circular as the laser also takes this shape. From running the simulation, the irradiance came out to be 15.12W/m^2 and the measured result came out to be 16.86W/m^2. The simulated result is within 10% of the measured result which indicates that it is a good simulation.

4.3 Optical Component selection

This section justifies the use of optical components in the system.

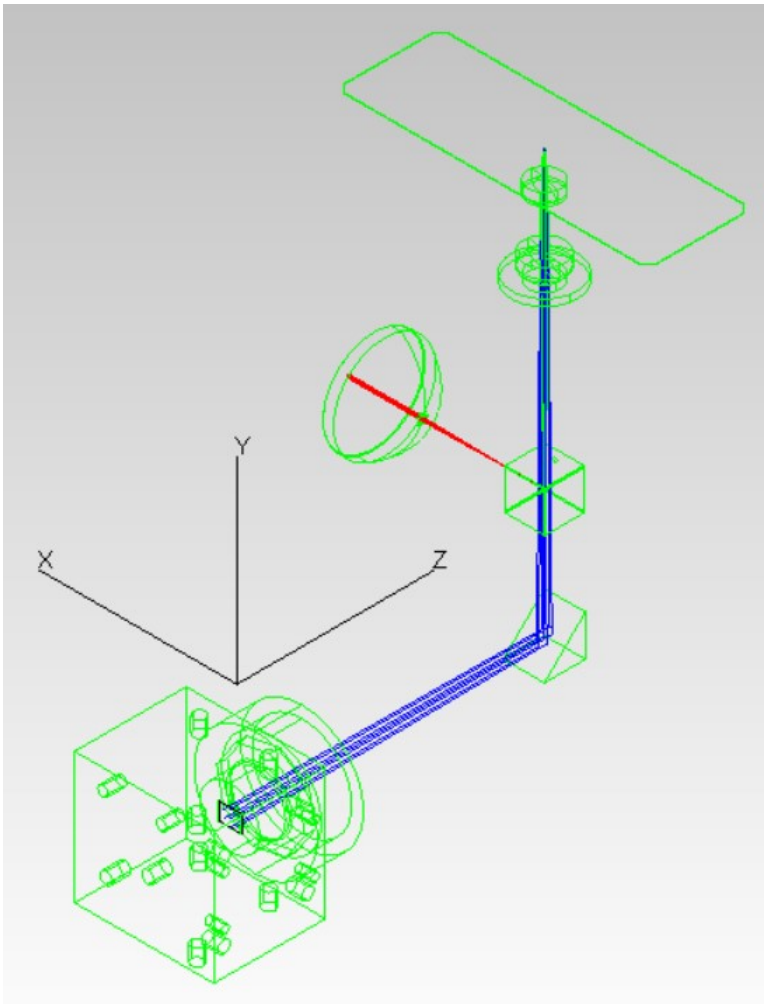

Figure 4.9: Laser simulation setup in TracePro

4.3.1 Mirror

4.3.1.1 Mirror Considerations

The light that we needed to reflect is in the 450nm – 700nm range. Ideally the light needs to be 100 percent reflected but it is understood that this cannot be the case in practice.

4.3.1.2 Mirror Choice

The mirror, MRA10-P01 from ThorLabs, was used. It is a silver coated mirror that has a reflectance of 97.5 percent in the 450nm to 20µm range (see Figure 4.11) which is ideal for our scenario because it reflects with minimal losses and targets the light spectrum range we require.

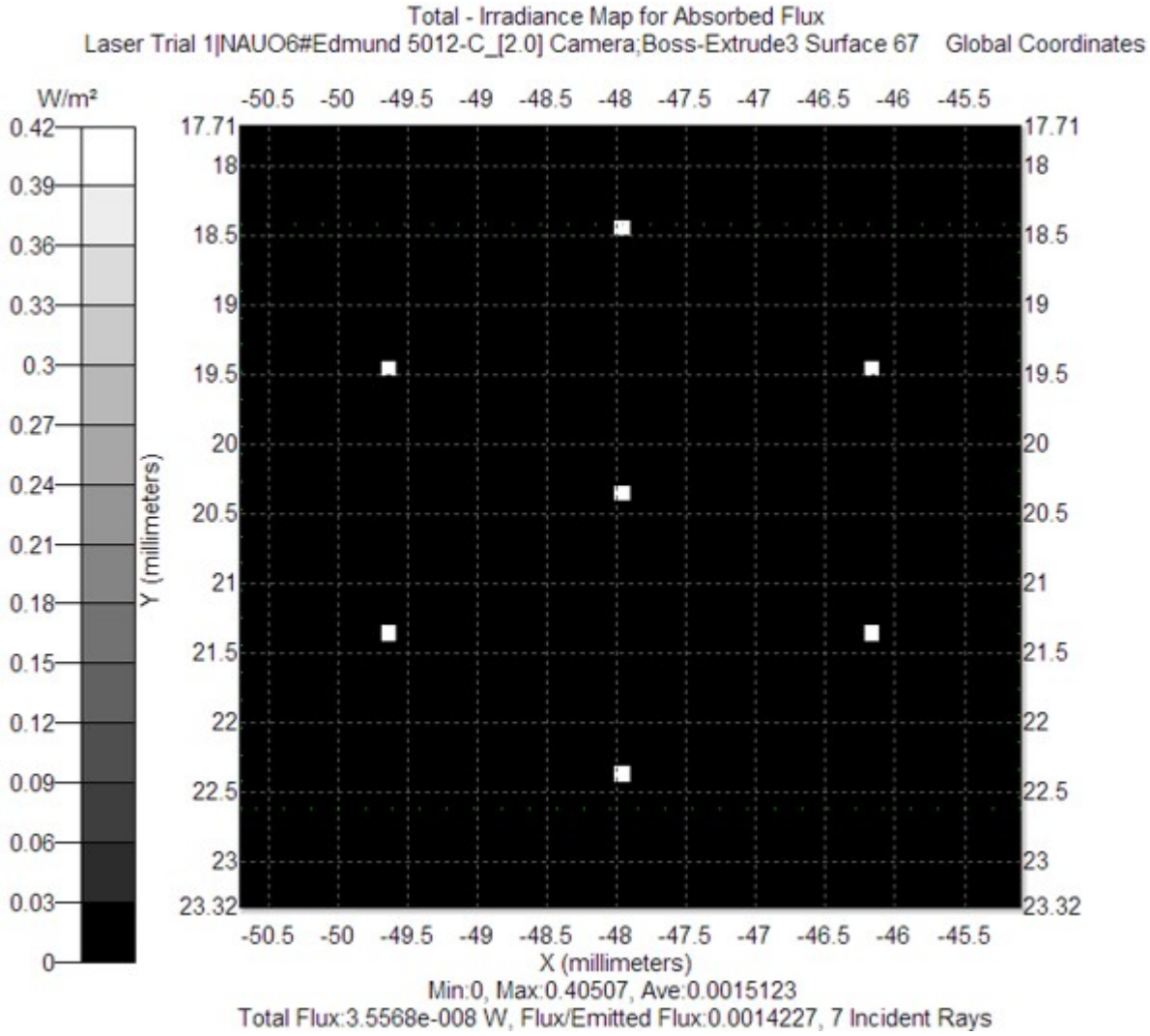

Figure 4.10: Laser Irradiance Plot

4.3.2 Beam-splitter

4.3.2.1 Beam Splitter Requirements

We need a beam splitter than can accurately separate the beam of light with minimal losses, has a range in the visible spectrum: 400-700nm and does not produce ghost images.

4.3.2.2 Beam-Splitter Choice

The beam-splitter that was chosen was Thorlabs BS010. This beam splitter has a 47±10% reflectance and transmission capability (see Figure 4.12) and has a wavelength range between 400nm -700nm. The use of the beam-splitter also facilitates epi-illumination: allowing the light to go through the objective lens and then come back and go through the beam-splitter again

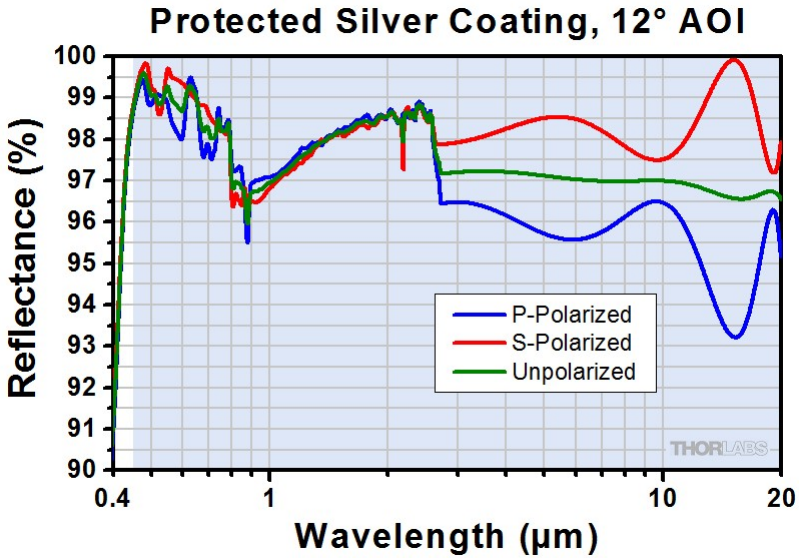

Figure 4.11: Reflectance of MRA10-P01 mirror (found in [27])

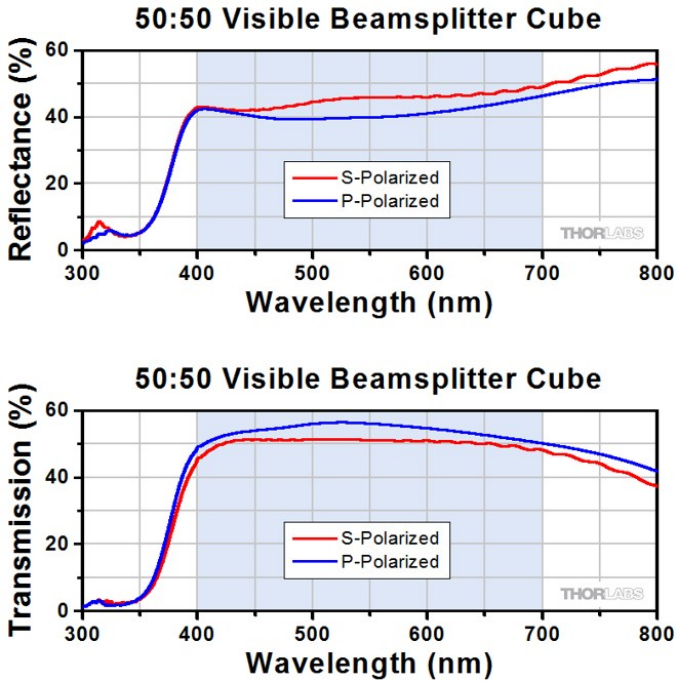

Figure 4.12: Reflectance and transmission of BS010 beam-splitter (found in [28])

towards the sensor.

4.3.3 Collimator Lens

The collimator lens allows scattered and divergent light to become collimated and uniform. This uniform light reduces the vignetting effect of images which increases the quality of the

images and makes them easier to put through image processing applications such as stitching. In our system, we used the ThorLabs ACL2520U-A Aspheric condenser lens which is ideal for collimating light because it has a larger aperture and lower f# ratios than spherical lenses [114].

4.3.4 Tube Lens

As with most other microscopes, the lens tube focused the rays from the objective lens onto the sensor plane of the camera. Due to our sizing restraints, we used Thorlabs LA1251-A lens which has a 100mm focal distance. This allowed us to focus the image while maintaining a compact size.

4.3.5 Optical Tubes/Lens Tube

The optical tubes used to house the LED's and the length of the optical track leading up to the sensor plane of the camera were chosen from Thor Labs selection. These tubes are threaded so can contain elements that can be secured with retaining rings. The tubes were also coloured matte black so that there is minimal reflectance inside the tube. This stops light from reflecting inside the surface.

4.3.6 Fluorescent Filter Cube

4.3.6.1 Working principle

The fluorescent filter cube is used in fluorescent microscopy for the purpose of illuminating a sample with excited light and then viewing only the fluorescing parts of the sample. The process, as seen in Figure 4.13 works by first illuminating light through an excitation filter, where a dichroic mirror reflects the excited light onto the sample. The sample then fluoresces from the excited light and emits another wavelength of light different to the wavelength of the excited light. This emitted light passes through the dichroic mirror and emission filter whereby only the fluorescing material parts of the sample are filtered through. This filtered light is then captured on a camera.

4.3.6.2 Filter Cube Selection

In our system, we used the Nikon B-2A filter cube. One reason for using this type of cube is because we can image a large amount of biological samples that emit green light when excited with blue light. The filter has an excitation filter that allows wavelengths of 450-490nm, an emission filter that allows greater than 515nm onwards and a dichroic mirror that allows greater than 500nm.

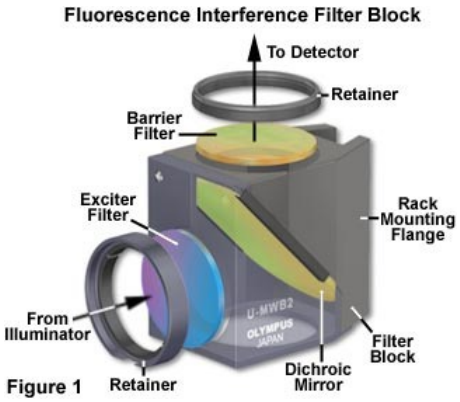

Figure 4.13: Fluorescence Filter Cube (found in [29])

4.4 Illumination Mode Change Design

This section details the calculations to verify the mechanical simulation model for the beam-splitter/fluorescence cube slide and illumination source slide motors. The mechanical simulation model was verified with the following three steps:

1. Determine the torque of the motor with hand calculations
2. Simulate the torque on the motor with the conditions presented in the hand calculations in SolidWorks motion study and compare to hand calculations
3. Confirm if the motor was able to successfully move the required load in the physical system

4.4.1 Beam-splitter/Fluorescence Cube

This section details the calculations of the filter cube slide. The following are a list of relevant masses for the calculations:

- $m_{Beam-SplitterCube} = m_{BSC} = 25g = 0.025kg$
- $m_{FluorescenceCube} = m_{FC} = 30.5g = 0.0305kg$
- $m_{ap} = 4.6g = 0.0046kg$
- $m_{Total} = m_T = m_{BSC} + m_{FC} + m_{ap} = 0.0601kg$

The force due to gravity is:

$$F_W = m_T \cdot g \tag{4.1}$$

$$= 0.0601kg \cdot 9.81ms^{-2}$$

$$= 0.590N$$

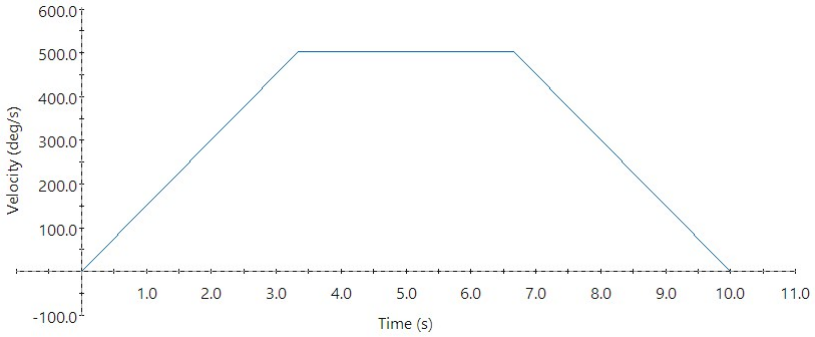

Figure 4.14: Motion profile of motor-shaft of beam-splitter/fluorescence cube slide

The slide will move against the acrylic base it is sitting on. The coefficeint of static friction of acrylic on acrylic is 0.2. As the load is not sitting on an angle the normal force is equal to the force due to gravity. The force due to friction is therefore:

(4.2)
$$F_F = \mu \cdot F_N$$
$$= (0.2) \cdot 0.589581N$$
$$= 0.118N$$

We would like the slide to move 28mm within 10seconds. In order to achieve this we need to first determine the angular velocity of the motor-shaft. We know the lead of the screw is 3mm and assuming a trapezoidal motion profile: with acceleration time of 3.33 seconds, constant velocity time of 3.33 seconds and deceleration time of 3.33 seconds (see Figure 4.14), the angular velocity works out to be:

$$\omega = 504^\circ s^{-1} = 8.80 rads^{-1}$$

With this angular velocity, the linear velocity of the slide will also follow the same trapezoidal motion profile (see Figure 4.15). The linear velocity comes out to be:

$$v = 4.2mms^{-1} = 4.2 \cdot (10^{-3} ms^{-1})$$

The acceleration required will be:

(4.3)
$$a = \frac{\Delta v}{t}$$
$$= \frac{4.2 \cdot (10^{-3} ms^{-1})}{3.33s}$$
$$= 1.26 \cdot (10^{-3} ms^{-2})$$

The force due to acceleration is therefore:

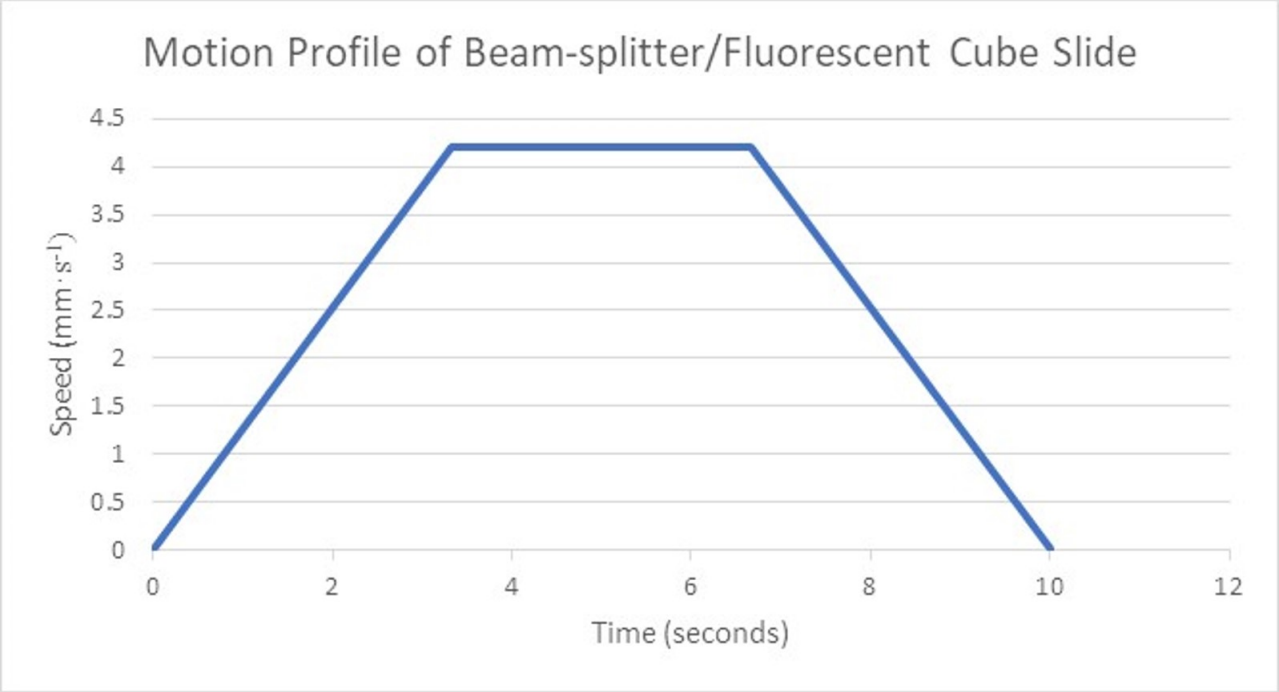

Figure 4.15: Motion profile of beam-splitter/fluorescence cube slide

(4.4)
$$F_a = m \cdot a$$
$$= 0.0601 \cdot (1.26 \cdot 10^{-3} ms^{-1})$$
$$= 7.57x10^{-5} N$$

The total force comes out as:

(4.5)
$$F_T = F_F + Fa$$
$$0.118N$$

If we assume that the mechanism follows the principle of a power screw mechanism, we can model the forces on the screw as per Figure 4.16.

The formula for the torque then becomes:

(4.6)
$$\tau = \frac{F_T \cdot d_m}{2} \cdot \left(\frac{l + \pi \cdot f \cdot d_m}{\pi \cdot d_m - f \cdot l} \right)$$

Where d_m is the mean diameter of the screw, f is the coefficient of friction with the normal force and l is the lead of the screw. As the contact between the dry steel screw and the base is

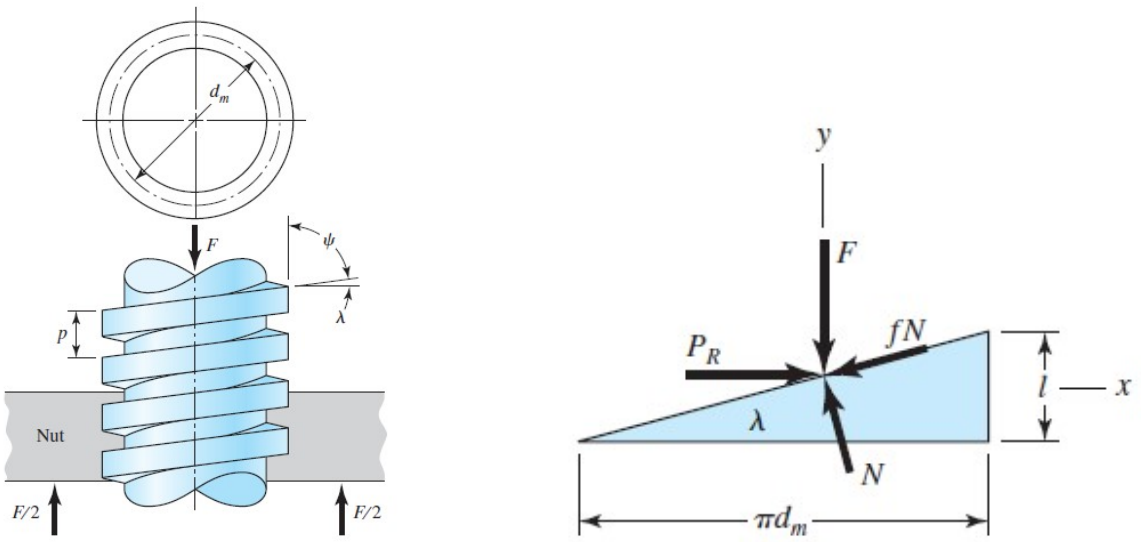

(a) (b)

Figure 4.16: (a) Shows the overall forces on a power-screw (b) Shows the forces present on an unwrapped screw. These two figures are found as Figures 8-5 and 8-6(a) in [30]

connected with a dry steel contact, the coefficent of friction table [115] states that the coefficient of friction between these two would be 0.7. Thus for our calculations we will take $f = 0.7$.

Using the datasheet seen in Appendix C we get the remaining values we require:

$$d_m = \frac{OutsideDiameter + MinorDiameter}{2} = \frac{3mm + 2mm}{2} = 2.5mm = 0.0025m \tag{4.7}$$

$$l = 3mm = 0.003m$$

Substituting the values into Equation 4.6 we get:

$$\tau = \frac{0.118N \cdot 0.0025m}{2} \cdot \left(\frac{0.003m + \pi \cdot 0.7 \cdot 0.0025m}{\pi \cdot 0.0025m - 0.7 \cdot 0.003m} \right)$$

$$= 2.17 \cdot 10^{-4} Nm = 0.217Nmm$$

To confirm that this result is good approximation, we modelled the motion using SolidWorks Motion Analysis. The set-up was as follows:

- 'Rotary Motor' feature on the motor-shaft followed the same motion profile as per Figure 4.14
- 'Solid Body Contact Feature' between the contact and the screw with the material being set to 'Dry steel'

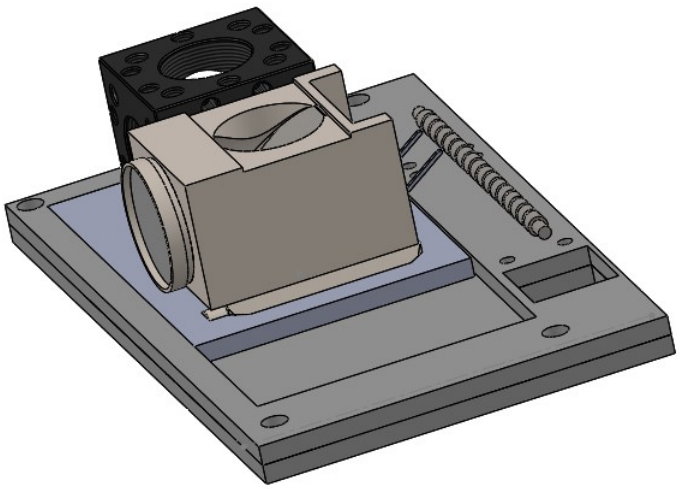

Figure 4.17: SolidWorks Motion Analysis Set-up for Beam-splitter/Fluorescence Cube Slide

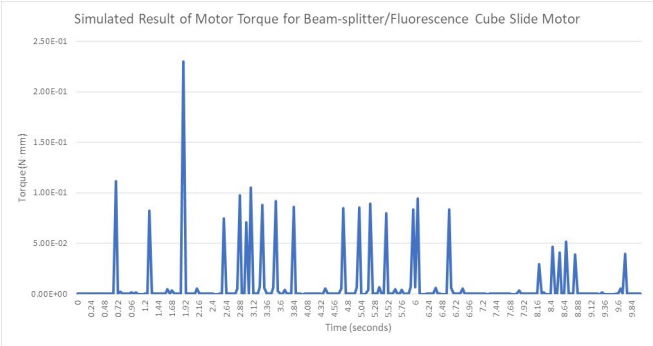

Figure 4.18: Simulated Motor Torque for Beam-splitter/Fluorescence Cube Slide Motor

- Time was set to go for 10 seconds: matching the time duration of the motion profile as per Figure 4.14

The CAD set-up can be seen in Figure 4.17 and the results of the analysis can be seen in Figure 4.18. The results show that the maximum torque engaged on the shaft is 0.230Nmm. Our calculated result of 0.217Nmm matches within 5.8% of the simulated result indicating that it is a good estimate. In the physical system, the motor moved the required load as expected.

4.4.1.1 Resolution of Motor

As per Appendix C, the motor has 20 steps in one revolution and a pitch of 3mm. Using the Trinamic 6110 microcontroller, we were able to get 256 microsteps so the total amount of distance per step worked out as:

$$\frac{3mm}{20 \cdot 256\ steps} = 0.000586mm\ per\ step$$

4.4.2 Illumination source slide motor calculation

This section details the calculations of the illumination slide. The following are a list of relevant masses for the calculations:

- $m_{Bright-field\ Light} = m_{BFL} = 21.1g = 0.0211kg$
- $m_{Fluorescence\ Light} = m_{FL} = 30.5g = 0.0305kg$
- $m_{Laser} = m_L = 10g = 0.0010kg$
- $m_{Base} = m_B = 30.85g = 0.003085kg$
- $m_{Total} = m_T = m_{BFL} + m_{FL} + m_L + m_B = 0.06475kg$

The force due to gravity is:

$$F_W = m_T \cdot g$$
$$= 0.06475kg \cdot 9.81ms^{-2}$$
$$= 0.635N$$

The slide will move against the acrylic base it is sitting on. The coefficeint of static friction of acrylic on acrylic is 0.2 [115]. As the load is not sitting on an angle the normal force is equal to the force due to gravity. The force due to friction is therefore:

$$F_F = \mu \cdot F_N$$
$$= (0.2) \cdot 0.635N$$
$$= 0.127N$$

We would like the slide to move 55mm within 10seconds. In order to achieve this we need to first determine the angular velocity of the motor-shaft. We know the lead of the screw is 3mm and assuming a trapezoidal motion profile: with acceleration time of 3.33 seconds, constant velocity time of 3.33 seconds and deceleration time of 3.33 seconds (see Figure 4.19), the angular velocity works out to be:

$$\omega = 990^\circ s^{-1} = 17.28rads^{-1}$$

With this angular velocity, the linear velocity of the slide will also follow the same trapezoidal motion profile (see Figure 4.20). The linear velocity comes out to be:

$$v = 8.25mms^{-1} = 8.25 \cdot (10^{-3}ms^{-1})$$

The acceleration required will be:

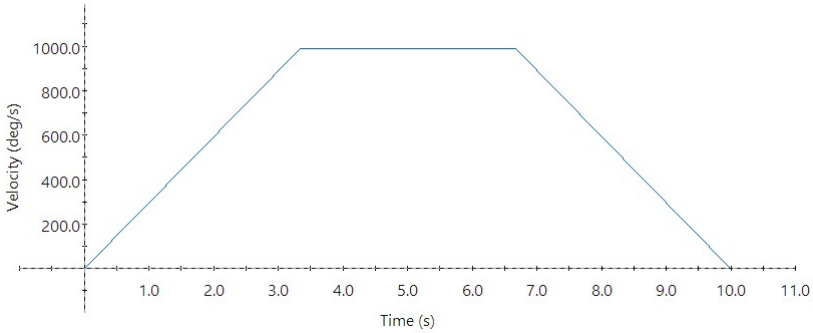

Figure 4.19: Motion profile of motor-shaft of illumination slide

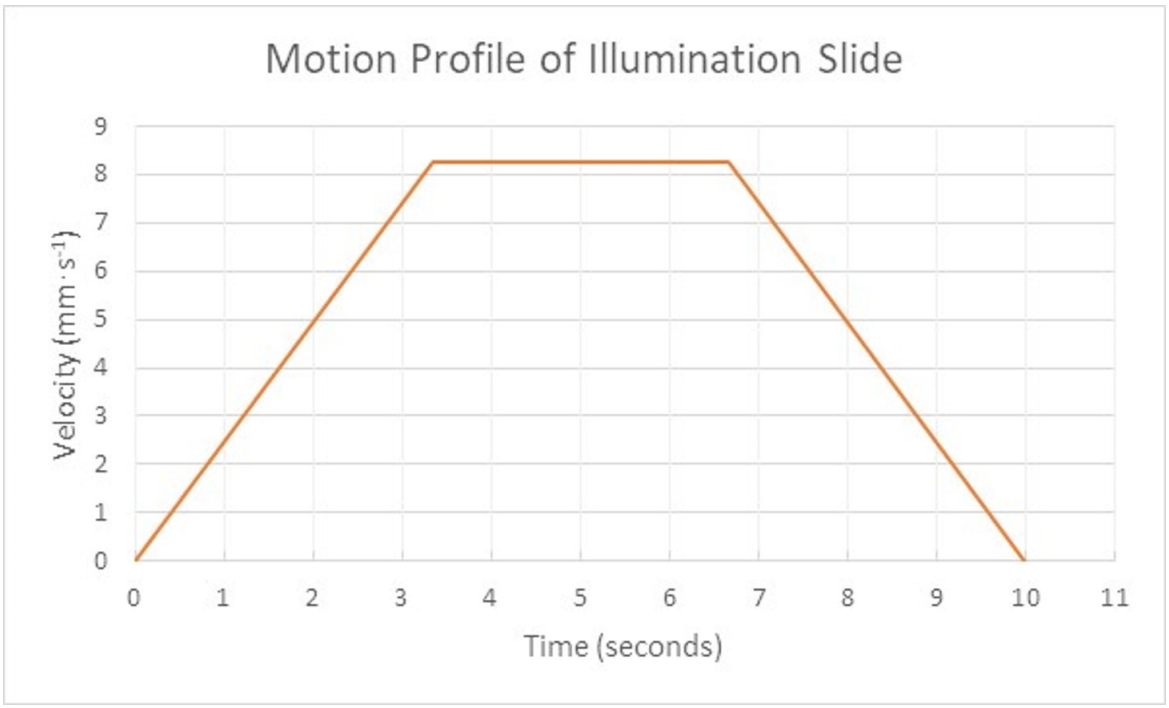

Figure 4.20: Motion profile of illumination slide

$$a = \frac{\Delta v}{t}$$
$$= \frac{8.25 \cdot (10^{-3} ms^{-1})}{3.33s}$$
$$= 2.48 \cdot (10^{-3} ms^{-2})$$

The force due to acceleration is therefore:

$$F_a = m \cdot a$$
$$= 0.06475 \cdot (2.48 \cdot 10^{-3} ms^{-1})$$
$$= 1.61 \cdot 10^{-4} N$$

The total force comes out as:

$$F_T = F_F + Fa$$
$$0.127N$$

As per Section 4.4.1, the same power screw mechanism applies here (see Figure 4.16). Therefore we will use Equation 4.6 to calculate the torque:

$$\tau = \frac{F_T \cdot d_m}{2} \cdot \left(\frac{l + \pi \cdot f \cdot d_m}{\pi \cdot d_m - f \cdot l} \right)$$

As the contact between the dry steel screw and the base is connected with a dry steel contact, the coefficient of friction between these two would be 0.7 [115]. Thus for our calculations we will take: f = 0.7.

Additionally, the remaining values are as follows:

$$d_m = \frac{OutsideDiameter + MinorDiameter}{2} = \frac{3mm + 2mm}{2} = 2.5mm = 0.0025m$$
$$l = 3mm = 0.003m$$

Substituting the values into Equation 4.6 we get:

$$\tau = \frac{0.127N \cdot 0.0025m}{2} \cdot \left(\frac{0.003m + \pi \cdot 0.7 \cdot 0.0025m}{\pi \cdot 0.0025m - 0.7 \cdot 0.003m} \right)$$
$$= 2.34 \cdot 10^{-4} Nm = 0.234Nmm$$

To confirm that this result is good approximation, we modelled the motion using SolidWorks Motion Analysis. The set-up was as follows:

- 'Rotary Motor' feature on the motor-shaft followed the same motion profile as per Figure 4.19

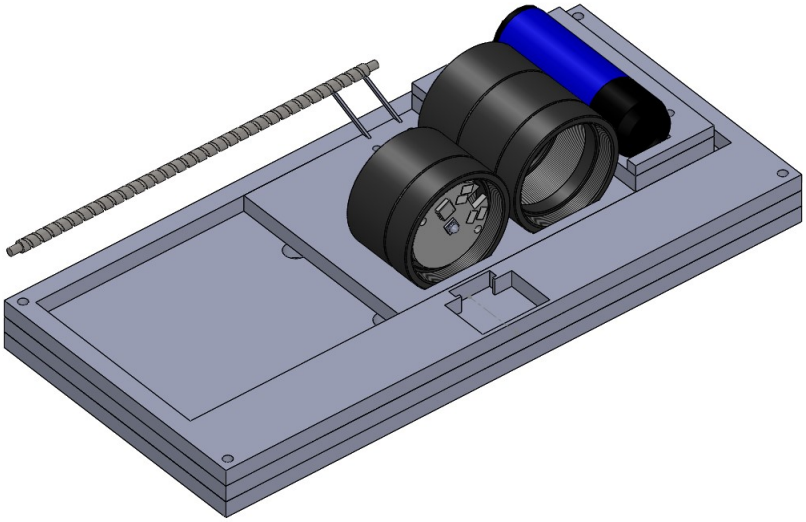

Figure 4.21: SolidWorks Motion Analysis Set-up for Illumination Source Slide

- 'Solid Body Contact Feature' between the contact and the screw with the material being set to 'Dry steel'
- Time was set to go for 10 seconds: matching the time duration of the motion profile as per Figure 4.14

The CAD set-up can be seen in Figure 4.21 and the results of the analysis can be seen in Figure 4.22. The results show that the maximum torque engaged on the shaft is 0.272Nmm. Our calculated result of 0.234Nmm matches within 15% of the simulated result indicating that it is a good estimate. We used small disk-drive stepper motors whose datasheet can be seen in Appendix C. From the data-sheet, the torque-speed characteristics show that the pull-out torque can be approximately as low as $6.5{\cdot}10^{-1}$ Nmm if the drive frequency is 2400PPS. This means that the torque provided by the motor is at least 2x larger than the maximum torque, of 0.272Nmm, found through simulations or calculations. For this reason, the selected motor will provide sufficient torque. In the physical system, the motor moved the required load as expected. For the resolution see Section 4.4.1.1.

4.5 Mechanical Stage Design

This section details the calculations to verify the mechanical simulation model for the motors used in the stage design. The mechanical simulation model was verified with the following three steps:

1. Determine the torque of the motor with hand calculations

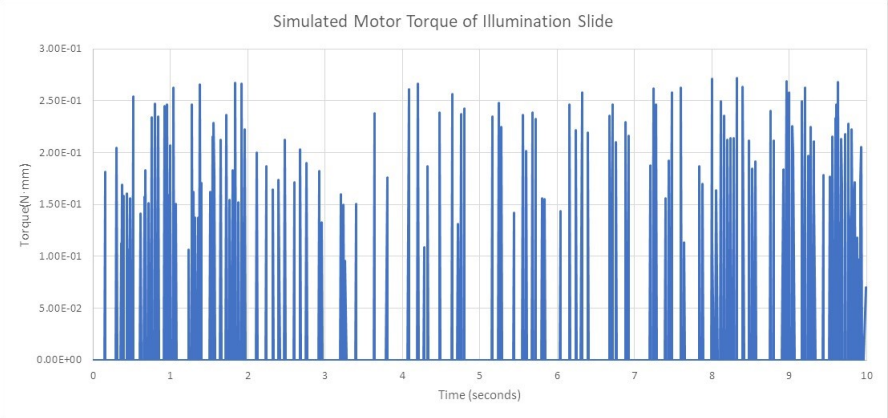

Figure 4.22: Simulated Motor Torque for Illumination Slide Motor

2. Simulate the torque on the motor with the conditions presented in the hand calculations in SolidWorks motion study and compare to hand calculations

3. Confirm if the motor was able to successfully move the required load in the physical system

4.5.1 X and Y axis motors

This section details the calculations of the x-y axis motors. The stage has a total mass of:

$$m_{stage} = 435g = 0.435kg$$

The force due to gravity is:

$$F_W = m_T \cdot g$$

$$= 0.435kg \cdot 9.81ms^{-2}$$

$$= 4.27N$$

The stage moves with THK precision slides that have a coefficient of static friction of 0.003. The normal force, $F_N = F_W = 4.27N$. The force due to friction is therefore:

$$F_F = \mu \cdot F_N$$

$$= (0.003) \cdot 4.27N$$

$$= 0.01281N$$

If we make a requirement that the motion of the stage has to go the distance the precision slides can move i.e. 13.78mm in 3 seconds, then taking that the motion of the system follows a trapezoidal profile (see Figure 4.23), the linear velocity of the stage comes to:

$$v = 6.89mms^{-1}$$

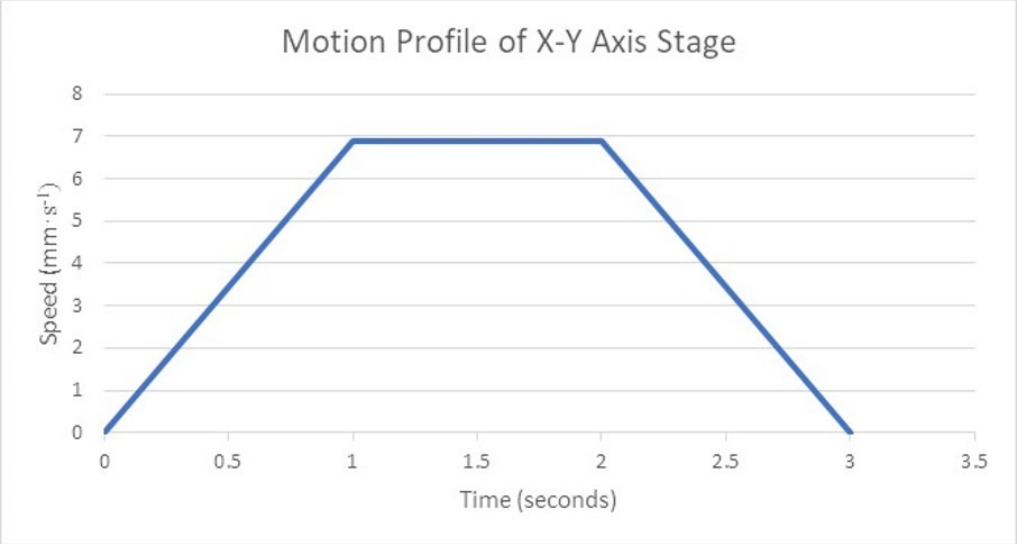

Figure 4.23: Linear motion profile of xy-axis stage

Therefore the acceleration is:

$$a = 6.89 mms^{-2} = 6.89 \cdot 10^{-3} ms^{-2}$$

The force required to accelerate the load is:

$$F_a = ma = (0.435kg) \cdot (6.89 \cdot 10^{-3} ms^{-2}) = 2.997 \cdot 10^{-3} N$$

The total force is:

$$F_T = F_F + F_a = 0.015799N \approx 15.8 \cdot 10^{-3} N$$

Taking that the stage moves through a screw mechanism the torque of the screw can be calculated using Equation 4.6:

$$\tau = \frac{F_T \cdot d_m}{2} \cdot \left(\frac{l + \pi \cdot f \cdot d_m}{\pi \cdot d_m - f \cdot l} \right) = \frac{(15.8 \cdot 10^{-3} N) \cdot (0.0025m)}{2} \cdot \left(\frac{0.003m + \pi \cdot 0.1 \cdot 0.0025m}{\pi \cdot 0.0025m - 0.1 \cdot 0.003m} \right)$$

$$= 9.896 \cdot 10^{-6} Nm = 9.896 \cdot 10^{-3} Nmm$$

To confirm that this result is a good approximation, we modelled the motion using SolidWorks Motion Analysis. Before we could proceed with the analysis, we first needed to know the speed at which to run the motor-shaft. We know that the motor-shaft is a screw with a pitch of 3mm: for every revolution, the stage moves 3mm forward. Therefore, to move the load at a speed of $6.89 \cdot 10^{-3} \text{ms}^{-1}$, the motor-shaft will have to move at:

$$\omega = \frac{6.89 \cdot 10^{-3} ms^{-1}}{0.003m} = 2.297 revs^{-1} = 14.43 rads^{-1} = 862.8^{\circ} s^{-1}$$

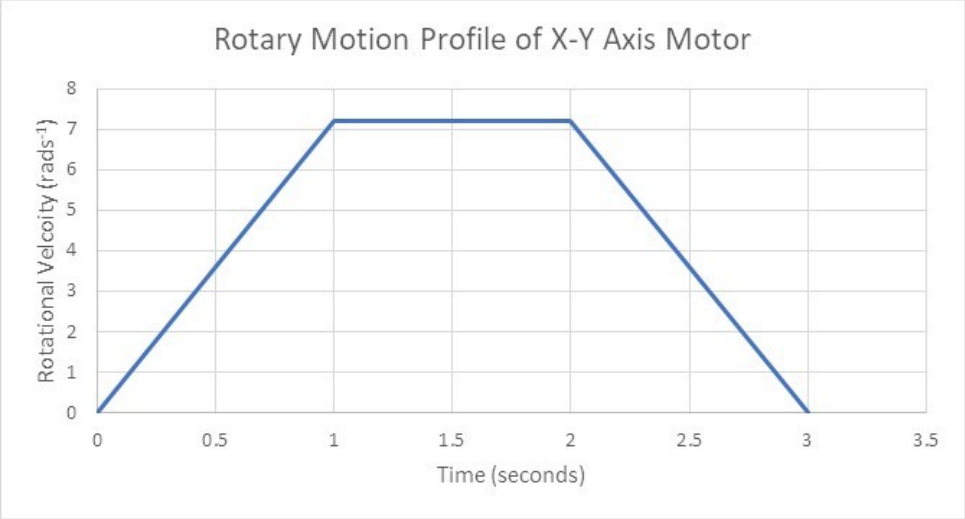

Figure 4.24: Rotational motion profile of xy-axis motor

The rotational motion profile can be seen in Figure 4.24.

- 'Rotary Motor' feature on the motor-shaft followed the same motion profile as per Figure 4.24
- 'Solid Body Contact Feature' between the nylon pickup and the dry steel screw
- 2 x 'Solid Body Contact Feature' between the precision slides and their housing
- 'Gravity' set at $9.80665 ms^{-1}$

The CAD set-up can be seen in Figure 4.25 and the results of the analysis can be seen in Figure 4.26. The results show that the maximum torque engaged on the motor-shaft is $8.925 \cdot 10^{-3}$Nmm. Our calculated result of $9.896 \cdot 10^{-3}$Nmm matches within 10% of the simulated result indicating that it is a good estimate. We used small disk-drive stepper motors whose datasheet can be seen in Appendix C. From the data-sheet, the torque-speed characteristics show that the pull-out torque can be approximately as low as $6.5 \cdot 10^{-1}$ Nmm if the drive frequency is 2400PPS. This means that the torque provided by the motor is at least 65x larger than the maximum torque, of $9.896 \cdot 10^{-3}$Nmm, found through simulations or calculations. For this reason, the selected motor will provide sufficient torque. In the physical system, the motor moved the required load as expected. For the resolution see Section 4.4.1.1.

4.5.2 Z-axis

This section details the calculations of the z-axis motors. We used an eBay z-axis that resembled a standard z-axis platform available from suppliers such as Edmund optics. We chose this one because of three reasons: the weight added stability to the platform, it was wide enough to house

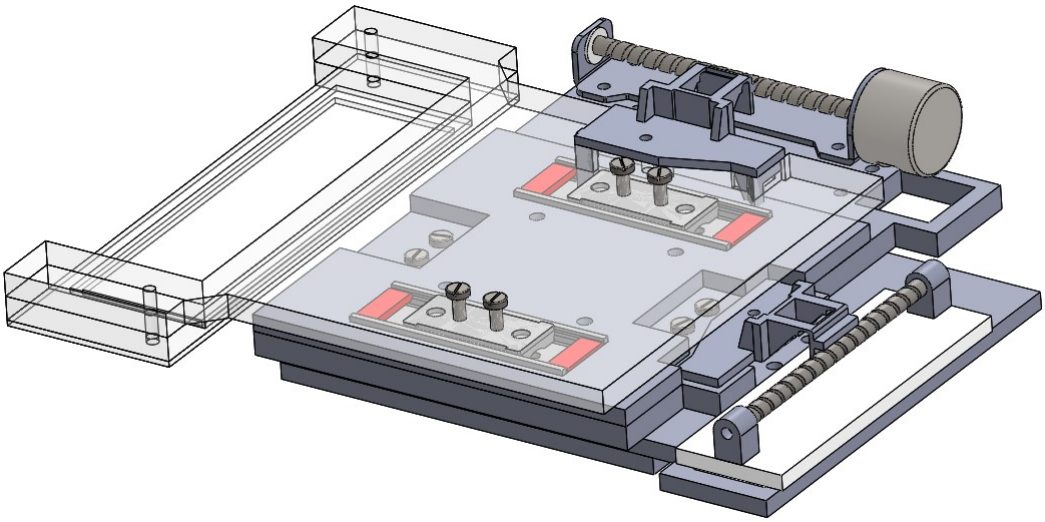

Figure 4.25: CAD Setup of xy-axis motion analysis

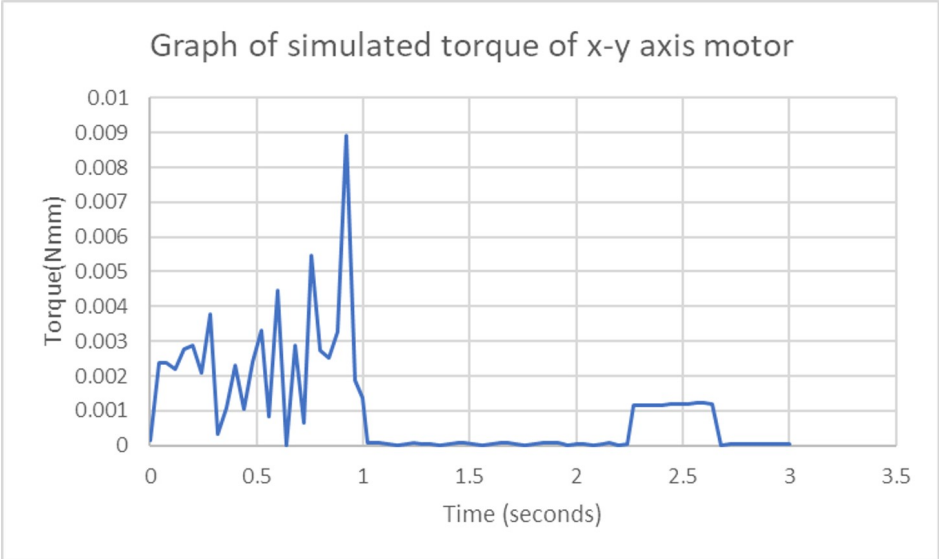

Figure 4.26: Simulated result of torque on xy-axis motor

the sample slide and the size of the platform made sense considering that, on using the tube lens with 100mm focal length, the camera would make the system much longer than the z-axis, coupled with the motor, could provide. The z-axis mechanism was controlled with a stepper motor. This motors shaft had a 3-D printed gear design that was very thick. As it rotated, an acrylic-cut gear placed on the focusing knob of the z-axis mechanism, would turn. This would allow the focus to be adjusted automatically. The motion of the system goes as follows: the motor turns the shaft which turns the 3-D printed gear on it. This then meshes with an acrylic gear that rotates the focusing knob on the microscope. The microscope knob pushes against a lever that pushes against the top part of the stage causing it to move up. A pre-attached spring added tension between the moving part of the stage to the base.

The following are a list of masses that are relevant to the calculations:

- $m_{X-Y\ Stage} = 435g = 0.435kg$
- $m_{Z-Axis\ Stage\ Block} = 279g = 0.279kg$
- $m_T = 714g = 0.714kg$

There are three forces that are acting towards the pivot: the force of the mass due to gravity, the force of the spring that adds tension to the z-axis stage as it moves up and the force of accelerating the load.

The force of the mass due to gravity:

$$F_W = m_T \cdot g$$

$$= 0.714kg \cdot 9.81ms^{-2}$$

$$= 7.00N$$

To get the force of the spring we need to first work out the spring constant. The spring constant was worked out by a simple method of measuring the extension of the spring with gradual increments of weights. Appendix D details the measurements to find the spring constant. The spring constant from Appendix D is:

$$k = 1892.2Nm^{-1} = 1.8922Nmm^{-1}$$

Therefore the force of the spring at an extension of 4mm is:

$$F_{spring} = k \cdot x = 1888Nm^{-1} \cdot 0.004m = 7.57N$$

The force required to accelerate the load will first require the motion of the stage to be defined. If we make a requirement that the stage has to move 4mm in height within 11.8 seconds and also take the initial velocity to be a constant one, as the microscope shaft has already reached

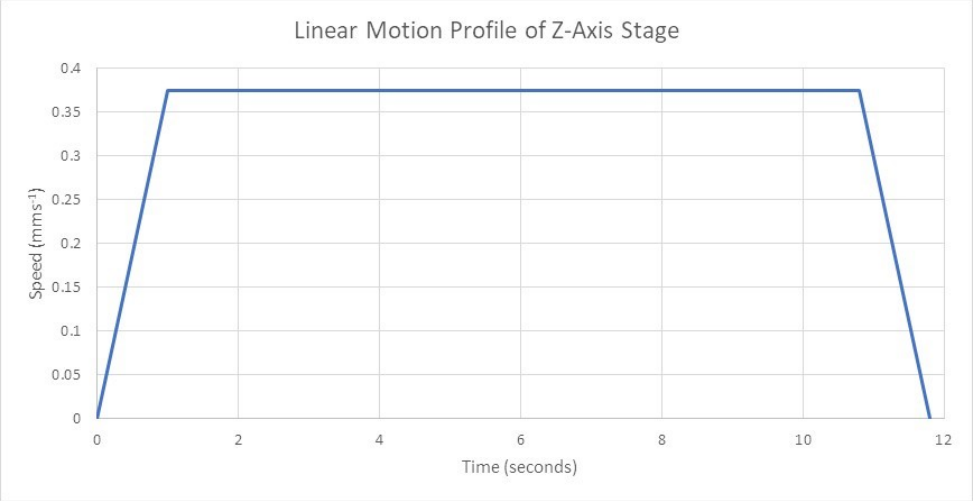

Figure 4.27: Linear motion profile of z-axis stage

constant velocity by the time it starts to do work on the load (see Figure 4.27), then the load velocity will be:

$$v = 0.325mms^{-1} = 0.375 \cdot 10^{-3}ms^{-1}$$

The acceleration is:

$$a = \frac{0.375 \cdot 10^{-3}ms^{-1}}{(\frac{1}{10})} = 3.75 \cdot 10^{-3}ms^{-2}$$

The force required to accelerate the load is therefore:

$$F_{acc} = ma = 0.174kg \cdot 3.75 \cdot 10^{-3}ms^{-2} = 6.53 \cdot 10^{-4}N$$

The total force acting on the microscope shaft is:

$$F_T = F_W + F_{spring} + F_{acc} = 14.57N$$

As the microscope shaft is a screw mechanism, as per Section 4.4.1, the torque required to produce this force can be calculated using Equation 4.6:

$$\tau = \frac{F_T \cdot d_m}{2} \cdot \left(\frac{l + \pi \cdot f \cdot d_m}{\pi \cdot d_m - f \cdot l} \right) = \frac{14.57N \cdot 0.00347m}{2} \cdot \left(\frac{0.00186m + \pi \cdot 0.23 \cdot 0.00347m}{\pi \cdot 0.00347m - 0.23 \cdot 0.00186m} \right) = 10.54Nm$$

Taking the gear ratio to be 22:14, the torque on the motor shaft will be:

$$\tau = \frac{10.54Nm}{(\frac{22}{14})} = 6.71Nm$$

To confirm that this result is a good approximation, we modelled the motion using SolidWorks Motion Analysis. Before we could proceed with the analysis, we first needed to know the speed

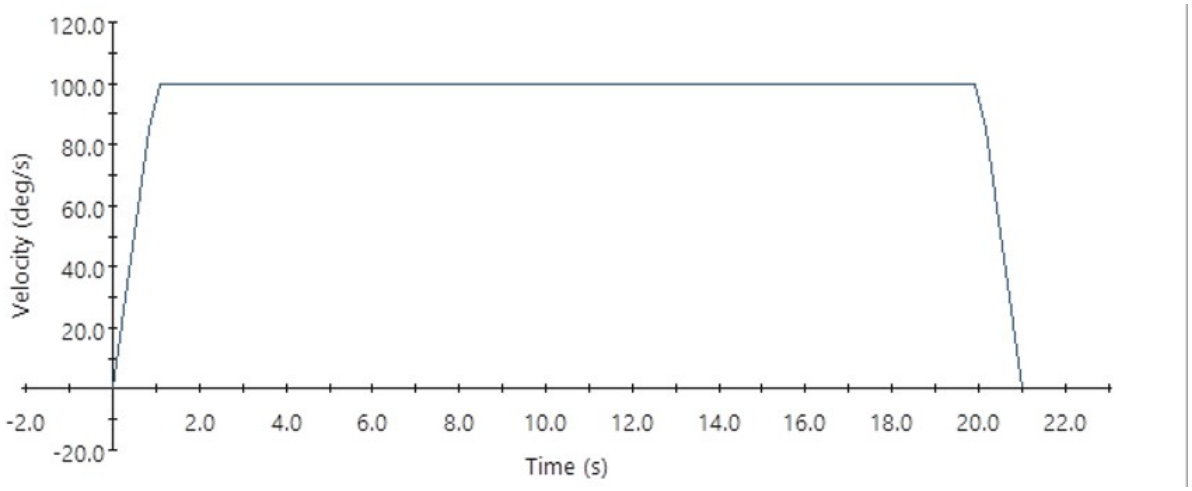

Figure 4.28: Rotational motion profile of z-axis motor-shaft

at which to run the motor-shaft. We know that the microscope shaft is a screw with a pitch of 1.86mm: for every revolution, the shaft moves 1.86mm forward. Therefore, to move the load at a speed of $0.375 \cdot 10^{-3} \mathrm{ms}^{-1}$, the microscope shaft will have to move at:

$$\omega = \frac{0.375 \cdot 10^{-3} ms^{-1}}{0.00186m} = 0.1747 revs^{-1} = 1.09 rads^{-1} = 62.90^{\circ} s^{-1}$$

The gear ratio between the two gears is $\frac{22}{14}$, so the speed that the motor-shaft spins at is:

$$\frac{62.90}{\frac{14}{22}} = 98.8^{\circ} s^{-1} \approx 100^{\circ} s^{-1}$$

Figure 4.28 shows the rotational motion profile of the motor-shaft.
The set-up was as follows:

- 'Rotary Motor' feature on the motor-shaft followed the same motion profile as per Figure 4.28
- 'Solid Body Contact Feature' between the acrylic gear on the microscope shaft and the 3-D printed gear on the motor shaft
- 'Solid Body Contact Feature' between the microscope-shaft and the pivot on the base
- 'Solid Body Contact Feature' between the pivot and the load
- 'Gravity' set at $9.80665 \mathrm{ms}^{-1}$
- 'Linear Spring' with settings:

  Exponent of spring force expression: linear

  Spring Constant: 1.88N· mm

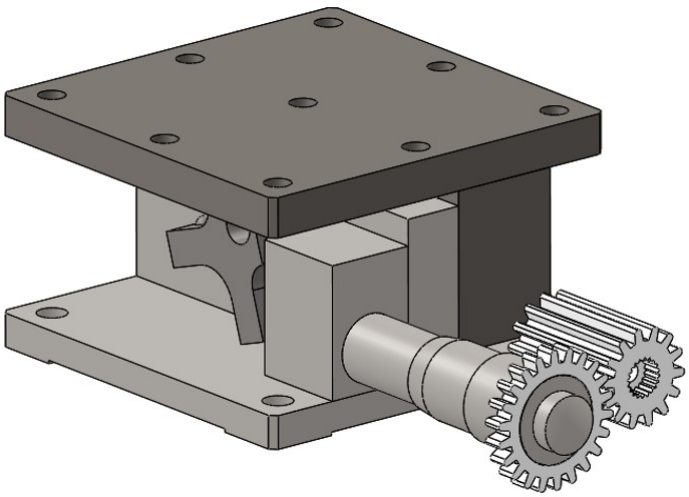

Figure 4.29: CAD Setup of z-axis motion analysis

Free length: 22.24mm

Coil Diameter: 4.5mm

Number of Coils: 25mm

Wire Diameter: 0.59mm

- 'Force' of the stage was applied as a constant force of 4.27N on the face of the load stage

The CAD set-up can be seen in Figure 4.29 and the results of the analysis can be seen in Figure 4.30. The results show that the maximum torque engaged on the motor-shaft is 5.58Nmm. Our calculated result of 6.7Nmm matches within 18.2% of the simulated result indicating that it is a good estimate. The motor we used was the ICAN28H2P3205A4 which has a holding torque of 60Nmm. This torque is around 9x our calculated torque result making it sufficient for our application. In the physical system, the motor was able to move the load as expected. In terms of resolution the calculation works out as follows:

The motor, coupled with 256 microsteps, had a step angle of:

$$\frac{1.8^\circ}{256\ steps} = \frac{0.0070^\circ}{step}$$

Accounting for the gear ratio and the fact that the stage moves up 1.86mm per revolution of the microscope shaft we get:

$$\frac{(\frac{0.0070^\circ}{step} \cdot \frac{14}{22})}{360^\circ} \cdot 1.86mm = \frac{2.31 \cdot 10^{-5} mm}{step}$$

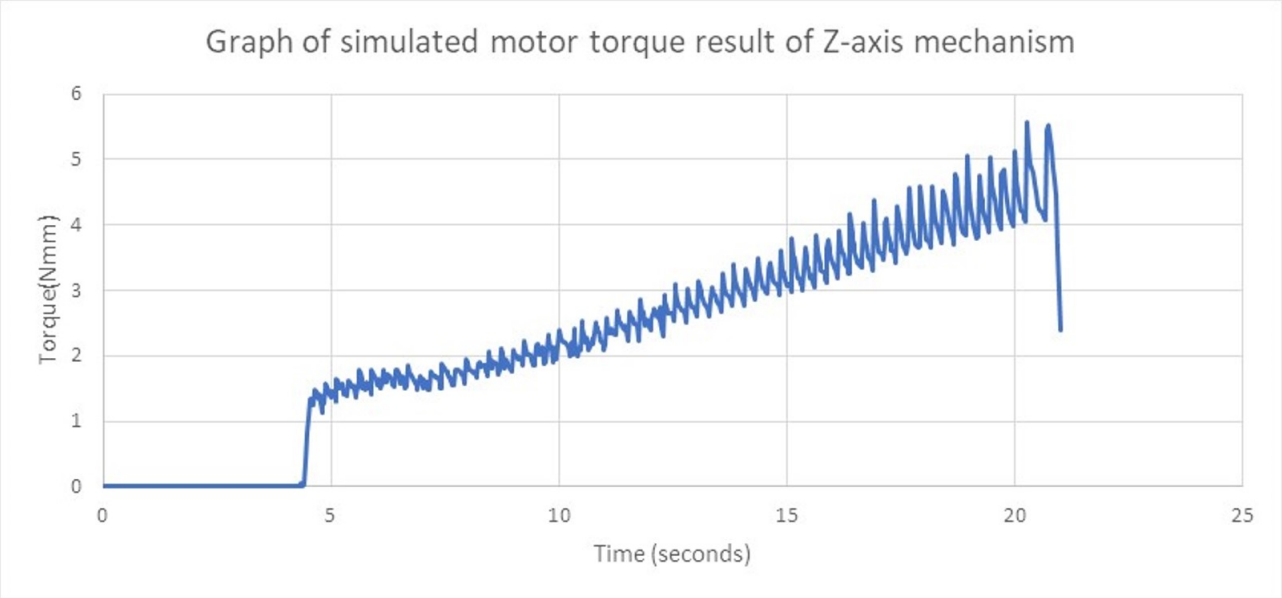

Figure 4.30: Simulated result of torque on z-axis motor

4.6 Variable Magnification Change Design

This section covers the calculations to verify the mechanical simulation model for the motor that controls the rotation of the objective lens turret. The mechanical simulation model was verified with the following three steps:

1. Determine the torque of the motor with hand calculations
2. Simulate the torque on the motor with the conditions presented in the hand calculations in SolidWorks motion study and compare to hand calculations
3. Confirm if the motor was able to successfully move the required load in the physical system

The list of masses are as follows:

- $m_{Motorshaft} = 12.5g$
- $m_{3-Dprintedgearholder} = 1.31g$
- $m_{Gear1} = 2.84g$
- $m_{Gear2} = 46.46g$
- $m_{10xObjectiveLens} = 85.80g$
- $m_{40xObjectiveLens} = 119.72g$

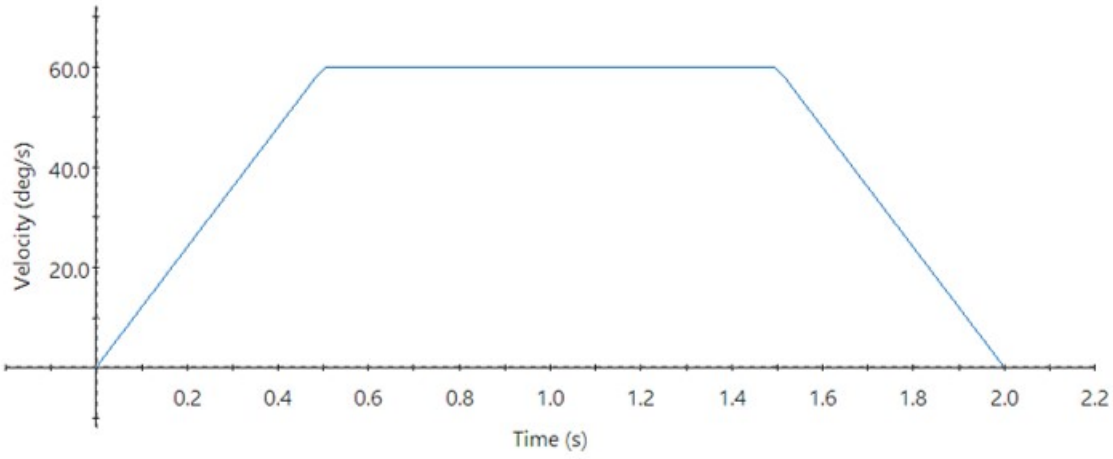

Figure 4.31: Motion profile of turret

- $m_{100xObjectiveLens} = 131g$

List of inertias are as follows:

- $J_{Motor-shaft} = 38.91gmm^2$
- $J_{Gear1} = 381.01gmm^2$
- $J_{Gear2} = 28339.08gmm^2$
- $J_{Gear2+objectives} = 261843.29gmm^2$
- $J_{3-DPrint} = 83.52gmm^2$

We desire that the turret can move 90° in two seconds. The gear ratio is:

$$N_{TurretGear} : N_{MotorGear}$$
$$= 90 : 40$$
$$N_{GearRatio} = \frac{90}{40}$$

If we take a trapezoidal motion profile, accelerating to a set angular velocity in 0.5 seconds, continuing at a constant angular velocity for 1 second and then finally decelerating to a stop within 0.5 seconds (see Figure 4.31), we find that the angular velocity of the turret calculates to:

$$\omega_{Turret} = 60°s^{-1} = \frac{\pi}{3}rads^{-1}$$

Subsequently, the angular acceleration calculates to :

$$\alpha_{Turret} = \frac{\omega_{Turret}}{\Delta t}$$

$$= \frac{60° s^{-1}}{0.5 sec}$$

$$= 120° s^{-2} = \frac{2\pi}{3} rads^{-2}$$

Using the gear ratio, the angular velocity of the motor shaft works out to be:

$$\alpha_{Motor-shaft} = \frac{2\pi}{3} rads^{-2} \cdot N_{GearRatio}$$

$$= \frac{3\pi}{2} rads^{-2}$$

The inertia on the motor-shaft axis itself is:

$$J_{Motor} = J_{Motor-shaft} + J_{Gear1} + J_{3-DPrint} = 503.44 gmm^2$$

The inertia on the turret axis is:

$$J_{Turret} = J_{Gear2+objectives} = 261843.29 gmm^2$$

The total reflected inertia on the motor shaft is:

$$J_T = \frac{J_{Turret}}{N^2} + J_{Motor}$$

$$= \frac{261843.29 gmm^2}{(\frac{90}{40})^2} + 503.44 gmm^2$$

$$= 5225.57 gmm^2$$

The torque on the motor is:

$$\tau = I \cdot \alpha$$

$$= 5225.57 gmm^2 \cdot (\frac{3\pi}{2} rads^{-2})$$

$$= 0.246 N \cdot mm$$

To confirm that this result is good approximation, we modelled the motion using SolidWorks Motion Analysis. The set-up was as follows:

- 'Rotary Motor' feature on the motor-shaft followed the same motion profile as per Figure 4.31
- 'Solid Body Contact Feature' between the two sets of gears with the material being set to 'Acrylic'
- Time was set to go for 2 seconds: matching the time duration of the motion profile as per Figure 4.31

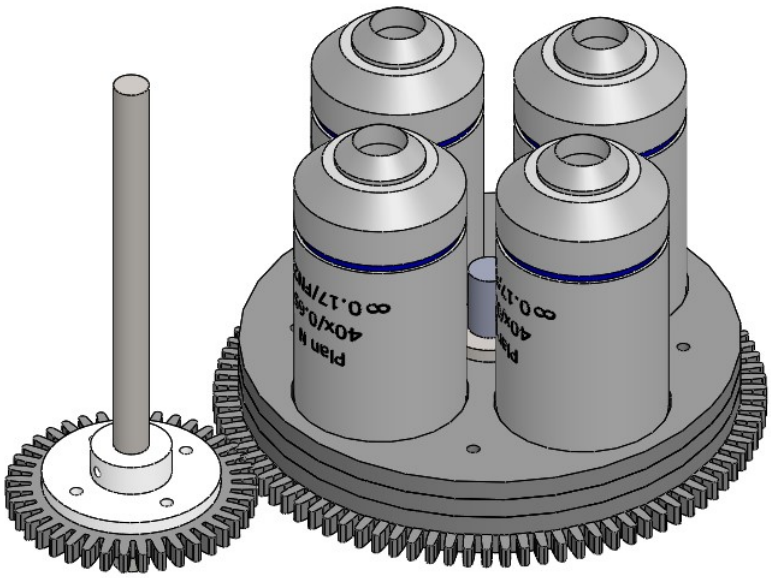

Figure 4.32: SolidWorks Motion Analysis Set-up

The physical set-up can be seen in Figure 4.32 and the results of the analysis can be seen in Figure 4.33. The results show that the maximum torque engaged on the shaft is 0.2798N·mm. Our calculated result matches within 12.9% of the simulated result indicating that it is a good estimate. The motor we used was a 17HW4410N-03AD-Z which had a detent torque of 12Nmm. This is 43x our calculated/simulated result making it sufficient for our application. In the physical system, the motor was able to move the load as expected. In terms of resolution, the calculations are as follows:

$$\frac{(\frac{0.9^\circ}{step})}{256} \cdot \frac{40}{90} = \frac{0.00156^\circ}{step}$$

4.7 Folded Optics

4.7.1 Mirror

The mirror was placed below the beam splitter, or fluorescent cube, and redirected the reflected sample light onto the CMOS sensor of the EO5012C camera. By using this mirror, the optical path was folded allowing the design to be more compact.

4.7.2 Beam Splitter

The beam-splitter was used to redirect the illumination rays towards the objective and also to let the reflected rays pass through to the mirror when they came back.

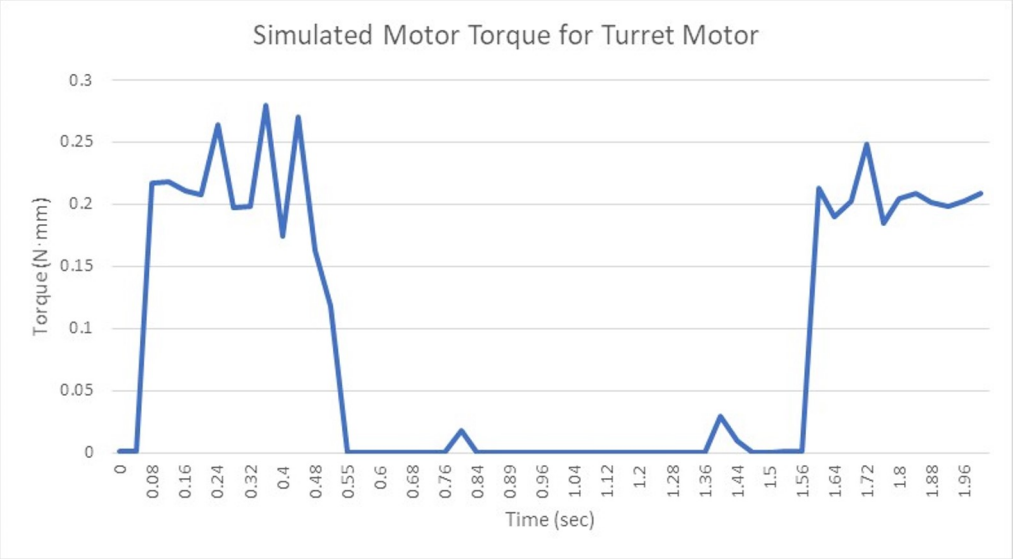

Figure 4.33: Simulated Motor Torque for Turret Motor

4.8 Portability

From our literature review, we found optical systems, in Section 2.2.1, used folded optics and batteries to reduce their overall size and we also saw systems in Section 2.4 that had range of sizes in what they considered as portable systems. For this reason, the idea of a portable system can vary. Our design characterized portability as the ability to function from a battery and have overall dimensions of 167mm x 180mm x 250mm. For the application of a battery, we had to first calculate the maximum power consumed before we could decide on which one to use. The power consumption of the electrical components can be seen in Table 4.2 below.

Table 4.2: Power Consumption of Components

Component	**Voltage (V)**	**Current (A)**	**Power(W)**
White LED	3.2	0.21	0.672
Blue LED	3.2	0.21	0.4
Laser	5	0.08	0.26
X-Axis Motor	5	0.03	0.15
Y-Axis Motor	5	0.03	0.15
Z-Axis Motor	4.95	0.11	0.54
Turret Motor	4.2	0.17	0.714
Light Slide Motor	5	0.15	0.75
BS Cube/Fluorescence Filter Cube Slide Motor	5	0.11	0.55
Microcontroller + Motors at Stall Torque	12	0.14	1.68
		1.24	**5.87**

The maximum power required would be 5.87W. The maximum voltage required is 12V from the micro-controller and the maximum current drawn is 1.24A. Going by the maximum voltage of

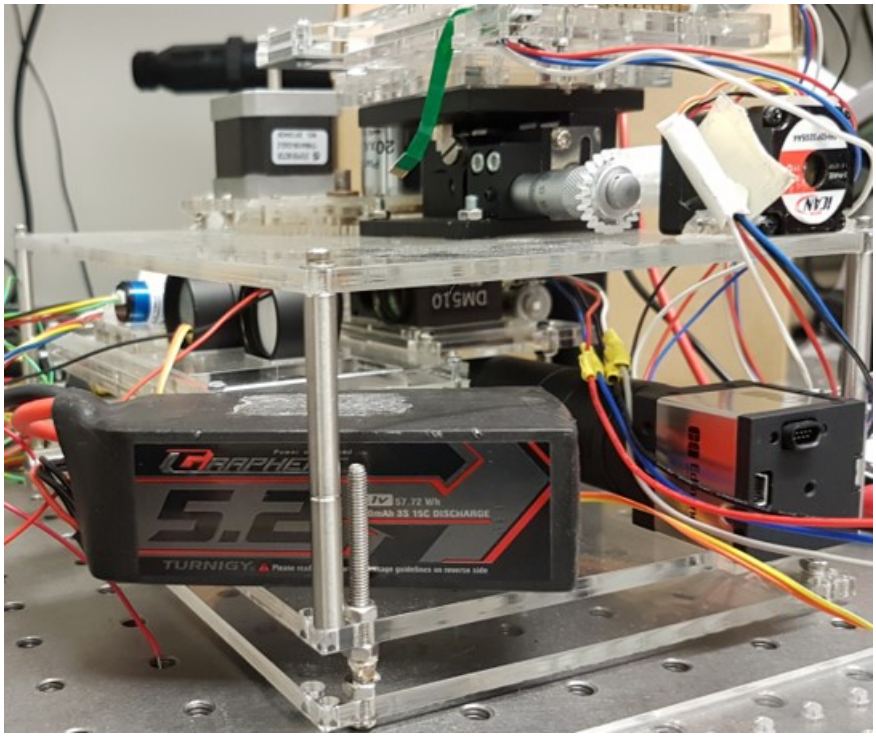

Figure 4.34: Micro-imaging system with battery

12V, we needed a battery of 12V that would supply 12V to micro-controller and stepped down to 3.2V and 5V for the LEDs and laser. The battery we used was a Turnigy LiPo 12V 5200mAh-3S 15C discharge. Figure 4.34 shows the system with the battery.

4.9 Electrical Development

4.9.1 Camera

We used the EO-5012c camera because it has a lot of built in features and has ready libraries for C# visual studio making application development easier.

4.9.2 Motor Controller

We used the motor controller, TMCL6110, because we needed to control five motors: the board has the capacity to control six motors. It also provided up to 256 micro-steps which came in useful for the x and y axis motors especially. A motor could also draw a maximum of 1.5A per channel so was sufficient for the motors we were using.

4.9.3 Optical Stops

The EESX4134 optical stops were chosen because they were small, so did not cause massive space requirements, and because they were readily available. These were used as limit switches for the motors.

4.9.4 LED

The LEDs used were the M470D2 and the MCWHD2. From the embodiment design stage (see Section 3.1.3.3), these LED's were found to provide enough light for our application. Normally for fluorescence illumination a Xenon or Mercury lamp is chosen [8] because the high intensity of light that they produce gets filtered and only a set wavelength comes out. Looking at this problem, we used the blue LED M470D2 because, when shone with only blue light, most of this light gets through the filter meaning a higher irradiance and a much more illuminated image.

4.9.5 Laser

The laser was chosen because it provided the required laser light that was needed and used only 4mW of power.

4.10 System Layout

Figure 4.35 shows the block diagram of the overall system layout.

4.11 Discussion

This section had three main parts: optical model verification, mechanical model verification and electrical development. The optical model was verified by comparing the simulated irradiance, from a model built in TracePro, against the irradiance measured using the optical sensor, detailed in Section 4.1.1. From our results, the bright-field model was within 5%, fluorescence model was within 3.52% and laser simulation was within 10%. These are relatively good results and indicate that simulation model holds up well against the real world whilst it also indicates that, if there was a change in the optical design, the simulation could be relied on to achieve a good approximation.

We used optical components to achieve the folded optics required for contributing to the portability of the system. We used mirrors with a high reflectance of 97.5% and a beam-splitter that had a 47±10% rating. The collimator and tube lens were standard components we required to collimate light into a uniform beam and to bring the light to a focus on the lens of the camera respectively. The choice of a beam-splitter and mirrors is similar to what standard microscopes use to direct the beam of light and reduce the size of their system. For fluorescence illumination

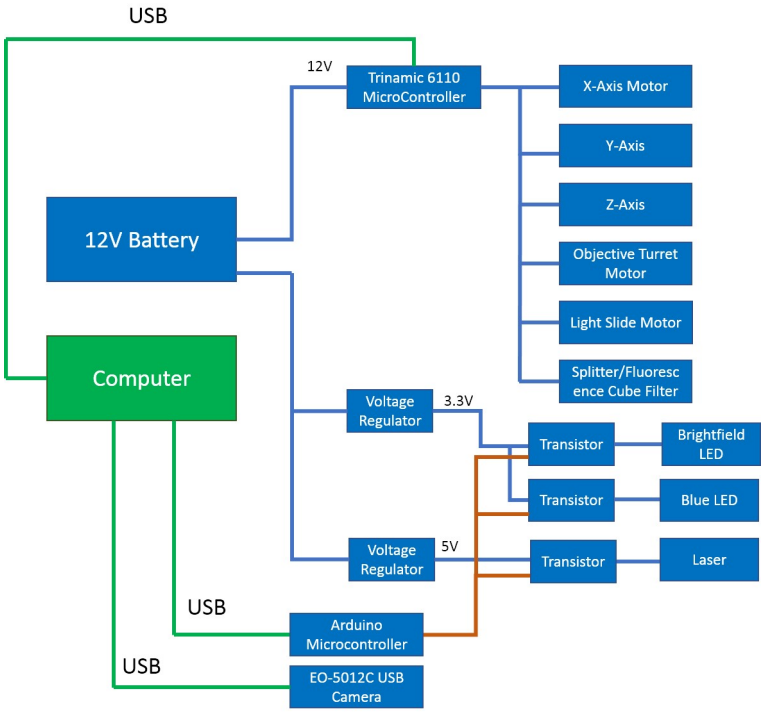

Figure 4.35: Block Diagram

mode, the filter cube that was used was chosen because it could image large amounts of biological samples that emit green light when excited with blue light. The fluorescence cube also served a similar purpose as the beam-splitter in the sense that it directed and received beams of light.

The mechanical motion model was verified by comparing the hand calculations against the simulated torque from the Solidworks Motion Analysis model, as well as physical observations of motor moving the required load. After running the simulations, we found they were accurate with the most deviation coming from the z-axis motors of 18.2%. This value indicates that the motion analysis model is accurate and can be used for future simulations whilst maintaining its accuracy.

We characterized the system as being portable by using a battery for power and having the size of 167mm x 180mm x 250mm. From our literature review, we found that lithium ion battery was the best candidate among the three that were studied for our electrical needs. We therefore integrated a 12V lithium polymer battery to make the system portable and found it lasted between 3-4 hours of use. The battery happened to be readily available and had been a dated model used for other projects so that could be the reason why it fluctuated at 3-4 hours instead of a consistent 4 hours each time.

CHAPTER 5

SOFTWARE DEVELOPMENT

5.1 Development Environment

Visual Studio C# environment was selected as the development environment to build the software platform for this application. It was selected because the uEye camera that we used had libraries in C# so naturally it would make sense to use the same development environment. C# also had a number of image processing libraries, such as Aforge or EmguCV, written for it which could benefit our application for areas such as particle counting or particle size estimation.

5.2 Image Stitching

5.2.1 Image Stitcher Capability Test

From the literature review, we studied three stitching tools available that have been used in research. From the discussion in Section 2.6.2.2, it was concluded that preliminary tests would have to be done for stitching applications. This section therefore presents a test of the stitching capability of the three stitching tools studied: Microsoft Image Composite Editor, OpenCV and ImageJ. It is worth noting that having selected a C# development environment means that the OpenCV will be assessed using its C# wrapper, EmguCV.

The test will consist of a set of images produced from our system in both bright-field and fluorescence illumination. The test will look for a correctly aligned image, seam blend smoothness, how many images it stitched and how long it took to complete.

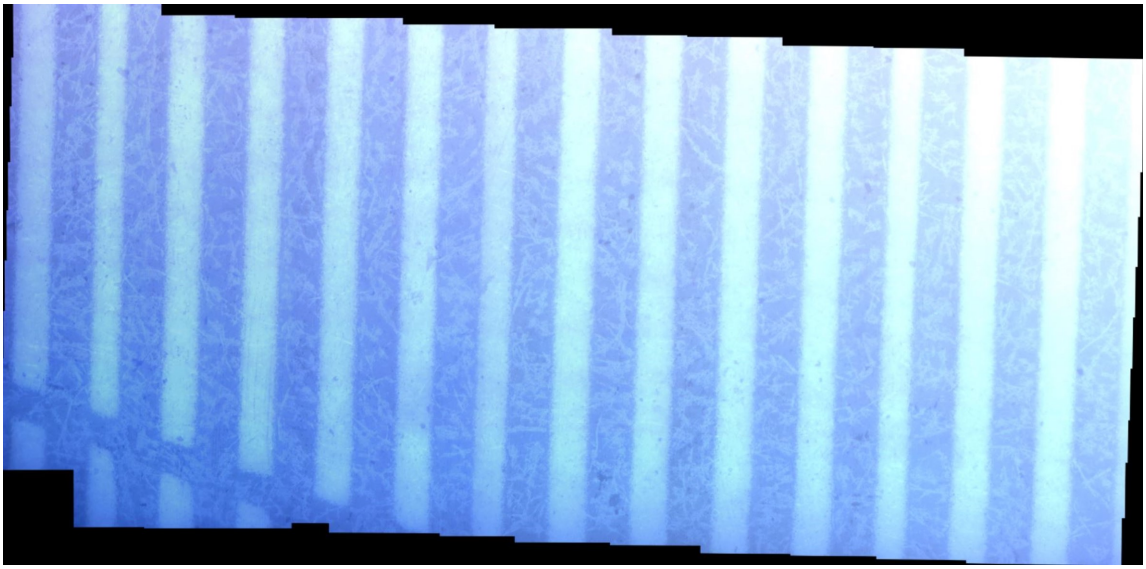

Figure 5.1: Stitched bright-field image of raw scanned images at 10x magnification, produced by ICE

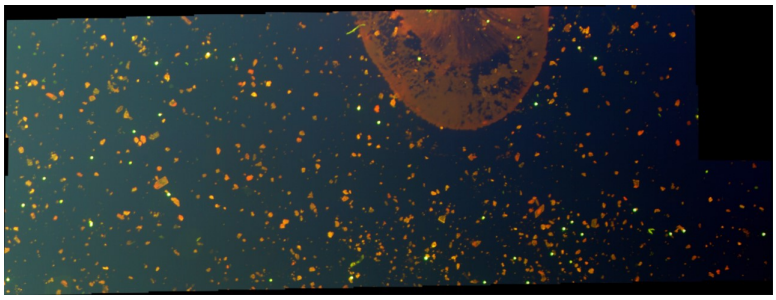

Figure 5.2: Stitched fluorescence image of raw scanned images at 10x magnification, produced by ICE

5.2.1.1 Microsoft Image Composite Editor

5.2.1.1.1 Bright-field Illumination

Out of 108 images presented for stitching, ICE had stitched 107 of them, see Figure 5.1. The image had no distortions and a smooth seam blend that looked like one complete image. ICE automatically adjusts the composition of the image so one side was found to be brighter than the other side for these set of images. ICE took approximately 7 minutes and 4 seconds to stitch the images together.

5.2.1.1.2 Fluorescence Illumination

Out of 59 images presented for stitching, ICE had stitched 31 of them, see Figure 5.2. The image was aligned correctly, had a smooth seam blend that looked like one complete image. ICE took approximately 8 minutes and 37 seconds to stitch the images together.

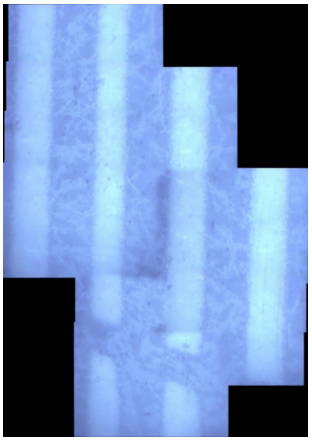

Figure 5.3: Stitched bright-field image of raw scanned images at 10x magnification, produced by EmguCV

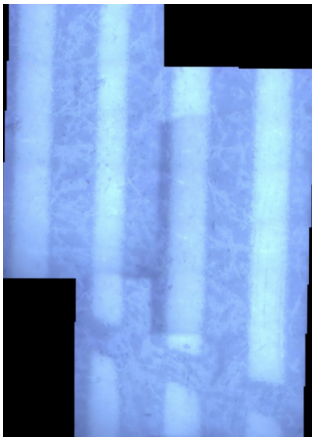

Figure 5.4: Stitched bright-field image of raw scanned images at 10x magnification with 'PanoConfidenceThresh' = 0.5, produced by EmguCV

5.2.1.2 EmguCV

5.2.1.2.1 Bright-field Illumination

Out of 108 images presented for stitching, EmguCV had stitched approximately 9 of them, see Figure 5.3. The image had no distortions but did not achieve a smooth seam blend. EmguCV took approximately 3 minutes and 47 seconds to stitch the images together. It was suspected that the 'PanoConfidenceThresh' parameter default setting of 1.0 may have been too high, therefore it was reduced to 0.5. The resulting stitch took 7 minutes and 27 seconds, seen in Figure 5.4, and had a small improvement because it was able to stitch approximately one more image. Reducing the 'PanoConfidenceThresh' further to 0.1 did not produce any image because the operation was aborted when it took longer than 52 minutes to stitch.

Figure 5.5: Stitched fluorescent image of raw scanned images at 10x magnification, produced by EmguCV

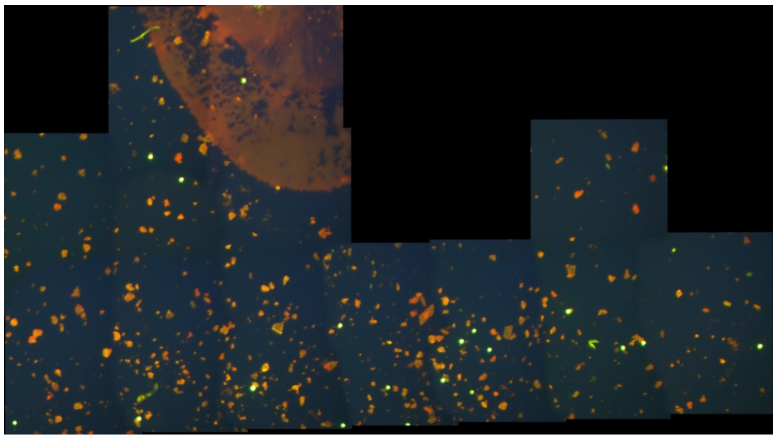

Figure 5.6: Stitched fluorescent image of raw scanned images at 10x magnification with 'PanoConfidenceThresh' = 0.5, produced by EmguCV

5.2.1.2.2 Fluorescence Illumination

Out of 59 images presented for stitching, EmguCV had stitched approximately 10 of them, see Figure 5.5. The image had no distortions and did not achieve a smooth seam blend. EmguCV took approximately 20 seconds to stitch the images together. The 'PanoConfidenceThresh' parameter default setting of 1.0 was reduced to 0.5 and the resulting stitch can be seen in Figure 5.6 which is an improvement because it was able to stitch approximately 3 more images. Increasing the 'PanoConfidenceThresh' further to 0.1 resulted in a reduction of images stitched in the final image, as can be seen in Figure 5.7.

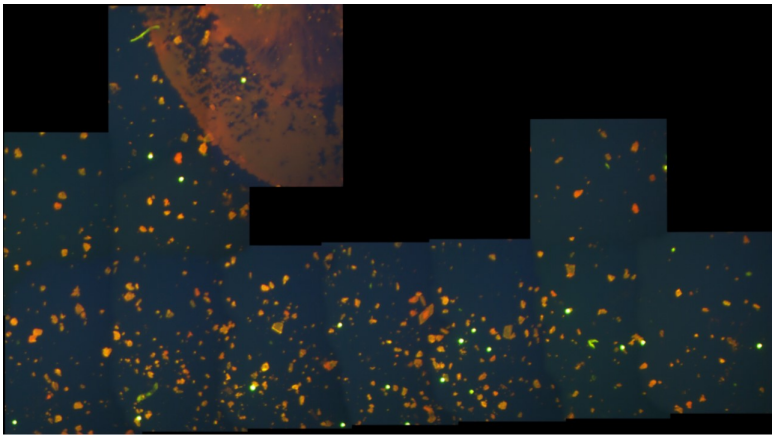

Figure 5.7: Stitched fluorescent image of raw scanned images at 10x magnification with 'PanoConfidenceThresh' = 0.1, produced by EmguCV

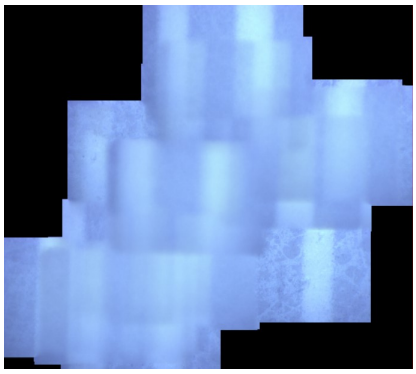

Figure 5.8: Attempt at stitching produced by ImageJ of bright-field raw scanned images at 10x magnification

5.2.1.3 ImageJ

5.2.1.3.1 Bright-field Illumination

Out of 108 images presented for stitching, Fiji had produced an image from eight of them, see Figure 5.8. For reference, the images were treated as 'sequential' because they had been scanned by the system: therefore the 'Sequential Images' mode of stitching was used. The other parameters can be seen in Figure 5.9. The resulting image was not aligned at all despite having only used approximately 8 out of the 108 images and took 41 minutes and 37 seconds to produce.

5.2.1.3.2 Fluorescence Illumination

Out of 59 images presented for stitching, Fiji had produced an image from 15 of them, see Figure 5.10. For reference, it used the same parameters as those used for bright-field illumination. The resulting image was not aligned at all despite having only used approximately 15 out of the 59 images and took approximately 17 minutes and 27 seconds to produce.

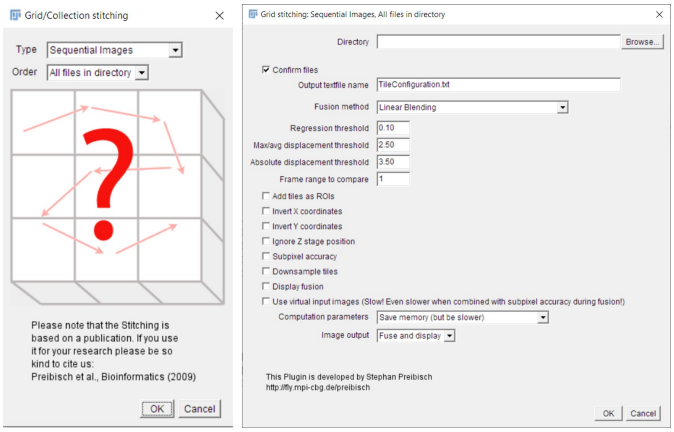

Figure 5.9: Parameters used for ImageJ stitching in 'Sequential Images' stitching mode

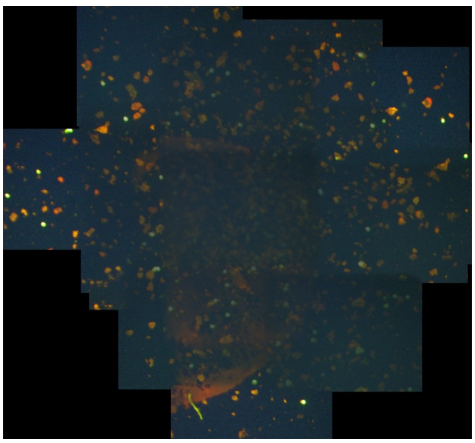

Figure 5.10: Attempt at stitching produced by ImageJ of fluorescent raw scanned images at 10x magnification

5.2.2 Image Stitching Tool Selection

From the stitcher test undertaken in Section 5.2.1, we found that Image Composite Editor (ICE) was the most suitable stitching tool for stitching the images produced from our system. Both ICE and EmguCV had correctly aligned images, but ICE was able to stitch more images and produced a final stitched image that had a smooth seam blend. ImageJ did not produce correctly aligned images so the other parameters of assessment have no standing. ICE is therefore selected as the stitching tool we will use to stitch images for our application.

5.3 Image Processing Tool Selection

Following from the literature review, we studied two image processing tools: OpenCV and Aforge. Our discussion concluded that the choice of which tool to use could depend on the hardware selected. Our choice of using the uEye camera meant that we would use a C# development

environment. While this environment can be suitable for both OpenCV, through the use of its C# wrapper EmguCV, or Aforge, it was found that, where both tools had been used, Aforge was used more for image processing whereas EmguCV had been used more for data processing. Our application will use basic image processing techniques such as particle counting or particle size estimation, and therefore it would make sense to mainly use Aforge instead of EmguCV. However, if the use of EmguCV is required, we can apply it as well.

5.4 Particle Counting and Particle Concentration

Particle counting was done with Aforge libraries. Specifically, we used the blob counter class to count them. We then expanded this method to count only the green fluorescent particles in the image using the 'HSL Filtering' class from the Aforge framework. We did this by setting the 'Saturation' to a minimum of 0f and maximum of 1.0f, setting the 'Luminance' to a minimum of 0.3f and maximum of 1.0f and setting the 'Hue' to a minimum of 50 and maximum of 200. We also kept the minimum height and width of the particles to 50.

5.5 Particle Area Estimation

Particle size was determined using the Aforge libraries. Within the blob-counter class there is an option to find the area of each blob detected. Using this, we could determine the size of each particle with respect to the magnification and depth of field of the image. To calibrate our measurements, we measured an object of known size beforehand at a given magnification to determine what each pixel represents in terms of length. From our measurements, at 10x magnification, 1 pixel represents $1.31 \cdot 10^{-7}$ mm^2 in area.

5.6 Particle Perimeter Estimation

Perimeter could be determined by counting the pixels of each blob and translating them into real dimensions based on the magnification and depth of field of the image. Just like with area, we calibrated our measurements by measuring an object of known size beforehand at a given magnification to determine what each pixel represents in terms of length. From our measurements, at 10x magnification, 1 pixel represents $3.62 \cdot 10^{-4}$ mm.

5.7 X-Y Drift Correction

X-Y drift describes the phenomenon where, in the context of our system, the stage accumulates error in the x and y direction causing the final stitched image to appear skewed. The reasons for this can come from several factors including that the motors suffer from backlash and are simply not accurate or exhibit inaccuracy due to not being in a closed loop system where their

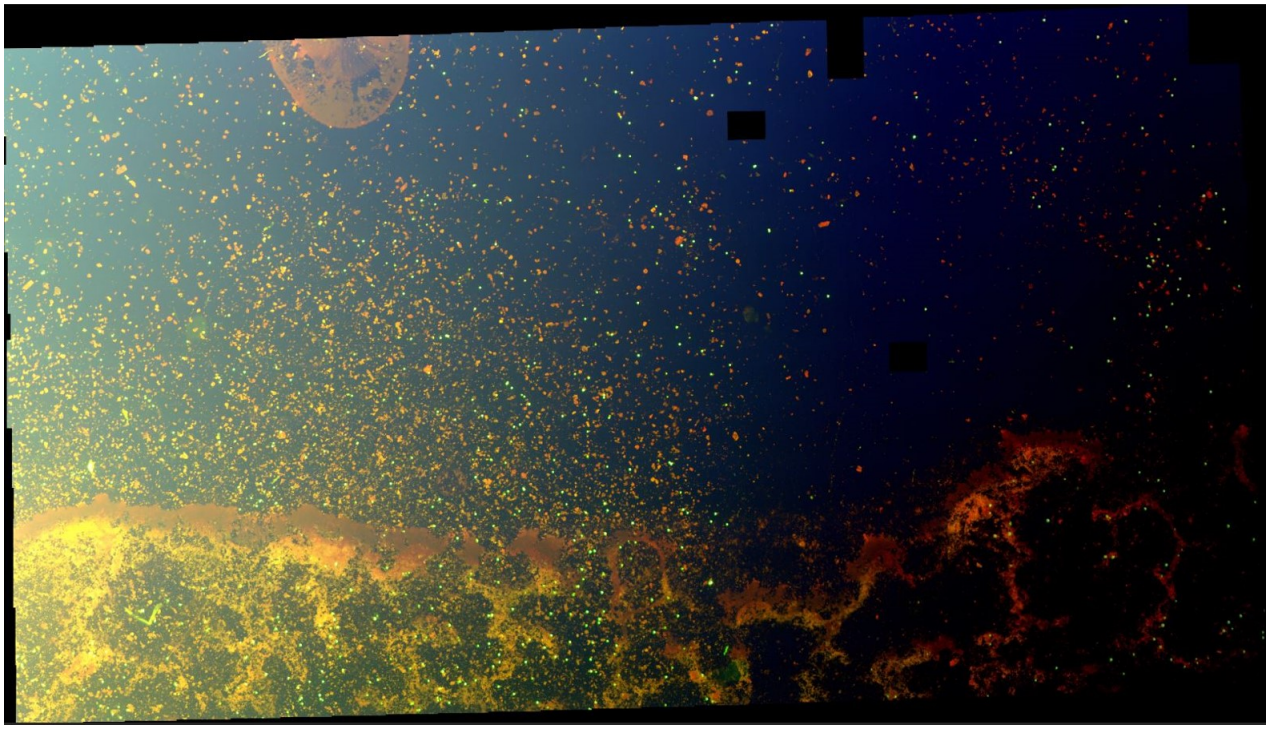

Figure 5.11: Stitched fluorescent image from raw scanned images at 10x Magnification

accumulation of error is continually corrected. From the stitched photo seen in Figure 5.11 a clear x-y drift is present. It is also worth noting that from Figure 5.12 the x-y drift is significantly less for 4x magnification. This is most likely due to the fact that there are less images taken at 4x magnification because it has a larger field of view hence needing fewer images to traverse the entire scanable area and therefore accumulating a lower amount of error. Although the image can be left as it is, we sought to correct this with the image processing libraries available to us. We implemented an algorithm combining OpenCV's match template, basic statistics and image size reduction.

We estimated that the there would be 20% backlash from the x and y-axis motors and therefore programmed the scan to move to the next point so that it maintained a 30 percent overlap with the previous point to compensate for this. As such, if we took a cropped image within the 30 percent overlap in the safe region, then we could find a feature in it. Around this feature a square template region was taken and compared to the next image to find where it best matched. We now calculated the x coordinate of the template and compared it with the x-coordinate of the image being compared to: if there was a difference, we moved the motor to correct this difference. Figure 5.13 shows a flowchart illustrating the steps of the algorithm and Figure 5.14 shows it in practice during a 10x fluorescent scan.

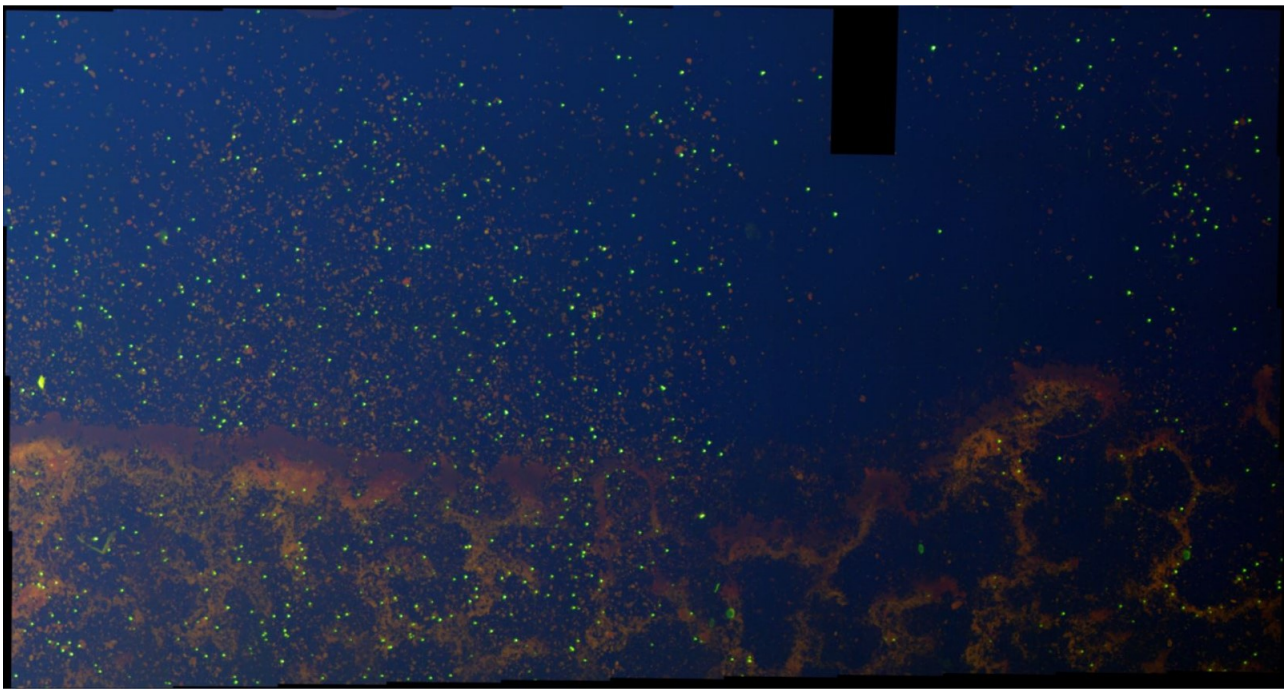

Figure 5.12: Stitched fluorescent image from raw scanned images at 4x Magnification

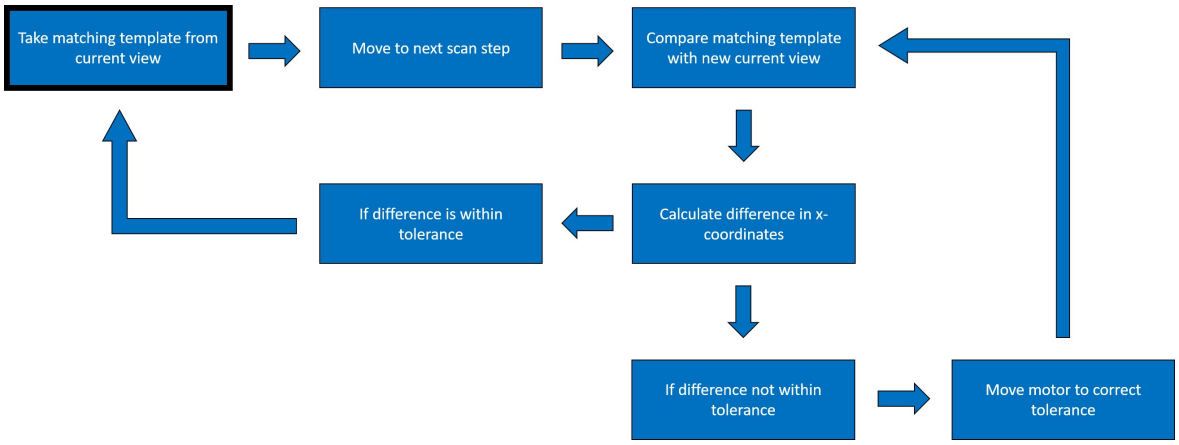

Figure 5.13: Flowchart illustrating x-y drift correction algorithm

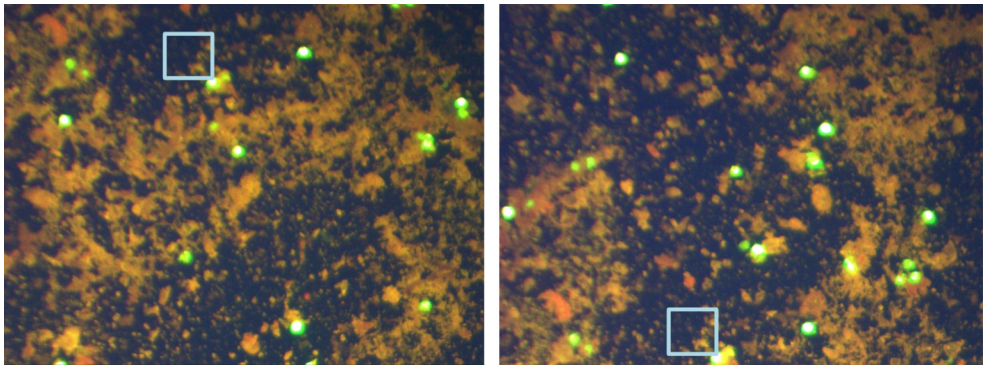

Figure 5.14: X-Y drift correction in practice for a 10x fluorescent scan. Notice the template movement between the change in images

5.8 Auto Focus

We used the tenengrad auto-focus algorithm taken from the works complied by [85]. The algorithm was mentioned in another paper by Pacheco et al. [86] in the context of bright-field microscopy, where it was found as the best among the other algorithms they evaluated.

5.9 Dynamic Z-Drift Correction

We created a very basic algorithm to correct for z-drift in the platform. This involved modelling the plane, that is being scanned, as having variable heights. It worked by going to each corners of what the stage could reach and manually adjusting the focus of the system to be in focus. The algorithm would then interpolate, based on the z-axis position of these four corners, what the focus position would probably be when it went somewhere else in the plane.

5.10 GUI Development

GUI development was developed on a functional basis: where if a function was required it was added to the GUI, such as 'Live View', 'Scan' or moving the turret or illumination slide mechanisms. Some conceptual drawings were still made for the GUI to assess positioning of certain elements but its development did not follow a more rigorous development cycle, such as the Systematic Design method used for the mechanical design, because it did not require it. As the focus of the GUI was mainly functional, simple windows forms elements were used for buttons and the file menu.

5.10.1 Live View Mode

The live view mode is accessible through the operations tool strip menu and it is the main way a user can see a live view of the sample. The concept sketch for its layout can be seen in Figure 5.15

Figure 5.15: GUI - Live view mode layout concept sketch

which shows the idea of having movement-buttons on the right and a large live view panel on the left. The final layout can be seen in Figure 5.16. A user presses the 'Start Live View' button and, provided the camera is connected, a live view feed will begin to display. The 'Enable Stage Control' button gives the user control of the motors in the system through a series of buttons below it. These buttons are listed as follows:

- 'W', 'S', 'A' and 'D' keys control the x and y-axis translation of the stage
- F and G keys control the movement of the stage in the z direction
- 'FL Cube' and 'B Splitter' control whether the fluorescence cube or beam-splitter is selected respectively
- 'Rotate Turret' moves the turret 90°
- 'Fluorescence', 'Bright-field', 'Laser' moves the illumination slide to the chosen illumination mode

5.10.2 Scan Mode

The scan mode is also accessible through the operations tool strip menu. This is the mode where a user can choose to scan the sample. The concept sketch for its layout can be seen in Figure 5.17 and the final layout can be seen in Figure 5.18. The layout of this mode is mainly the same as 'Live View Mode' but with the addition of the scan feature below. It works by getting the user to

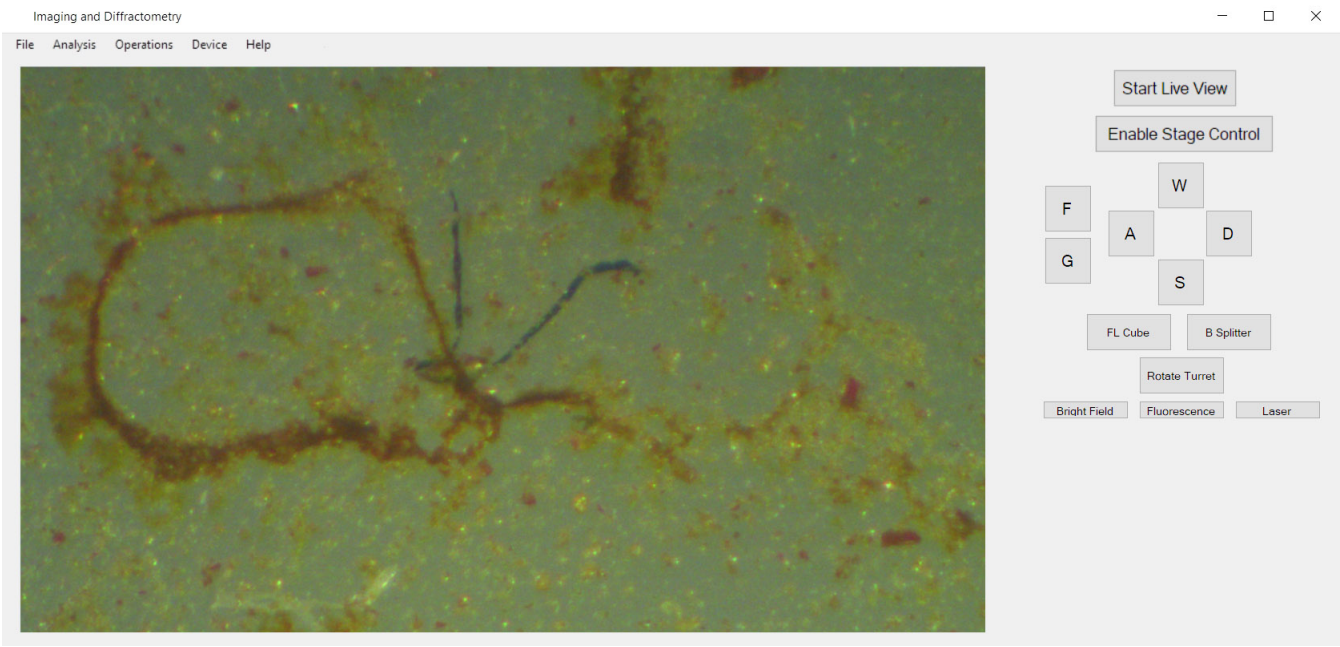

Figure 5.16: GUI - Live view mode layout

go through and select four approximate corners that they want scanned. As they select a corner the user presses 'Set' and then a thumbnail appears to let the user know that their corner choice has been registered. When they have selected their four corners, they then press 'Scan' and the system starts scanning the slide. The algorithm is summarised here:

1. User selects four corners of the area that they want to scan
2. They select the magnification currently set
3. Press scan. Based on the magnification set, the scan will calculate the step size and number of steps to take
4. Scan will run through the steps and complete the required scan

5.10.3 Camera Display Parameters

Both the live view and scan mode load the camera parameters that appear by default when using the 'Optimal colours' mode of the uEye cockpit software for bright-field, fluorescence and ambient illumination. For laser diffraction mode, the settings were changed to be less sensitive to light by reducing the gain. This is because the laser beam produced much higher irradiance than the other forms of illumination. The two files used can be found in the Github page [116] associated with this research.

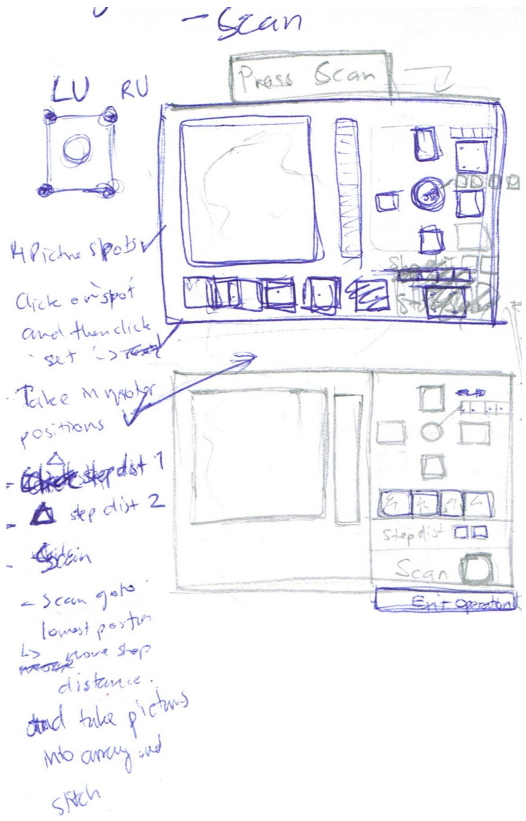

Figure 5.17: GUI - Scan mode layout concept

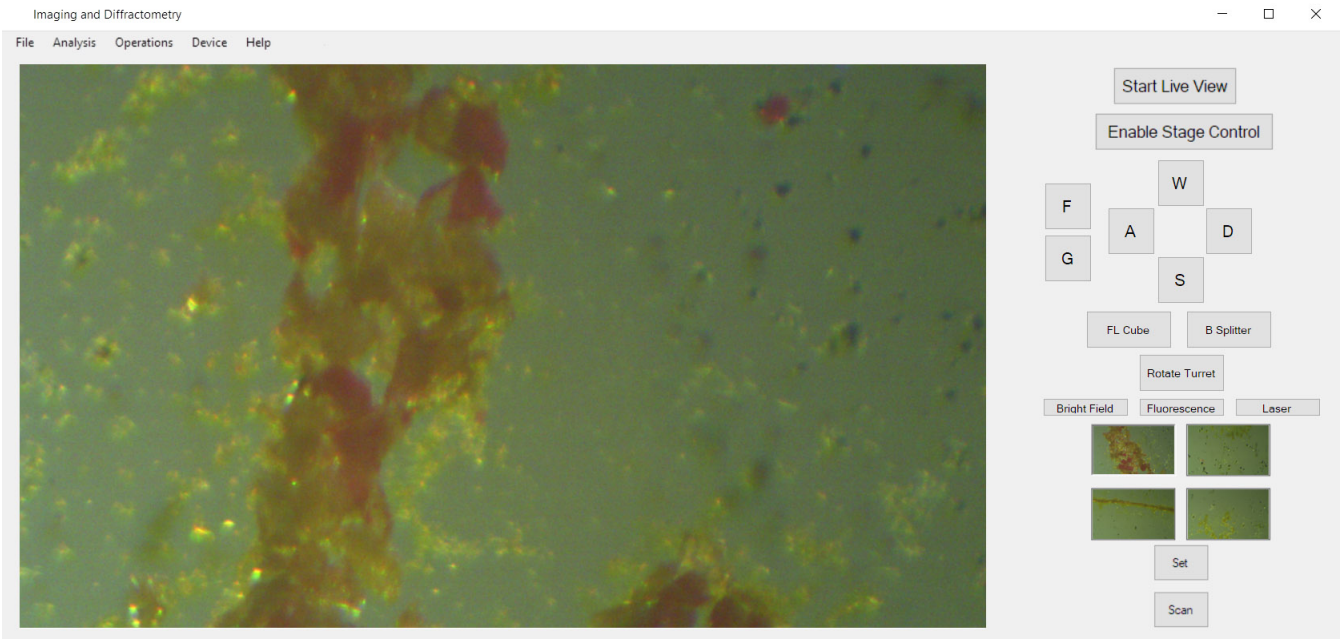

Figure 5.18: GUI - Scan mode layout

5.11 Discussion

Several development environments could have been chosen to develop the software but C# was found to be used consistently and had a lot of libraries written for it, including wrappers from other environments, so we chose to use it. This decision was also guided by our choice of camera which used C# libraries.

Following from the literature review, it was undecided on what image stitching tool to use. A test was therefore devised to stitch images that consisted of both bright-field and fluorescence illumination taken from our system by the three stitching tools discussed. We assessed the stitched images produced by four measures: proper image alignment, smoothness of seam blending, number of images stitched and how long it took to stitch. ImageJ was the poorest stitching tool with respect to the parameters and stitching mode we used: it did not produce an aligned image. For the remaining two, Microsoft's Image Composite Editor performed better than EmguCV in all four categories of assessment. It is true that EmguCV was faster than ICE, but that cannot really be counted as it was stitching around 8% of the images that ICE had stitched for bright-field and 31% of the images ICE had stitched for fluorescence. It was also found that a small improvement was made to the number of stitched images from EmguCV by changing the 'PanoConfidenceThresh' feature from 1.0 to 0.5. From the results of the test, it was therefore decided to use ICE as the stitching tool for stitching images for this work.

It was decided that the main image processing tools used would be the Aforge library and, if required, EmguCV. This was because, in the literature review, it was found that where both had been used, Aforge was used mainly for image processing and EmguCV for data processing. As our application required basic image processing tasks then we could use the libraries the same way.

Aforge libraries were used for the tasks of particle counting, particle area estimation and perimeter estimation. Particle counting was applied at counting the fluorescent spherical particles inside the fluorescent images produced. The 'HSL Filtering' class was used to isolate the fluorescent green parts of the image and then the 'blob counter' class was used to find the number of particles in the isolated image. Particle area estimation was also done with the 'blob counter' class but in conjunction with the 'blob' class that can estimate the area of a specific blob. Perimeter estimation of a blob was done by counting the pixels of a blob and, by interpolating from an object of known size, working out what each pixel represents as a measurement.

We found that the scanning routine produced a drift that was evident in the final stitched image. We sought to correct this by using EmguCV's matching template. A template of one part of the image was compared against the image from the next scan step. If there was a difference in the x direction, the motor was moved to correct for this difference.

Autofocus was done with the tenengrad algorithm and z-drift was accounted for with a basic algorithm that modelled the plane being scanned with variable heights relating to the four corners, or limits, of the plane. Interpolation of the z-axis was then used for any coordinates inside the area of the four corners.

The GUI for the system was developed through initial concepts but mainly through a functional basis where, if a feature was required, it was implemented. There were two distinct modes that ran off the same GUI: live view mode and scan mode. The scan mode worked by taking a user input of the four corners of the desired scan area and working out the steps to scan that particular area.

Camera view parameters for the uEye camera were saved from the 'Optimal Colours' mode for bright-field, fluorescence and ambient illumination. Laser diffraction had its gain reduced because of its much higher irradiance than the other forms of illumination.

CHAPTER 6

RESULTS

In this chapter we present the stitched bright-field, fluorescent and ambient images from the micro-imaging system at 10x and 4x magnification. We also also present images of biological samples from ESR, taken at 20x magnification, to characterize the system in an industrial application. The quality of the images will be assessed on two criteria: sharpness and noise. Justification for how these quality measurement methods will be implemented are discussed in Section 6.1. We will also assess the performance of algorithms, that were both developed and also ones that came from libraries, to achieve a better quality image as compared to without using them. Additionally, we have made Section 6.2 in this chapter to the sample preparation of the Dragon Green FS07f fluorescent microspheres catalyzed with bromophenol blue.

6.1 Image Quality Measurement Methods

6.1.1 Sharpness

The sharpness was measured using gray-level local variance method. This was proposed by Pech-Pacheco et al [86] and summarized in the work of Pertuz et al. [85]. The method, in the context of auto-focusing, was demonstrated in the field of automated bright-field microscopic imaging for use in diatom detection. Its proven practical application in microscopy further helped in selecting it for measuring the sharpness in our micro-imaging system. The higher the value the better the sharpness.

6.1.2 Noise

The noise was measured using a noise level estimation method proposed in [117] and [118]. The method is a patch based noise level estimation algorithm that can estimate noise levels for the

three colour channels: Red, Green and Blue. For our measurements, the image size of 2560 x 1920 produced by the EO-5012C was too large to process so sub-sampling of half the image size was used instead. The lower the number the lower the amount of noise in the image.

6.2 Dragon Green Sample Preparation

The sample was prepared with Bangs Laboratories Dragon Green FS07f Fluorescent Microspheres mixed with bromophenol blue. The bromophenol blue was used because it turns yellow at a low pH which is useful because the Nikon B-2A filter cube only filters out light after 515nm so therefore will pick up the yellow colour of the sample. The fluorescent microspheres we used specifically had a mean diameter of 15μm and were contained in a 1mL container. The sample was prepared by first putting in 1-2μL of the microspheres, taken with a Thermoscientific fine pippette, onto a standard microscope slide. Next 1mg of bromophenol blue was measured and put on the 1-2μL of microspheres that were put on the slide. Finally, the two were then mixed together using tweezers and another sample slide was put on top to sandwich the sample together.

6.3 Bright-field 10x Magnification

6.3.1 Speed, Size and Field of View

The stitched image at 10x magnification with bright-field illumination can be seen in Figure 6.1. The image is of a printed paper with lines spaced 0.5mm apart and consists of 107 images that cover an area of approximately 46mm^2 (7.83mm by 5.87mm). It took approximately 4 minutes to complete the scan and an additional 7 minutes and 4 seconds to stitch the images together.

6.3.2 Sharpness

The sharpness of the image was measured to be 10.4014.

6.3.3 Noise

The noise of the RGB channels of the image are as follows:

- Red = 0.0000 + 0.0000i
- Green = 0.0000 + 0.0000i
- Blue = 0.0757 + 0.0000i

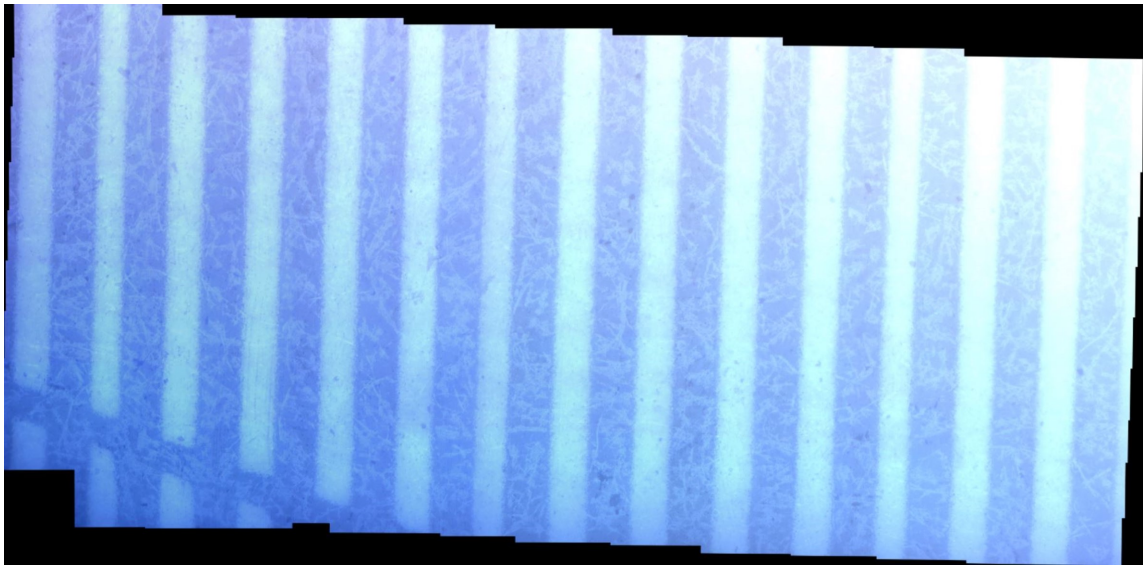

Figure 6.1: Stitched bright-field image of raw scanned images at 10x magnification

6.4 Bright-field 4x Magnification

6.4.1 Speed, Size and Field of View

The stitched image at 4x magnification with bright-field illumination can be seen in Figure 6.2. The image is of nickel-5% aluminium powder, consisting of 21 images and covering an area of approximately 104mm^2 (13mm by 7.96mm). It took approximately 1 minute and 2 seconds to complete the scan and an additional 48 seconds to stitch the images together.

6.4.2 Sharpness

The sharpness was measured to be 359.4564.

6.4.3 Noise

The noise of the RGB channels of the image are as follows:

- Red = 0.1115
- Green = 0.1475
- Blue = 0.0538

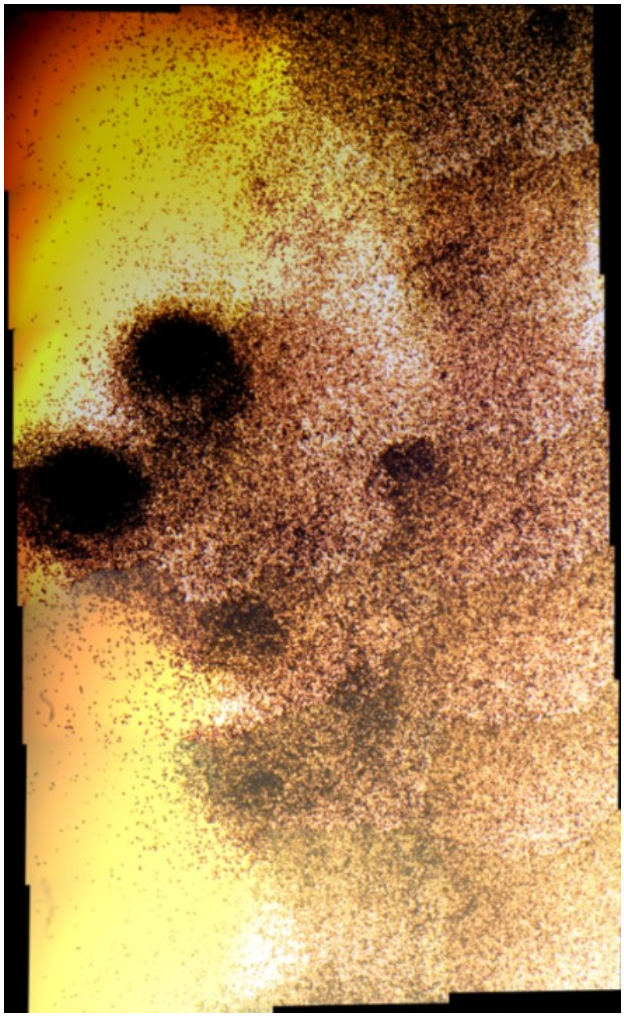

Figure 6.2: Stitched bright-field image of raw scanned images at 4x magnification

6.5 Fluorescent 10x Magnification

6.5.1 Speed, Size and Field of View

The stitched image at 10x magnification with fluorescent illumination can be seen in Figure 6.3. The image is of Bangs Laboratories Dragon Green polystyrene microspheres, mixed with bromophenol blue, and consists of 264 images that cover an area of approximately 62.58mm^2 (10.43mm by 6mm). It took approximately 9 minutes to complete the scan and an additional 25 minutes to stitch the images together.

6.5.2 Sharpness

The sharpness was measured to be 95.0206.

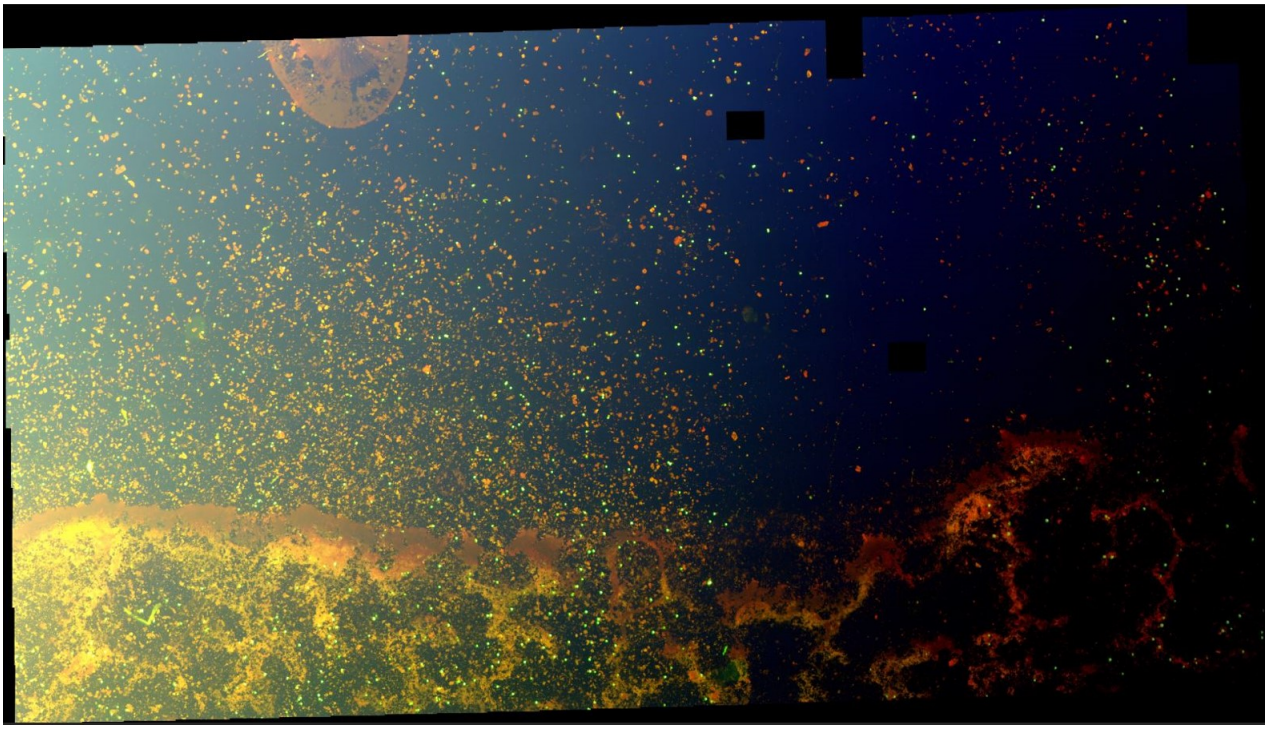

Figure 6.3: Stitched fluorescent image from raw scanned images at 10x Magnification

6.5.3 Noise

The noise of the RGB channels of the image are as follows:

- Red = 0.0411
- Green = 0.1323
- Blue = 0.1370

6.6 Fluorescent 4x Magnification

6.6.1 Speed, Size and Field of View

The stitched image at 4x magnification with fluorescent illumination can be seen in Figure 6.4. The image is of Bangs Laboratories Dragon Green polystyrene microspheres, mixed with bromophenol blue, and consists of 44 images that cover an area of 60.43mm^2 (10.64mm by 5.68mm). It took approximately 1 minute and 38 seconds to complete the scan and an additional 1 minute to stitch the images together.

6.6.2 Sharpness

The sharpness of the image was measured to be 111.7372.

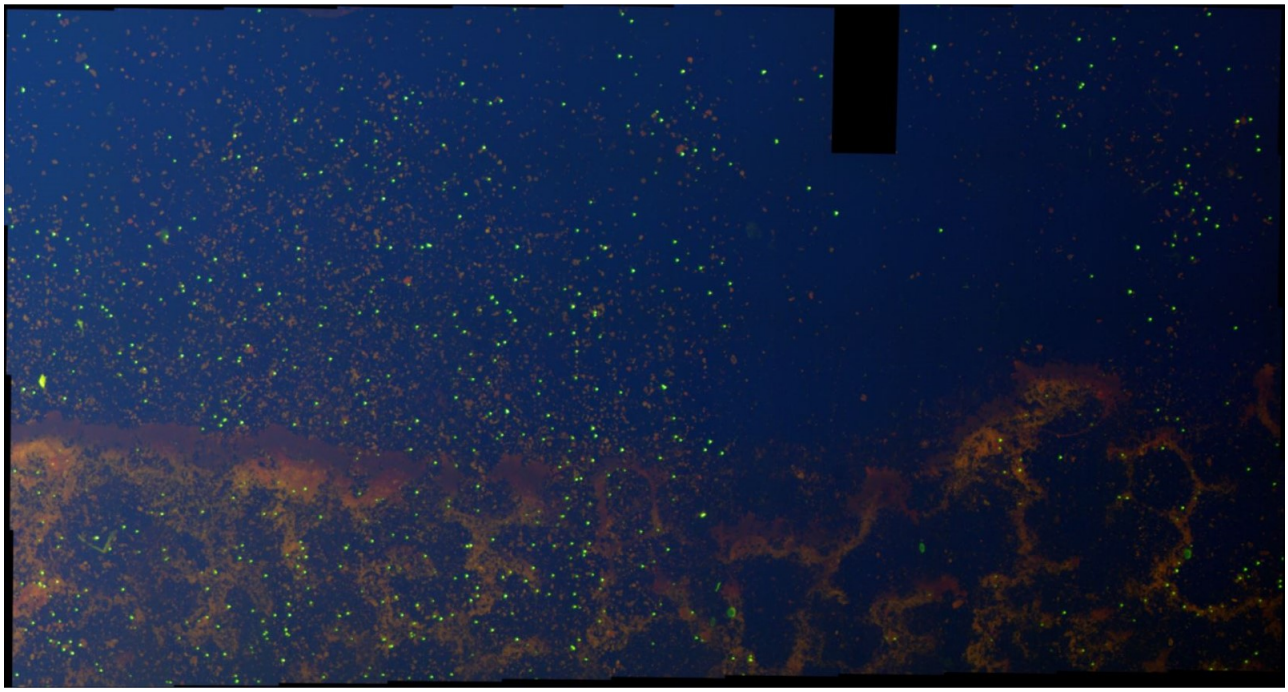

Figure 6.4: Stitched fluorescent image from raw scanned images at 4x Magnification

6.6.3 Noise

The noise of the RGB channels of the image are as follows:

- Red = 0.7619
- Green = 0.6924
- Blue = 0.8980

6.7 Ambient 10x Magnification

6.7.1 Speed, Size and Field of View

The stitched image at 10x magnification with ambient illumination can be seen in Figure 6.5. The image is of Bangs Laboratories Dragon Green polystyrene microspheres, mixed with bromophenol blue, and consists of 872 images that cover an area of 80.78mm^2 (10.8mm by 7.5mm). It took approximately 32 minutes and 27 seconds to complete the scan and an additional 100 minutes to stitch the images together.

6.7.2 Sharpness

The sharpness was measured to be 84.1871.

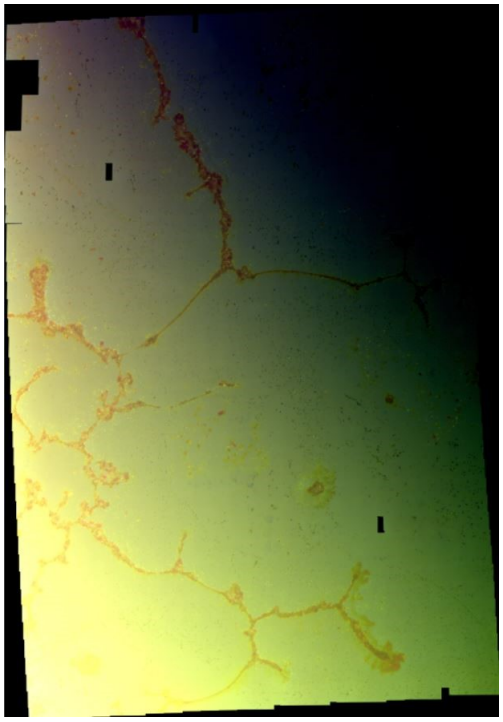

Figure 6.5: Stitched ambient image from raw scanned images at 10x Magnification

6.7.3 Noise

The noise of the RGB channels of the image are as follows:

- Red = 0.6789
- Green = 0.6396
- Blue = 0.8482

6.8 Ambient 4x Magnification

6.8.1 Speed, Size and Field of View

The stitched image at 4x magnification with ambient illumination can be seen in Figure 6.6. The image is of Bangs Laboratories Dragon Green polystyrene microspheres, mixed with bromophenol blue, and consists of 30 images and covers an area of 39.17mm^2 (6.39mm by 6.13mm). It took approximately 1 minute and 14 seconds to complete the scan and an additional 39 seconds to stitch the images together.

6.8.2 Sharpness

The sharpness was measured to be 84.2831.

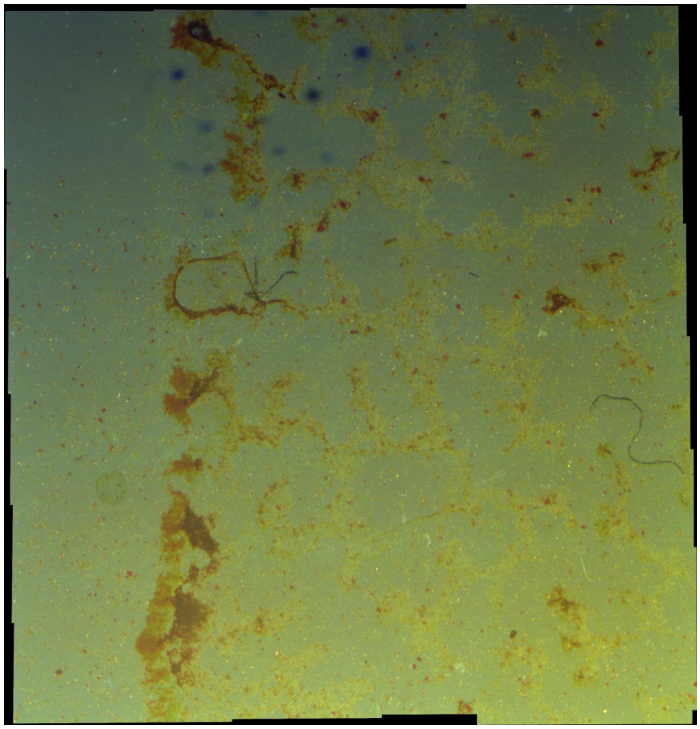

Figure 6.6: Stitched ambient image from raw scanned images at 4x Magnification

6.8.3 Noise

The noise of the RGB channels of the image are as follows:

- Red = 0.6947
- Green = 0.6426
- Blue = 0.8468

6.9 Nikon LV100ND Desktop Microscope

This section details images taken from the Nikoon LV100ND desktop microscope that were used as a benchmark against which images produced from the micro-imaging system could be compared. The light used was a Nikon DSRi2 and the images were taken at 20X magnification of the Dragon Green sample.

6.9.1 Speed and Size

The final stitched image can be seen in Figure 6.7 and is comprised of 29 images with a size of 39mb. As this was not an automated microscope, it took approximately 22 minutes and 34 seconds

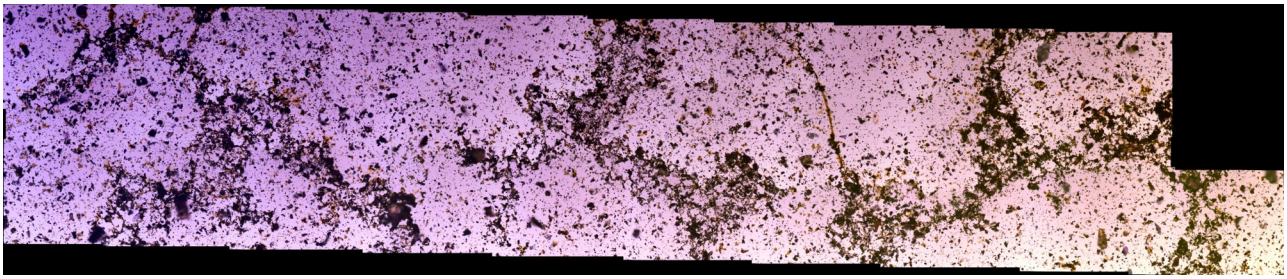

Figure 6.7: Nikon LV100ND stitched image from raw scanned images at 20x Magnification

to scan 29 images. Using Microsoft Image Composite Editor the images took approximately 41 seconds to stitch.

6.9.2 Sharpness

The sharpness of the image came out as 319.311

6.9.3 Noise

The noise of the RGB channels of the image are as follows:

- Red = 0.6385
- Green = 0.4182
- Blue = 0.8643

6.10 ESR

This section details the industry application of the system. It deals with imaging samples from the Institute of Environmental Science and Research (ESR) prepared by Amelia Gamblin (BSc. MSc.) who is a scientist working at ESR. The specific objective was to characterize the images produced by the current system with the samples prepared. Preparation of the samples is described in Section 6.10.1 by Amelia Gamblin.

6.10.1 Sample Preparation

6.10.1.1 Slides

The slides have been prepared according to the ESR standard operating procedures. They contain biological material that has been stained and set under a coverslip. The specimen on the slides may contain a combination of semen, buccal cells, vaginal cells and/or blood (human or pig blood).

The stain used is Christmas tree stain and consists of:

1. Nuclear Fast Red Stain: Aluminium sulphate, nuclear fast red and distilled water
2. Picroindigo carmine: Picric acid, indigo carmine and distilled water

Entellen has been used as a mountant to seal the coverslip onto the slide.

6.10.1.2 Specimen Stain

The stain uses Nuclear Fast Red to stain nuclear material. The counterstain is indigo carmine (blue) and picric acid (stains protein yellow). Generally, sperm heads stain a brilliant crimson with the head region being paler than the tail region. The tail stains blue-grey/green. In a few instances some sperm stain purple, in which case the contrast with epithelial cells is reduced. This is more likely to happen when there are very large amounts of sperm present. Epithelial cell staining can be quite variable, even within one preparation. The cytoplasmic colours range from translucent shades of apricot to blues, purples and greens. The nuclei stain pale red to purple, sometimes blue. The variation in staining seems to be unavoidable.

6.10.2 Image characterization

The images were illuminated with bright-field illumination. As we were imaging sperm, which have a general size of 50μm, we therefore used a 20X objective lens. It would have been better to use the 40X objective lens, however it was not able to be used because the inverted design does not allow the use of any objectives with a working distance less than the thickness of the cover-slip: 1mm. The following shows the sharpness and noise of the three kinds of samples we were given: Christmas tree stain, nuclear fast red stain and no stain.

6.10.2.1 Christmas Tree Stain (CTS)

The stitched image of the sperm samples stained with christmas tree stain can be seen in Figure 6.8.

6.10.2.1.1 Image Sharpness

The image sharpness was measured to be 6.3756.

6.10.2.1.2 Noise The noise of the RGB channels of the image are as follows:

- Red = (0.0000 + 0.3159i) x 10^{-4}
- Green = (0.0000 + 0.0000i) x 10^{-4}
- Blue = (0.0000 + 0.0000i) x 10^{-4}

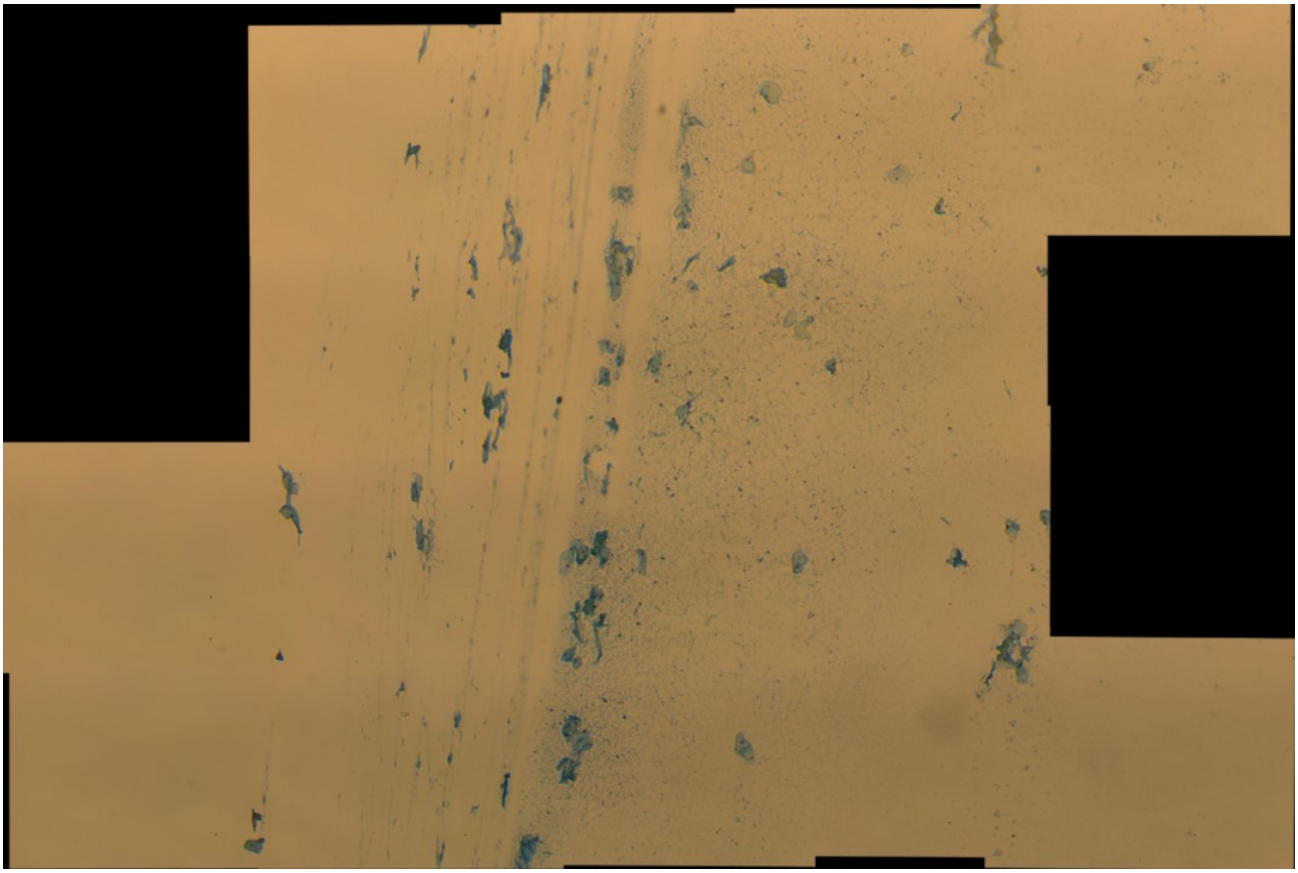

Figure 6.8: Stitched raw bright-field image of ESR samples stained with christmas tree stain at 20x magnification

6.10.2.2 Nuclear Fast Red Stain

The stitched image of the sperm samples stained with nuclear fast red stain can be seen in Figure 6.9.

6.10.2.2.1 Image Sharpness

The image sharpness was measured to be 26.4989.

6.10.2.2.2 Noise

The noise of the RGB channels of the image are as follows:

- Red = 0.1636
- Green = 0.1657
- Blue = 0.1964

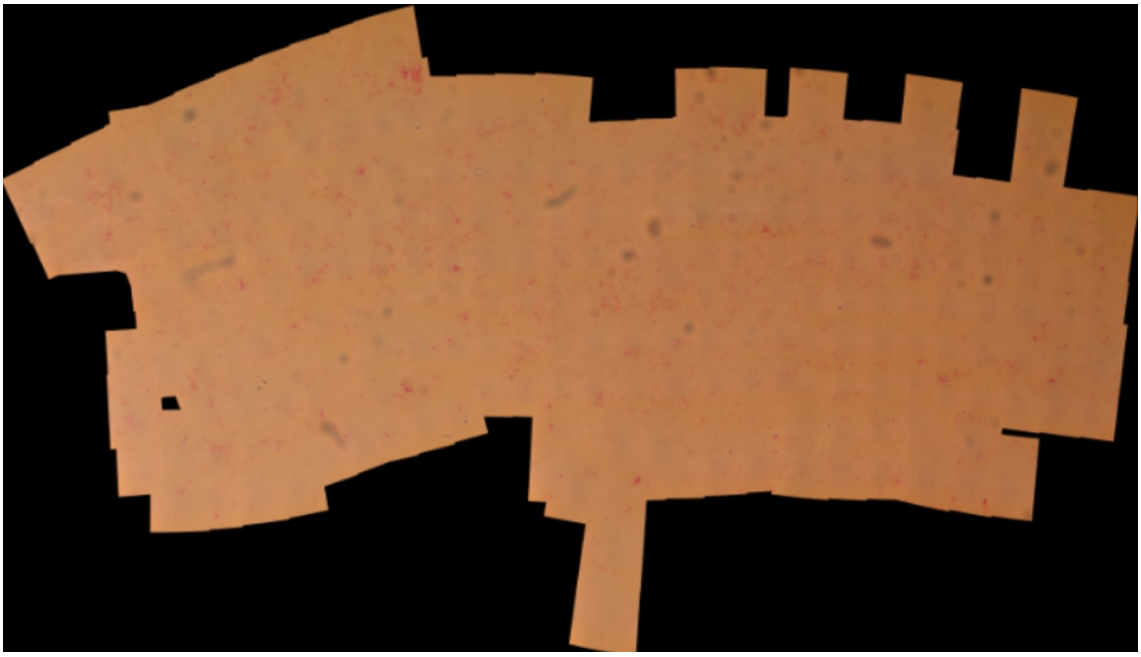

Figure 6.9: Stitched raw bright-field image of ESR samples stained with nuclear fast red stain at 20x magnification

6.10.2.3 No Stain

The stitched image of the ESR samples with no stain can be seen in Figure 6.10.

6.10.2.3.1 Image Sharpness

The image sharpness was measured to be 16.6934.

6.10.2.3.2 Noise

The noise of the RGB channels of the image are as follows:

- Red = (0.0000 + 0.2287i) x 10^{-4}
- Green = (0.0000 + 0.0000i) x 10^{-4}
- Blue = (0.0000 + 0.0689i) x 10^{-4}

6.11 Laser Diffraction

Laser diffraction was done with a Edmund Optics EO-1918C 1/1.8" CCD Colour USB Camera. We used this camera instead of the EO-5012C because it has a larger sensing area so was able to pick up more diffracted modes. We used the GH25-12V 1200/mm holographic reflective diffraction grating from Thorlabs and it produced the diffracted modes seen in Figure 6.11.

Figure 6.10: Stitched raw bright-field image of ESR samples with no stain 20x magnification

6.12 Stitching

6.12.1 Speed

Microsoft Image Composite Editor is able to stitch 312 images each at 2560 x 1920 resolution in 30 minutes producing a 120mb stitched image. The application also produced empty blocks within the final stitched image, seen in Sections 6.5, 6.6 and 6.7 as well as in all the ESR final stitched images.

6.13 System Performance

6.13.1 Scan Speed

The scan speed was on average 2.13 seconds per image.

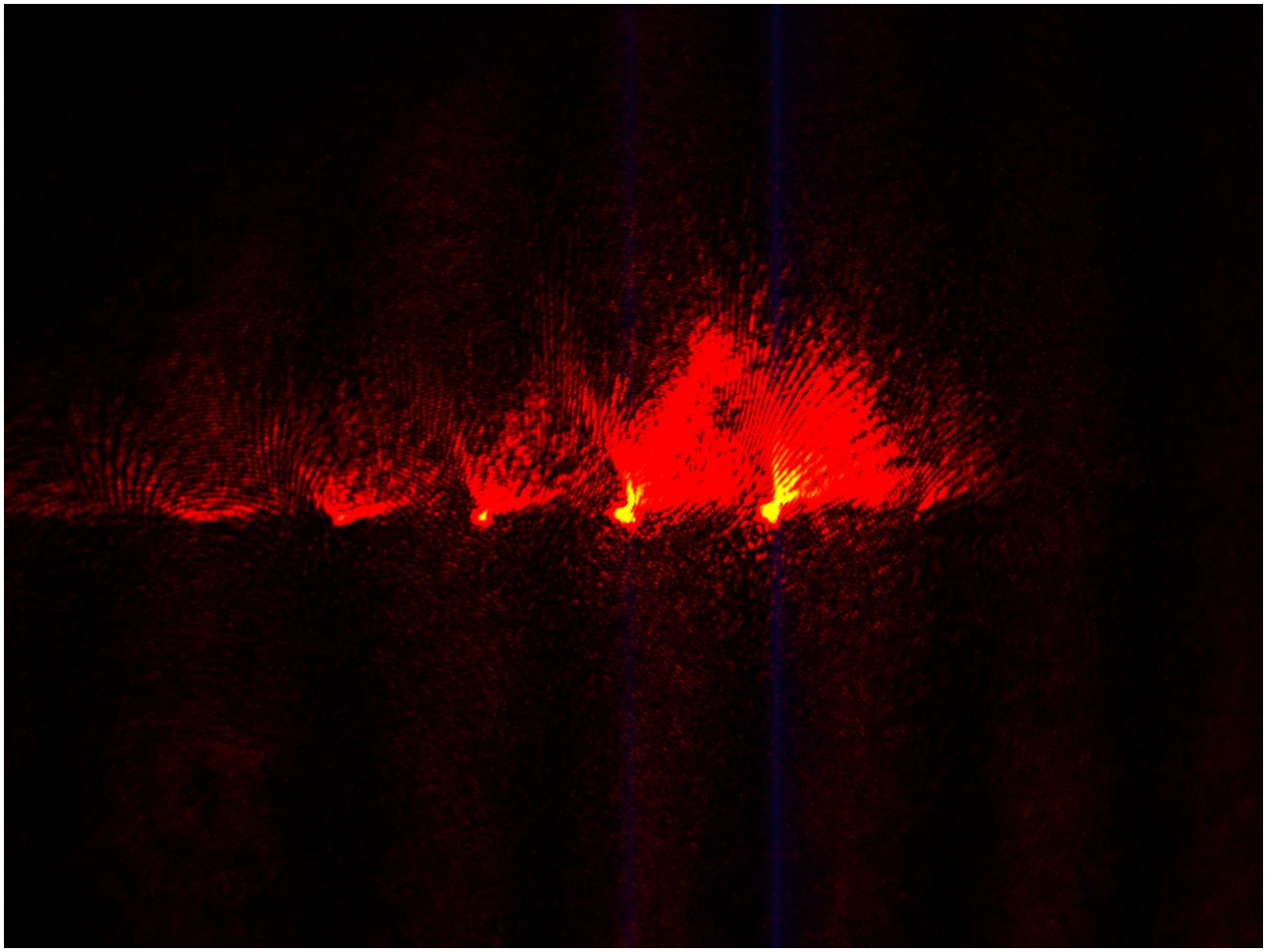

Figure 6.11: Image of diffracted modes seen on EO-1918C Camera using 40X objective lens with 0.65NA

6.13.2 Stage Responsiveness

In the context of live view, the stage was responsive to the directions it was moving. The stage started moving immediately and there was no noticeable delay.

6.13.3 Portability

The system utilized folded optics making it compact and a battery to allow to have the ability to be used in the field. The system was able to successfully work with the battery and managed to operate for 3-4 hours at a time.

6.13.3.1 Size

The size of the system was 167mm x 180mm x 250mm which is still comparably smaller than most desktop systems. This compactness greatly contributes to the systems portability.

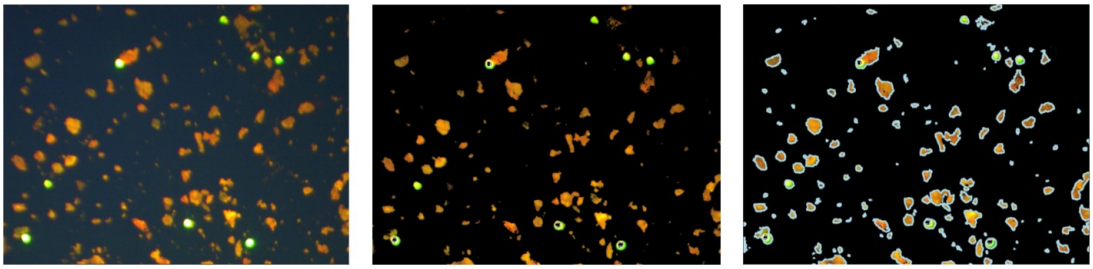

Figure 6.12: Example of blob counter class, from Aforge framework, counting particles displayed as light blue outline

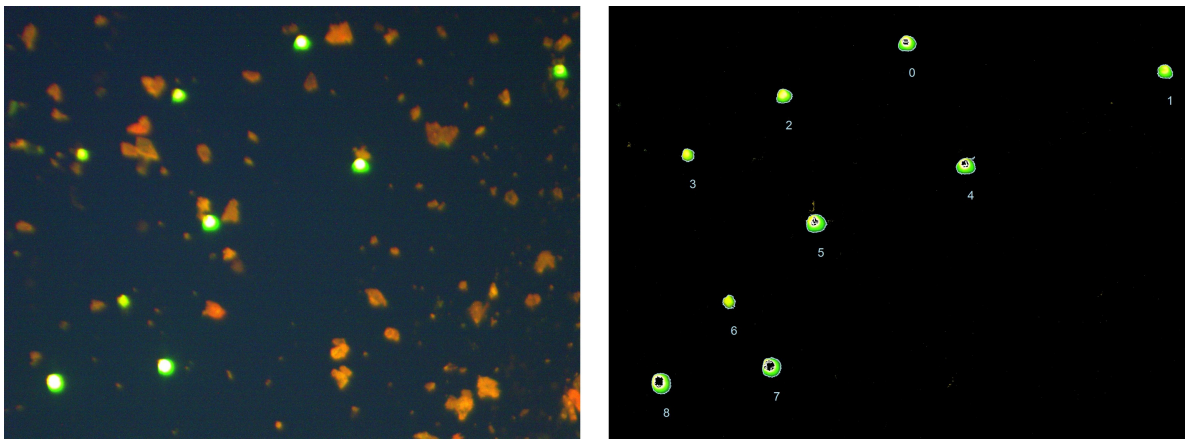

Figure 6.13: Isolation of green fluorescent particles in image. Note the count starts at 0

6.14 Algorithm Performance

6.14.1 Particle Counting and Particle Concentration

The blob counter class from the Aforge framework was able to successfully count the particles. An example is shown in Figure 6.12 where it shows the particles being highlighted with a light blue outline for a fluorescent image at 10x magnification. The particle concentration of the fluorescent microspheres was able to be successfully determined and can be seen in Figure 6.13.

6.14.2 Particle Area Estimation

The area estimation algorithm counts the number of pixels inside a particle. We knew that the FS07f fluorescent microspheres were 15μm in diameter which means their area would be approximately $1.767 \cdot 10^{-4}$mm^2. Within the context of our calibration method, our measurements of several fluorescent microspheres' area could at best get to $3.14 \cdot 10^{-4}$mm^2 which is within 78% of the real value.

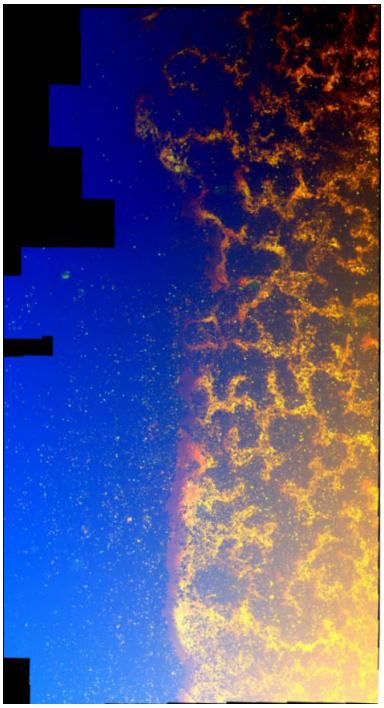

Figure 6.14: Stitched image from x-y drift corrected scanned images

6.14.3 Perimeter Size Estimation

The perimeter size estimation counted the number of pixels around a particular particle. We knew that the FS07f fluorescent microspheres were 15μm in diameter which means their perimeter would be approximately 0.047123mm. Counting the pixels, we produced a range of perimeters ranging from 0.068mm to 0.091mm. Within the context of our calibration method, we estimate that the perimeter size estimation algorithm is accurate to within 44% at best.

6.14.4 Scan Algorithm

The scan algorithm was able to successfully scan the area required. The standalone scan accumulated error and we address this error in Section 5.7 with the x-y drift correction algorithm.

6.14.5 X-Y Drift Correction

The X-Y drift correction algorithm successfully corrected the x and y drift of the images. It did this to the extent that the final stitched image looked very rectangular with minimal effects of drift present (see Figure 6.14).

6.14.6 Z-Axis Mapping/Z-Drift Correction

Mapping the interpolated z-axis values by first going to each corner and focusing the image has worked well for our design. The auto-focus did not have to work as hard to achieve a focused image so it saved time.

6.14.7 Auto-focus

The algorithm performed well and brought the sample to a focus as expected.

CHAPTER 7

DISCUSSION

In this chapter, we discuss our image quality results in Chapter 6 in comparison to other research and commercial based systems, performance of algorithms and also limitations and suggested improvements of the system.

7.1 Overall System Capacity

The system is able to output images at bright-field, fluorescence and ambient illumination as well as do laser diffraction. It can change magnification through a turret system that has the capacity to hold four objective lenses. It has an automated x, y and z-axis and can scan a sample slide over a maximum area of approximately 131mm^2.

7.2 Image Quality

7.2.1 Sharpness

7.2.1.1 Bright-field vs Fluorescence vs Ambient

As shown in the results section, the bright-field image at 4x magnification was ranked as having the highest sharpness, of 359.4564, and the image at 10x magnification was at 10.4014. The large difference in sharpness measures between the magnifications is because they image different samples. The sample imaged at 4x has much stronger contrast and so naturally produces a higher sharpness score. Comparing fluorescence and ambient illumination we image the same type of sample. Here the average fluorescent sample sharpness score of 103.38 is 22.73% higher than the average ambient sample sharpness score of 84.2351. This could be because in fluorescence illumination, a set wavelength band is filtered to the camera so the areas that are not the

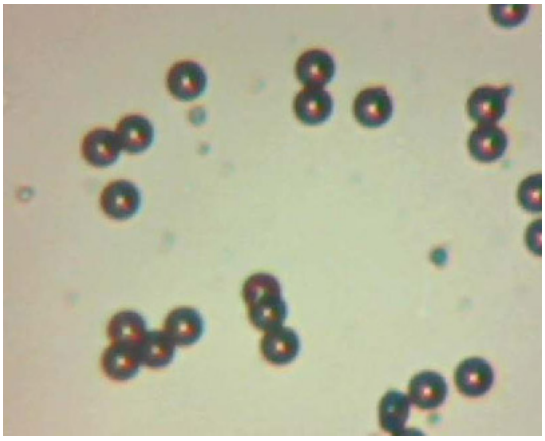

Figure 7.1: Bright-field image from [19]

sample are usually black. The black, combined with the fluorescent particles, produces a much more vivid contrast than the ambient therefore would have a better sharpness score. One other notable aspect of the images is that the ambient illumination is the one with the most consistent sharpness score in the context of different magnifications. The sharpness scores only differ by about 0.1% of each other. The reason for this could be because the ambient illumination came into the objective much more evenly, unlike bright-field and fluorescence which had to use a condenser lens to achieve a collimated beam.

7.2.1.2 System vs Comparable Research Systems

In comparison to multi-modal research level microscopes that were discussed in the literature review, we measured the sharpness of their images and compared against our images. The first being the one developed by students at the University of British Columbia [19]. The bright-field image can be seen in Figure. 7.1 and the fluorescence image can be seen in Figure. 7.2 The bright-field image was measured to have a sharpness of 39.9021 and the fluorescent image was measured to have a sharpness of 8.3162. From these results, we can see that the sharpness of the images produced by our system has a higher score. The reason for this could be that our system uses more standard optical components, notably a better camera and standard objective lens, whereas in their system, they use a webcam to image the samples and the lens from the optical drive to magnify the image.

7.2.1.3 System vs Standard Desktop Microscope

In comparison to modern microscope systems, we took the example of the same sample we used for fluorescence seen in Figure 6.3, and imaged it with a Nikon LV100ND microscope. The image came out as per Figure 6.7 with a sharpness score of 319.311. Clearly, the sharpness of the images coming out of the desktop microscope are better by at least three times when compared to the

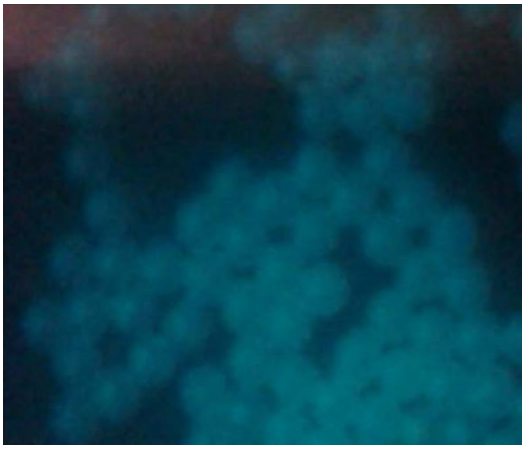

Figure 7.2: Fluorescence image from [19]

images of the same type of sample. This result is clearly attributable to the fact that a standard desktop microscope has been manufactured and aligned to a much higher standard than the micro-imaging system made in this research so will naturally have a higher sharpness.

7.2.2 Noise

7.2.2.1 Bright-field vs Fluorescence vs Ambient

The image that had the highest amount of noise in all channels was the one imaged at 4x magnification using fluorescence illumination. The reason for this level of noise could be that the objective had a smaller numerical aperture so naturally took in less light. Additionally, as it was using fluorescence illumination, the light that reached the sensor had already undergone wavelength filtering, by the filter cube, so could have also contributed to the reduced amount of light on the sensor. Reduction in the light would have caused the camera to automatically adjust its ISO value meaning that the final image seen would have more noise. Another notable observation, similar to the sharpness values, is that the noise of the ambient images only differs by a maximum of 0.5%. As stated in Section 7.2.1.1, the reason for this could be that the ambient light comes into the objective much more evenly than the bright-field and fluorescence illumination so would produce a more evenly illuminated image.

7.2.2.2 System vs Comparable Research Systems

In comparison to multi-modal research level microscopes that were discussed in the literature review, we measured the noise of their images and compared against our images. The first being the one developed by students at the University of British Columbia [19]. The bright-field image can be seen in Figure. 7.1 and the fluorescence image can be seen in Figure. 7.2. The bright-field image was measured to have RGB noise levels of 0.0587,0.0584 and 0.0537 respectively and the fluorescent image was measured to have RGB noise levels of 0.1352, 0.1615 and 0.2240. From

these results, we can see that the images from our system have similar or better noise levels for bright-field or fluorescent illumination at 10x magnification but higher noise levels than their system for 4x magnification. The reason for this could be that different results are achieved with different types of samples: our system images fluorescent microspheres mixed with bromophenol blue whereas they image microbeads. Samples with more concentration of particles, such as the one of bright-field at 4x magnification, also produced higher noise levels.

7.2.2.3 System vs Standard Desktop Microscope

The Nikon microscope produced RGB noise levels of 0.6385, 0.4142 and 0.8643 respectively. Compared to the noise levels of images from the same sample, fluorescence generally has less noise at 10x magnification and relatively the same at 4x magnification - except for the green channel where the Nikon microscope has less noise. Ambient illumination seems to be somewhat equal in its level of noise for both 10x and 4x magnification. The reason for fluorescence at 10x magnification having less noise could be because less particles seem to be focused as compared to the Nikon image so naturally would produce higher noise levels.

7.2.3 Stitching

The stitching was done with the Microsoft Image Composite Editor software application after it was found to be the best application to use in comparison to EmguCV and ImageJ in Section 5.2.1. Using this application meant that the entirety of the alignment and composition was done with it. For the majority of the final stitched images, the individual images used for stitching managed to stitch properly producing well aligned images. However, as can be seen in Sections 6.5, 6.6 and 6.7 as well as all the ESR stitched images, the final stitched image also had empty blocks where some individual images failed to stitch. The empty blocks could have occurred because those images that were not there may have had less prominent features so the application was not able to match them with features from other nearby images. Less prominent features are most present in the ESR samples which also suffered from the most amount of empty blocks showing a correlation between having less prominent features in individual images and not being able to stitch those same images.

7.3 System Performance

7.3.1 Portability

The system used a 12V 5200mAh battery. It allowed the system to work within a range of 3-4 hours. In comparison to other systems, such as the one developed by [90] where they used two AA batteries, our system uses a much bigger battery. This is mainly because we have more sources that use power, namely the five stepper motors and the the three light sources. This is

disadvantageous because it uses more power, but the advantage is that the stage is completely automated, able to use brighter LED's and can also do laser diffraction.

7.3.2 Scan Speed

The scan speed was on average 2.13 seconds per image. This is mainly in part because using the EO-5012C camera had a refresh rate of 4.4fps and it was able to stabilize the image after approximately 2.13 seconds. As such we kept the stabilization time to around that much allowing the images to not appear to suffer from motion blur.

7.4 Algorithm Performance

7.4.1 X-Y Drift Correction

The algorithm for the x-y drift correction corrected the drift to the extent that the final stitched image did not distinctly show the drift of the stage. Figure 6.3 shows a stitched image without x-y drift correction and Figure 6.14 shows a stitched image without it. The difference is clearly visible. Drift correction is much more accurate as the magnification decreases. This is probably because the drift accumulates error as the amount of images increases and, as with larger magnification imaging the same area, the amount of images has to naturally increase.

7.4.2 Z-Axis Mapping/Z-Drift Correction

The z-drift correction algorithm implemented allowed the auto-focus algorithm to focus in less time.

7.4.3 Auto-focus

The tenengrad algorithm used performed well and brought the sample to a focus as expected.

7.4.4 Particle Counting and Particle Concentration

The particle counting and particle concentration algorithm worked successfully. Particularly, the particle concentration was most likely successful because of the simplicity in isolating the hue for fluorescent images. This may not be the case for other biological samples imaged in, say, bright-field illumination.

7.4.5 Particle Area and Perimeter Estimation

Both of these algorithms were not accurate in determining the size of the 15μm fluorescent microspheres. The reason for this could be that our calibration method for determining the

pixel:mm measurement was not accurate and using a more robust method such as measuring the USAF test target, seen in works such as [19], would improve these estimations.

Another reason could be that the microspheres were not consistently the same size. This could be a valid reason because, as per our perimeter measurements, we were seeing a general size difference in the perimeters measured.

7.5 Systematic Design Methodology

Systematic design was successfully used to create a new design. With its flexibility, especially in the embodiment stage, it can be used to create new novel solutions for research directions. In Section 3.3, it was discussed that the design method could be improved with the integration of TRIZ in the concept production stage - a view paralleled by [109] who had done similar and achieved a successful result. In their work, the integration of TRIZ reduced design time by making the process of finding solutions faster. They found the design time was nearly three times faster with the integration of TRIZ.

7.6 Limitations

7.6.1 Alignment

7.6.1.1 Acrylic Material

The misalignment of the system may have contributed to the quality of the images. Misalignment may have been caused by the use of acrylic for the base of the system. The acrylic base was laser cut from a VLS laser cutter that had a laser beam of thickness of approximately 0.01mm. Almost all other structures that acted to support an element, such as the filter cube/beam-splitter or illumination sources or even the objective lenses, were made out acrylic.

7.6.1.2 Bolts

Another contributor to misalignment was the use of bolts as legs for the light and beam-splitter bases. These worked by fixing the nuts to a desired length and then using them as spacers to acquire the necessary height. Although we used digital calipers accurate to 0.01mm to make sure that the nuts were at the same distance, they could have still been misaligned and caused the image to not appear as well as it could have.

7.6.1.3 Alignment of mirror

The mirror used to direct the light onto the camera had been rotated to the desired position by digital calipers and we did not have a method, or rig, to properly centre it inside the cube that it sat in.

7.6.2 Camera Sensor Area

The main camera we used was a EO-5012C camera that had a sensor size of 5.6mm x 4.2mm. This size showed its limitations when we had to use the E0-1918C camera that had a larger sensor size of 7.04mm x 5.28mm allowing us to see the modes of diffraction in laser diffraction mode.

7.6.3 Inverted Design

Ambient light, although an additional mode of illumination, may have limited the system in combination with the uncovered inverted design. When using the fluorescence illumination mode, the inverted design causes ambient light to enter which prevents a proper fluorescence image to appear on the camera. As such, when fluorescence mode was active, the system had to be in complete darkness in order for the proper image to be seen on the camera. Using the inverted design also limits the use of our system to objective lenses with working distances of 1mm or higher because the sample slide has a thickness of 1mm.

7.6.4 Calibration for Particle Size Measurements

As discussed in Section 6.13, the calibration method may have caused our size estimations to not be as accurate.

7.7 Assumptions

7.7.1 Light Irradiance

It was assumed that because the irradiance measured vs the irradiance simulated were similar, that the TracePro simulation model was accurate.

7.7.2 Motor Torque

It was assumed that the motor torque from the PL150S datasheet could translate to all other stepper motors of similar size retrieved from disk-drives. If they had less torque than was stipulated in the datasheet then they could have consumed more power.

7.8 Improvements

A number of improvements could be made to the system. The system currently uses a condenser lens in front the illumination source that then goes to the beam-splitter (or fluorescence cube). The purpose of the condenser lens is to collimate the light so that it stops it spreading and losing irradiance that could otherwise be used to illuminate the sample. An improvement to this could

be to use fibre optic cables that connect directly from the light source and go straight to the beam-splitter. This would ensure that less light is lost in the system while giving the flexibility to position the light source almost anywhere in the design.

The Z-axis achieved fine movements through the use of gears alongside a motor-controller configured for 256 micro-steps. Future designs could use a piezo-stack for even finer movements in the z direction.

Currently the system only uses one filter cube that limits the system to one form of fluorescence illumination. More filters could be added to accommodate a wider range of fluorescence modes.

Control through platforms such as Android could also be integrated into the system on various levels. This could allow the design to benefit from such merits as wireless connectivity, on-board camera and on-board image processing.

The design could also be made to have a cover so that the ambient light does not interfere with fluorescence illumination. With this modification, the ambient light mode would no longer be applicable, however, an additional light source could be placed above the sample area to compensate for this if needed.

A sturdier base could be made out of a more rigid material such as aluminium with a CNC machine. This would greatly improve the alignment of the system especially in areas where mirrors or beam-splitters are seated.

The calibration could be improved by using a USAF test target to determine the pixel:mm measurement.

The Systematic Design method used could be improved by using it in conjunction with TRIZ in the concept design phase of the process.

CHAPTER 8

CONCLUSION

The project was able to successfully make a research platform that could use bright-field, fluorescence and laser diffraction. It could scan images, stitch them through Microsoft Image Composite Editor and was able to have variable magnification through an objective turret. The system was also tested in an industrial application by scanning stained biological samples from ESR.

The images produced had a sharpness measures of different values depending on the type of samples imaged. Samples that had high contrast generally had higher image scores.

Future work could involve the use of fibre-optics to connect the light sources to the beam-splitter. This could allow a more compact design and the light sources can be placed anywhere else and not necessarily pointed right at the beam-splitter. More filters could be used to accommodate more fluorescence modes. A piezo-stack could be implemented to achieve finer focus in the z direction. Android could also be combined to offer benefits such as wireless communication, on-board cameras and on-board image processing. The design could also be housed inside a cover to allow fluorescence illumination to not be influenced by ambient lighting and materials such as aluminium could also be used to increase the sturdiness and stability of the system. The calibration method used to determine the size of particles could be improved by using a USAF test target to determine the pixel:mm measurement. Finally, the Systematic design method could be improved by using it in conjunction with TRIZ in the concept design phase to help in reducing the design time.

APPENDIX A

APPENDIX A

This appendix details a portion of the custom optical characteristics put in for the Nikon B-2A excitation filter, emission filter and dichroic mirror in TracePro. The full files for the Nikon filter can be found in the Github page for this thesis [119]. These characteristics were based on the official data shown in Figure.A.1.

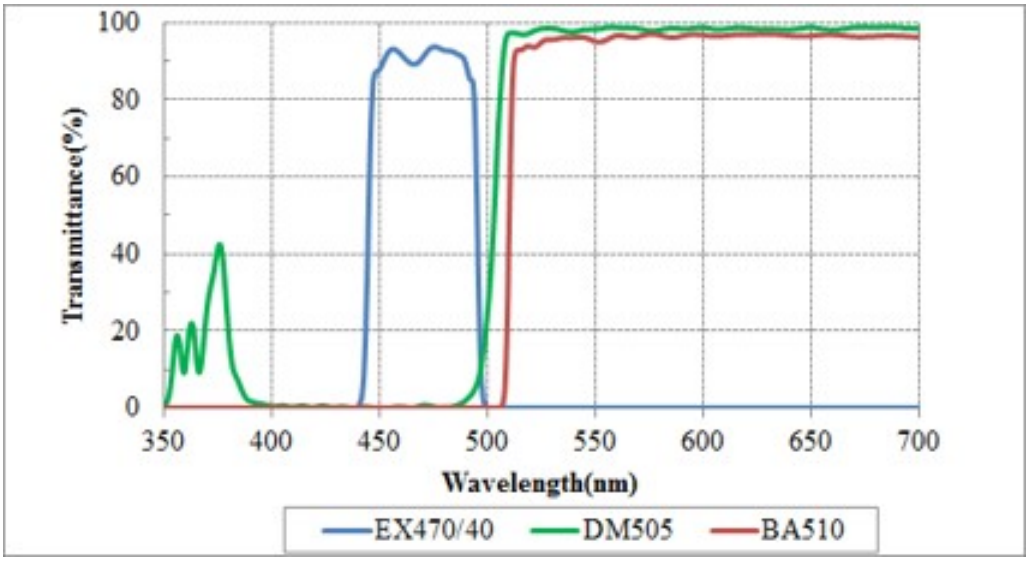

Figure A.1: Optical characteristics of the three filters used in Nikon B-2A filter cube (found in [31])

The legend for tables A.1, A.2 and A.3 is as follows:

(A) Temperature (Kelvin)

(B) Wavelength (Microns)

(C) Angle of incidence (degrees)

(D) Azimuth Angle (in degrees)

(E) Specular Absorptance for S polarization

(F) Specular Absorptance for P polarization

(G) Specular Reflectance for S polarization

(H) Specular Reflectance for P polarization

(I) Specular Transmittance for S polarization

(J) Specular Transmittance for S polarization

(K) Phase change for Transmittance

(L) Phase change for Transmittance

(M) A coefficient of BRDF

(N) B coefficient of BRDF

(O) B coefficient of BRDF

(P) g coefficient of BRDF

(Q) g coefficient of BRDF

(R) A coefficient of BTDF

(S) B coefficient of BTDF

(T) B coefficient of BTDF

(U) g coefficient of BTDF

(V) g coefficient of BTDF

A.1 Excitation Filter

Table A.1: Custom optical characteristics of excitation filter for Nikon B-2A filter cube

A	B	C	D	E	F	G	H	I	J	K	L	M	N	O	P	Q	R	S	T	U	V
300	0.4388	0	0	0	0	0.999999	0.999999	8.00E-07	8.00E-07	0	0	0	0.1	0.1	0	0	0	0.1	0.1	0	0
300	0.439	0	0	0	0	0.999999	0.999999	1.40E-06	1.40E-06	0	0	0	0.1	0.1	0	0	0	0.1	0.1	0	0
300	0.4392	0	0	0	0	0.999998	0.999998	2.40E-06	2.40E-06	0	0	0	0.1	0.1	0	0	0	0.1	0.1	0	0
300	0.4394	0	0	0	0	0.999996	0.999996	4.30E-06	4.30E-06	0	0	0	0.1	0.1	0	0	0	0.1	0.1	0	0
300	0.4396	0	0	0	0	0.999992	0.999992	8.00E-06	8.00E-06	0	0	0	0.1	0.1	0	0	0	0.1	0.1	0	0
300	0.4398	0	0	0	0	0.999985	0.999985	1.55E-05	1.55E-05	0	0	0	0.1	0.1	0	0	0	0.1	0.1	0	0
300	0.44	0	0	0	0	0.999969	0.999969	3.13E-05	3.13E-05	0	0	0	0.1	0.1	0	0	0	0.1	0.1	0	0
300	0.4402	0	0	0	0	0.999934	0.999934	6.59E-05	6.59E-05	0	0	0	0.1	0.1	0	0	0	0.1	0.1	0	0
300	0.4404	0	0	0	0	0.999855	0.999855	0.000145	0.000145	0	0	0	0.1	0.1	0	0	0	0.1	0.1	0	0
300	0.4406	0	0	0	0	0.999664	0.999664	0.000336	0.000336	0	0	0	0.1	0.1	0	0	0	0.1	0.1	0	0
300	0.4408	0	0	0	0	0.999189	0.999189	0.000811	0.000811	0	0	0	0.1	0.1	0	0	0	0.1	0.1	0	0
300	0.441	0	0	0	0	0.997946	0.997946	0.002054	0.002054	0	0	0	0.1	0.1	0	0	0	0.1	0.1	0	0
300	0.4412	0	0	0	0	0.994498	0.994498	0.005502	0.005502	0	0	0	0.1	0.1	0	0	0	0.1	0.1	0	0
300	0.4414	0	0	0	0	0.984013	0.984013	0.015987	0.015987	0	0	0	0.1	0.1	0	0	0	0.1	0.1	0	0
300	0.4416	0	0	0	0	0.947216	0.947216	0.052784	0.052784	0	0	0	0.1	0.1	0	0	0	0.1	0.1	0	0
300	0.4418	0	0	0	0	0.795014	0.795014	0.204986	0.204986	0	0	0	0.1	0.1	0	0	0	0.1	0.1	0	0
300	0.442	0	0	0	0	0.317726	0.317726	0.682274	0.682274	0	0	0	0.1	0.1	0	0	0	0.1	0.1	0	0
300	0.4422	0	0	0	0	0.16653	0.16653	0.83347	0.83347	0	0	0	0.1	0.1	0	0	0	0.1	0.1	0	0
300	0.4424	0	0	0	0	0.285867	0.285867	0.714133	0.714133	0	0	0	0.1	0.1	0	0	0	0.1	0.1	0	0
300	0.4426	0	0	0	0	0.289536	0.289536	0.710464	0.710464	0	0	0	0.1	0.1	0	0	0	0.1	0.1	0	0
300	0.4428	0	0	0	0	0.212175	0.212175	0.787825	0.787825	0	0	0	0.1	0.1	0	0	0	0.1	0.1	0	0
300	0.443	0	0	0	0	0.124428	0.124428	0.875572	0.875572	0	0	0	0.1	0.1	0	0	0	0.1	0.1	0	0

A.2 Emission Filter

Table A.2: Custom optical characteristics of emission filter for Nikon B-2A filter cube

A	B	C	D	E	F	G	H	I	J	K	L	M	N	O	P	Q	R	S	T	U	V
300	0.515	0	0	0	0	0.04514	0.04514	0.95486	0.95486	0	0	0	0.1	0.1	0	0	0	0.1	0.1	0	0
300	0.5152	0	0	0	0	0.04514	0.04514	0.95486	0.95486	0	0	0	0.1	0.1	0	0	0	0.1	0.1	0	0
300	0.5154	0	0	0	0	0.04514	0.04514	0.95486	0.95486	0	0	0	0.1	0.1	0	0	0	0.1	0.1	0	0
300	0.5156	0	0	0	0	0.04514	0.04514	0.95486	0.95486	0	0	0	0.1	0.1	0	0	0	0.1	0.1	0	0
300	0.5158	0	0	0	0	0.04514	0.04514	0.95486	0.95486	0	0	0	0.1	0.1	0	0	0	0.1	0.1	0	0
300	0.516	0	0	0	0	0.04514	0.04514	0.95486	0.95486	0	0	0	0.1	0.1	0	0	0	0.1	0.1	0	0
300	0.5162	0	0	0	0	0.04514	0.04514	0.95486	0.95486	0	0	0	0.1	0.1	0	0	0	0.1	0.1	0	0
300	0.5164	0	0	0	0	0.04514	0.04514	0.95486	0.95486	0	0	0	0.1	0.1	0	0	0	0.1	0.1	0	0
300	0.5166	0	0	0	0	0.04514	0.04514	0.95486	0.95486	0	0	0	0.1	0.1	0	0	0	0.1	0.1	0	0
300	0.5168	0	0	0	0	0.04514	0.04514	0.95486	0.95486	0	0	0	0.1	0.1	0	0	0	0.1	0.1	0	0
300	0.517	0	0	0	0	0.04514	0.04514	0.95486	0.95486	0	0	0	0.1	0.1	0	0	0	0.1	0.1	0	0
300	0.5172	0	0	0	0	0.04514	0.04514	0.95486	0.95486	0	0	0	0.1	0.1	0	0	0	0.1	0.1	0	0
300	0.5174	0	0	0	0	0.04514	0.04514	0.95486	0.95486	0	0	0	0.1	0.1	0	0	0	0.1	0.1	0	0
300	0.5176	0	0	0	0	0.04514	0.04514	0.95486	0.95486	0	0	0	0.1	0.1	0	0	0	0.1	0.1	0	0
300	0.5178	0	0	0	0	0.04514	0.04514	0.95486	0.95486	0	0	0	0.1	0.1	0	0	0	0.1	0.1	0	0
300	0.518	0	0	0	0	0.04514	0.04514	0.95486	0.95486	0	0	0	0.1	0.1	0	0	0	0.1	0.1	0	0
300	0.5182	0	0	0	0	0.04514	0.04514	0.95486	0.95486	0	0	0	0.1	0.1	0	0	0	0.1	0.1	0	0
300	0.5184	0	0	0	0	0.04514	0.04514	0.95486	0.95486	0	0	0	0.1	0.1	0	0	0	0.1	0.1	0	0
300	0.5186	0	0	0	0	0.04514	0.04514	0.95486	0.95486	0	0	0	0.1	0.1	0	0	0	0.1	0.1	0	0
300	0.5188	0	0	0	0	0.04514	0.04514	0.95486	0.95486	0	0	0	0.1	0.1	0	0	0	0.1	0.1	0	0
300	0.519	0	0	0	0	0.04514	0.04514	0.95486	0.95486	0	0	0	0.1	0.1	0	0	0	0.1	0.1	0	0
300	0.5192	0	0	0	0	0.04514	0.04514	0.95486	0.95486	0	0	0	0.1	0.1	0	0	0	0.1	0.1	0	0
300	0.5194	0	0	0	0	0.04514	0.04514	0.95486	0.95486	0	0	0	0.1	0.1	0	0	0	0.1	0.1	0	0

A.3 Dichroic Mirror

Table A.3: Custom optical characteristics of dichroic mirror for Nikon B-2A filter cube

A	B	C	D	E	F	G	H	I	J	K	L	M	N	O	P	Q	R	S	T	U	V
300	0.5	0	0	0	0	0.04514	0.04514	0.95486	0.95486	0	0	0	0.1	0.1	0	0	0	0.1	0.1	0	0
300	0.5002	0	0	0	0	0.04514	0.04514	0.95486	0.95486	0	0	0	0.1	0.1	0	0	0	0.1	0.1	0	0
300	0.5004	0	0	0	0	0.04514	0.04514	0.95486	0.95486	0	0	0	0.1	0.1	0	0	0	0.1	0.1	0	0
300	0.5006	0	0	0	0	0.04514	0.04514	0.95486	0.95486	0	0	0	0.1	0.1	0	0	0	0.1	0.1	0	0
300	0.5008	0	0	0	0	0.04514	0.04514	0.95486	0.95486	0	0	0	0.1	0.1	0	0	0	0.1	0.1	0	0
300	0.501	0	0	0	0	0.04514	0.04514	0.95486	0.95486	0	0	0	0.1	0.1	0	0	0	0.1	0.1	0	0
300	0.5012	0	0	0	0	0.04514	0.04514	0.95486	0.95486	0	0	0	0.1	0.1	0	0	0	0.1	0.1	0	0
300	0.5014	0	0	0	0	0.04514	0.04514	0.95486	0.95486	0	0	0	0.1	0.1	0	0	0	0.1	0.1	0	0
300	0.5016	0	0	0	0	0.04514	0.04514	0.95486	0.95486	0	0	0	0.1	0.1	0	0	0	0.1	0.1	0	0
300	0.5018	0	0	0	0	0.04514	0.04514	0.95486	0.95486	0	0	0	0.1	0.1	0	0	0	0.1	0.1	0	0
300	0.502	0	0	0	0	0.04514	0.04514	0.95486	0.95486	0	0	0	0.1	0.1	0	0	0	0.1	0.1	0	0
300	0.5022	0	0	0	0	0.04514	0.04514	0.95486	0.95486	0	0	0	0.1	0.1	0	0	0	0.1	0.1	0	0
300	0.5024	0	0	0	0	0.04514	0.04514	0.95486	0.95486	0	0	0	0.1	0.1	0	0	0	0.1	0.1	0	0
300	0.5026	0	0	0	0	0.04514	0.04514	0.95486	0.95486	0	0	0	0.1	0.1	0	0	0	0.1	0.1	0	0
300	0.5028	0	0	0	0	0.04514	0.04514	0.95486	0.95486	0	0	0	0.1	0.1	0	0	0	0.1	0.1	0	0
300	0.503	0	0	0	0	0.04514	0.04514	0.95486	0.95486	0	0	0	0.1	0.1	0	0	0	0.1	0.1	0	0
300	0.5032	0	0	0	0	0.04514	0.04514	0.95486	0.95486	0	0	0	0.1	0.1	0	0	0	0.1	0.1	0	0
300	0.5034	0	0	0	0	0.04514	0.04514	0.95486	0.95486	0	0	0	0.1	0.1	0	0	0	0.1	0.1	0	0
300	0.5036	0	0	0	0	0.04514	0.04514	0.95486	0.95486	0	0	0	0.1	0.1	0	0	0	0.1	0.1	0	0
300	0.5038	0	0	0	0	0.04514	0.04514	0.95486	0.95486	0	0	0	0.1	0.1	0	0	0	0.1	0.1	0	0
300	0.504	0	0	0	0	0.04514	0.04514	0.95486	0.95486	0	0	0	0.1	0.1	0	0	0	0.1	0.1	0	0
300	0.5042	0	0	0	0	0.04514	0.04514	0.95486	0.95486	0	0	0	0.1	0.1	0	0	0	0.1	0.1	0	0

APPENDIX B

APPENDIX B

This appendix details a portion of the custom fluorescent properties assigned to the sample in the TracePro simulation based on the data that it is excited at 480nm and emits at 520nm. The full file can be seen in the Github repository [120].

B.1 Custom optical properties assigned for Bangs Laboratories FS07f excitation state

Table B.1: Custom optical properties assigned for Bangs Laboratories FS07f excitation state

Temperature	Excitation Wavelength	Relative Absorption	Relative Excitation
300	0.251	0.5835376	0.5835376
300	0.252	0.5923188	0.5923188
300	0.253	0.6030468	0.6030468
300	0.254	0.6146783	0.6146783
300	0.255	0.6228474	0.6228474
300	0.256	0.6293058	0.6293058
300	0.257	0.6386145	0.6386145
300	0.258	0.6445415	0.6445415
300	0.259	0.6514704	0.6514704
300	0.26	0.6564309	0.6564309
300	0.261	0.6586749	0.6586749

B.2 Custom optical properties for Bangs Laboratories FS07f emission state

Table B.2: Custom optical properties assigned for Bangs Laboratories FS07f emission state

Temperature	Emission Wavelength	Relative Emission
300	0.475	0.00979202
300	0.476	0.007017655
300	0.477	0.004852089
300	0.478	0.004840133
300	0.479	0.005698063
300	0.48	0.007110866
300	0.481	0.00860956
300	0.482	0.01069875
300	0.483	0.01345994
300	0.484	0.01668182
300	0.485	0.02103955
300	0.486	0.02581697
300	0.487	0.03224486
300	0.488	0.03944527
300	0.489	0.04848526
300	0.49	0.05912594
300	0.491	0.07095542
300	0.492	0.08524304
300	0.493	0.1020722
300	0.494	0.1218995
300	0.495	0.1454477
300	0.496	0.1712979
300	0.497	0.2015777
300	0.498	0.2353367

APPENDIX C

This appendix shows the datasheet for the PL15S-020 disk-drive stepper motor.

NMB-MAT
Minebea-Matsushita Motor Corporation
eMINEBEA.COM

PL15S-020

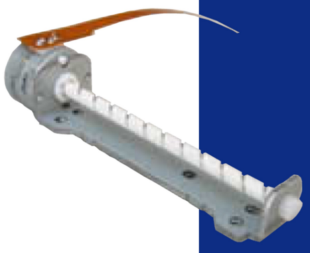

PM Motor
PL Type

Applications

Head Drive for Floppy Disk Drive
Pick Up Drive for CD
Pick Up Drive for DVD

Reference Characteristics

Moter Size	PL15S-020
Number of Steps per Rotation	20
Drive Method	2-2 PHASE
Drive Circuit	BIPOLAR CONST. VOLT.
Drive Voltage	5[V]
Coil Resistance/Phase	10[Ω]
Magnet Material	Nd-Fe-B bonded magnet (MS70)
Holding Torque	30[X10^{-4} N.m]
Maximum PULL-IN Frequency	1450[PPS]

Typical Torgue Characteristics

Driver Frequency	400[PPS]	1400[PPS]
PULL-OUT Torque	25[X10^{-4} N.m]	13[X10^{-4} N.m]

Switching Sequence
(Viewed from Lead Screw Side)

STEP \ TERMINAL	A1	A2	B1	B3
1	−	+	+	−
2	−	+	−	+
3	+	−	−	+
4	+	−	+	−

CW ↓ ↑ CCW

Torque Characteristics

PL LEAD SCREW TYPE(at 5[V],10[Ω])

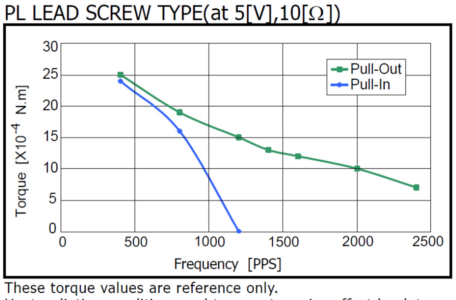

These torque values are reference only.
Heat radiation conditions and temperature rise effect by duty are different on each equipment, therefore please select motors after considering the heat conditions in the actual equipment.

Lead Screw Spec

OUTSIDE DIA.	ϕ3
MINOR DIA.	ϕ2
PITCH DIA.	ϕ2.4
PITCH	3.0
LEAD ANGLE	21°41" 49'
LEAD DIRECTION	RIGHT-HAND SINGLE THREAD
SIMPLE PITCH ERROR	0.020
CUMULATIVE PITCH ERROR	0.030

Dimensions

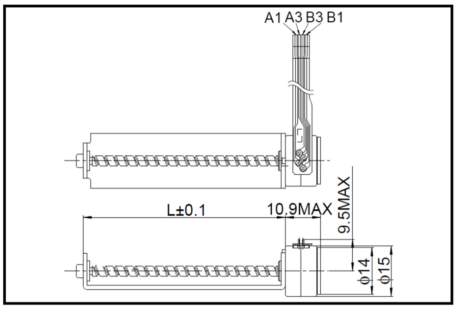

Detail of Screw

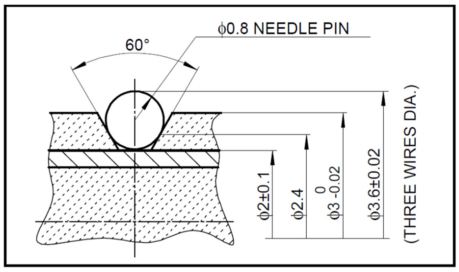

Performance values shown on this website are representative.
Motor design and specifications are subject to change without notice.

Figure C.1: PL15S-020 Datasheet

APPENDIX D

APPENDIX D

This appendix details the measurements taken of the extension lengths of the spring on the z-axis stage. The measurements were then used to determine the spring constant of the spring.

D.1 Spring Extension Measurement Setup

D.1.1 Weight Measurement

The weights were measured using Saritorius electronic scale accurate to 0.0001g. Figure D.1 shows an example of how the weights were measured.

D.1.2 Spring Extension Setup

The spring was attached to a screw that was itself part of an existing jig. The weights would be hung on the end of the spring and the extension was measured with digital calipers accurate to 0.01mm. Figure D.2 shows the setup.

D.2 Spring Extension Measurements

Table D.1 shows the measurements taken of spring extension under two different weights. We used the average of the measurements taken at 0kg as the pre-extension lengths of the spring for the two weight measurements.

The legend for Table D.1 is as follows:

(A) Measurement Number

(B) Mass

Figure D.1: Example of how weights were measured

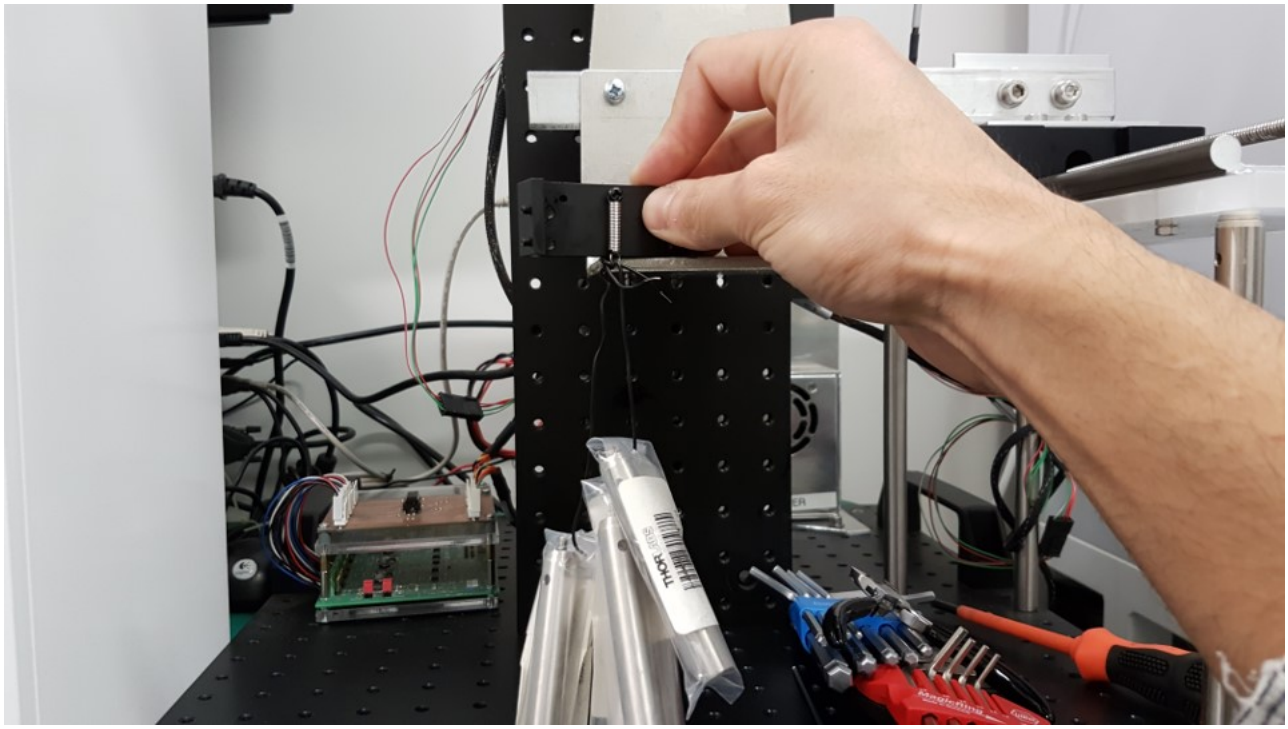

Figure D.2: Spring extension test jig setup

(C) Pre-Extension Length

(D) Post-Extension Length

(E) Extension

Table D.1: Extension measurements of spring from z-axis stage

A	**B**	**C**	**D**	**E**
1	0	19.28		
2	0	19.15		
3	0	19.29		
4	0	19.22		
5	0	19.3		
6	0	19.26		
7	0	19.17		
8	0	19.25		
9	0	19.16		
10	0	19.18		
Average		19.226		
1	493.3697	19.226	20.93	1.704
2	493.3697	19.226	20.95	1.724
3	493.3697	19.226	20.79	1.564
4	493.3697	19.226	20.75	1.524
5	493.3697	19.226	20.67	1.444
6	493.3697	19.226	20.83	1.604
7	493.3697	19.226	20.8	1.574
8	493.3697	19.226	20.77	1.544
9	493.3697	19.226	20.94	1.714
10	493.3697	19.226	20.74	1.514
Average				**1.591**
1	687.1657	19.226	22.89	3.664
2	687.1657	19.226	22.61	3.384
3	687.1657	19.226	22.91	3.684
4	687.1657	19.226	22.44	3.214
5	687.1657	19.226	22.68	3.454
6	687.1657	19.226	22.62	3.394
7	687.1657	19.226	22.66	3.434
8	687.1657	19.226	22.84	3.614

Continued on next page

Table D.1 – continued from previous page

A	B	C	D	E
9	687.1657	19.226	22.85	3.624
10	687.1657	19.226	22.81	3.584
Average				**3.505**

D.3 Spring Constant

The average extension lengths were plotted against the weights in the graph seen in Figure D.3. The gradient was estimated as 1.8922Nmm^{-1} or 1892.2 Nm^{-1} and taken as the spring constant.

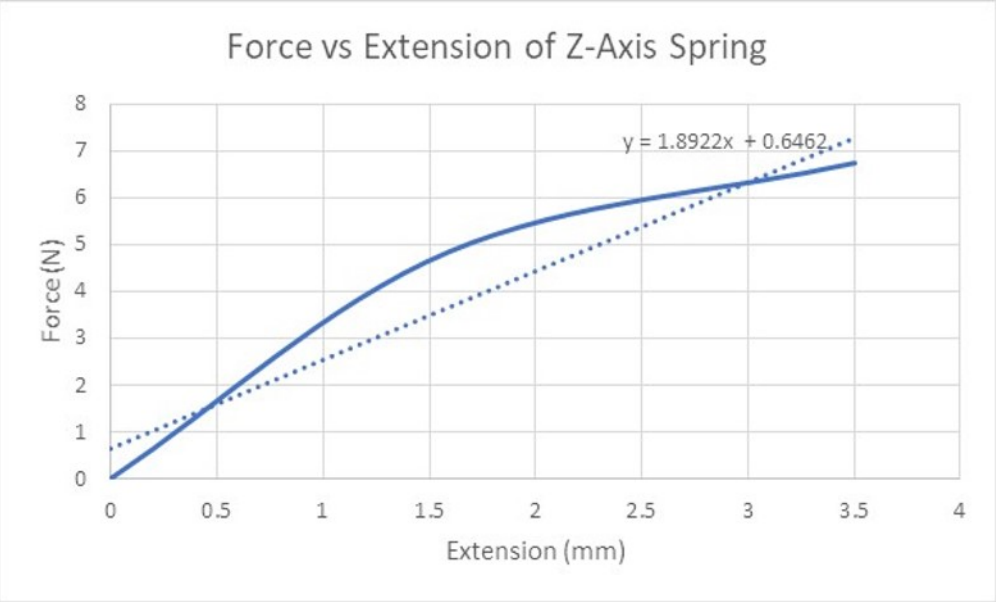

Figure D.3: Graph of Force(N) vs Extension(mm) of spring. Note the estimated trendline which indicates a gradient of 1.8922Nmm^{-1}

BIBLIOGRAPHY

[1] H.-T. Liu, "Product design and selection using fuzzy qfd and fuzzy mcdm approaches," *Applied Mathematical Modelling*, vol. 35, no. 1, pp. 482–496, 2011.

[2] https://discoveries-project.weebly.com/, "One of leeuwenhoek's many microscopes," http://discoveries-project.weebly.com/uploads/2/3/9/0/23900140/6355383.jpg?330, [Online; accessed 30 December, 2018].

[3] R. Hooke, *Micrographia: or some physiological descriptions of minute bodies made by magnifying glasses, with observations and inquiries thereupon*. Courier Corporation, 2003.

[4] https://en.wikipedia.org, "Principle of the periscope," https://en.wikipedia.org/wiki/Periscope#/media/File:Periscope_simple.svg0, [Online; accessed 30 September, 2018].

[5] Antilived, https://en.wikipedia.org, "A typical porro prism binoculars design," https://en.wikipedia.org/wiki/Binoculars#/media/File:Binocularp.svg, [Online; accessed 30 September, 2018].

[6] Szőcs Tamás, https://en.wikipedia.org, "Light path in a cassegrain reflecting telescope," https://en.wikipedia.org/wiki/Cassegrain_reflector#/media/File:Cassegrain.en.png, [Online; accessed 31 October, 2018].

[7] E. J. Tremblay, R. A. Stack, R. L. Morrison, and J. E. Ford, "Ultrathin cameras using annular folded optics," *Applied optics*, vol. 46, no. 4, pp. 463–471, 2007.

[8] D. B. Murphy, *Fundamentals of light microscopy and electronic imaging*. John Wiley & Sons, 2002.

[9] N. Feidenhans'l, "Optical detection for polymer based bio-sensors," Ph.D. dissertation, 07 2013.

[10] https://www.microscopyu.com, "Hela cell mitochondria," https://www.microscopyu.com/gallery-images/hela-cell-mitochondria-1, [Online; accessed 1 January, 2019].

[11] https://m.nikoninstruments.com, "Fluorescence filter cubes from nikon," https://m.nikoninstruments.com/content/.../Fluorescence_Filter_Cubes_2CE-MRJH-3.pdf, [Online; accessed 1 January, 2019].

[12] T.-j. Chen, R. Zitter, and R. Tao, "Laser diffraction determination of the crystalline structure of an electrorheological fluid," *Physical review letters*, vol. 68, no. 16, p. 2555, 1992.

[13] P. Schall, "Laser diffraction microscopy," *Reports on Progress in Physics*, vol. 72, no. 7, p. 076601, 2009.

[14] http://www.microscopy-uk.org.uk, "An illustration of the light path in darkfield illumination," http://www.microscopy-uk.org.uk/mag/imgapr02/darkfieldexpl.gif, [Online; accessed 27 January, 2019].

[15] https://www.microscopyu.com, "Fibers in brightfield and darkfield illumination," https://www.microscopyu.com/techniques/stereomicroscopy/darkfield-illumination, [Online; accessed 2 January, 2019].

[16] https://www.microscope-antiques.com, "History of mcarthur microscopes," https://www.microscope-antiques.com/mcarthurs.html, [Online; accessed 13 January, 2019].

[17] D. A. Stewart, "Objective lens changer for optical instruments," Apr. 24 2018, US Patent 9,952,419.

[18] R. Seifert and J. Fölling, "Microscope stage," Sep. 17 2013, US Patent 8,537,462.

[19] S. Schaefer, S. A. Boehm, and K. J. Chau, "Automated, portable, low-cost bright-field and fluorescence microscope with autofocus and autoscanning capabilities," *Applied optics*, vol. 51, no. 14, pp. 2581–2588, 2012.

[20] M. Brown and D. G. Lowe, "Automatic panoramic image stitching using invariant features," *International journal of computer vision*, vol. 74, no. 1, pp. 59–73, 2007.

[21] S. Najmaei, Z. Liu, W. Zhou, X. Zou, G. Shi, S. Lei, B. I. Yakobson, J.-C. Idrobo, P. M. Ajayan, and J. Lou, "Vapour phase growth and grain boundary structure of molybdenum disulphide atomic layers," *Nature materials*, vol. 12, no. 8, p. 754, 2013.

[22] docs.opencv.org, "Stitching pipeline," https://docs.opencv.org/2.4/modules/stitching/doc/introduction.html#bl07, [Online; accessed 2 November, 2019].

[23] S. Preibisch, S. Saalfeld, and P. Tomancak, "Globally optimal stitching of tiled 3d microscopic image acquisitions," *Bioinformatics*, vol. 25, no. 11, pp. 1463–1465, 2009.

[24] J. Fabic, I. Turla, J. Capacillo, L. David, and P. Naval, "Fish population estimation and species classification from underwater video sequences using blob counting and shape analysis," in *2013 IEEE International Underwater Technology Symposium (UT)*. IEEE, 2013, pp. 1–6.

[25] G. E. Dieter and L. C. Schmidt, *Engineering design*. Boston : McGraw-Hill Higher Education, c2009, 2009. [Online]. Available: http://ezproxy.massey.ac.nz/login?url=http://search.ebscohost.com/login.aspx?direct=true&db=cat00245a&AN=massey.b1942666&site=eds-live&scope=site

[26] https://www.youtube.com, "An illustration of the light path in darkfield illumination," https://www.youtube.com/watch?v=zwDeO5u3aEo, [Online; accessed 27 January, 2019].

[27] https://www.thorlabs.com/, "Reflectance of silver coated mirror vs wavelength," https://www.thorlabs.com/newgrouppage9.cfm?objectgroup_id=905&pn=MRA10-P01, [Online; accessed 4 January, 2019].

[28] ——, "Reflectance and transmission of non-polarizing cube beam-splitter," https://www.thorlabs.com/newgrouppage9.cfm?objectgroup_id=754&pn=BS010, [Online; accessed 4 January, 2019].

[29] https://www.olympus-lifescience.com, "Fluorescence filters," https://static5.olympus-lifescience.com/data/olympusmicro/primer/techniques/fluorescence/images/fluorescencecube.jpg?rev=DCDC, [Online; accessed 28 January, 2019].

[30] R. G. Budynas and K. J. Nisbett, "Shigley's mechanical engineering design (in si units)," 2014.

[31] https://www.nikon.com, "Fluorescence filter cubes," https://www.nikon.com/products/microscope-solutions/lineup/accessory/filter_cubes/, [Online; accessed 3 January, 2019].

[32] E. S. Jaffe, N. L. Harris, H. Stein, and P. G. Isaacson, "Classification of lymphoid neoplasms: the microscope as a tool for disease discovery," *Blood*, vol. 112, no. 12, pp. 4384–4399, 2008.

[33] H. Benveniste, G. Einstein, K. R. Kim, C. Hulette, and G. A. Johnson, "Detection of neuritic plaques in alzheimer's disease by magnetic resonance microscopy," *Proceedings of the National Academy of Sciences*, vol. 96, no. 24, pp. 14 079–14 084, 1999.

[34] H. Ramachandraiah, M. Amasia, J. Cole, P. Sheard, S. Pickhaver, C. Walker, V. Wirta, P. Lexow, R. Lione, and A. Russom, "Lab-on-dvd: standard dvd drives as a novel laser scanning microscope for image based point of care diagnostics," *Lab on a Chip*, vol. 13, no. 8, pp. 1578–1585, 2013.

[35] P. J. de Groot and J. F. Biegen, "A new class of wide-field objectives for 3d interference microscopy," in *Optical Measurement Systems for Industrial Inspection IX*, vol. 9525. International Society for Optics and Photonics, 2015, p. 95250N.

[36] X. Heng, D. Erickson, L. R. Baugh, Z. Yaqoob, P. W. Sternberg, D. Psaltis, and C. Yang, "Optofluidic microscopy—a method for implementing a high resolution optical microscope on a chip," *Lab on a Chip*, vol. 6, no. 10, pp. 1274–1276, 2006.

[37] S. C. Gopinath, T.-H. Tang, Y. Chen, M. Citartan, and T. Lakshmipriya, "Bacterial detection: From microscope to smartphone," *Biosensors and Bioelectronics*, vol. 60, pp. 332–342, 2014.

[38] C. W. Pirnstill and G. L. Coté, "Malaria diagnosis using a mobile phone polarized microscope," *Scientific reports*, vol. 5, p. 13368, 2015.

[39] H. Zhu, S. O. Isikman, O. Mudanyali, A. Greenbaum, and A. Ozcan, "Optical imaging techniques for point-of-care diagnostics," *Lab on a Chip*, vol. 13, no. 1, pp. 51–67, 2013.

[40] M. K. Kanakasabapathy, M. Sadasivam, A. Singh, C. Preston, P. Thirumalaraju, M. Venkataraman, C. L. Bormann, M. S. Draz, J. C. Petrozza, and H. Shafiee, "An automated smartphone-based diagnostic assay for point-of-care semen analysis," *Science translational medicine*, vol. 9, no. 382, p. eaai7863, 2017.

[41] W. J. Croft, *Under the microscope. [electronic resource] : a brief history of microscopy.*, ser. Series in popular science: v. 5. Hackensack, NJ : World Scientific, ©2006, 2006. [Online]. Available: http://ezproxy.massey.ac.nz/login?url=http://search.ebscohost.com/login.aspx?direct=true&db=cat00245a&AN=massey.b3604155&site=eds-live&scope=site

[42] D. Bardell, "The invention of the microscope," *Bios*, vol. 75, no. 2, pp. 78–84, 2004. [Online]. Available: http://www.jstor.org/stable/4608700

[43] A. Baranne and F. Launay, "Cassegrain: un célèbre inconnu de l'astronomie instrumentale cassegrain: a famous unknown of instrumental astronomy," *Journal of Optics*, vol. 28, no. 4, p. 158, 1997.

[44] J. Sant. (2018) The early reflecting telescope:cassegrain, mersenne, and cavalieri. [Online]. Available: http://www.scientus.org/Reflecting-Telescope-History.html

[45] D. Linden and T. B. Reddy, "Handbook of batteries. 3rd," *McGraw-Hill*, 2002.

[46] B. J. Furman, J. Christman, M. Kearny, F. Wojcik, and M. Tortonese, "Battery-operated atomic force microscope," *Review of scientific instruments*, vol. 69, no. 1, pp. 215–220, 1998.

[47] D. Erickson, D. Sinton, and D. Li, "A miniaturized high-voltage integrated power supply for portable microfluidic applications," *Lab on a Chip*, vol. 4, no. 2, pp. 87–90, 2004.

[48] S.-L. Tsai, Y. Chiang, M.-H. Wang, M.-K. Chen, and L.-S. Jang, "Battery-powered portable instrument system for single-cell trapping, impedance measurements, and modeling analyses," *Electrophoresis*, vol. 35, no. 16, pp. 2392–2400, 2014.

[49] M. Renz, "Fluorescence microscopy—a historical and technical perspective," *Cytometry Part A*, vol. 83, no. 9, pp. 767–779, 2013.

[50] D. B. Murphy and M. W. Davidson, *Fundamentals of light microscopy and electronic imaging. [electronic resource].* Hoboken, N.J. : Wiley-Blackwell, ©2013, 2013. [Online]. Available: http://ezproxy.massey.ac.nz/login?url=http://search.ebscohost.com/login.aspx?direct=true&db=cat00245a&AN=massey.b3321762&site=eds-live&scope=site

[51] K. Maxwell and G. N. Johnson, "Chlorophyll fluorescence—a practical guide," *Journal of experimental botany*, vol. 51, no. 345, pp. 659–668, 2000.

[52] S. A. Lee and C. Yang, "A smartphone-based chip-scale microscope using ambient illumination," *Lab on a Chip*, vol. 14, no. 16, pp. 3056–3063, 2014.

[53] M. G. Giacomelli, T. Yoshitake, L. C. Cahill, H. Vardeh, L. M. Quintana, B. E. Faulkner-Jones, J. Brooker, J. L. Connolly, and J. G. Fujimoto, "Multiscale nonlinear microscopy and widefield white light imaging enables rapid histological imaging of surgical specimen margins," *Biomedical optics express*, vol. 9, no. 5, pp. 2457–2475, 2018.

[54] X. Ma, G. An, and B. Li, "Design and implementation of an automated microscope stage," in *Information Technology and Applications, 2009. IFITA'09. International Forum on*, vol. 1. IEEE, 2009, pp. 603–605.

[55] R. A. Campbell, R. W. Eifert, and G. C. Turner, "Openstage: a low-cost motorized microscope stage with sub-micron positioning accuracy," *PloS one*, vol. 9, no. 2, p. e88977, 2014.

[56] P. Thévenaz and M. Unser, "User-friendly semiautomated assembly of accurate image mosaics in microscopy," *Microscopy research and technique*, vol. 70, no. 2, pp. 135–146, 2007.

[57] B. Ma, T. Zimmermann, M. Rohde, S. Winkelbach, F. He, W. Lindenmaier, and K. E. Dittmar, "Use of autostitch for automatic stitching of microscope images," *Micron*, vol. 38, no. 5, pp. 492–499, 2007.

[58] M. R. Group. (2019) Image composite editor. [Online]. Available: https://www.microsoft.com/en-us/research/project/image-composite-editor/

[59] J. W. Gross and B. W. Heumann, "A statistical examination of image stitching software packages for use with unmanned aerial systems," *Photogrammetric Engineering & Remote Sensing*, vol. 82, no. 6, pp. 419–425, 2016.

[60] S. Winder, G. Hua, and M. Brown, "Picking the best daisy," in *2009 IEEE conference on computer vision and pattern recognition*. IEEE, 2009, pp. 178–185.

[61] A. Agarwala, M. Dontcheva, M. Agrawala, S. Drucker, A. Colburn, B. Curless, D. Salesin, and M. Cohen, "Interactive digital photomontage," in *ACM Transactions on Graphics (ToG)*, vol. 23, no. 3. ACM, 2004, pp. 294–302.

[62] A. Gulati, A. Jabbour, T. F. Ismail, K. Guha, J. Khwaja, S. Raza, K. Morarji, T. D. Brown, N. A. Ismail, M. R. Dweck *et al.*, "Association of fibrosis with mortality and sudden cardiac death in patients with nonischemic dilated cardiomyopathy," *Jama*, vol. 309, no. 9, pp. 896–908, 2013.

[63] H. S. Faridul, J. Stauder, and A. Trémeau, "Illumination and device invariant image stitching," in *2014 IEEE International Conference on Image Processing (ICIP)*. IEEE, 2014, pp. 56–60.

[64] Y. Wu, "Research on bank intelligent video image processing and monitoring control system based on opencv," in *2009 3rd International Conference on Anti-counterfeiting, Security, and Identification in Communication*. IEEE, 2009, pp. 211–214.

[65] I. Culjak, D. Abram, T. Pribanic, H. Dzapo, and M. Cifrek, "A brief introduction to opencv," in *2012 proceedings of the 35th international convention MIPRO*. IEEE, 2012, pp. 1725–1730.

[66] T. Keatsamarn and C. Pintavirooj, "Foot plantar pressure measurement system using optical sensor," in *2016 9th Biomedical Engineering International Conference (BMEiCON)*. IEEE, 2016, pp. 1–4.

[67] Y. J. Vaishnav, S. A. Rucker, K. Saharia, and N. A. McNamara, "Rapid, automated mosaicking of the human corneal subbasal nerve plexus," *Biomedical Engineering/Biomedizinische Technik*, vol. 62, no. 6, pp. 609–613, 2017.

[68] J. Schindelin, I. Arganda-Carreras, E. Frise, V. Kaynig, M. Longair, T. Pietzsch, S. Preibisch, C. Rueden, S. Saalfeld, B. Schmid *et al.*, "Fiji: an open-source platform for biological-image analysis," *Nature methods*, vol. 9, no. 7, p. 676, 2012.

[69] S. K. S. Kumar, "Implementation of a closed-loop microscopy pipeline to stitch and segment images of growing cell populations," Master's thesis, Eidgenössische Technische Hochschule Zürich, Department of Computer Science . . . , 2013.

[70] B. A. Millis and M. J. Tyska, "High-resolution image stitching as a tool to assess tissue-level protein distribution and localization," in *Molecular Profiling*. Springer, 2017, pp. 281–296.

[71] V. Mönkemöller, C. Øie, W. Hübner, T. Huser, and P. McCourt, "Multimodal super-resolution optical microscopy visualizes the close connection between membrane and the cytoskeleton in liver sinusoidal endothelial cell fenestrations," *Scientific reports*, vol. 5, p. 16279, 2015.

[72] V. Lempitsky and A. Zisserman, "Learning to count objects in images," in *Advances in neural information processing systems*, 2010, pp. 1324–1332.

[73] A. Lehmussola, P. Ruusuvuori, J. Selinummi, H. Huttunen, and O. Yli-Harja, "Computational framework for simulating fluorescence microscope images with cell populations," *IEEE Transactions on Medical Imaging*, vol. 26, no. 7, pp. 1010–1016, 2007.

[74] D. N. Breslauer, R. N. Maamari, N. A. Switz, W. A. Lam, and D. A. Fletcher, "Mobile phone based clinical microscopy for global health applications," *PloS one*, vol. 4, no. 7, p. e6320, 2009.

[75] J. L. Goldberg, C. L. Zanella, Y. M. Janssen, C. R. Timblin, L. A. Jimenez, P. Vacek, D. J. Taatjes, and B. T. Mossman, "Novel cell imaging techniques show induction of apoptosis and proliferation in mesothelial cells by asbestos," *American journal of respiratory cell and molecular biology*, vol. 17, no. 3, pp. 265–271, 1997.

[76] S. Chen, M. Zhao, G. Wu, C. Yao, and J. Zhang, "Recent advances in morphological cell image analysis," *Computational and Mathematical Methods in Medicine*, vol. 2012, 2012.

[77] aforgenet.com, "Aforge.net framework celebrates its 5 years birthday," http://aforgenet.com/news/2011.12.21.five_years_framework.html, [Online; accessed 3 November, 2019].

[78] ——, "Aforge.net framework," http://www.aforgenet.com/framework/docs/, [Online; accessed 3 November, 2019].

[79] F. I. Sholeh, "White blood cell segmentation for fresh blood smear images," in *2013 International Conference on Advanced Computer Science and Information Systems (ICACSIS)*. IEEE, 2013, pp. 425–429.

[80] H. Sharma, N. Zerbe, I. Klempert, O. Hellwich, and P. Hufnagl, "Deep convolutional neural networks for automatic classification of gastric carcinoma using whole slide images in digital histopathology," *Computerized Medical Imaging and Graphics*, vol. 61, pp. 2–13, 2017.

[81] M. S. I. Khan, "Implementation of edge & shape detection techniques and their performance evaluation," *Copyright by Mohammad Shahnoor Islam Khan*, 2012.

[82] M. Gupta, "Cell identification by blob detection," *UACEE International Journal of Advances in Electonics Engineering*, vol. 2, pp. 56–59, 2012.

[83] D. Li, B. Liang, and W. Zhang, "Real-time moving vehicle detection, tracking, and counting system implemented with opencv," in *2014 4th IEEE International Conference on Information Science and Technology*. IEEE, 2014, pp. 631–634.

[84] D. Kong, D. Gray, and H. Tao, "Counting pedestrians in crowds using viewpoint invariant training." in *BMVC*, vol. 1. Citeseer, 2005, p. 2.

[85] S. Pertuz, D. Puig, and M. A. Garcia, "Analysis of focus measure operators for shape-from-focus," *Pattern Recognition*, vol. 46, no. 5, pp. 1415–1432, 2013.

[86] J. L. Pech-Pacheco, G. Cristóbal, J. Chamorro-Martinez, and J. Fernández-Valdivia, "Diatom autofocusing in brightfield microscopy: a comparative study," in *Pattern Recognition, 2000. Proceedings. 15th International Conference on*, vol. 3. IEEE, 2000, pp. 314–317.

[87] L. Firestone, K. Cook, K. Culp, N. Talsania, and K. Preston Jr, "Comparison of autofocus methods for automated microscopy," *Cytometry: The Journal of the International Society for Analytical Cytology*, vol. 12, no. 3, pp. 195–206, 1991.

[88] A. Santos, C. Ortiz de Solórzano, J. J. Vaquero, J. Pena, N. Malpica, and F. Del Pozo, "Evaluation of autofocus functions in molecular cytogenetic analysis," *Journal of microscopy*, vol. 188, no. 3, pp. 264–272, 1997.

[89] Y. Sun, S. Duthaler, and B. J. Nelson, "Autofocusing in computer microscopy: selecting the optimal focus algorithm," *Microscopy research and technique*, vol. 65, no. 3, pp. 139–149, 2004.

[90] A. R. Miller, G. L. Davis, Z. M. Oden, M. R. Razavi, A. Fateh, M. Ghazanfari, F. Abdolrahimi, S. Poorazar, F. Sakhaie, R. J. Olsen *et al.*, "Portable, battery-operated, low-cost, bright field and fluorescence microscope," *PLoS One*, vol. 5, no. 8, p. e11890, 2010.

[91] G. Pahl, K. Wallace, and L. T. M. Blessing, *Engineering design : a systematic approach*. London : Springer, 2007, 2007. [Online]. Available: http://ezproxy.massey.ac.nz/login?url=http://search.ebscohost.com/login.aspx?direct=true&db=cat00245a&AN=massey.b1910495&site=eds-live&scope=site

[92] T. Bakker, J. Bontsema, J. Müller *et al.*, "Systematic design of an autonomous platform for robotic weeding," *Journal of Terramechanics*, vol. 47, no. 2, pp. 63–73, 2010.

[93] F. Ore, L. Hansson, and M. Wiktorsson, "Method for design of human-industrial robot collaboration workstations," *Procedia Manufacturing*, vol. 11, pp. 4–12, 2017.

[94] T. Tomiyama, P. Gu, Y. Jin, D. Lutters, C. Kind, and F. Kimura, "Design methodologies: Industrial and educational applications," *CIRP annals*, vol. 58, no. 2, pp. 543–565, 2009.

[95] P. Nguyen, "Biomimicry."

[96] A. Muralidhar and A. Krishnan, "Why study birds?"

[97] N. P. Suh *et al.*, *The principles of design*. Oxford University Press on Demand, 1990, no. 6.

[98] S. Lo and M. G. Helander, "Use of axiomatic design principles for analysing the complexity of human–machine systems," *Theoretical Issues in Ergonomics Science*, vol. 8, no. 2, pp. 147–169, 2007.

[99] F. Xi, Y. Xu, and G. Xiong, "Design and analysis of a re-configurable parallel robot," *Mechanism and Machine Theory*, vol. 41, no. 2, pp. 191–211, 2006.

[100] L. Chen, F. Xi, and A. Macwan, "Module selection methodology for designing reconfigurable machining systems," in *ASME 2002 International Mechanical Engineering Congress and Exposition*. American Society of Mechanical Engineers, 2002, pp. 541–550.

[101] W. Dong, H. Shah, and F. Wongt, "Fuzzy computations in risk and decision analysis," *Civil Engineering Systems*, vol. 2, no. 4, pp. 201–208, 1985.

[102] L. P. Khoo and N. C. Ho, "Framework of a fuzzy quality function deployment system," *International Journal of Production Research*, vol. 34, no. 2, pp. 299–311, 1996.

[103] L.-H. Chen and H.-W. Lu, "An approximate approach for ranking fuzzy numbers based on left and right dominance," *Computers & Mathematics with Applications*, vol. 41, no. 12, pp. 1589–1602, 2001.

[104] H. Rommelfanger, "Interactive decision making in fuzzy linear optimization problems," *European Journal of Operational Research*, vol. 41, no. 2, pp. 210–217, 1989.

[105] R. Rädle, H.-C. Jetter, N. Marquardt, H. Reiterer, and Y. Rogers, "Huddlelamp: Spatially-aware mobile displays for ad-hoc around-the-table collaboration," in *Proceedings of the Ninth ACM International Conference on Interactive Tabletops and Surfaces*. ACM, 2014, pp. 45–54.

[106] S. Yilmaz and C. M. Seifert, "Creativity through design heuristics: A case study of expert product design," *Design Studies*, vol. 32, no. 4, pp. 384–415, 2011.

[107] G. Fantoni, D. Gabelloni, and J. Tilli, "Concept design of new grippers using abstraction and analogy," *Proceedings of the institution of mechanical engineers, part B: journal of engineering manufacture*, vol. 227, no. 10, pp. 1521–1532, 2013.

[108] F. Zwicky, "Entdecken, erfinden, forschen im morphologischen weltbild," *Muenchen: Droemer,| c1966*, 1966.

[109] M. Mayda and H. R. Börklü, "An integration of triz and the systematic approach of pahl and beitz for innovative conceptual design process," *Journal of the Brazilian Society of Mechanical Sciences and Engineering*, vol. 36, no. 4, pp. 859–870, 2014.

[110] Y. Reich, "A critical review of general design theory," *Research in Engineering Design*, vol. 7, no. 1, pp. 1–18, 1995.

[111] https://www.thorlabs.com, "Pm160, pm160t, pm160t-hp user manual," https://www.thorlabs.com/drawings/20ca1312af87b7ec-8637451D-C999-31CB-68436AC81A5EA4B0/PM160-Manual.pdff, [Online; accessed 12 November, 2018].

[112] M. Laikin, *Lens Design, 4th Edition*. CRC Press, 2006.

[113] E. J. Cohen, A. B. Hull, J. Escobedo-Torres, D. D. Barber, R. A. Johnston, D. W. Small, A. Prata, and E. R. Freniere, "Optical design of the ultralight-weight first telescope," in *Radio Telescopes*, vol. 4015. International Society for Optics and Photonics, 2000, pp. 559–567.

[114] https://www.thorlabs.com/, "Aspheric condenser lenses," https://www.thorlabs.com/newgrouppage9.cfm?objectgroup_id=3835&pn=ACL2520U-A, [Online; accessed 4 January, 2019].

[115] http://atc.sjf.stuba.sk, "Table of static, dynamic and restitution coefficient of friciton," http://atc.sjf.stuba.sk/files/mechanika_vms_ADAMS/Contact_Table.pdf, [Online; accessed 12 January, 2019].

[116] https://github.com/optoMech/, "Github repository containing ueye camera parameter files," https://github.com/optoMech/Micro-imaging-Results/tree/master/uEye%20Camera%20Parameters, [Online; accessed 25 January, 2019].

[117] X. Liu, M. Tanaka, and M. Okutomi, "Noise level estimation using weak textured patches of a single noisy image," in *Image Processing (ICIP), 2012 19th IEEE International Conference on*. IEEE, 2012, pp. 665–668.

[118] ——, "Single-image noise level estimation for blind denoising," *IEEE transactions on image processing*, vol. 22, no. 12, pp. 5226–5237, 2013.

[119] https://github.com/optoMech/, "Github repository containing nikon b-2a filter files," https://github.com/optoMech/Micro-imaging-Results/tree/master/Nikon%20B-2A%20Filter%20Cube, [Online; accessed 23 January, 2019].

[120] ——, "Github repository containing fs07f file," https://github.com/optoMech/Micro-imaging-Results/tree/master/Bangs%20Laboratories%20FS07F, [Online; accessed 23 January, 2019].